Université de Montréal

Étude de la variabilité photométrique dans le vent des étoiles Wolf-Rayet

par

Guillaume Lenoir-Craig

Département de physique
Faculté des arts et des sciences

Mémoire présenté en vue de l'obtention du grade de
Maître ès sciences (M.Sc.)
en Astrophysique

31 août 2020

© Guillaume Lenoir-Craig, 2020

Résumé

Ce mémoire présente une analyse de données photométriques d'étoiles de type Wolf-Rayet ayant pour objectif de caractériser les causes de la variabilité stochastique à court terme omniprésente chez ces étoiles, ainsi que la variabilité périodique due aux éclipses atmosphériques dans deux systèmes particuliers.

À l'aide de données de la mission spatiale BRITE, les éclipses initialement supposées atmosphériques des systèmes WR22 et WR48 ont été investiguées avec un modèle analytique, suivi d'une modélisation numérique de l'éclipse pour WR22. Le taux de perte de masse de l'étoile Wolf-Rayet, $\dot{M}_{WR}$, la profondeur optique du vent, τ_0, et l'angle d'inclinaison du système, i, ont été déterminés avec précision pour WR22, tandis que des valeurs-plafonds pour ces paramètres ont été obtenues avec un angle i tiré de la littérature pour WR48.

L'étude de la variabilité stochastique dans le vent de 55 étoiles Wolf-Rayet galactiques a été conduite en utilisant 70 séries temporelles obtenues avec les satellites MOST, BRITE-Constellation et TESS. L'application d'un modèle semi-Lorentzien aux périodogrammes des observations a permis d'obtenir des paramètres caractéristiques : l'amplitude typique, la fréquence caractéristique et le taux d'augmentation de l'amplitude de variabilité.

Des comparaisons entre les paramètres obtenus et ceux de la littérature nous ont permis de contextualiser le rôle de divers processus physiques dans l'origine de la variabilité, tel l'instabilité du processus d'entraînement du vent, d'une zone de convection subsurfacique engendrée par l'ionisation partielle des éléments du groupe du fer, ainsi qu'une possible contribution d'ondes de gravité générées à l'interface du coeur convectif et de la zone radiative.

Mots clés : étoiles : Wolf-Rayet, vents, binaires : éclipsantes - Techniques : photométrique

Abstract

We present an analysis of photometric observations of Wolf-Rayet stars in an effort to characterize their ubiquitous short-term stochastic variability and the origin of the periodic variability due to atmospheric eclipses in two specific systems.

With data from BRITE-Constellation, we investigated what we initially thought to be atmospheric eclipses in the WR22 and WR48 systems. Both stars' datasets were first analyzed using an analytical atmospheric eclipse model, and then a fully numerical core and wind eclipse model was used to better characterize the ambiguous case of WR22. The mass-loss rate of the Wolf-Rayet component $\dot{M}_{WR}$, the optical depth of the wind, τ_0, and the inclination angle of the system, i, were accurately determined for WR22, whereas for WR48 an upper limit was found for $\dot{M}_{WR}$ and τ_0 using an inclination angle from the litterature.

The study of the short-term stochastic variability in the winds of 55 Wolf-Rayet stars was obtained with 70 time-series produced by MOST, BRITE and TESS. The amplitude spectra of these stars were analyzed using a semi-Lorentzian function that allowed us to extract characteristic parameters. Comparisons between the values we obtained and those from the litterature were carried out and we discuss the possible contribution to the variability of various physical processes, namely the line de-shadowing instability, the presence of a subsurface iron-group driven convection zone and possibly of internal gravitational waves generated at the boundary between the convective core and the radiative layer to the observed variability.

Keywords : stars : Wolf-Rayet, winds, binaries : eclipsing - Techniques : photometric

Table des matières

Résumé 3

Abstract 5

Liste des tableaux 11

Table des figures 13

Liste des sigles et des abréviations 19

Remerciements 21

Introduction 23

1.1. Les étoiles Wolf-Rayet 23

1.2. Variabilité 26

1.2.1. Inhomogénéités à petite échelle 26

1.2.2. Structures à grande échelle 27

1.2.3. Binarité 29

First Article. Precision photometric monitoring from space of the multiple system θ Muscae including the WR binary WR48 33

Contributions de Guillaume Lenoir-Craig à l'article 34

1. Introduction 37

2. Observations 38

3. Results 39

4. Discussion 48

5. Conclusions 49

Acknowledgements 50

References 51

Second Article. The bright H-rich WR star WR22 and its single eclipse per 80-day orbit : photospheric or atmospheric ?........ 55

Contributions de Guillaume Lenoir-Craig à l'article 56

1. Introduction 59

2. Observations 59

3. Modelling 61
  3.1. light-curve analysis strictly as an atmospheric eclipse 63
  3.2. Light-curve analysis as a photospheric and wind eclipse 67
  3.3. Roche lobe model plus wind eclipse 68

4. Discussion 78

5. Conclusions 79

Acknowledgements 79

References 79

Troisième article. A study of the stochastic photometric variability in the winds of Galactic Wolf-Rayet stars 83

Contributions de Guillaume Lenoir-Craig à l'article 84

1. Introduction 87

2. Observations 88
2.1. BRITE Photometry 88
2.2. TESS Photometry 90
2.3. MOST Photometry 92
3. Data Analysis 93
3.1. Frequency Analysis 93
3.2. Fit of the Stochastic Variability 94
3.3. Wavelet Analysis 97
4. Discussion 100
4.1. Line De-Shadowing Instability 100
4.2. Sub-Surface Convection Zones 103
4.3. Core-Generated Gravity Waves 104
5. Conclusions 105
Acknowledgements 106
Bibliographie 107
Conclusion 111
Annexe A : Courbes de lumières 113
TESS 113
BRITE 122
MOST 125
Annexe B : Périodogrammes avec modèle de bruit ajusté 127
TESS 127

BRITE 136

MOST 139

Annexe C : Analyses en ondelettes 141

TESS 141

BRITE 158

MOST 163

Liste des tableaux

2.1 Parameters of the L96 model with F values intercepting the 99.9% confidence level 48

3.1 Parameters of the adopted light-curve solution. 66

3.2 Parameters that determine if there are photospheric eclipses. All radii are in $R_\odot$. i is assumed to be 80°. 68

3.3 Major A13 model parameters. 71

4.1 BRITE photometric datasets of WR stars used in this study. 89

4.2 TESS photometric datasets of WR stars used in this study. 91

Table des figures

1.1 Représentation schématique de la formation d’un profil P Cygni dans le vent d’une étoile massive chaude. La composante en absorption provient de la partie du vent devant l’étoile qui diffuse des photons hors de la ligne de visée de l’observateur, tandis que les composantes bleues et rouges en émission proviennent d’une région symétrique autour de l’étoile. Figure adaptée de la figure 18.2 de Walker (2017).. 25

1.2 Courbe de lumière TESS de l’étoile WR24 (WN6ha), dans laquelle est visible la variabilité photométrique stochastique typique des étoiles Wolf-Rayet. Une constante C = 2 456 998.5 a été soustraite des dates juliennes barycentrées (BJD) par le pipeline de réduction de données de TESS. 26

1.3 Évolution dans le temps de la structure en vélocité (à gauche) et en densité (à droite) de la région interne d’un vent non-perturbé en tenant compte de la force radiative exercée par la diffusion de multiples raies. Les régions externes du vent montrent des perturbations en vélocité autoexcitées, tandis que les parties internes restent lisse. Figure tirée de Sundqvist et al. (2013). 28

1.4 Structure en densité du vent tiré d’une simulation hydrodynamique d’une étoile O en rotation, avec deux taches brillantes placées à la base du vent sur des faces opposées simulant un flux radiatif perturbé. La région (I) correspond à la zone de densité augmentée par la tache, (II) est nommée précurseur prograde, la région (III) est la zone de compression du gaz dans la structure du CIR, (IV) correspond à une région de raréfaction du CIR causée par l’interaction entre les écoulements de matière à différentes vitesses dans le vent. En (V) se forme un gradient de vélocité radiale, qui entre en collision avec la zone de raréfaction à grande distance radiale de l’étoile pour ensuite disparaître. Figure tirée d’Owocki (1996). 30

1.5 Simulation hydrodynamique de deux vents adiabatiques en collision, dont le ratio des flux de quantité de mouvement est $R = \sqrt{5}$. Les lignes pleines correspondent à des isocontours de densité. La ligne en pointillé correspond à la surface où les quantités de mouvement des vents s’équivalent. Figure tirée de Stevens et al. (1992). 31

2.1 De-correlated, time-dependent light-curve of θ Muscae obtained by the BRITE-Toronto satellite in a red optical filter. 38

2.2 Periodogram of the WR48 light-curve presented in Figure 2.1, with the Hill et al. (2002) orbital period shown by a red dashed line. The inset shows the amplitude spectrum up to the Nyquist frequency of the satellite. 40

2.3 Top : BRITE light-curve of WR48. The red dashed line is the combined result of the Inverse Wavelet Transform of the wavelet analysis performed using the Mexican-hat mother function on the signal. Bottom : The power-spectrum of the wavelet analysis. The black region corresponds to the cone of influence (COI) of the period of the wavelets. The large, relatively uniform feature observed around $t = 500d$ is caused by the lack of data, as can be seen in the light-curve. The contour lines enclose regions with greater than 95% confidence level 41

2.4 BRITE amplitude spectrum of WR48 fitted with a semi-Lorentzian noise model shown as a solid green line, comprised of a red and white component, respectively shown as a red and a blue dashed line. 42

2.5 Phased light-curve with only BRITE-orbit binning of the θ Mus data using the Hill et al. (2002) ephemeris. No dip near phase zero due to an atmospheric eclipse is obvious. We neglect the small uncertainty of the period brought forward by 417 cycles from the Hill et al. study to the BRITE data, amounting to an accumulated error of about $1d$. 43

2.6 Calculated F values plotted against the injected artificial $\dot{M}$ in a light-curve with a length and a Gaussian noise level emulating the real BRITE light-curve of θ Mus. The F value corresponding to the ratio of the reduced χ^2 of the flat model divided by the reduced χ^2 of the L96 model on the BRITE data of θ Mus is shown in black. The dashed green line represents the running mean of those values with a 200-point window and the yellow dashed lines show the corresponding running standard deviations. The solid red (blue) line is set at the F value representing a 99% (99.9%) confidence level. Both red and blue dashed lines show the intercept of the running average with their respective confidence levels. The average $\dot{M}$ for a WC5/6 star calculated from Sander et al. (2019) is marked by a dashed gray line, and the area encompassing a standard deviation from that value is shown as a filled gray area. 45

2.7 Calculated χ^2 of the flat and L96 models shown against the injected artificial $\dot{M}$ in the corresponding artificial light-curve. For more clarity in the followed trends for both χ^2, running averages of 200 points are shown as a red dashed line for the L96 model and as a blue dashed line for the flat model. 46

2.8 Calculated F values of artificial light-curves containing varying numbers of 19.1375 days cycles. The solid blue and red lines respectively correspond to a 99% and 99.9% confidence level in the detection. The solid black line corresponds to the average F value of 500 simulations over the shown cycles, with the gray area representing three standard deviations from this value. 47

3.1 De-correlated time-dependent light-curve of WR22 obtained by the BRITE-Heweliusz satellite in its 2017 coverage of the Carina field, after subtracting off the mean. The two eclipses separated by ∼80 days are clearly seen. 61

3.2 As in Fig.1 but for 2018. The single eclipse observed near the middle of the run is easily distinguished. 61

3.3 Top : periodogram of the light-curve presented in Figure 3.1 for 2017. Middle : periodogram of the fitted eclipse model without the data but following the same point sampling as the data. The high number of oscillating harmonics is due to the presence of two eclipses in that time-series, which interfere with one another in the Fourier dimension. Bottom : periodogram of the 2017 observations after subtracting the fitted model. The frequency position of the 80.336d orbital period is marked with a red vertical dashed-line in all periodograms. 62

3.4 Top : periodogram of the light-curve presented in Figure 3.2 for 2018. Middle : periodogram of the fitted eclipse model without the data but following the same point sampling as the data. This time, the harmonic spectrum is still seen, albeit at somewhat lower amplitude but without the extreme oscillations, due to the presence of only one eclipse. Bottom : periodogram of the 2018 observations after subtracting the fitted model. As in Figure 3.3, the 80.336 *d* orbital period is marked with a red vertical dashed-line in all periodograms. 63

3.5 Phased light-curve of WR22 for 2017 and 2018 combined from the BHr satellite. 64

3.6 Top : Phased light-curve of WR22's eclipses from 2017 and 2018, fitted in red (for the whole light-curve, not just the part shown here) with Lamontagne et al.

(1996) equation for a WR wind with $\beta = 1$. Blue dots correspond to the data acquired around the time of 2017's first observed eclipse, magenta dots are for 2017's second eclipse and green dots for 2018's only eclipse. Bottom : Residuals obtained from subtracting the fit from the data. 67

3.7 Best fit model parameters as function of the WR temperature. Left : Model 1, $R_{\rm O} = 7.53$ R$_\odot$ (luminosity class V). Right : Model 2, $R_{\rm O} = 13.38$ R$_\odot$ (luminosity class III). The dashed lines in top panels show 99% significance level. The red lines show χ^2 curves at the assumed observational uncertainty 0.0108 (see the text). The dashed lines in the inclination plots mark the borders between wind-only, partial geometric, and total eclipses. 73

3.8 Best-fit light-curves corresponding to the respective χ^2 minima from the previous figure. Left : Model 1. Right : Model 2. The red solid line is the best fit Roche+Wind light-curve. The black solid line shows the Roche model component only, i.e. not including the wind absorption of the O-star flux. The colors of the observed data points in the lower panel correspond to those in the L96 best fit plot. 75

3.9 Characteristic best fit light-curves for Model 1 (left) and 2 (right). The observed light-curve is shown by colored dots (the color legend as above). The model light-curves are shown by solid red lines. The black lines show the Roche component of light-curves, i.e. not including wind absorption of the O star. The values of reduced χ^2, $T_{\rm WR}$, inclination, flux ratio, and $\dot{M}$ (in units $10^{-5}\,{\rm M}_o dot\,{\rm yr}^{-1}$) are shown at each individual light-curve. 76

3.10 Sky plane view of the system in best fit Models 1 (top) and 2 (bottom) at orbital phases before, at the moment, and after conjunction.The phase difference with the conjunction moment is ±0.01. 77

4.1 Brite orbital-mean magnitudes of WR24 as a function of the Heliocentric Julian Date, after subtraction of the mean, showing the stochastic photometric variability of this star. 90

4.2 TESS light-curve of WR40 after subtration of the mean magnitude. 92

4.3 MOST light-curve of WR121. 93

4.4 Amplitude spectrum of WR24 as observed by BHr in 2017 (black solid line). The solid green line corresponds to the fit of the semi-lorentzian distribution and the red and white noise components are respectively shown as red- and blue-dashed lines. 94

4.5 Fitted white noise levels plotted against their corresponding cadence, for the TESS light-curve of WR24. 96

4.6 Superimposed fits of the semi-lorentzian profiles of the WR stars in our sample characterizing the morphology of low-frequency variability, color-coded by bolometric luminosity and separated by satellite cadence and data accuracy. 97

4.7 Fitted parameters of the red noise component, α_0, ν_{char} and γ as a function of various wind and stellar parameters. Blue points are for TESS data, black for BRITE and red for MOST. Inverted triangles are for WC stars and filled circles are for WN stars. The slope of the fitted straight lines together with its error is given in the top-right corner of each panel. 98

4.8 Zoom of the anti correlation between the level of variability characterized by the α_0 parameter with the stellar temperature. The points are colour-coded with the bolometric luminosity. 99

4.9 Top : two-minute sampled TESS light-curve of WR24 binned to have one data-point per hour. The red dashed line is the result of the Inverse Wavelet Transform of the wavelet analysis performed using the Mexican-hat mother function on the signal. Bottom : The power-spectrum of the wavelet analysis. The hashed region corresponds to the cone of influence (COI) of the period of the wavelets. The large, relatively uniform feature observed around t = 1582 d corresponds to the lack of data as seen in the light-curve. The contour lines enclose regions with greater than 95% confidence for a red-noise process, with a lag-1 auto-correlation coefficient between successive data points of 0.72. 100

4.10 Amplitude of variability α_0 versus the percentage f of scattered starlight for the biggest simulated clump. 101

4.11 steepness of the periodogram γ as a function of various model parameters of the scattering of stellar light on clumps in the wind and versus the mass-loss rate and stellar radius. 102

4.12 Steepness of amplitude spectrum γ as a function of absolute magnitude 105

Liste des sigles et des abréviations

CIR	Région d'interaction en corotation, de l'anglais *Corotating Interaction Region*
DAC	Composante d'absorption discrète, de l'anglais *Discrete Absorption Component*
DFT	Transformée de Fourier discrète, de l'anglais *Discrete Fourier Transform*
FeCZ	Zone de convection subsurfacique engendrée par des ions du groupe du fer, de l'anglais *Iron-group driven subsurface convection zone*
IGW	Ondes de gravité internes, de l'anglais *Internal Gravity Waves*
LDI	Instabilité de désombrage de raie, de l'anglais *Line De-shadowing Instability*
$M_{\odot}$	Masse solaire = 1.98×10^{30} kg
LBV	Variable Bleue Lumineuse, de l'anglais *Luminous Blue Variable*
v_{∞}	Vitesse terminale du vent stellaire

WR	Wolf-Rayet

Remerciements

Je tiens d'abord à adresser mes remerciments les plus sincères à ma directrice de thèse Nicole St-Louis, qui m'a fait découvrir la beauté et la complexité des étoiles Wolf-Rayet et de leurs vents stellaires. Son positivisme, sa rigueur, ainsi que ses excellentes capacités d'enseignement et de communication m'ont grandement aidé à progresser en tant que chercheur. Je tiens à chaudement remercier Anthony Moffat pour tout le support qu'il m'a offert pendant ma maîtrise. Ses grandes connaissances des vents stellaires m'ont guidé pendant mes travaux et nos discussions toujours aussi instructives qu'agréables m'ont doublement motivé à vouloir en savoir toujours plus. Je tiens aussi à remercier Paul Charbonneau de m'avoir en tout premier donné la piqûre de la recherche, qui a été déterminante dans ma résolution à poursuivre dans cette voie. Je remercie également Igor Antokhin et Eleonora Antokhina pour leurs contributions inestimables à l'article sur l'éclipse atmosphérique de WR22, ainsi que Herbert Pablo pour nos discussions sur la variabilité des étoiles Wolf-Rayet et sur les techniques de dé-corrélation des données BRITE. Un remerciment spécial à Tahina Ramiaramanantsoa pour le cours éclair sur la dé-corrélation de données satellites dans les premiers jours de ma maîtrise. Merci à Ken Gayley pour sa patience et ses explications détaillées sur les instabilités à petites échelles, ainsi qu'à Dominic Bowman pour des discussions très pertinentes sur la variabilité des étoiles massives. Je me dois aussi de remercier l'équipe de BRITE-Constellation pour la bourse m'ayant permis de financer les premiers mois de cette maîtrise, sans laquelle rien de tout ceci n'aurait été possible.

En terminant je veux remercier mes parents, Suzanne et Gilles, qui m'ont de tout temps encouragé dans ma fascination pour ce gigantesque Univers nous entourant et mon désir d'en comprendre toujours plus le fonctionnement.

Introduction

1.1. Les étoiles Wolf-Rayet

Les étoiles Wolf-Rayet doivent leur appelation aux astronomes français les ayant observées pour la première fois en 1867, Charles Wolf et George Rayet . Elles sont, pour la plupart, les descendantes évolutives d'étoiles de la séquence principale de type O possédant des masses initiales dépassant $25M_{\odot}$ (Crowther & Smartt, 2007). Quelques étoiles O encore sur la séquence principale ont développé des vents ayant la signature spectrale des Wolf-Rayet et sont donc aussi catégorisées comme tel. Ces étoiles sont pourvues des vents stellaires stables les plus denses et puissants de l'univers, avec des vitesses terminales $v_{\infty} \sim 2000$ km/s et des taux de perte de masse typiques de $\dot{M} \sim 10^{-6} - 10^{-5} M_{\odot}$/année. La densité de leurs vents est si élevée qu'elle rend ces derniers optiquement épais, dissociant ainsi la surface hydrostatique de la photosphère. On distinguera alors le rayon hydrostatique, défini comme la distance à laquelle l'opacité de Rosseland est très élévée (environ 10), R_{*}, du rayon photosphérique, R_{ph}, où l'opacité de Rosseland $\sim 2/3$, ce dernier pouvant se situer à plusieurs rayons stellaires de la surface hydrostatique. De plus, les étoiles Wolf-Rayet ont typiquement des températures à la surface hydrostatique entre 30 000 et 210 000 K, les classant parmi les objets les plus chauds de l'Univers. Le taux de perte de masse d'un vent stationnaire à symétrie sphérique peut être décrit par l'équation de continuité, qui indique que rien n'est détruit ou créé dans ce vent (Lamers et Cassinelli, 1999),

$$\dot{M} = 4\pi r^2 \rho(r) v(r), \tag{1}$$

où r est la distance au centre de l'étoile, alors que ρ(r) et v(r) sont respectivement la structure en densité et la loi de vitesse du vent. La masse éjectée de la surface de l'étoile est accélérée asymptotiquement jusqu'à la vitesse terminale v_{∞}, un paramètre important pour l'étude des vents stellaires. Il est d'ailleurs utilisé dans une approximation très utilisée pour décrire la loi de vitesse du vent, considérée proche de la réalité, appelée loi β (Lamers & Cassinelli, 1999) :

$$v(r) \approx v_{\infty}(1 - R_{*}/r)^{\beta} \tag{2}$$

où $v(r)$ est la vitesse du vent au point r, R_* est le rayon stellaire et β est un paramètre libre décrivant la raideur du profil de vitesse, valant $\approx 1/2$ pour les étoiles massives chaudes. Ces denses flux de matière perdus par les Wolf-Rayet sont la propriété principale gouvernant leurs temps caractéristiques d'évolution et influencent aussi leurs compagnons si elles font partie de systèmes multiples, tels que révélé par la détection de rayons X durs issus de vents en collision créant des chocs dans des systèmes WR+O (e.g. Skinner et al. 2006). De plus, ces taux de perte de masse élevés sont la cause de la perte de l'enveloppe d'hydrogène de ces étoiles et sont donc la raison pour laquelle les étoiles Wolf-Rayet sont pauvres en hydrogène.

La phase Wolf-Rayet compte pour environ 10% de la vie de ces étoiles, dont on pense qu'elles terminent leurs vies en explosion supernova de types variés, dépendamment de leur masse initiale. Les Wolf-Rayet sont des objets rares dans le cosmos ; 667 ont été catalogués à ce jour dans la Voie Lactée selon le *Galactic Wolf Rayet Catalogue*[1] sur un total estimé de 1200 ± 200 (Rosslowe & Crowther, 2015). Bien qu'en faible nombre, les étoiles Wolf-Rayet jouent un rôle d'avant-plan dans l'écosystème galactique. Leurs vents injectent de grandes quantités d'énergie sous forme d'énergies cinétique et radiative dans le milieu interstellaire, contribuant à la formation de nouvelles étoiles tout en enrichissant leur environnement en éléments chimiques lourds (Skinner, 2018).

Les puissants vents des Wolf-Rayet sont, de plus, la source de leurs spectres d'allure particulière montrant de larges raies d'émission d'hélium, de carbone, d'azote ou d'oxygène. Les ratios de la force de ces raies spectrale les uns par-rapport aux autres déterminent à quelle sous-catégorie spectrale appartiennent les Wolf-Rayet ; les WN sont particulièrement riches en hélium et azote, les WC en héliun et carbone et les WO en hélium et oxygène. Ces raies sont souvent accompagnées de profils en absorption décalés vers le bleu nommés P Cygni, d'après l'étoile variable lumineuse bleue (LBV) du même nom découverte en 1600 par Willem Janszoon Blaeu (de Groot, 1988). Ces profils particuliers sont dus au fort vent stellaire en expansion, qui tel que présenté à la figure 1.1, entraîne l'apparition d'une composante en absorption décalée vers le bleu additionnée à une composante en émission s'étendant du bleu au rouge.

Les études observationnelles des Wolf-Rayet sont cependant compliquées par la grande opacité de leurs vents. En effet, puisque la profondeur optique $\tau = 2/3$ correspondant à la source d'émission du flux continu de l'étoile se situe dans le vent, la photosphère ne coïncide donc pas avec la surface hydrostatique et les données collectées par photométrie proviennent uniquement de leurs vents opaques. Il en va de même avec les observations spectroscopiques, bien que la structure en émissivité des vents permette dans ce cas d'observer à différentes distances dans ces derniers en fonction des raies d'émissions choisies.

---

[1] http ://pacrowther.staff.shef.ac.uk/WRcat/index.php

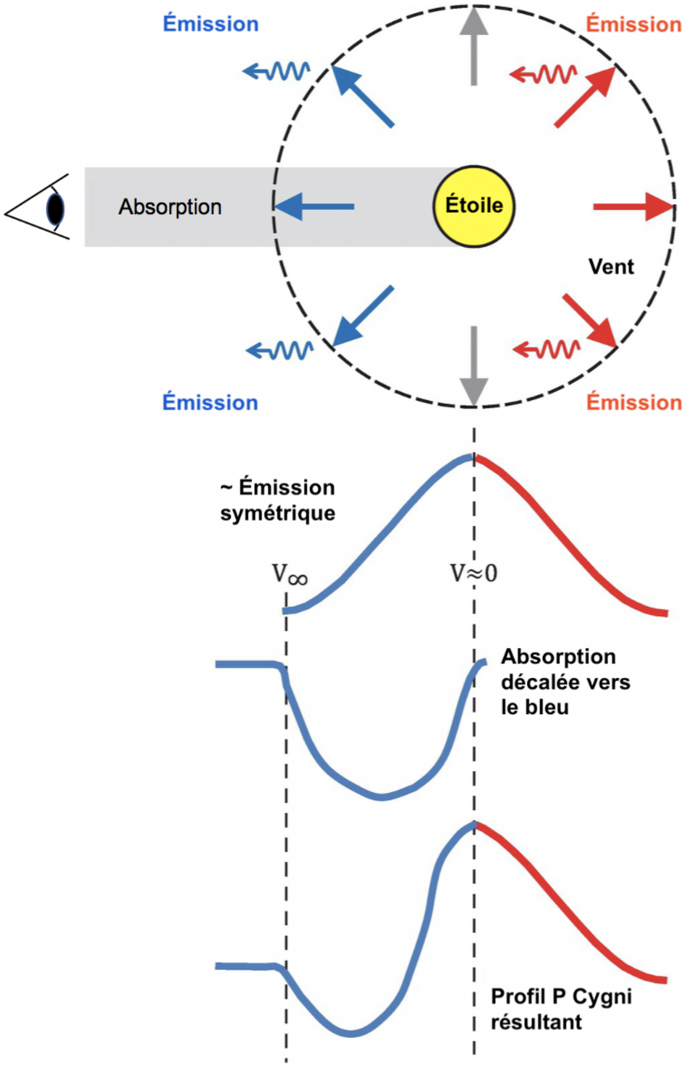
Émission
Émission
Absorption
Étoile
Vent
Émission
Émission
~ Émission symétrique
V∞
V≈0
Absorption décalée vers le bleu
Profil P Cygni résultant

Figure 1.1. Représentation schématique de la formation d'un profil P Cygni dans le vent d'une étoile massive chaude. La composante en absorption provient de la partie du vent devant l'étoile qui diffuse des photons hors de la ligne de visée de l'observateur, tandis que les composantes bleues et rouges en émission proviennent d'une région symétrique autour de l'étoile. Figure adaptée de la figure 18.2 de Walker (2017).

Les vents des Wolf-Rayet ont longtemps été modélisés comme étant homogènes, stationnaires en équilibre thermodynamique et possédant une symétrie sphérique (Hamann 1985, Hillier 1990). Cependant, l'observation de signaux variables dans les données photométriques et spectrométriques à diverses longueurs d'ondes, de façon périodique ou non, a fait tomber ces suppositions. Un exemple typique de cette variabilité non-périodique est observable dans la courbe de lumière TESS de l'étoile WR24 (WN6ha) présentée à la figure 1.2.

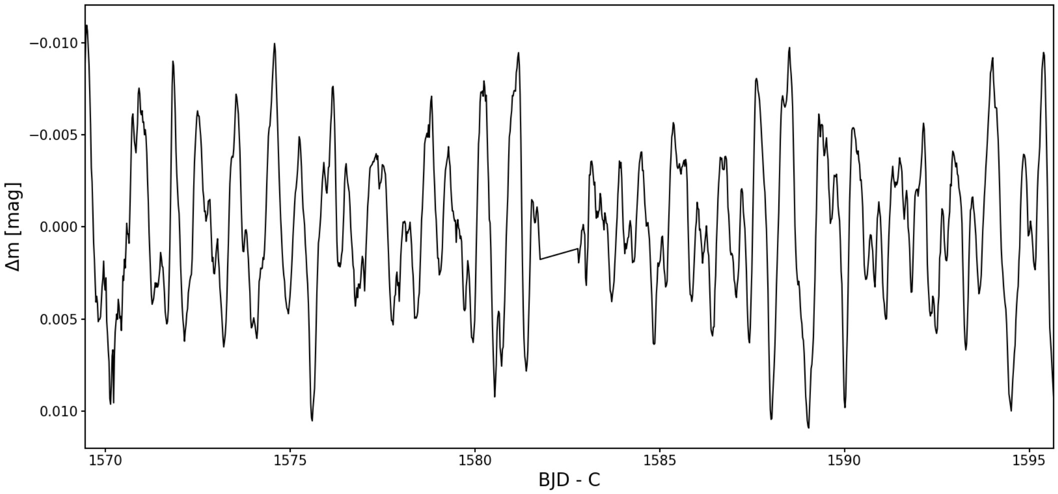

Figure 1.2. Courbe de lumière TESS de l'étoile WR24 (WN6ha), dans laquelle est visible la variabilité photométrique stochastique typique des étoiles Wolf-Rayet. Une constante C = 2 456 998.5 a été soustraite des dates juliennes barycentrées (BJD) par le pipeline de réduction de données de TESS.

1.2. Variabilité

1.2.1. Inhomogénéités à petite échelle

Tel que souligné par Brown et al. (1995), les études photométrique, polarimétrique et spectroscopique semblent indiquer une origine physique commune aux phénomènes transitoires aléatoires observés dans les vents des Wolf-Rayet. Ce fut Robert (1992) qui fut la première à observer une corrélation entre les variabilités temporelles stochastiques dans les données photométrique et spectroscopique des Wolf-Rayet. Plus récemment, Ramiaramanantsoa et al. (2018) ont démontré qu'une fois la composante périodique des données photométriques de l'étoile ζ Puppis enlevée, la variabilité observée est fortement corrélée avec les sous-pics d'émission présents dans la raie d'HeII à 4686 Å. Cependant, afin d'être en mesure de comprendre l'origine physique commune de ces phénomènes, un cadre théorique cohérent avec les observations doit être mis en place.

Les études théoriques sur la nature non-linéaire de l'évolution des instabilités dans les vents des étoiles massives chaudes révélèrent qu'elles grandissent de manière exponentielle et forment des structures en densité et vitesse ayant des tailles caractéristiques de l'ordre d'une longueur de Sobolev ($l_{Sob} = v_{th}/(dv/dr)$) (e.g. Lucy (1984), Owocki (1994), Feldmeier et al. (1995), Sundqvist et al., 2013, 2018). Tel que présenté à la figure 1.3, de substantielles instabilités se développent dépassé 1.1 – 1.5 R_* dans le vent. Les coquilles de densité élevée observées dans les premières 80 ks disparaissent pour laisser place à un état d'équilibre. Ces structures sont autoexcitées, c'est-à-dire que la rétrodiffusion de raie depuis les régions externes vers les régions internes déclenche en retour des instabilités se déplaçant vers l'extérieur.

Brown et al. (1995), au terme de leur interprétation quantitative de données simultanément collectées en spectroscopie, photométrie et polarimétrie d'étoiles Wolf-Rayet, furent en mesure d'en tirer des conclusions qui peuvent être résumées comme suit :

- Les sous-pics observés sur les raies en émission optiquement minces sont causés par des augmentations locales de densités dans le vent, nommés "blobs" par les auteurs. L'observation simultanée de plusieurs de ces structures est interprétée par la présence de plusieurs blobs s'éloignant de leur étoile dans des directions différentes selon notre ligne de visée.
- Les phénomènes transitoires en photométrie et polarimétrie sont dus à l'émissivité des blobs et à leur diffusion du flux lumineux stellaire ou du flux du continu émis par le vent.
- Les phénomènes transitoires révèlent des angles de polarisation aléatoires, suggérant qu'ils sont produits par des sources locales réparties à travers l'entièreté du vent stellaire.
- La baisse de variabilité photométrique et polarimétrique mesurée lorsque l'intervalle de longueurs d'ondes observée est plus large s'inscrit bien dans le contexte d'un vent stellaire produisant des clumps, puisque les contributions mineures de ces derniers deviennent de moins en moins importantes en comparaison avec l'émission globale non-polarisée du vent.

Ainsi, ces modélisations suggèrent que les vents entraînés par la radiation sont intrinsèquement instables et que leur structure est donc susceptible d'être influencée par des perturbations à la base du vent.

1.2.2. Structures à grande échelle

Les vents des étoiles massives chaudes étant propulsés par l'accélération radiative induite par l'absorption et la réémission de photons ultraviolets dans des raies de résonnance d'éléments lourds, observer ces vents dans le domaine UV est pertinent pour l'étude des structures y existant. C'est ce qui fut accompli avec la mission d'observation spatiale *International Ultraviolet Explorer* (IUE) lancée en 1978, qui permit de collecter pendant ses 18 années de fonctionnement plus de 104 000 spectres UV à haute et basse résolutions d'une panoplie d'objets célestes. Des composantes d'absorption discrètes (DACs), soit des augmentations de profondeur optique dans un intervalle de longueur d'onde restreint, furent découvertes

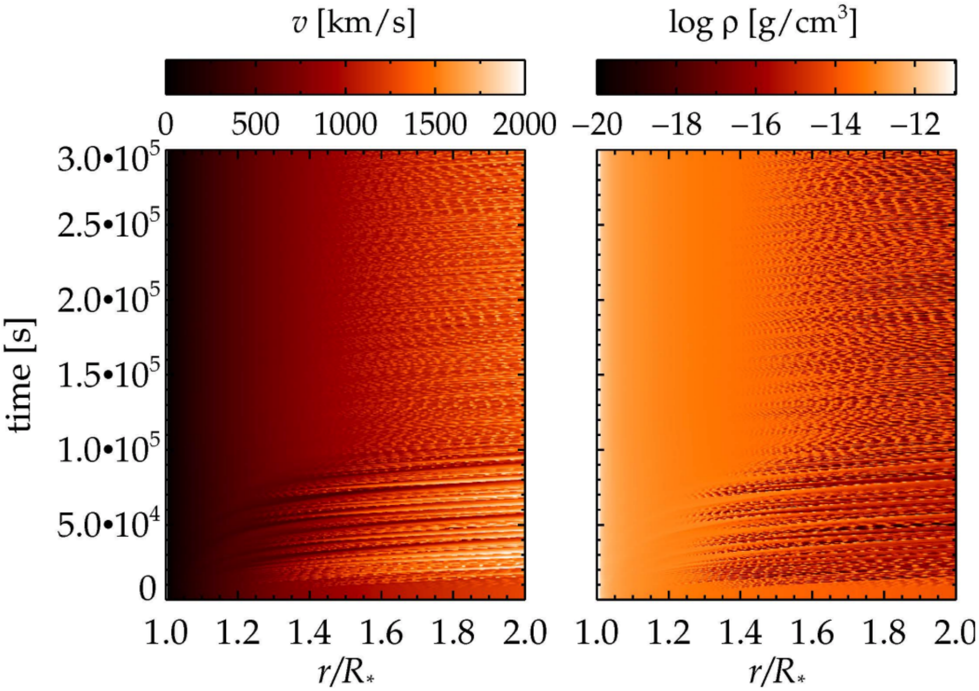

Figure 1.3. Évolution dans le temps de la structure en vélocité (à gauche) et en densité (à droite) de la région interne d'un vent non-perturbé en tenant compte de la force radiative exercée par la diffusion de multiples raies. Les régions externes du vent montrent des perturbations en vélocité autoexcitées, tandis que les parties internes restent lisse. Figure tirée de Sundqvist et al. (2013).

dans des profils P Cygni UV non-saturés de la majorité des étoiles O et B observées par IUE (Grady, Bjorkman & Snow, 1987 ; Howarth et Prinja, 1989).

Apparaissant de manière périodique sur une échelle de temps cohérente avec la période de rotation des étoiles, ces DACs migrent vers l'aile bleue des profils P Cygni depuis leur emplacement de formation à basse vitesse dans la raie et deviennent plus étroites alors qu'elles approchent de v_∞ (Puls et al. 2008). La profondeur optique d'absorption, la corrélation avec la vitesse de rotation de l'étoile ainsi que les basses vitesses auxquelles semblent se former ces structures nous indiquent qu'elles prennent naissance à la base du vent (Massa et Prinja, 2015). Afin de produire les creux d'absorption observés, la structure à l'origine des DACs doit être suffisament grande pour couvrir une fraction substantielle du disque stellaire (Cranmer et Owocki, 1995). De plus, la non-détection de structures variables en émission dans les raies P Cygni du domaine UV ainsi que la non-détection de variations significatives dans l'infrarouge (Howarth, 1992) permet d'écarter l'idée d'une structure à symétrie sphérique comme source des DACs.

Cranmer et Owocki (1996) furent les premiers à mettre au point des simulations hydrodynamiques 2D de vents d'étoiles O en rotation soumises à des perturbations du flux radiatif à la base du vent, simulant une surface stellaire influencée par des pulsations non-radiales ou des phénomènes de nature magnétique y prenant place. Ces perturbations engendrent des flux de particules ayant des vitesses différentes de celles du vent non-perturbé, qui entrent en collision avec ce dernier à cause de la rotation de l'étoile et crééent ainsi une structure en densité et vitesse de forme spirale autour de l'étoile, nommée région d'interaction en corotation (CIR), tel que présenté à la figure 1.4. Ces modèles prédisent l'apparition de composantes étroites en absorption superposées aux profils P Cygni très similaires aux DACs.

Bien qu'omniprésentes chez les étoiles O, les CIRs sont rarement observées chez leurs descendantes Wolf-Rayet. L'explication en est simple : la grande majorité des composantes d'absorption des profils P Cygni des étoiles Wolf-Rayet sont saturées. Conséquemment, St-Louis et al. (2009) et Chené et St-Louis (2011) ont examiné un ensemble de 64 étoiles Wolf-Rayet afin de tenter d'y détecter la présence de CIRs causant des variations périodiques à grande échelle dans de larges raies *en émission*. Ils ont trouvé que $\sim$ 20% des étoiles observées ont révélé des variations qui pourraient être associées à de telles structures. Ces dernières peuvent aussi avoir un impact sur les observations photométriques, tel que révélé par la présence d'un signal périodique non-attribuable à la binarité, de période P = 4.08 jours dans le flux lumineux de WR110 (Chené et al., 2011).

1.2.3. Binarité

Les modèles de formation d'amas stellaires sans mécanismes de rétroaction montrent que la fragmentation de nuages moléculaires turbulents peut entraîner la formation de plusieurs centaines d'étoiles (Clarke, Bonnell & Hilolenbrand, 1999). Les plus massives d'entre elles se forment au milieu des puits de potentiels gravitationnels du nuage, où elles y accrètent plus rapidement la matière environnante que les étoiles situées plus loin (Bonnell et al. 2001a). Ce processus d'accrétion ne devient réellement efficace que lorsque plusieurs étoiles sont présentes et compétitionnent pour le réservoir de masse, permettant ainsi aux plus massives d'accréter davantage (Bonnel et al., 2004). De plus, le gaz tombant vers le centre des sous-amas est accompagné d'étoiles s'étant formées en-dehors de ce dernier, augmentant à la fois la masse et le nombre d'étoiles de la région et accélérant encore plus le processus d'accrétion.

Dans ce contexte, il est peu surprenant que des modèles d'évolution stellaires prédisent que $\sim$70% des étoiles de type O vont avoir des échanges de masse avec un compagnon au courant de leur vie, qui mèneront à une éventuelle fusion stellaire dans le tiers des cas (Sana et al. 2012). La théorie générale de l'évolution des systèmes binaires massifs prédit la séquence évolutive suivante pour les paires d'étoiles O + O (van den Heuvel & de Loore, 1973) :

$$\mathrm{O+O} \rightarrow \mathrm{WR+O} \rightarrow \mathrm{c+O} \rightarrow \mathrm{c+WR} \rightarrow \mathrm{c+c}$$

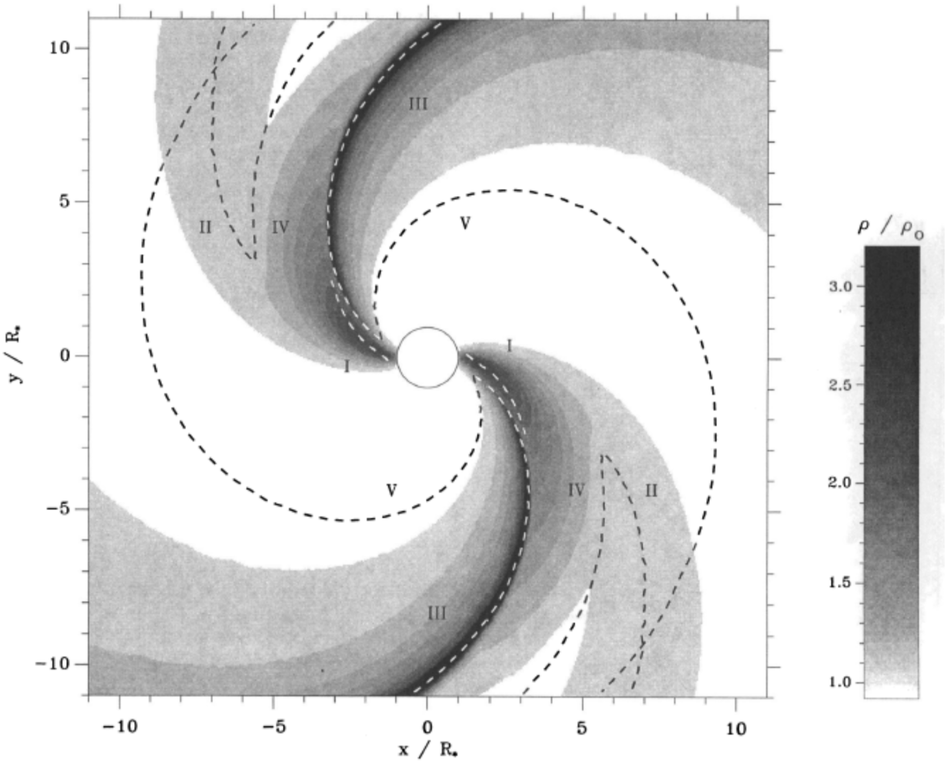

Figure 1.4. Structure en densité du vent tiré d'une simulation hydrodynamique d'une étoile O en rotation, avec deux taches brillantes placées à la base du vent sur des faces opposées simulant un flux radiatif perturbé. La région (I) correspond à la zone de densité augmentée par la tache, (II) est nommée précurseur prograde, la région (III) est la zone de compression du gaz dans la structure du CIR, (IV) correspond à une région de raréfaction du CIR causée par l'interaction entre les écoulements de matière à différentes vitesses dans le vent. En (V) se forme un gradient de vélocité radiale, qui entre en collision avec la zone de raréfaction à grande distance radiale de l'étoile pour ensuite disparaître. Figure tirée d'Owocki (1996).

où c correspond à un objet compact, soit une étoile à neutron ou un trou noir, résultant de l'explosion en supernova d'une des Wolf-Rayet. Dans certains cas, l'explosion supernova permet au système binaire d'acquérir une vitesse de l'ordre de plusieurs centaines de km/s et de s'éloigner du plan galactique, devenant alors un système en fuite. Les étoiles Wolf-Rayet avec une grande vitesse et une haute latitude galactique furent d'ailleurs parmi les premiers candidats où il fut tenté, sans succès, d'observer un duo WR + c (van den Heuvel, 1976 ; Moffat et al., 1982).

Tel que présenté à la figure 1.5, les systèmes binaires massifs ont comme particularité d'avoir de forts vents en collisions, créant une région discontinue en densité au point de contact qui prend ensuite une forme conique dont l'ouverture entoure l'étoile ayant le vent le plus faible (Stevens et al., 1992). Lorsque les étoiles sont suffisament rapprochées, la région de contact des vents peut être chauffée à plusieurs fois 10^7K et produit alors des rayons X durs,

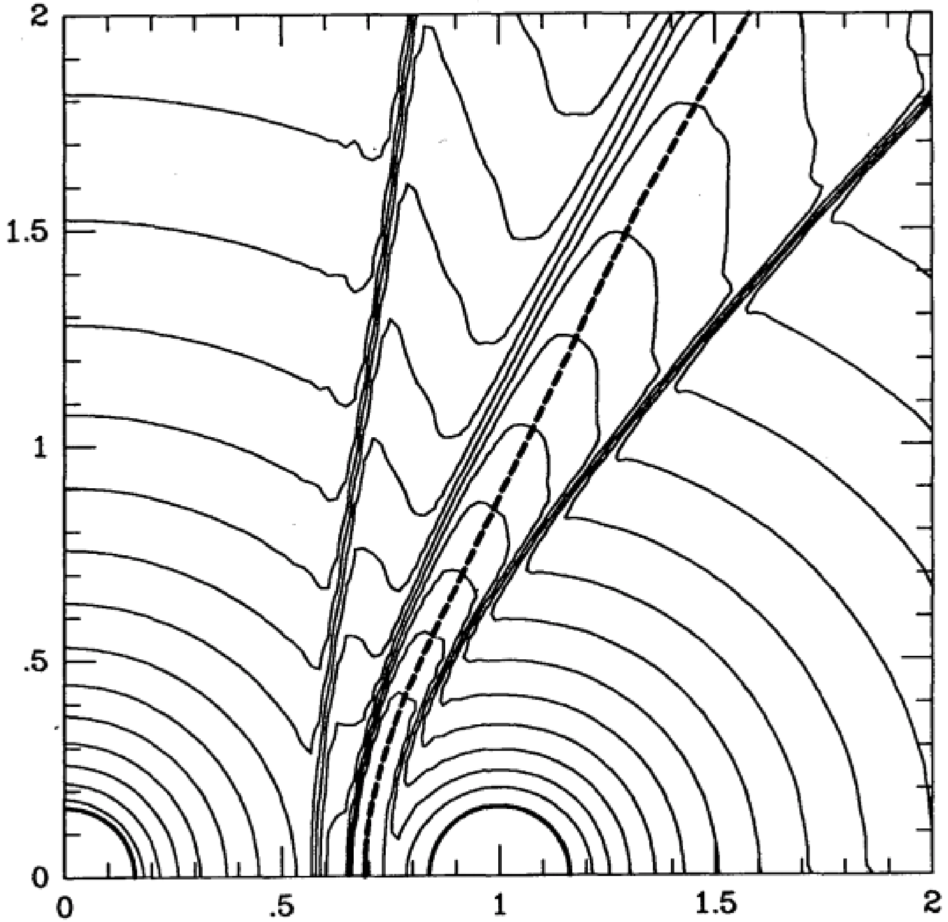

Figure 1.5. Simulation hydrodynamique de deux vents adiabatiques en collision, dont le ratio des flux de quantité de mouvement est $R = \sqrt{5}$. Les lignes pleines correspondent à des isocontours de densité. La ligne en pointillé correspond à la surface où les quantités de mouvement des vents s'équivalent. Figure tirée de Stevens et al. (1992).

permettant entre autres de diagnostiquer la structure des vents en collision (e.g. Hill et al. 2018, Pittard & Dawson, 2018).

Les systèmes binaires avec une composante Wolf-Rayet ne sont pas rares par rapport à la population totale de ces étoiles : 103 des 667 Wolf-Rayet galactiques répertoriées à ce jour dans le *Galactic Wolf-Rayet Catalogue* sont des binaires confirmées. De ce nombre, 22 systèmes sont des binaires visuelles montrant au moins une éclipse dans leurs observations photométriques. Cependant, toutes ces éclipses ne sont pas des éclipses « traditionnelles »ou photosphériques. Alors que ces dernières se produisent lorsque le disque de la photosphère d'un des membres du système cache celui de son compagnon, les éclipses atmosphériques sont dus à la nature étendue et diffuse des vents des Wolf-Rayet. Les denses vents des Wolf-Rayet contiennent de copieuses quantités d'électrons libres qui entraînent une atténuation de la lumière du compagnon par diffusion électronique quand ce dernier passe derrière le vent selon notre ligne de visée. La caractérisation de la forme d'une telle éclipse peut ainsi nous renseigner sur le taux de perte de masse du vent ainsi que sur l'inclinaison du système binaire par-rapport à notre ligne de visée.

Le premier des articles qui suit est une investigation de la présence d'une potentielle éclipse atmosphérique dans le système multiple WR48 (WC6/7+O), aussi appelé θ Mus. Le second article vise à déterminer si l'éclipse observée dans le système binaire WR22 (WN7h+09III-V) est purement atmosphérique ou si une composante photosphérique est aussi présente. Le troisième article est la première caractérisation de la variabilité photométrique stochastique dans les vents des étoiles Wolf-Rayet galactiques.

First Article.

Precision photometric monitoring from space of the multiple system θ Muscae including the WR binary WR48

by

Guillaume Lenoir-Craig[1], N. St-Louis[1], A.F.J. Moffat[1], and H. Pablo[2]

([1]) Dépt. de physique, Univ. de Montréal, C.P. 6128, Succ. C-V, Montréal, QC, H3C 3J7, Canada, and Centre de Recherche en Astrophysique du Québec

([2]) American Association of Variable Star Observers, 49 Bay State Road, Cambridge, MA 02138, USA

This article will be submitted in Monthly Notices of the Royal Astronomical Society.

Contributions de Guillaume Lenoir-Craig à l'article

Mes contributions à l'article qui suit sont, tout d'abord, la dé-corrélation des données BRITE utilisées, puis l'adaptation en Python du modèle d'éclipse atmosphérique de Lamontagne et al. (1996) ainsi que l'analyse des données avec celui-ci. J'ai aussi proposé l'idée d'utiliser un angle i trouvé dans la littérature afin de lever la dégénérescence avec le paramètre, ainsi que l'idée de comparer un modèle d'éclipse utilisant l'éphéméride de Hill et al. (2002) avec un modèle y additionnant un décalage en phase comme paramètre libre. J'ai de plus produit toutes les figures et formaté le texte aux standard LateX. Anthony Moffat a amené l'idée d'investiguer le sous-système WR48 afin de tenter d'y déceler une potentielle éclipse atmosphérique. Il a écrit la majorité du texte de la première version de l'article. Il a aussi proposé de comparer les différents fits produits pour différents binnings. Nicole St-Louis a suggéré des tests plus approfondis au niveau de la caractérisation du niveau de bruit, afin de s'assurer de la significance du pic observé. Bert Pablo avait produit une première dé-corrélation des données de WR48 à la demande d'Anthony Moffat et a été consulté quant à la possibilité d'une éclipse atmosphérique aussi ténue.

Résumé. Θ Mus (HD 113904) est un système multiple d'étoiles massives contenant la binaire WR48 (WC6/7+O), possédant une orbite circulaire de période P = 19 jours. Les tentatives précédentes visant à caractériser les propriétés photométriques variables du sous-système binaire ont échouées en raison de la présence d'une étoile bleue supergéante (BSG) à 46 *mas*, dont le flux lumineux, 10 fois plus intense, est dominé par des variations stochastiques. Cependant, à l'aide de données photométriques collectées sur une longue période de temps dans le spectre visible par un des satellites de BRITE-Constellation, nous avons pu réduire l'importance de la variabilité stochastique intrinsèque provenant de la BSG pour révéler une possible éclipse atmosphérique du sous-système WC+O ayant une profondeur de $\sim$ 8 mmag. De ceci et en utilisant une valeur d'inclinaison orbitale provenant d'une source plus précise, nous obtenons un estimé du taux de perte de masse pour la composante WR du système de $4.0 \times 10^{-5} \mathrm{M}_\odot$/année, ce qui est similaire aux pertes de masse d'autres étoiles de type WC5/6.

Mots clés : Technique : photométrie ; étoiles : Wolf-Rayet, binaires

Abstract. Θ Mus = HD 113904 is a massive multiple system containing the 19.1d WC6/7+O6/7V binary WR48 in a circular orbit. Previous attempts to constrain the variable photometric properties of the binary sub-system have been thwarted by the dominating stochastically variable light from a ten-times brighter blue supergiant (BSG), located only 46 *mas* away. Even now, with extensive optical space-based photometry from one of the BRITE-Constellation satellites, we were unable to beat down the intrinsic stochastic variability from the BSG enough to detect a possible low-level atmospheric eclipse of the WC+O system, as often seen in other short-period WR+O systems. We explore the variability of the dominating BSG, and find that its behaviour is similar to that of other BSGs, with a forest of low-frequency Fourier peaks likely from stochastic gravity waves arriving at the stellar surface. Then, by adopting an orbital inclination from another more reliable source, we obtain a clumping-independent, linear-density-dependent upper limit of the mass-loss rate for the WR component of $4.7 \times 10^{-5} M_{\odot}/yr$, which is consistent with values of other WC5/6 subtypes. This corresponds to an upper limit of 3.6 *mmag* for the depth of the atmospheric eclipse in the WR48 sub-system.

Keywords: Technique : photometry ; stars : Wolf-Rayet, eclipsing

1. Introduction

Massive stars exhibit a high binary fraction, providing a useful method to empirically determine some of their basic stellar parameters. This is especially important for Wolf-Rayet stars, where the hydrostatic surface is hidden by a strong wind. On the other hand, the strong WR wind has the advantage that it can lead to detectable *atmospheric* eclipses of their O-type companions, which are much more common among WR+O binaries than *photospheric* eclipses, that require higher orbital inclinations for them to occur. Such atmospheric eclipses can lead in a simple way to useful information, such as the determination of the orbital inclination (needed to convert observed values of $M\sin^3 i$ into real masses, M) and a mass-loss rate estimate of the WR wind (Lamontagne et al., 1996). A useful distinction between atmospheric and photospheric eclipses is that the former only produce one detectable dip in the orbital light-curve, when the WR component is at inferior conjunction, while the latter normally produce a dip at each conjunction. The only exception for the latter is in some highly elliptical systems where only one photospheric eclipse occurs - towards periastron, while the stars are too far apart to produce another photospheric eclipse diametrically opposite in the orbit, e.g. in the $80d$, $e = 0.6$ WR+O binary WR22 = HD 92740 : Rauw et al. (1996) ; Schweickhardt et al. (1999), Lenoir-Craig et al. (in prep.).

A first systematic attempt to explore a substantial number of WR+O systems in search of atmospheric eclipses was made by Lamontagne et al. (1996), who examined the ground-based light-curves of 13 WR+O binaries with periods below 30 days (excluding three known photospheric WR+O eclipsers), where the chance of detection is enhanced. Among these 13 systems only two (WR97 and WR141) failed to show dips in their light-curves at inferior WR conjunction (and one, WR31, is marginal), possibly because the WR mass-loss rates are unusually low and/or the potential atmospheric eclipses are masked by noise. These three systems deserve to be re-examined with higher-quality data, while several other WR+O systems are now known that lacked data at the time of the Lamontagne et al. (1996) study.

In addition, Lamontagne et al. (1996) excluded two short-period WR binaries due to complications. The first was WR43, located in the highly crowded and dense core (HD 97950) of the compact giant HII region NGC 3603, which has now been resolved by HST into three WNLh stars (among other luminous hot stars), two of which are binaries with $P = 3.8d$ and $8.9d$, respectively, the former showing photospheric eclipses (Moffat et al. 2004, Schnurr et al. 2008). The second was WR48 in the multiple system θ Muscae, with $P \sim 18d$ and an anomalous light-curve (Moffat and Seggewiss 1977). More recently, the circular orbital period of WR48 was updated to a much more precise value of $19.1375(25)d$ based on extensive new RV observations (Schnurr 1999, Hill et al. 2002). An attempt to determine a double-wave linear polarization curve (as seen in many other WR+O binaries) of the $19d$ orbit in six contiguous

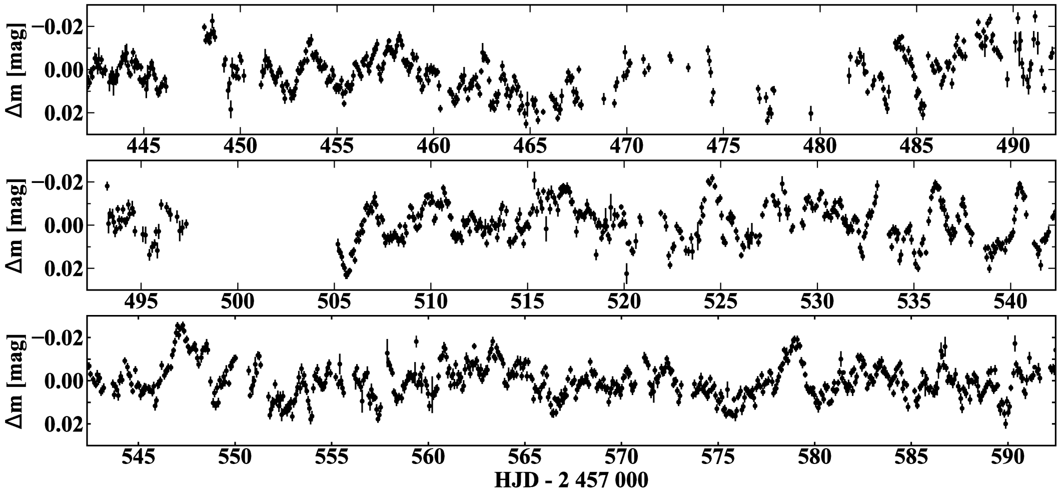

Figure 2.1. De-correlated, time-dependent light-curve of θ Muscae obtained by the BRITE-Toronto satellite in a red optical filter.

weeks of high-precision data of WR48 only revealed a noisy curve, presumably mainly from the bright blue supergiant (BSG) (St-Louis et al., 1987). In this paper we re-examine WR48 based on new, extensive precision space-based photometric monitoring of θ Mus.

2. Observations

Given the lack of a clear $\sim 19d$ signal expected for an atmospheric eclipse from electron scattering off free electrons in the WR wind in WR48 during previous ground-based photometric and polarimetric observing runs lasting up to only about a month at a time, it seemed appropriate to try to beat down the stochastic variability, which we will refer to as noise from the 10x brighter BSG companion, by obtaining contiguous multi-month precision photometry from space. The BRITE-Constellation nano-satellites seemed like the best option. The TESS satellite has also observed WR48 but only for about a month, which is also too short to be useful in this context. TESS's higher precision, although worthy, doesn't help much in this matter compared to the much higher noise level from the BSG, whose compensation requires a much longer observing run.

BRITE-Constellation (Weiss et al. 2014 ; Pablo et al. 2016) as originally planned consists of a network of six nano-satellites each housing a 35-mm format KAI-11002M CCD imaging detector fed by a 30-mm diameter f/2.3 telescope through either a blue (b) filter ($390 - 460$ nm) or a red (r) filter ($545 - 695$ nm) : BRITE-Austria (BAb), Uni-BRITE (UBr), BRITE-Heweliusz (BHr), BRITE-Lem (BLb), BRITE-Toronto (BTr) and BRITE-Montreal (BMb). With the exception of BMb that failed to detach from the upper stage module of its Dnepr launch vehicle, all the remaining satellites were launched into low-earth orbits of period $\sim$ 100 *mins*, and are now fully operational. With a $\sim 24° \times 20°$ effective field of view, each component of BRITE-Constellation performs simultaneous monitoring of 15 – 30 stars brighter than $V \sim 6$ *mag*. A given field is observed typically over a $\sim$ 6-month time base.

The 15th field monitored by BRITE was Crux/Carina I, for which simultaneous photometry of 45 stars was extracted, including the two WR stars θ Mus (WR48) and WR24 = HD 93131, along with η Carinae and the O8.5 blue supergiant(BSG) HD 112244. The BRITE detector pixel size is 27.3", and the point spread function (PSF) ~8 pixel resolution thus encircles the whole θ Mus system with component A (the WR+O binary plus a BSG separated by 46 mas) and component B, an O9III star located 5.3" away and two magnitudes fainter than A. Observations of WR48 in this field were performed only by BTr during 5 contiguous months between January and July, 2016. Short, 1 s exposures were taken at a median cadence of 20s during ~15 – 30% (Pablo et al., 2016) of each $\sim$ 100 min BRITE orbit, the remaining time being unused due to stray-light interference, blocking by the Earth, and limited data download capacity. All observations were performed in chopping mode (Pablo et al. 2016 ; Popowicz 2016 ; Popowicz et al. 2017). Raw light-curves were extracted using the BRITE reduction pipeline, which also includes corrections for intra-pixel sensitivity (Popowicz et al., 2017). Then, post-reduction decorrelations to remove instrumental effects due to CCD temperature and centroid-position variations, along with satellite orbital phase, were performed on each observational setup according to the method described by Pigulski et al. (2016).

In the resulting final decorrelated light-curve, we do not see any obvious variations on timescales shorter than the BRITE orbital period that could be qualified as intrinsic rather than pure instrumental noise. Therefore, in order to gain precision, we calculated mean fluxes per satellite orbit to create the final light-curves in the red band. Even if there were less-obvious, small-scale linear trends during each satellite pass, this technique would be impervious to them. We also removed outliers during the decorrelation process, such that it is reasonable to adopt orbital mean fluxes.

3. Results

We show the reduced BRITE light-curve with mean brightness per BRITE orbit in Figure 2.1. The de-trended data presented in this figure is available online : see the Data Availability section at the end of this article. As mentioned above, the light-curve includes the three stellar components of θ Mus A along with θ Mus B. According to the Gaia DR2 archive, more than 2000 other flux sources are present within a radius of 108 arc-seconds around θ Mus, corresponding to the size of the PSF. However, since the most luminous of these sources is $\sim$ 6 magnitudes fainter than θ Mus, their contribution to the total observed flux can be

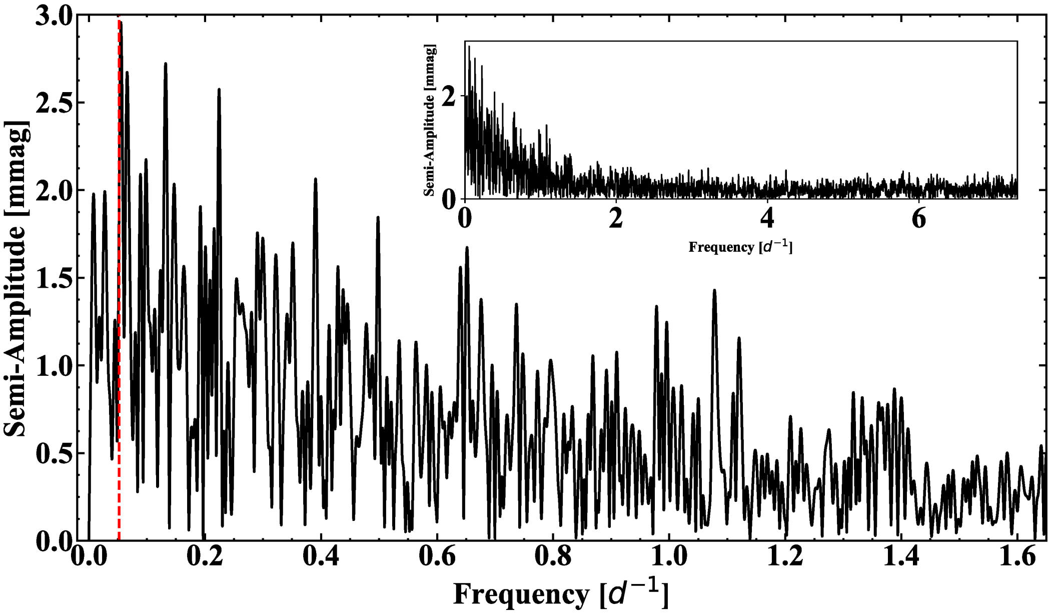

Figure 2.2. Periodogram of the WR48 light-curve presented in Figure 2.1, with the Hill et al. (2002) orbital period shown by a red dashed line. The inset shows the amplitude spectrum up to the Nyquist frequency of the satellite.

safely ignored. Ultimately, the light of θ Mus is dominated by the O9.5/B0Iab supergiant, which is 2-3 magnitudes brighter than the combined light of the 19d WC5/6 + O6/7V binary (Sugawara et al. 2008 ; Hartkopf et al. 1999).

A first search for periodicity is shown in the Fourier transform (FT) presented in Figure 2.2. We note that the resemblance of the WR48 light-curve and corresponding periodogram with that of the mid-O giant Xi Per and the early-O supergiant Zeta Puppis is remarkable (Ramiaramanantsoa et al. 2014, Ramiaramanantsoa et al. 2018), with a forest of low-frequency peaks suggesting that they primarily arise from variable bright regions on the O9.5/B0Iab stellar surface that likely lead to stochastic clumps in its wind. This is a reasonable assumption, given the overwhelmingly greater brightness of the BSG compared to WR48 and θ Mus B. This assumption is further supported by the similarity in lifetime and frequency scale between the stochastic features observed in the wavelet analysis of the θ Mus light-curve shown in Figure 2.3 and the time-frequency analysis of Xi Per and Zeta Puppis shown respectively in Ramiaramanantsoa et al. (2014) & Ramiaramanantsoa et al. (2018).

Taking this to be the case, we fit both red and white noise simultaneously to the FT as done by Bowman et al. (2020) for other BSGs (see Figure 2.4). We see that the BSG in θ Mus matches other BSGs quite well, with red-noise parameters $\alpha_0 = (7.3 \pm 0.2) \times 10^{-4} mag$,

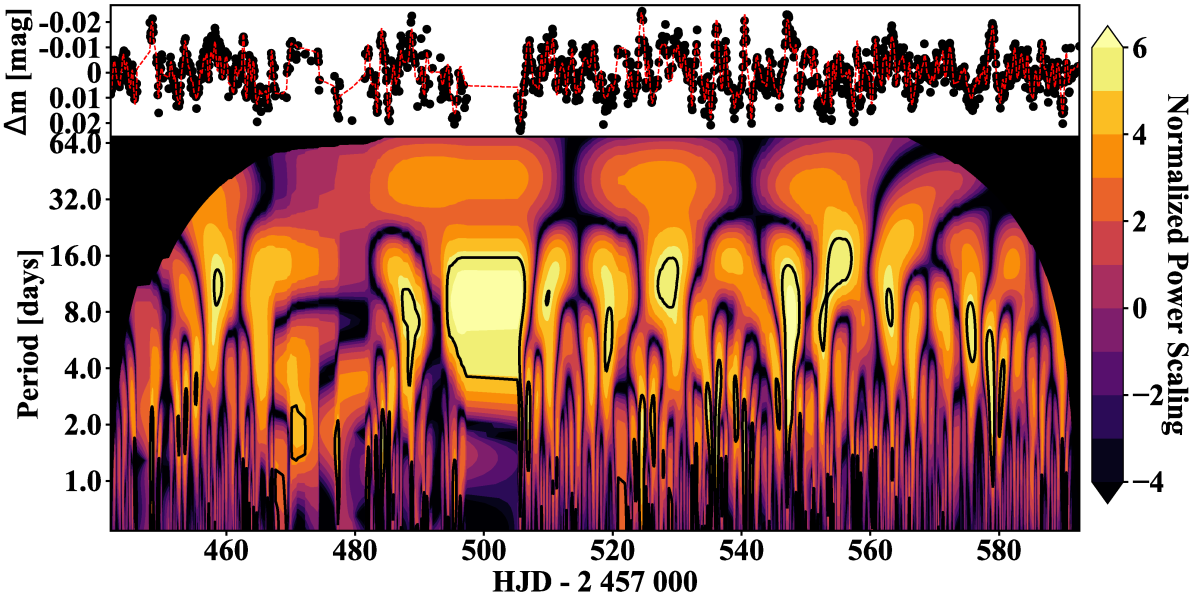

Figure 2.3. Top : BRITE light-curve of WR48. The red dashed line is the combined result of the Inverse Wavelet Transform of the wavelet analysis performed using the Mexican-hat mother function on the signal. Bottom : The power-spectrum of the wavelet analysis. The black region corresponds to the cone of influence (COI) of the period of the wavelets. The large, relatively uniform feature observed around $t = 500d$ is caused by the lack of data, as can be seen in the light-curve. The contour lines enclose regions with greater than 95% confidence level

$\nu_{char} = 0.69 \pm 0.02d^{-1}$ and $\gamma = 2.26 \pm 0.06$ having consistent values with what Bowman et al. (2019) found for their sample of BSGs, along with a white noise level of 0.1 mmag. We note that the low-frequency region with the highest peaks in Figure 2.2 corresponds to randomly superposed events in the wavelet analysis at corresponding long periods. This is consistent with the idea that such stochastic events are associated with some kind of perturbation (e.g. a packet of gravity waves) reaching the stellar surface.

Returning to Figure 2.1 we see that the light variations reach a peak-to-valley amplitude of $\sim 0.04\ mag$ and appear to consist of random and therefore diluted noise at many different timescales, as noted above. Figure 2.2 shows one power peak that stands out near the frequency close to the 19.1d orbit at $f = 0.056 \pm 0.005d^{-1}$ (i.e. within the Fourier resolution of 1/T, where $T = 150d$ for the overall data-string length), corresponding to a period of $P = 17.9 \pm 1.6d$. Such an uncertainty estimate based on the frequency resolution is probably overly pessimistic, since one can normally determine the peak centroid much better than the Fourier resolution. By fitting the peak with a Gaussian function and taking its standard deviation as an estimate of the error, we obtain an uncertainty in frequency for the position

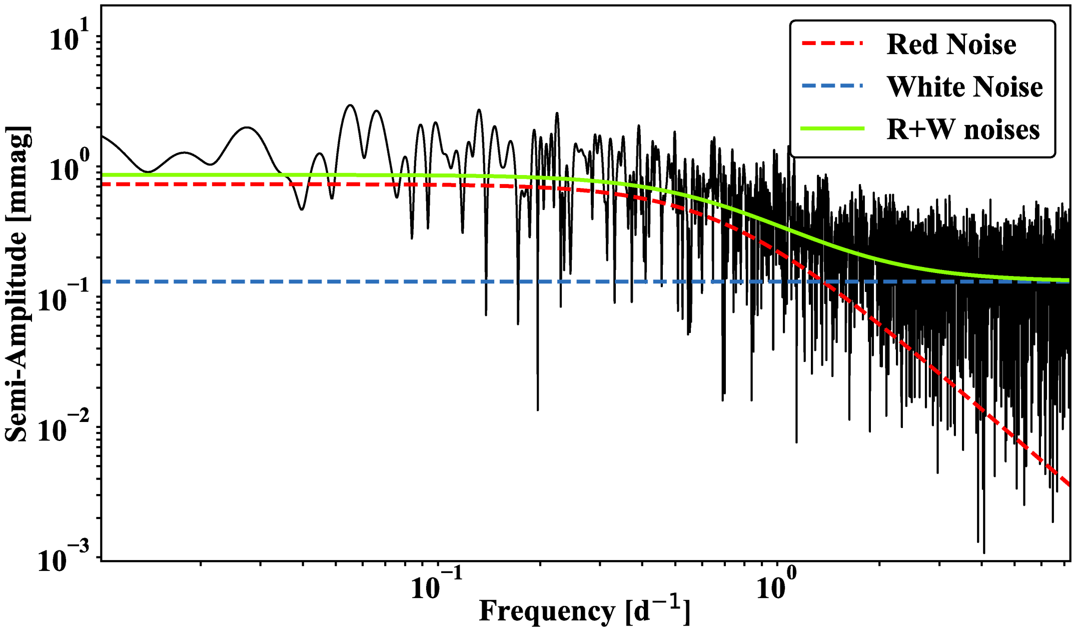

Figure 2.4. BRITE amplitude spectrum of WR48 fitted with a semi-Lorentzian noise model shown as a solid green line, comprised of a red and white component, respectively shown as a red and a blue dashed line.

of the centroid of the peak of $2.2 \times 10^{-5} d^{-1}$, corresponding to a period error of $0.007d$ and thus rendering the coincidence of this observed peak with the WR+O binary period highly unlikely. This peak is close to 24 times the amplitude of the white noise obtained by fitting a constant to the power spectrum above $\sim 4d^{-1}$ up to the Nyquist frequency ; the remaining discrete low-frequency peaks are most likely due to stochastic processes in the BSG. Taking a more pessimistic estimate of the noise level as the sum of white and red noise at this frequency (i.e. 0.86 *mmag*), the signal-to-noise ratio (SNR) of this peak becomes only 3.5. Noise peaks in space photometry quite often have SNRs over 4 and since this peak also significantly deviates from the central frequency corresponding to WR48 orbital period, it appears more likely that it originates in the BSG.

However, taking a more optimistic stance and assuming the FT peak at $f = 0.056d^{-1}$ does in fact coincide with the much more precise and reliable radial-velocity (RV) orbital period of the WR component obtained by Hill et al. (2002), based in large part on the extensive RV data of Schnurr (1999) : $P = 19.1375 \pm 0.0025d$. This latter period is in turn compatible with one of the first-ever periods obtained in the θ Mus binary-discovery results of Moffat and Seggewiss (1977), although too early to be recognized as such in that investigation, after

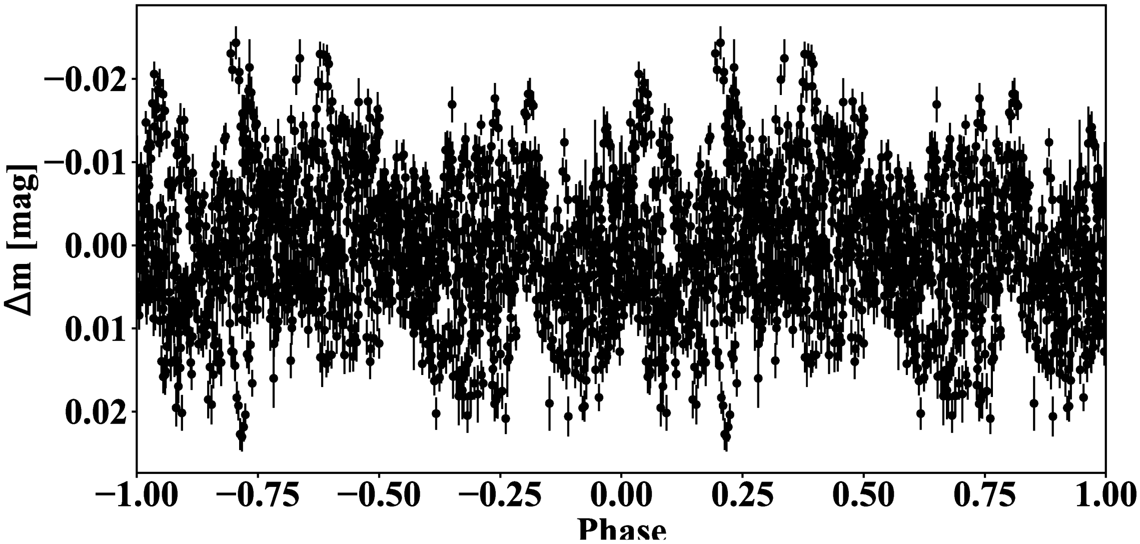

Figure 2.5. Phased light-curve with only BRITE-orbit binning of the θ Mus data using the Hill et al. (2002) ephemeris. No dip near phase zero due to an atmospheric eclipse is obvious. We neglect the small uncertainty of the period brought forward by 417 cycles from the Hill et al. study to the BRITE data, amounting to an accumulated error of about $1d$.

allowing for gap aliasing : $P = 19.128 \pm 0.008d$.[2] The Hill et al. (2002) and Schnurr (1999) data did not suffer in the same way from such gaps, making the $19.1375d$ period quite secure.

Figure 2.5 shows the same data as Figure 2.1 but phased with the Hill et al. (2002) ephemeris. It is difficult to judge from this if there is a significant dip at or near phase zero, as expected from Lamontagne et al. (1996).

In order to test whether there is significant variability due to an atmospheric eclipse in the BRITE light-curve shown in Figure 2.1, we conduct two-sample F-tests where we evaluate whether the Lamontagne et al. (1996) analytic atmospheric eclipse model (we refer to this as the L96 model) characterizes the data significantly better than a model with no flux variation over time, which we will subsequently refer to as the flat model. Below is the equation for the L96 atmospheric eclipse model with a beta-law exponent $\beta = 0$, since using $\beta = 1$ or higher has negligible effect, as we are only sensitive to the outer part of the WR wind where the terminal wind velocity has essentially been reached.

---

[2] We note that Moffat and Seggewiss (1977) actually give an overall best period of $18.341 \pm 0.008d$ (the corresponding error in frequency is $0.000024d^{-1} = 1/(30T)$, where T is the total data-string length, which is reasonable for the determination of FT centroid peaks), although they note that, due to the aliasing of a gap ($T \sim 1335d$) between the two data sets used to determine this period, that other aliases, e.g. $18.596d$ and $18.858d$ with similar errors, are also possible. The corresponding separation in successive frequency among these three periods, none of which matches the Hill et al. (2002) value, is constant (as expected for such aliasing) at $1/T = 0.000748d^{-1}$. Adding this value to the frequency corresponding to the alias above at $18.858d$, leads to another alias with a period of $19.128 \pm 0.008d$, which *does* match the Hill et al. (2002) value with a difference of $0.010 \pm 0.008d$. This means that the old Moffat and Seggewiss (1977) data do indeed contain the correct period within the errors and they demonstrate that the 19.1d period has not changed in ~20 years.

$$\Delta m = \Delta m_0 + A \times \frac{\pi/2 + \arcsin(\epsilon)}{\sqrt{1-\epsilon^2}}, \tag{3.1}$$

with the constant A and the independent variable ϵ corresponding to

$$A = \frac{2.5\log(e)k}{\dfrac{I(WR)+I(BSG)+I(O9III)}{I(O6/7)}+1}, \tag{3.2}$$

$$\epsilon = \sin(i)\cos(2\pi\phi), \tag{3.3}$$

where $i = 49°$ and the constant k being equal to

$$k = \frac{\alpha\sigma_e\dot{M}}{4\pi m_p v_\infty a}, \tag{3.4}$$

where ϕ is the orbital phase ($\phi = 0$ when the WR star is in front at inferior conjunction), Δm_0 is the magnitude zero-point, v_∞ is the WR-wind terminal velocity, the I values are the relative visual intensities of the stars, a is the orbital separation between the centres of the stars, α is the number of free electrons per baryon mass m_p in the WR wind, and σ_e is the Thomson scattering cross-section.

We use a non-linear least squares algorithm to fit the A and $\Delta \mathrm{m}_0$ parameters of the L96 model to the phased light-curve presented in Figure 2.5. Dividing the reduced χ^2 of the flat model by the reduced χ^2 of the fitted L96 model, we get an F value of 1.02. This value corresponds to a cumulative probability in the associated F distribution of 65% ($\sim 1\sigma$), which is well below the generally accepted 99.9% (3.3σ) confidence level.

Although we are not able to claim the discovery of a significant atmospheric eclipse in the WR48 sub-system, we can still evaluate an upper limit for $\dot{M}_{WR}$ by finding what $\dot{M}$ corresponds to a 99.9% detection confidence level for a 151 day long BRITE light-curve. To that end, we simulated 50 000 artificial light-curves, each containing 8 cycles of 19.1375 days to match our BRITE data-set observation length of 151 days, with data points every 100 minutes plus a superposed random 10-second standard deviation on their temporal positions to simulate the dispersion in BRITE data time-sampling. The intensity level of each data point is then assigned a random Gaussian noise signal centered on zero with a standard deviation equal to the RMS of the standard deviations of the stellar orbital cycles in our BRITE median-subtracted light-curve, each containing at least 200 data points (out of a

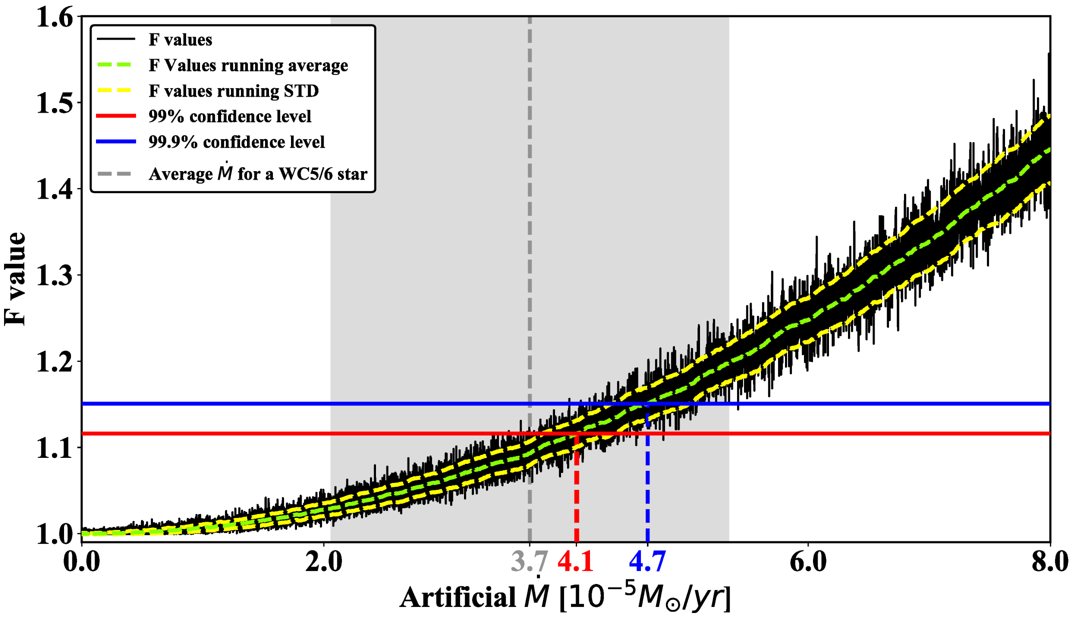

Figure 2.6. Calculated F values plotted against the injected artificial $\dot{M}$ in a light-curve with a length and a Gaussian noise level emulating the real BRITE light-curve of θ Mus. The F value corresponding to the ratio of the reduced χ^2 of the flat model divided by the reduced χ^2 of the L96 model on the BRITE data of θ Mus is shown in black. The dashed green line represents the running mean of those values with a 200-point window and the yellow dashed lines show the corresponding running standard deviations. The solid red (blue) line is set at the F value representing a 99% (99.9%) confidence level. Both red and blue dashed lines show the intercept of the running average with their respective confidence levels. The average $\dot{M}$ for a WC5/6 star calculated from Sander et al. (2019) is marked by a dashed gray line, and the area encompassing a standard deviation from that value is shown as a filled gray area.

maximum of 276). We assume that this noise level was not significantly affected by any atmospheric eclipse signal, since in this case, none was actually detected. We refer to this as the "flat" model. We then injected these light-curves with artificial atmospheric eclipse signals using the L96 model with increasingly higher values for the A parameter, corresponding to increasing $\dot{M}$ for the WR component of WR48. We used a non-linear least squares algorithm to fit both the flat and L96 models to these artificial data sets and then calculated the corresponding χ^2 and F values for each. We present the results of these simulations in Figure 2.6, where we also show the 99% and 99.9% confidence levels, respectively as a red and a blue horizontal line. The parameters used in the L96 model and the results at a 99.9% confidence level are shown in Table 2.1.

The jitter of the calculated F values appearing in Figure 2.6 is directly related to the randomness in the distribution of the artificial Gaussian noise we have added to each light-curve.

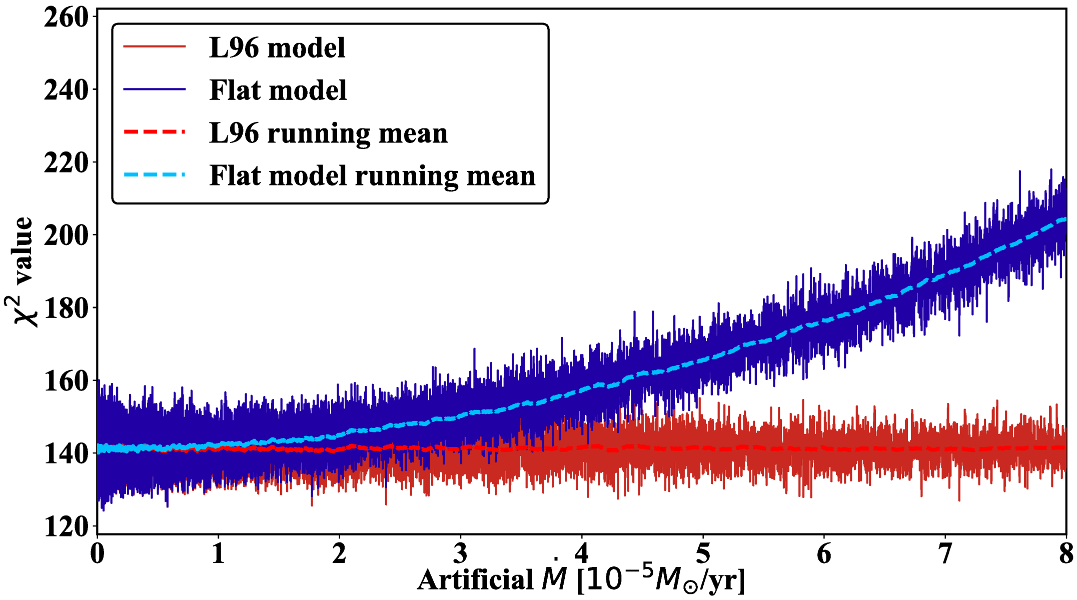

Figure 2.7. Calculated χ^2 of the flat and L96 models shown against the injected artificial $\dot{M}$ in the corresponding artificial light-curve. For more clarity in the followed trends for both χ^2, running averages of 200 points are shown as a red dashed line for the L96 model and as a blue dashed line for the flat model.

Since our sample of light-curves with artificial $\dot{M}$ generates eclipse depths reaching a maximum of 80% of the standard deviation of the Gaussian noise, both the flat and L96 models' χ^2 values follow similar stochastic variations for each artificial light-curve, with an increasing difference between both χ^2 values for increasing $\dot{M}$, as shown in Figure 2.7. The increasing difference in χ^2 also explains the growing amplitude of the jitter of the F values seen in Figure 2.6, as the average χ^2 of the flat model follows an increasing trend with growing $\dot{M}$ that gradually reduces the similarities between both χ^2 stochastic variations.

The running average of the calculated F values and its standard deviation, respectively shown as green and yellow dashed lines in Figure 2.6, gives us the mean F value and its uncertainty for a chosen $\dot{M}$ that one can expect from observing θ Mus for 153.1 days with a BRITE-Constellation satellite, assuming no gap in the data. We find that $\dot{M} = (4.1 \pm 0.3) \times 10^{-5} M_\odot/yr$ corresponds to a 99% confidence in a detection under that assumption, while the 99.9% confidence level corresponds to a $\dot{M} = (4.7 \pm 0.3) \times 10^{-5} M_\odot/yr$, which is associated with an atmospheric eclipse depth of (3.6 ± 0.3) *mmag*.

Also, by choosing a value of $\dot{M}$ for the WR component equal to the average value of $\dot{M} = (3.7 \pm 1.6) \times 10^{-5}$ $\mathrm{M}_\odot$/yr for WC5/6 stars (Sander et al., 2019) , we can determine the minimum number of orbital cycles of WR48 that a BRITE-Constellation satellite would

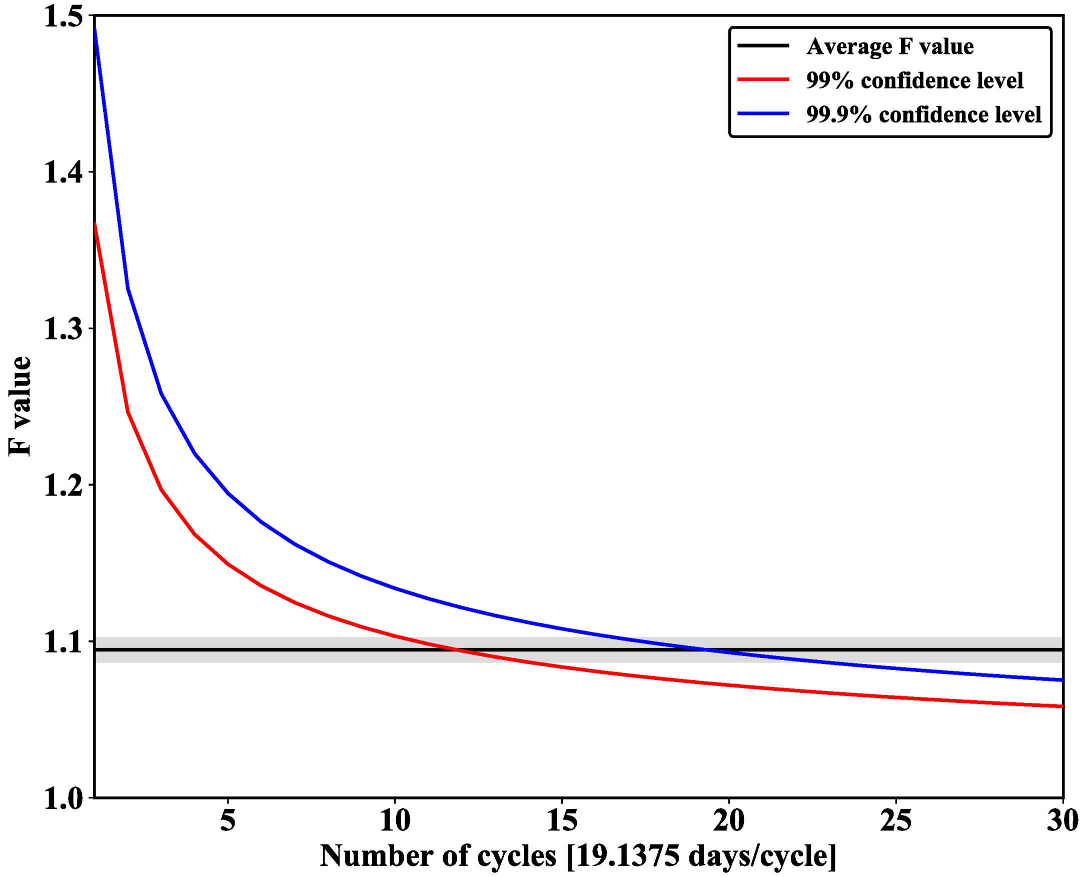

Figure 2.8. Calculated F values of artificial light-curves containing varying numbers of 19.1375 days cycles. The solid blue and red lines respectively correspond to a 99% and 99.9% confidence level in the detection. The solid black line corresponds to the average F value of 500 simulations over the shown cycles, with the gray area representing three standard deviations from this value.

need to observe in order to detect the corresponding atmospheric eclipse signal. We proceed by creating artificial light-curves containing an increasing integer number of cycles of 19.1375 days, with the same artificial cadence and Gaussian noise level as previously. For each cycle of each light-curve, we then add an atmospheric eclipse signal corresponding to $\dot{M} = 3.7 \times 10^{-5}$ $M_{\odot}$/yr with the L96 model. Each light-curve was subsequently phase-folded with the WR48 orbital period, a non-linear least squares algorithm was used to fit both the flat and L96 models on each phased data set and the corresponding F values were then calculated. The average of the F values acquired over 500 such simulations was then calculated, along with it's corresponding standard deviation. The results are shown in Figure 2.8.

Table 2.1. Parameters of the L96 model with F values intercepting the 99.9% confidence level

Parameter	Value
Assumed Parameters	
P [days]	19.1375 ± 0.0025
E_0 [HJD]	2 451 377.51 ± 0.45
v_∞ [km/s]	2525 [a]
a [$R_\odot$]	108 [b]
i [°]	49 [c]
α	0.50 [d]
M_v(WC5/6)	-4.8 [a]
M_v(O9.5/B0Iab)	-6.3 [e]
M_v(O6/7V)	-4.8 [e]
M_v(O9III)	-5.2 [e]
Derived Parameters (99.9% confidence)	
dm_0 [mag]	$(-2.718 \pm 0.003) \times 10^{-3}$
$\dot{M}_{WR}$ [$M_\odot$ / year]	$< (4.7 \pm 0.3) \times 10^{-5}$
A [mag]	$< (3.6 \pm 0.3) \times 10^{-3}$

[a] Sander et al. (2019), for a typical WC5/6 star

[b] Calculated with Kepler's third law, and the masses of the WR and O components (18 and 29 $M_\odot$, respectively), based on the mean spectral-type calibrations of Sander et al. (2019) and Martins et al. (2005), respectively.

[c] Hill et al. (2002)

[d] Lamontagne et al. (1996)

[e] Martins et al. (2005), from modeled spectral types.

Taking the average for a WC5/6 $\dot{M} = 3.7 \times 10^{-5} M_\odot/yr$ from Sander et al. (2019) and assuming no gap in the data, we find that to detect the atmospheric eclipse at a 99% confidence level would require the observation of 12 ± 2 orbital cycles of 19.1375 days with a BRITE-Constellation satellite, whereas a 99.9% confidence in the detection would require the observation of 20 ± 3 cycles.

4. Discussion

The only other previous extensive photometric datasets for WR48 were from (1) ground-based optical continuum data of Moffat and Seggewiss (1977), showing random short-term fluctuations, similar to the much higher-cadence and longer-duration BRITE space photometry, and (2) Hipparcos photometry by Marchenko et al. (1998). The latter, although less precise per data-point, stretched over 3 years and showed a period of $18.0 \pm 0.3d$ with a ~ 0.02 *mag* peak-to-peak variability amplitude, whose time of relatively narrow *maximum* coincided with inferior conjunction of the WR star using the available orbital ephemeris at the time. We have updated this determination using the more accurate ephemeris of Hill et al. (2002), which puts the broad *minimum* of Marchenko et al. (1998) at phase -0.138 ± 0.04, significantly displaced from 0.00, as expected if due to an atmospheric eclipse. If this light-curve behaviour is real, we have no explanation for it.

As for the origin of the random, low-frequency fluctuations, as mentioned above, the most likely scenario is that they arise from gravity waves arriving from below in the surface of the blue supergiant, which is $\sim 10\times$ brighter than the combined light of the WR+O system. Furthermore, the linear broadband polarimetry taken over 6 weeks by St-Louis et al. (1987) also failed to show any periodic WR-orbit component, but rather just intrinsic noise probably also arising from wind clumping triggered by the gravity waves in the very bright BSG.

Our results also enable us to check whether the period could have changed as a result of the high mass-loss rate of the WR component over the ~22 years between Hill et al. (2002) and the current BRITE data. Following Khaliullin (1974) for the most likely model of a spherically symmetric outflow from the WR component beyond the system, one has $\dot{P}/P = -2\dot{M}_{WR}/M_{WR} \times q/(1+q)$, where $q = M_{WR}/M_O \sim 15/30 = 0.5$. Then with $\dot{M}_{WR} < 4.7 \times 10^{-5} M_{\odot}/yr$, we find for WR48 $\dot{P} < 2.9\ sec/yr = 7.5 \times 10^{-4}$ day over 22 years, which is negligible compared to the precision with which the period has been obtained.

5. Conclusions

Thanks to the fact that the BRITE satellites are chosen to lock onto a field for up to six months, we were able to narrow down, though not determine, a light-curve for the 19.1d WR+O subsystem WR48 as part of the larger θ Mus with an upper limit to the WR mass-loss rate of an atmospheric eclipse, as is found in many other short-period WR + O systems. The advantage here was to cover enough orbital cycles to beat down the intrinsic noise of the 46 mas distant blue supergiant that dominates the light of the triple system (quadruple system counting much fainter star B). As a result, the upper limit of the amplitude of the atmospheric eclipse is very low ($A < 3.6\ mmag$).

A viable alternative and path to a real detection would be to observe the same way for much longer (at least 12-20 cycles ~ 8 - 13 months, depending on the actual WR mass-loss rate), or to observe with sufficient spatial resolution to be able to exclude the 46 mas distant BSG from contributing to the light budget of the 19d WR+O system. Then for the latter, an observing run of only a few weeks would probably suffice for a proper determination of WR48's atmospheric eclipse.

The supergiant itself also appears to be stochastically variable on timescales of hours/days at the 4% level peak-to-peak, although of much lower amplitude for the FT peaks due mainly to dilution from the rest of the light-curve, thus all but drowning out any similar variations of the WR-star, its MS O-type companion - without any binning with the known WR+O orbital period - or component B. Thus, θ Mus - the second-brightest WR star in the sky (however only so bright mainly because of the presence of the bright BSG) appears to be normal. Based on the atmospheric eclipse amplitude, the upper limit of the WR mass-loss rate, $4.7 \times 10^{-5} M_{\odot}/yr$, is consistent with values for a WR star of this sub-type (WC5-6).

Acknowledgements

NSL & AFJM are grateful to NSERC (Canada) for financial aid.

References

William I. Hartkopf, Brian D. Mason, Douglas R. Gies, Theo ten Brummelaar, Harold A. McAlister, Anthony F. J. Moffat, Michael M. Shara, and Debra J. Wallace. ICCD Speckle Observations of Binary Stars. XXII. A Survey of Wolf-Rayet Starsfor Close Visual Companions. *Astrophysical Journal*, 118(1) :509–514, July 1999. doi : 10.1086/300943.

G. M. Hill, A. F. J. Moffat, and N. St-Louis. Modelling the colliding-winds spectra of the 19-d WR + OB binary in the massive triple system θ Muscae. *Monthly Notices of the Royal Astronomical Society*, 335(4) :1069–1078, October 2002. doi : 10.1046/j.1365-8711.2002.05694.x.

Kh. F. Khaliullin. Mass loss by Wolf-Rayet stars. *Soviet Astronomy*, 18 :229, October 1974.

Robert Lamontagne, Anthony F. J. Moffat, Laurent Drissen, Carmelle Robert, and Jaymie M. Matthews. Photometric Determination of Orbital Inclinations and Mass Loss Rates for Wolf-Rayet Stars in WR+O Binaries. *Astrophysical Journal*, 112 :2227, November 1996. doi : 10.1086/118175.

S. V. Marchenko, A. F. J. Moffat, K. A. van der Hucht, W. Seggewiss, H. Schrijver, B. Stenholm, I. Lundstrom, D. Y. A. Setia Gunawan, W. Sutantyo, E. P. J. van den Heuvel, J. P. de Cuyper, and A. E. Gomez. Wolf-Rayet stars and O-star runaways with HIPPARCOS. II. Photometry. *Astronomy and Astrophysics*, 331 :1022–1036, March 1998.

F. Martins, D. Schaerer, and D. J. Hillier. A new calibration of stellar parameters of Galactic O stars. *Astronomy and Astrophysics*, 436(3) :1049–1065, June 2005. doi : 10.1051/0004-6361:20042386.

A. F. J. Moffat and W. Seggewiss. The Wolf-Rayet binary theta Muscae. *Astronomy and Astrophysics*, 54 :607–616, January 1977.

A. F. J. Moffat, V. Poitras, S. V. Marchenko, M. M. Shara, D. R. Zurek, E. Bergeron, and E. A. Antokhina. Hubble Space Telescope NICMOS Variability Study of Massive Stars in the Young Dense Galactic Starburst NGC 3603. *Astrophysical Journal*, 128(6) :2854–2861, December 2004. doi : 10.1086/425878.

H. Pablo, G. N. Whittaker, A. Popowicz, S. M. Mochnacki, R. Kuschnig, C. C. Grant, A. F. J. Moffat, S. M. Rucinski, J. M. Matthews, A. Schwarzenberg-Czerny, G. Handler, W. W. Weiss, D. Baade, G. A. Wade, E. Zocłońska, T. Ramiaramanantsoa, M. Unterberger, K. Zwintz, A. Pigulski, J. Rowe, O. Koudelka, P. Orleański, A. Pamyatnykh, C. Neiner, R. Wawrzaszek, G. Marciniszyn, P. Romano, G. Woźniak, T. Zawistowski, and R. E. Zee.

The BRITE Constellation Nanosatellite Mission : Testing, Commissioning, and Operations. *Publications of the Astronomical Society of the Pacific*, 128(970) :125001, December 2016. doi : 10.1088/1538-3873/128/970/125001.

A. Pigulski, H. Cugier, A. Popowicz, R. Kuschnig, A. F. J. Moffat, S. M. Rucinski, A. Schwarzenberg-Czerny, W. W. Weiss, G. Handler, G. A. Wade, O. Koudelka, J. M. Matthews, St. Mochnacki, P. Orleański, H. Pablo, T. Ramiaramanantsoa, G. Whittaker, E. Zocłońska, and K. Zwintz. Massive pulsating stars observed by BRITE-Constellation. I. The triple system β Centauri (Agena). *Astronomy and Astrophysics*, 588 :A55, April 2016. doi : 10.1051/0004-6361/201527872.

A. Popowicz, A. Pigulski, K. Bernacki, R. Kuschnig, H. Pablo, T. Ramiaramanantsoa, E. Zocłońska, D. Baade, G. Handler, A. F. J. Moffat, G. A. Wade, C. Neiner, S. M. Rucinski, W. W. Weiss, O. Koudelka, P. Orleański, A. Schwarzenberg-Czerny, and K. Zwintz. BRITE Constellation : data processing and photometry. *Astronomy and Astrophysics*, 605 :A26, September 2017. doi : 10.1051/0004-6361/201730806.

Adam Popowicz. *Image processing in the BRITE nano-satellite mission*, volume 9904 of *Society of Photo-Optical Instrumentation Engineers (SPIE) Conference Series*, page 99041R. 2016. doi : 10.1117/12.2229141.

Tahina Ramiaramanantsoa, Anthony F. J. Moffat, André-Nicolas Chené, Noel D. Richardson, Huib F. Henrichs, Sébastien Desforges, Victoria Antoci, Jason F. Rowe, Jaymie M. Matthews, Rainer Kuschnig, Werner W. Weiss, Dimitar Sasselov, Slavek M. Rucinski, and David B. Guenther. MOST detects corotating bright spots on the mid-O-type giant ξ Persei. *Monthly Notices of the Royal Astronomical Society*, 441(1) :910–917, June 2014. doi : 10.1093/mnras/stu619.

Tahina Ramiaramanantsoa, Anthony F. J. Moffat, Robert Harmon, Richard Ignace, Nicole St-Louis, Dany Vanbeveren, Tomer Shenar, Herbert Pablo, Noel D. Richardson, Ian D. Howarth, Ian R. Stevens, Caroline Piaulet, Lucas St-Jean, Thomas Eversberg, Andrzej Pigulski, Adam Popowicz, Rainer Kuschnig, Elżbieta Zocłońska, Bram Buysschaert, Gerald Hand ler, Werner W. Weiss, Gregg A. Wade, Slavek M. Rucinski, Konstanze Zwintz, Paul Luckas, Bernard Heathcote, Paulo Cacella, Jonathan Powles, Malcolm Locke, Terry Bohlsen, André-Nicolas Chené, Brent Miszalski, Wayne L. Waldron, Marissa M. Kotze, Enrico J. Kotze, and Torsten Böhm. BRITE-Constellation high-precision time-dependent photometry of the early O-type supergiant ζ Puppis unveils the photospheric drivers of its small- and large-scale wind structures. *Monthly Notices of the Royal Astronomical Society*, 473(4) :5532–5569, February 2018. doi : 10.1093/mnras/stx2671.

G. Rauw, J. M. Vreux, E. Gosset, D. Hutsemekers, P. Magain, and K. Rochowicz. WR22 : the most massive Wolf-Rayet star ever weighed. *Astronomy and Astrophysics*, 306 :771, February 1996.

A. A. C. Sander, W. R. Hamann, H. Todt, R. Hainich, T. Shenar, V. Ramachandran, and L. M. Oskinova. The Galactic WC and WO stars. The impact of revised distances from Gaia DR2 and their role as massive black hole progenitors. *Astronomy and Astrophysics*, 621 :A92, January 2019. doi : 10.1051/0004-6361/201833712.

O. Schnurr. Spektroskopie des Wolf-Rayet-Doppelsterns Theta Muscae. Master's thesis, University of Heidelberg, 1999.

O. Schnurr, J. Casoli, A. N. Chené, A. F. J. Moffat, and N. St-Louis. The very massive binary NGC 3603-A1. *Monthly Notices of the Royal Astronomical Society*, 389(1) :L38–L42, September 2008. doi : 10.1111/j.1745-3933.2008.00517.x.

J. Schweickhardt, W. Schmutz, O. Stahl, Th. Szeifert, and B. Wolf. Revised mass determination of the super massive Wolf-Rayet star WR 22. *Astronomy and Astrophysics*, 347 : 127–136, July 1999.

Nicole St-Louis, Laurent Drissen, Anthony F. J. Moffat, Pierre Bastien, and Santiago Tapia. Polarization Variability among Wolf-Rayet Stars. I. Linear Polarization of a Complete Sample of Southern Galactic WC Stars. *The Astrophysical Journal*, 322 :870, November 1987. doi : 10.1086/165782.

Y. Sugawara, Y. Tsuboi, and Y. Maeda. Redshifted emission lines and radiative recombination continuum from the Wolf-Rayet binary θ Muscae : evidence for a triplet system ? *Astronomy and Astrophysics*, 490(1) :259–264, October 2008. doi : 10.1051/0004-6361: 20079302.

W. W. Weiss, S. M. Rucinski, A. F. J. Moffat, A. Schwarzenberg-Czerny, O. F. Koudelka, C. C. Grant, R. E. Zee, R. Kuschnig, St. Mochnacki, J. M. Matthews, P. Orleanski, A. Pamyatnykh, A. Pigulski, J. Alves, M. Guedel, G. Handler, G. A. Wade, and K. Zwintz. BRITE-Constellation : Nanosatellites for Precision Photometry of Bright Stars. *Publications of the Astronomical Society of the Pacific*, 126(940) :573, June 2014. doi : 10.1086/677236.

Second Article.

The bright H-rich WR star WR22 and its single eclipse per 80-day orbit : photospheric or atmospheric ?

by

Guillaume Lenoir-Craig[1], N. St-Louis[1], A.F.J. Moffat[1], I.I. Antokhin[2], and E.A. Antokhina[2]

([1]) Dépt. de physique, Univ. de Montréal, C.P. 6128, Succ. C-V, Montréal, QC, H3C 3J7, Canada, et Centre de Recherche en Astrophysique du Québec

([2]) Moscow Lomonosov State University, Sternberg State Astronomical Institute, 119992 Universitetsky prospect, 13, Moscow, Russia

This article will be submitted in Monthly Notices of the Royal Astronomical Society.

Contributions de Guillaume Lenoir-Craig à l'article

Mes contributions à l'article qui suit sont, en premier lieu, la dé-corrélation des données BRITE utilisées, l'adaptation du modèle Python d'éclipse atmosphérique de Lamontagne (1996) pour des orbites elliptiques et la modélisation des données avec celui-ci. J'ai ensuite conduit des analyses statistiques sur la qualité des fits obtenus. J'ai aussi participé de façon secondaire à l'écriture de la section sur le modèle de Lamontagne 1996. J'ai de plus produit toutes les figures concernant la modélisation de l'éclipse avec le modèle modifié de Lamontagne 1996 et ait formaté le texte aux standard LateX. Anthony Moffat a tout d'abord suggéré l'étude de l'éclipse du système WR22 à l'aide du modèle d'éclipse atmosphérique de Lamontagne et al. (1996) et a rédigé la majorité de la version initiale de l'article jusqu'à la section sur l'analyse en éclipse photosphérique. Igor Antokin et Eleonora Antokhina ont respectivement écrit la section 3 sur l'analyse photométrique de l'éclipse et modélisé l'éclipse à l'aide d'un modèle numérique. Nicole St-Louis a participé à de nombreuses conversations pertinentes à l'avancement du projet.

RÉSUMÉ. WR22 (HD 92740) est une binaire visuelle (WN7h + O9III) dont la composante WR éclipse sa compagne O chaque ∼80 jours. La profondeur de l'éclipse apparaissant dans les trois courbes de lumières obtenues par BRITE-Constellation est de 8 mmag. Cet article vise à démontrer la nature atmosphérique ou photosphérique de cette éclipse et à contraindre la valeur du taux de perte de masse $\dot{M}_{WR}$ de la composante WR, ainsi que l'angle d'inclinaison du système i à l'aide de deux modèles. Le premier est un simple modèle analytique d'éclipse atmosphérique alors que le second est un modèle numérique plus complexe tenant compte des deux types d'éclipse. Ces modèles obtiennent $i \geqslant 80.56°$, avec des valeurs de $\dot{M}_{WR}$ très incertaines en raison du manque de contraintes observationnelles sur la valeur du ratio des flux des étoiles F_O/F_{WR}. Nous trouvons que l'éclipse ne peut être totalement atmosphérique, mais sa nature partiellement ou totalement photosphérique reste à déterminer.

Mots clés : Technique : photométrie ; étoiles : Wolf-Rayet, binaire

Abstract. WR22 (HD 92740) is a massive visual binary (WN7h + O9III) system with the Wolf-Rayet (WR) component eclipsing its O companion every 80 days. The eclipse depth of 8 mmag appears in three light-curves obtained by BRITE-Constellation. This article is an attempt to ascertain either the atmospheric or photospheric nature of this eclipse and to constrain the WR wind mass-loss rate $\dot{M}_{WR}$ and the angle of inclination of the system i using two models. The first is a simple analytical atmospheric-eclipse model and the second is a more complex numerical model. These models found $i \geqslant 80.56°$, with $\dot{M}_{WR}$ values greatly varying in response to the lack of observationnal constraints on the flux ratio of the stars F_O/F_{WR}. We find that the eclipse cannot be fully atmospheric, but its partly or fully photospheric nature is yet to be ascertained.

Keywords: Technique : photometry ; stars : Wolf-Rayet, binary

1. Introduction

When normal stars reveal core eclipses, there are usually two dips in the light-curve per orbit. However, when the orbit is highly elliptical there could be only one eclipse, depending on the stellar sizes in relation to the projected (variable) separation. Clearly though, a relatively high orbital inclination is required in any case, especially for longer orbital periods.

However, in the case of stars with extended envelopes, such as WR stars with very strong winds, there is also the possibility of an atmospheric eclipse when the WR star passes in front of its (usually) much weaker-wind O-type companion. This produces only one eclipse (via scattering by WR free electrons of O-star light out of the line-of-sight) per orbit, whether circular or not. It can also occur for inclination angles i much lower than 90°, although it may require high S/N to detect and characterize, especially for the lowest inclinations.

This led Lamontagne et al. (1996) to examine a fairly complete sample of known short-period ($P < 30$d) WR+O binaries known at the time, for such atmospheric eclipses. This significantly enlarged the number of binary systems with known inclinations and thus allowed more masses to be obtained from radial-velocity (RV) orbits, which only yield the value of $M \sin^3 i$. As an important by-product, it also allowed one to get an estimate of the WR mass-loss rate independent of clumping in the wind.

However, it was noted by Lamontagne et al. (1996) that the WN7h + O9III-V P = 80 d long-period binary system WR22 = HD 92740 shows only one relatively shallow but sharp eclipse near its periastron passage in its e = 0.6 elliptical orbit (Balona et al. (1989) ; Gosset et al. (1991)). There is no trace of a second eclipse half an orbit later near apastron, suggesting that the observed eclipse may be photospheric and partial. But the eclipse occurred when the WR-star passed in front of the O-star, leaving open the possibility of an atmospheric instead of a photospheric eclipse.

In this study, we explore the nature of WR22's eclipse in more detail, taking advantage of the ability of the nanosatellites of the BRITE Constellation to intensely monitor bright stars in precision optical photometry for up to half a year non-stop. Previous ground-based observations show only marginal coverage of WR22's eclipse due to both the long orbital period and the short (but not short enough for proper coverage from one site) two-day duration of the eclipse.

2. Observations

BRITE-Constellation (Weiss et al. 2014, Pablo et al. 2016) as originally planned consists of a network of six nanosatellites each housing a 35-mm format KAI-11002M CCD photometer fed by a 30-mm diameter f/2.3 telescope through either a blue filter (390 – 460 nm) or a red filter (545 – 695 nm) : BRITE-Austria (BAb), Uni-BRITE (UBr), BRITE-Heweliusz (BHr), BRITE-Lem (BLb), BRITE-Toronto (BTr) and BRITE-Montreal (BMb), the last letter of the abbreviations denoting the filter type ("b" for blue and "r" for red). With the exception of BMb, which failed to detach from the upper stage module of its Dnepr launch vehicle, all the satellites were launched into low-Earth orbits of orbital period of ∼100 min, commissioned and now fully operational. With a ∼24° × 20° effective field of view, each component of BRITE-Constellation performs the simultaneous monitoring of 15 – 30 stars brighter than V ∼ 6. A given field is observed typically over a ∼ 6-month time base.

WR22 was monitored by BHr in the BRITE Carinae field numbers 24 (2017 Jan 10 - July 12) and 36 (2018 Feb 15 - July 15). The BRITE detector pixel-size is 27.3", with a resolution of FWHM ∼5 pixels and thus comfortably including, yet isolating, the light from WR22. Short 1 s exposures were taken at a median cadence of 20 s during ∼1 – 30% of each ∼ 100 min BRITE orbit, the remaining time unused due to stray light interference, blocking by the Earth, and limited data-download capacity.

All observations were performed in chopping mode (Pablo et al. 2016 ; Popowicz 2016 ; Popowicz et al. 2017). Raw light-curves were extracted using the reduction pipeline for BRITE data which also includes corrections for intra-pixel sensitivity (Popowicz, 2016). Then post-reduction decorrelations with respect to instrumental effects due to CCD temperature variations, centroid position and satellite orbital phase were performed on each observational setup for each satellite according to the method described by Pigulski et al. (2016).

In the resulting final decorrelated light-curves, we did not notice any obvious and significant variations on timescales shorter than the BRITE orbital period that could be qualified as intrinsic to the star rather than to pure instrumental noise. Therefore in order to gain in precision we calculated mean fluxes per satellite orbit to create the final light-curves in the optical red band. This would also eliminate any linear trends, if any would be present. We note that we also performed the removal of outliers during the decorrelation process, such that it is reasonable to adopt orbital mean fluxes instead of median fluxes.

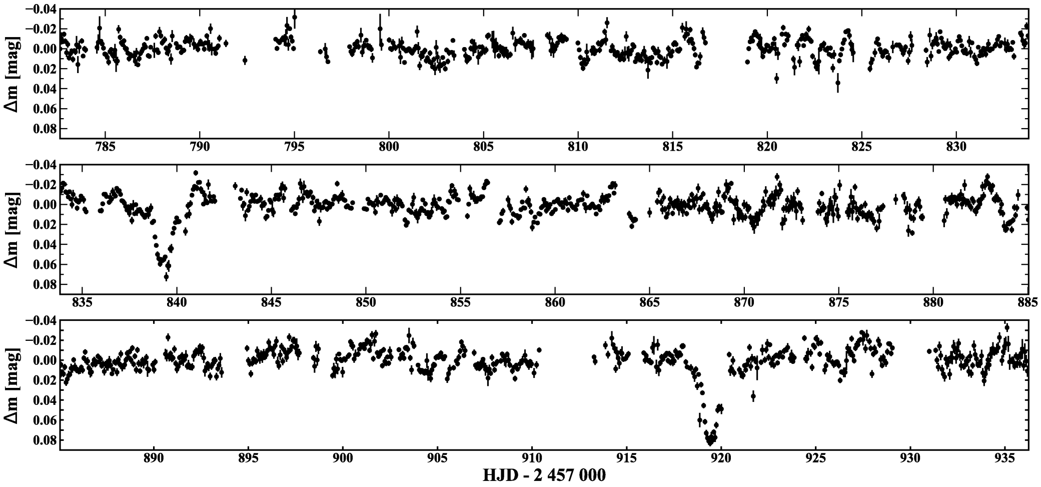

Figure 3.1. De-correlated time-dependent light-curve of WR22 obtained by the BRITE-Heweliusz satellite in its 2017 coverage of the Carina field, after subtracting off the mean. The two eclipses separated by ∼80 days are clearly seen.

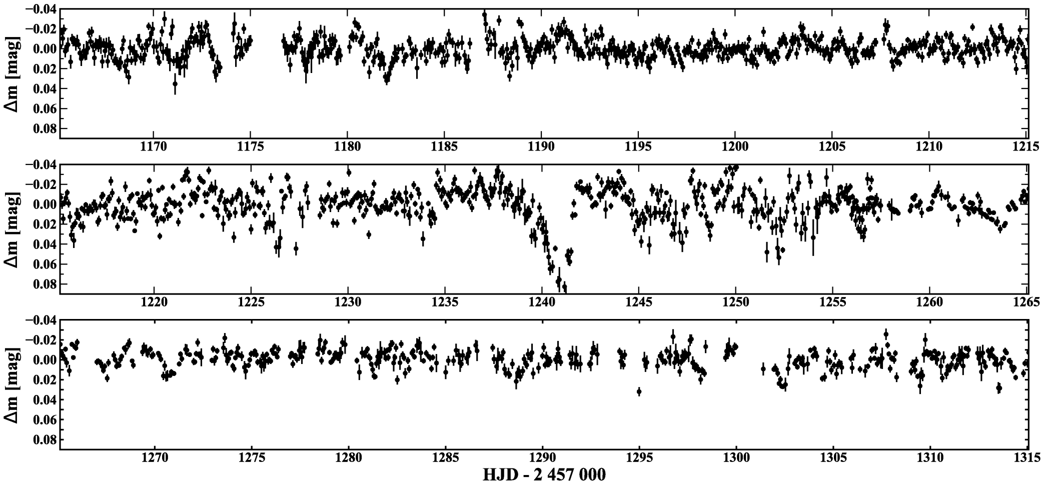

Figure 3.2. As in Fig.1 but for 2018. The single eclipse observed near the middle of the run is easily distinguished.

3. Modelling

We show the reduced BRITE light-curve from the 2017 and 2018 runs in Figures 3.1 and 3.2. A total of three eclipses were observed, that look basically identical except for the intrinsic noise pattern most likely from the blue supergiant (BSG), which will be examined in a separate study after subtracting off the best-fitted eclipse. The data from the 2018

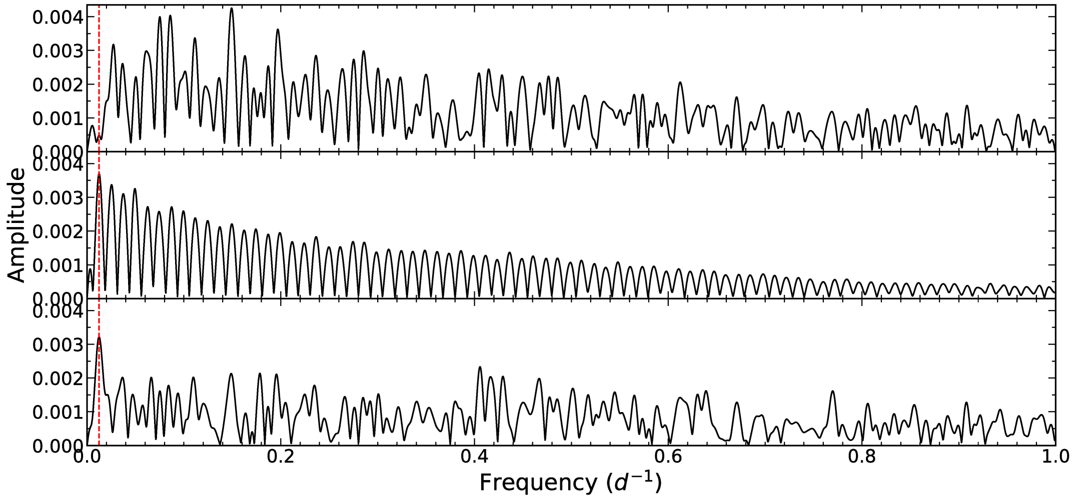

Figure 3.3. Top : periodogram of the light-curve presented in Figure 3.1 for 2017. Middle : periodogram of the fitted eclipse model without the data but following the same point sampling as the data. The high number of oscillating harmonics is due to the presence of two eclipses in that time-series, which interfere with one another in the Fourier dimension. Bottom : periodogram of the 2017 observations after subtracting the fitted model. The frequency position of the 80.336d orbital period is marked with a red vertical dashed-line in all periodograms.

run appear to show additional instrumental scatter associated with the general and gradual degradation of the detector.

Figures 3.3 and 3.4 show periodograms of the 2017 and 2018 data, respectively. These include power spectra for the observed data (upper panel), the model eclipse (see below) without data but for the same distribution of data-points (middle) and after subtraction of the model eclipse (bottom). The observed periodograms obtained after subtracting off the eclipse is dominated by a forest of low-frequency peaks that likely arise from random clumping in the WR wind (as in the WN8h star WR40 : (Ramiaramanantsoa et al. 2019), whose stochastic nature manifests itself in the lack of a match in the detailed power peaks for each run). The 2018 periodogram also appears somewhat different in overall nature with lower density of low-frequency power peaks, probably a result of what seems to be increased instrumental noise in the 2018 light-curve in Figure 3.2. The difference in the model eclipse periodogram for each run reflects the fact that there are two eclipses in 2017 and only one eclipse in 2018, leading to a higher amplitude and clearer harmonics in the former, due mainly to the narrow nature of the eclipse.

We then used the well-known ephemeris of WR22's binary parameters (Rauw et al. 1996 ; Schweickhardt et al. 1999, with priority for the latter due to its more precise value) to

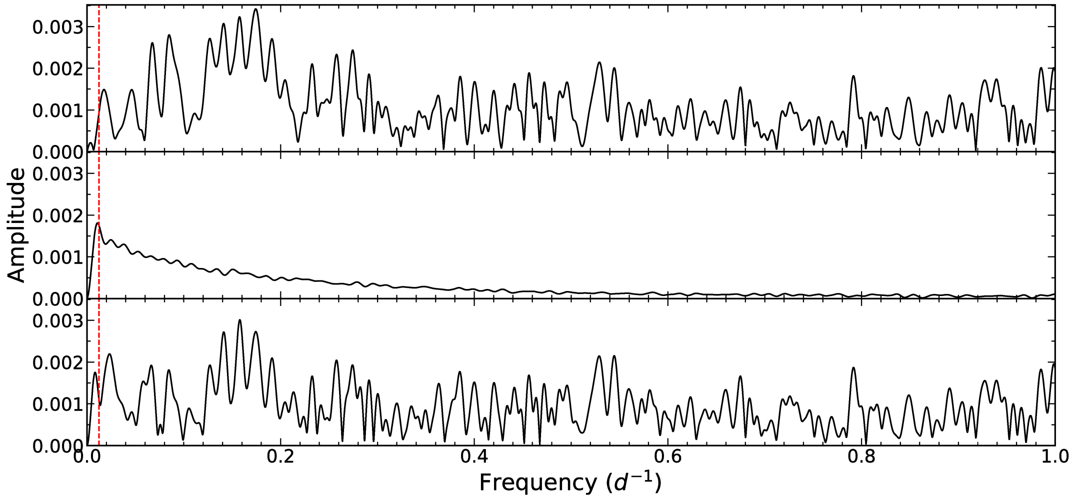

Figure 3.4. Top : periodogram of the light-curve presented in Figure 3.2 for 2018. Middle : periodogram of the fitted eclipse model without the data but following the same point sampling as the data. This time, the harmonic spectrum is still seen, albeit at somewhat lower amplitude but without the extreme oscillations, due to the presence of only one eclipse. Bottom : periodogram of the 2018 observations after subtracting the fitted model. As in Figure 3.3, the 80.336 d orbital period is marked with a red vertical dashed-line in all periodograms.

combine these three eclipses into one phased light-curve, as shown in Figure 3.5. Besides the eclipse itself, the stochastic nature of the rest of the light-curve is obvious, with a total spread of $\sim 0.06\ mag$.

From Figure 3.5 the basic question arises whether the eclipse is photospheric or atmospheric. In the former case, if the orbit were circular and the orbital inclination were high enough, one is likely to see two eclipses, one at either conjunction as each star in turn eclipses the other. But in an elliptical orbit as here for WR22, it is possible that one could only be seeing one eclipse close to periastron when the two stars are closer together, while the second eclipse is hindered by a larger orbital separation towards apastron. In the case of an atmospheric eclipse, the question of seeing more than one eclipse is irrelevant when the companion to the WR star is a weak-wind O-star, as is the case here. As for the nature of the eclipse, we first explore the possibility of an atmospheric eclipse.

3.1. light-curve analysis strictly as an atmospheric eclipse

We follow the simple recipe for fitting an atmospheric eclipse developed by Lamontagne et al. (1996) for short-period WR + O binary systems with circular orbits (L96). We adapt this to the longer elliptical orbit of WR22 using the orbital elements of Schweickhardt et al. (1999), which we slightly preferred over the earlier work of Rauw et al. (1996).

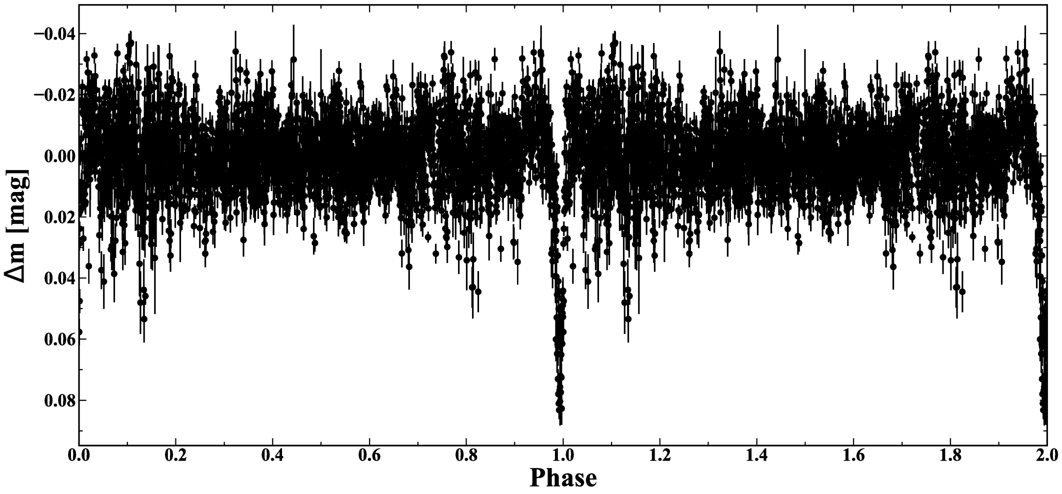

Figure 3.5. Phased light-curve of WR22 for 2017 and 2018 combined from the BHr satellite.

In the L96 model, the O star is assumed to be a point source. Flux variations are due to changing absorption of the WR wind and possibly to the geometrical eclipse of the O star by the WR disk. The wind absorption in the optical domain is due to electron scattering which is wavelength independent. Thus the optical depth is an integral along the line of sight from the O star to the observer is

$$\tau(\phi) = \tau_0 \int_{z_0/a}^{\infty} \frac{d(z/a)}{(r/a)^2 v(r/a)/V_\infty}, \tag{3.1}$$

where,

$$\begin{aligned}(r/a)^2 \;=\;& (d/a\cos(i)\cos(v+\omega-\pi/2))^2 \\ &+(d/a\sin(v+\omega-\pi/2))^2 \\ &+(z/a)^2,\end{aligned} \tag{3.2}$$

d is the current distance between the components, ω is the longitude of periastron of the O star, v is true anomaly and,

$$z_0/a = -d/a\sin(i)\cos(v+\omega-\pi/2), \tag{3.3}$$

the wind velocity law $v(r)$ follows the usual β-law,

$$v(r) = V_\infty\left(1-\frac{R_{\rm WR}}{r}\right)^{\beta}, \tag{3.4}$$

and τ_0 is defined as

$$\tau_0 = \sigma_T n_0 a, \tag{3.5}$$

where σ_T is Thomson cross-section, a is the major orbital semi-axis, n_0 is a fiducial electron density

$$n_0 = \frac{\dot{M}}{4\pi m_p \mu_e a^2 V_\infty}, \tag{3.6}$$

where $\dot{M}$ is the WR mass loss rate, m_p is the proton mass, $\mu_e \simeq 2/(1+X)$ is the mean electron molecular weight and X is the H fraction.

The observed light-curve is fitted by

$$\Delta m(\phi) = \Delta m_0 - 2.5 \log \frac{1 + F_r e^{-\tau(\phi)}}{1 + F_r e^{-\tau(\phi_0)}}, \tag{3.7}$$

where Δm_0 is the zero point accounting for the magnitude difference between the target and the comparison star, $F_r = F_{\mathrm{O}}/F_{\mathrm{WR}}$ is the O/WR flux ratio, ϕ_0 is the reference phase, while the relative magnitude (the second term in eq. 3.7) at this phase is equal to 0.

While computing a model light-curve, we verify at every orbital phase the condition for a total eclipse (that the plane of the sky projected distance between the O star and the center of WR is smaller than the WR radius). Thus our model can also be applied to the case of the total (geometrical) eclipse. However, as such an eclipse is not observed in WR22, we restrict the inclination angle so that the minimal projected distance is equal to R_{WR}. This maximal allowable inclination is defined by the simple formula

$$\tan(i) \leq \frac{a \sin(i)(1-e^2)}{(1 + e\cos(v_{con}))R_{\mathrm{WR}}}, \tag{3.8}$$

where $v_{con} = \pi/2 - \omega$ is the true anomaly at the upper conjunction.

The model parameters are Δm_0, F_{ratio}, R_{WR}, i and τ_0.

It is important to use the proper beta-law for the WR wind, since the eclipse is very narrow and thus includes part of the WR wind near its base, where the choice of the value of beta becomes more critical. As in other H-rich WNL stars and some extreme Of stars, we take beta ∼1 (Lépine and Moffat, 2008), as opposed to larger beta-values that might be appropriate for classical WR winds with higher density (Lepine and Moffat, 1999). For the hydrostatic radius of the WR component we take $R_\star = 22.65\,\mathrm{R}_\odot$ from Hamann et al. (2019). For the

Table 3.1. Parameters of the adopted light-curve solution.

Parameter	Value
Assumed Parameters	
P [days]	80.336 ± 0.0013 [a]
T_0 [HJD]	2 450 126.97 ± 0.14 [a]
e	0.598 ± 0.010 [a]
$\omega(WR)$ [^{o}]	268.2 ± 1.6 [a]
$\mathrm{a_{WR}} \sin i$ [10^6 km]	62.5 ± 0.9 [a]
$\mathrm{a}_O \sin i$ [10^6 km]	168.2 ± 9.0 [a]
α	1.0 [b]
$\mathrm{M}_v(WR)$	-6.8 [a]
$\mathrm{M}_v(O9V)$	-4.0 [a]
v_∞ [km/s]	1785 [c]
Fitted Parameters	
A	$(7.74 \pm 0.52) \times 10^{-4}$
dm_0 [mmag]	(-1.4 ± 0.2)
i [°]	80.56 ± 0.08
Derived Parameter	
$\dot{M}_{\mathrm{WR}}$ [$10^{-5}\mathrm{M}_\odot$ / year]	2.2 ± 0.1

[a] Schweickhardt et al. (1999) ; O9V preferred over O9III
[b] Lamontagne et al. (1996)
[c] Hamann et al. (2019)

visual brightness of the stars we adopt the absolute values $M_v = -6.8$ and -4.0 for the WR- and O-component, respectively, from Schweickhardt et al. (1999). Table 3.1 summarizes the parameters fitted and adopted. Figure 3.6 shows a zoomed-in version of the fit centred on the eclipse. It shows increased scatter during the eclipse, especially from one eclipse to the next, although apparently random without any obvious systematic effects. The reason for this may be that besides the continuing stochastic scatter off clumps present globally in the WR wind from the light of the WR star itself, even during the eclipse, there could be enhanced scattering of O-star light by WR clumps along the line of sight to the O-star.

Among the determined parameters in Table 3.1, of particular interest are the orbital inclination $i = 80.56 \pm 0.08°$ and the WR mass-loss rate $\dot{M}_{\mathrm{WR}} = (2.16 \pm 0.14) \times 10^{-5} \mathrm{M}_\odot$ /year. While the latter is within the normal range for luminous WN stars with hydrogen, there could have been a problem with the assumptions we adopted in the L96 model. In that model, we have assumed that the O-star is a point source and that the WR wind is optically thin, at least where the electron scattering occurs, leading to the observed eclipse. This could apply in principal but might become more of a problem for very high inclinations if the O star is eclipsed by the denser parts of the WR wind. Nevertheless, the fit may appear adequate, but the question remains whether it provides realistic parameters. We will test this in the next

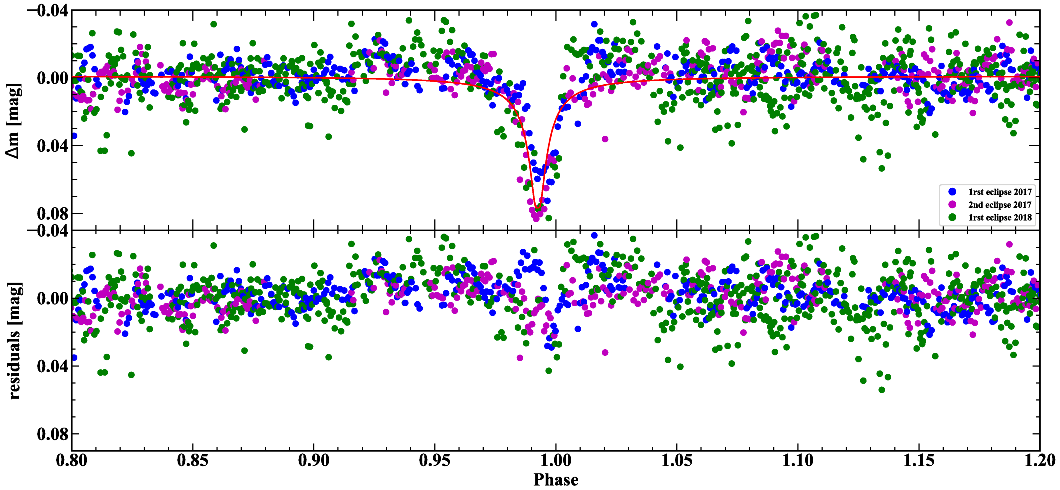

Figure 3.6. Top : Phased light-curve of WR22's eclipses from 2017 and 2018, fitted in red (for the whole light-curve, not just the part shown here) with Lamontagne et al. (1996) equation for a WR wind with $\beta = 1$. Blue dots correspond to the data acquired around the time of 2017's first observed eclipse, magenta dots are for 2017's second eclipse and green dots for 2018's only eclipse. Bottom : Residuals obtained from subtracting the fit from the data.

section, where we allow for a finite disk for the O-star plus multiple scattering in the WR wind, by looking at a photospheric eclipse, a much more complicated and difficult case.

3.2. Light-curve analysis as a photospheric and wind eclipse

We can gain information on the need to apply a photospheric plus atmospheric as opposed to an atmospheric eclipse only, by simply examining the conditions for photospheric eclipses, i.e. there will be no core eclipse if $r\cos(i) > R_{\rm WR} + R_{\rm O}$, where r is the separation between the centres of the two stars at the respective conjunctions and $R_{\rm WR}$, $R_{\rm O}$ are the photospheric radii of the stars. Taking $i = 80°$ as a preliminary although likely value, both from Rauw et al. (1996) and from the above fit, we list in Table 3.2 the relevant parameters during both eclipses at (almost exactly as it turns out) periastron (where we know that one eclipse does occur) and apastron (where a second eclipse might have occurred), based on the orbits of Rauw et al. (1996) and Schweickhardt et al. (1999). For the WR star we take $R_\star$ and $R_{2/3}$ as extreme values between the hydrostatic stellar radius (Hamann et al., 2019) and the pseudo-photosphere in the wind (Schweickhardt et al., 1999). For the O star we adopt radii for O9V stars and O9III stars (Martins et al., 2005), the former being more likely (Schweickhardt et al., 1999).

Table 3.2. Parameters that determine if there are photospheric eclipses. All radii are in $R_\odot$. i is assumed to be 80°.

Parameter	Rauw et al. (1996)	Schweickhardt et al. (1999)
e	0.559 ± 0.009	0.598 ± 0.010
a$\sim$ a sin i	361.1 ± 14.4	331.5 ± 12.9
r_{per} = a(1-e)	159.2	133.3
r_{ap} = a(1+e)	563.0	529.7
r_{per} cos i	27.64	23.15
r_{ap} cos i	97.76	91.98
	Minimum	Maximum
$R_{\rm WR}$	22.65($R_\star$)	28.5($R_{2/3}$)
R_O	7.73(V)	13.69(III)
$R_{\rm WR}$ + R_O	30.38	42.2

From Table 3.2, we see that, indeed, a photospheric eclipse is likely at periastron and unlikely at apastron. We therefore now explore the scenatio of one eclipse at periastron.

3.3. Roche lobe model plus wind eclipse

In this section, the light-curve is fitted by using the model (A13) of Antokhina et al. (2013) extending the standard Roche-lobe model by including a wind around one of the components. The model is calculated within a computer code that allows one to calculate light and radial velocity curves as was described by Antokhina (1988, 1996) and Antokhina et al. (2000). The code uses algorithms similar to Wilson and Devinney (1971), Wilson (1979) and has been applied to binary systems of various types. It allows to compute the light and radial velocity curves at circular or eccentric orbits.

The shapes of both components are computed according to a Roche-lobe geometry. The model subdivides the surfaces of both components in small areas and computes the flux of each area accounting for limb and gravitational darkening and mutual irradiation. The wind of the WR component is considered as being spherically symmetric and described by a velocity law (equation 3.4). $R_{\rm WR}$ in this equation is assumed to be equal to the radius of a sphere which volume is equal to the volume of the WR body computed in the Roche geometry. Wind absorption is computed for every elementary area of both components by numerically integrating equation 3.1. The model also accounts for the WR wind absorption when computing irradiation (i.e. emission of one component reflected off the other). The program computes monochromatic flux at the middle wavelength of the observations bandpass. The model parameters are as follows :

(1) P – orbital period ;

(2) T_0 – the date of zero phase (either conjunction or periastron) ;

(3) e – eccentricity ;

(4) ω – longitude of periastron for the O star ;

(5) $M_1 \sin^3 i$, $M_2 \sin^3 i$ – Masses of components multiplied by $\sin^3 i$;

(6) μ_1, μ_2 – Roche lobe filling factors, $\mu = R/R_c$, where R is the polar radius of a stellar body and R_c is the polar radius of the critical Roche lobe at periastron ($0 < \mu \leq 1$). At other orbital phases, μ_1, μ_2 are recomputed from the condition that the volumes of stellar bodies are constant ;

(7) T_1, T_2 – stellar temperatures. Note that as the program computes the monochromatic flux assuming black body spectrum, these temperatures are essentially the flux scaling parameters and do not directly correspond to the actual stellar temperatures, especially for the WR star ;

(8) F_1, F_2 – ratios of surface rotation rate to synchronous rate ;

(9) β_1, β_2 – gravity darkening coefficients ;

(10) A_1, A_2 – bolometric albedos ;

(11) $(x,y)_1$, $(x,y)_2$ – limb darkening coefficients ;

(12) λ – effective wavelength of the monochromatic light-curve ;

(13) Δm_0 – the zero point of stellar magnitude as in the L96 model ;

(14) $\Delta\phi$ – the phase shift of the observed light-curve (observed minus predicted phase) due to the inaccuracy of T_0 and/or of P ;

(15) β – parameter of the β-law ;

(16) V_∞ – terminal velocity of the WR wind ;

(17) μ_e – mean electron molecular weight ;

(18) $\dot{M}$ – WR mass loss rate ;

Note that the last three parameters are only used when solving the direct problem, i.e. computing the model light-curve with a given set of model parameters. These parameters are not independent and are linked by eqs. (3.5 and 3.6). When carrying out the fit, the actual key model parameter is τ_0. Once it is determined, e.g. $\dot{M}$ can be derived by assuming values for V_∞ and μ_e.

Several model parameters are either known from previous studies or can be adopted to reasonable values. P, T_0 (the periastron date), e, ω, $M_1 \sin^3 i$, $M_2 \sin^3 i$ where taken from Schweickhardt et al. (1999). The rotation of both components was assumed synchronous so $F_{1,2}$ were set to unity. The gravity darkening coefficients $\beta_{1,2} = 0.25$ were set according to von Zeipel (1924). The non-linear "square-root" limb darkening was computed according to van Hamme (1993). Albedos were set to unity as appropriate for radiative atmospheres. We set the wind velocity parameter $\beta = 1$ as in our L96 model. The effective wavelength λ was set to the middle wavelength of the *BRITE* satellite red band pass (6200Å).

Usually, the filling factors μ (i.e. stellar radii) are of greatest interest in binary studies along with the inclination angle, masses and temperatures. Reliable estimates are hampered by the fact that even in systems with two eclipses, these parameters correlate with other ones, most notably with inclination. In addition, in the A13 model, there is additional parameter degeneracy due to the wind. Given that WR22 has only one shallow eclipse we were forced to fix the radii to reasonable values.

As in the L96 model, we set a fixed radius for the WR component from Hamann et al. (2019). These authors did not fit every WR star individually. Instead, they pre-computed a grid of stellar atmosphere models and compared the observed WR spectra with the grid spectra to find the closest grid model. Therefore, they do not provide the formal errors of the stellar parameters. They state that the chosen model may be off by one or two grid cells. Their grid cell size was equal to 0.1 dex, thus we can roughly estimate the error of the WR radius as being $\sim 26\%$. Luckily, at least with wind-only absorption as the eclipse source, R_{WR} enters the model only through the wind velocity law $v(r)$ (see eq.3.4). With the adopted value of $\beta = 1$, the wind velocity increased very rapidly and thus $\sim 26\%$ change of the WR radius does not affect the density of most of the WR wind (and hence the results) significantly.

Unlike the L96 model, we must set the O-star radius as well. Thus the question if the O star has the luminosity class V or III becomes important. Schweickhardt et al. (1999) noted that the ratios of equivalent widths of several spectral lines pointed towards the luminosity class III. On the other hand, by assuming that the eclipse in WR22 was total (the exact shape of the eclipse was unknown at the time) they obtained the flux ratio which pointed towards the luminosity class V. They favored the latter based on the marginaly better quality of their equivalent width measurements. From the present data we know that the eclipse is not total. To explore all possibilities, we ran our fitting algorithm for two values of R_{O} corresponding to the luminosity class V and III (Models 1 and 2 respectively). The radii were assigned to the mean observed radii of a large sample of O9 stars by Martins et al. (2005). The list of the major model parameters (assumed, fitted, and derived) is shown in Table 3.3.

The main difference between the two models is the finite size of the O star in the A13 model as opposed to the point source O-star approximation in the L96 model. Thus, in the A13 model, the eclipse may be made up of two components – a partial geometric eclipse and the wind absorption. Another essential difference is that in the A13 model, the flux ratio F_r cannot be set as an input parameter. In this model, the emerging WR flux is equal to

Table 3.3. Major A13 model parameters.

Parameter	Value
Assumed Roche model parameters	
P	80.336 d [a]
T_0	HJD 2 450 127.47 [a]
$M_O \sin^3 i$	$20.6\,\mathrm{M}_\odot$ [a]
$M_{\mathrm{WR}} \sin^3 i$	$52.6\,\mathrm{M}_\odot$ [a]
e	0.598 [a]
ω_{O}	88.2 deg [a]
T_{O}	32900 K (Model 1) ; 31850 K (Model 2) [b]
T_{WR}	20 000 - 160 000 K
R_{O}	$7.53\,\mathrm{R}_\odot$ (Model 1) ; $13.38\,\mathrm{R}_\odot$ (Model 2) [b]
R_{WR}	$22.65\,\mathrm{R}_\odot$ [b]
Assumed Wind parameters	
β	1.0
V_∞	$1785\,\mathrm{km\,s^{-1}}$ [c]
μ_e	1.39 [c]
Best fit parameters	
Model 1 (WR + O9 V)	
T_{WR}	105 000 K (the grid point of the best fit model)
i	83.6 ± 0.4 deg
τ_0	0.0097 ± 0.0002
Δm_0	-0.00013 ± 0.00007
$\Delta\phi$	-0.0064 ± 0.0002
χ^2/d.o.f	$3797.10/3442 = 1.103$
Derived parameters	
$F_{\mathrm{O}}/F_{\mathrm{WR}}$	0.074
$\dot{M}_{\mathrm{WR}}$	$(2.80 \pm 0.05) \times 10^{-5}\mathrm{M}_\odot\ \mathrm{yr}^{-1}$
μ_{O}	0.187
μ_{WR}	0.344
M_{O}	$20.99\,\mathrm{M}_\odot$
M_{WR}	$56.34\,\mathrm{M}_\odot$
$\log(g)_{\mathrm{O}}$	4.00 [d]
$\log(g)_{\mathrm{WR}}$	3.05 [d]
Model 2 (WR + O9 III)	
T_{WR}	100 000 K (the grid point of the best fit model)
i	73.8 ± 0.2 deg
τ_0	0.011 ± 0.0002
Δm_0	-0.00004 ± 0.00012
$\Delta\phi$	-0.0064 ± 0.0002
χ^2/d.o.f	$3763.61/3442 = 1.093$
Derived parameters	
$F_{\mathrm{O}}/F_{\mathrm{WR}}$	0.28
$\dot{M}_{\mathrm{WR}}$	$(3.30 \pm 0.04) \times 10^{-5}\mathrm{M}_\odot\ \mathrm{yr}^{-1}$
μ_{O}	0.321
μ_{WR}	0.333
M_{O}	$23.24\,\mathrm{M}_\odot$
M_{WR}	$62.40\,\mathrm{M}_\odot$
$\log(g)_{\mathrm{O}}$	3.55 [d]
$\log(g)_{\mathrm{WR}}$	3.10 [d]

[a] Schweickhardt et al. (1999)

[b] Martins et al. (2005)

[c] Hamann et al. (2019)

[d] Logarithm of the surface gravity.

the “intrinsic” WR flux (i.e. the flux at the WR surface, not absorbed by the WR wind) processed (absorbed) by the WR wind. Thus, this flux (which corresponds to F_{WR} in the L96 model) depends not only on the WR temperature and radius, but also on the wind optical depth which is a model free parameter. The O star flux also depends on the heating caused by the radiation of the WR star. Thus, the O/WR flux ratio can be computed only after the fit is done. For this reason, we compute a grid of models similar to L96 above, for a range of T_{WR} instead of F_r. The dependence of the flux ratio on τ_0 causes important differences in the behaviour of the models, see below.

Since a binary light-curve contains only information about relative flux changes, light-curve analyses can only determine the ratio of the stellar temperatures and not their absolute values. Thus, usually the temperature of one component is adopted. We set the temperature of the O star to that of the average O9 V and III star temperatures for Models 1 and 2 from Martins et al. (2005).

At every trial T_{WR}, a best fit solution of the light-curve was found by the Levenberg-Marquardt (Strutz, 2016) method. The covariance matrix was used to estimate the errors of the best-fit parameters. As no total eclipse is observed, we used a penalty function restricting the orbital inclination by the maximal value defined by $d_{con}\cos(i_{max}) \geq R_{\mathrm{WR}} - R_{\mathrm{O}}$, where d_{con} is the orbital separation at the upper conjunction. The results of fitting on a grid of WR temperatures for Models 1 and 2 are shown in Figs.3.7-3.8 and in Table 3.3.

In Fig.3.7 the expected degeneracy between the flux ratio, orbital inclination, and O star radius is clearly seen. The value of χ^2 only weakly depends on the WR temperature or the flux ratio. Both Models 1 and 2 at the corresponding χ^2 minima are formally rejected at 99% significance level. However, the χ^2 value was computed assuming a normal distribution of data-point errors. Recall that the actual scatter of the observed data points outside eclipse is much larger than the photometric uncertainties of individual points due to the stochastic variability of the BSG star. The pattern of the outside of eclipse variability seems to be not completely random and may represent some kind of autoregressive process. This variability will be a subject of a separate paper. For the purpose of our modelling we considered it as random Gaussian noise and estimated the empirical data point error by computing the uncertainty $\sigma_{obs} = 0.010511$ in phase interval $0.1 - 0.9$. We then assigned this uncertainty to all data-points. Non-normal distribution of measurement errors usually results in decreasing the significance level of a model. To illustrate how a small change in the empirical uncertainty would influence the model goodness-of-fit, we show in Fig. 3.7 the χ^2 curves corresponding to the slightly changed $\sigma'_{obs} = 0.0108$ (red curves).

The above considerations show that while it is hard to obtain a robust estimate of the formal significance of the model, the overall agreement with the data seems to be acceptable.

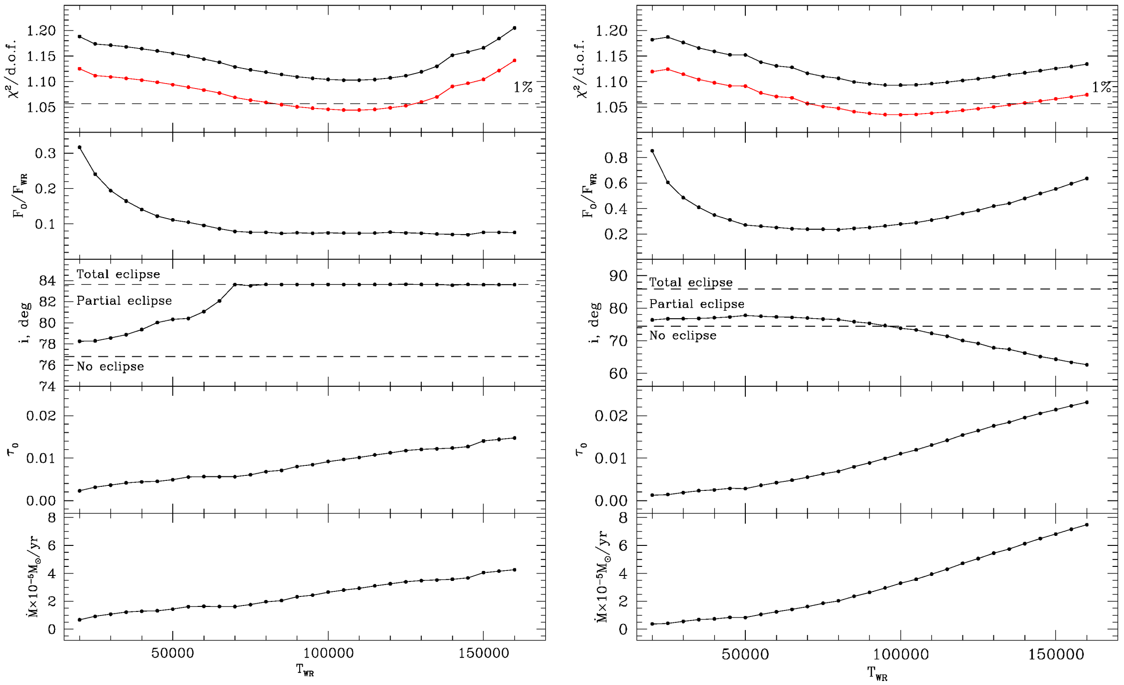

Figure 3.7. Best fit model parameters as function of the WR temperature. Left : Model 1, $R_{\rm O} = 7.53$ R$_\odot$ (luminosity class V). Right : Model 2, $R_{\rm O} = 13.38$ R$_\odot$ (luminosity class III). The dashed lines in top panels show 99% significance level. The red lines show χ^2 curves at the assumed observational uncertainty 0.0108 (see the text). The dashed lines in the inclination plots mark the borders between wind-only, partial geometric, and total eclipses.

Note that the errors of the model parameters given in Table 3.3 are also computed in the assumption of normal distribution of measurement errors and thus should be taken with caution.

One commonly used way to estimate the goodness-of-fit of a model and the confidence intervals of its parameters in the case of a non-normal distribution of measurement errors is to run Monte Carlo simulations. However, this approach requires the knowledge of the actual distribution of the measurement errors and is based on the assumption that this distribution is identical and independent in all data points. In WR22 this is not the case. The outside-of-eclipse variability changes with time and seems to resemble some kind of autoregressive process.

Due to the degeneracy of the parameters it is impossible to obtain a unique solution of the light-curve. While at fixed values of the WR temperature and/or O star radius, the orbital inclination and the WR mass-loss rate are defined with good accuracy, it is still possible to choose various almost equally good solutions with quite different parameters. In Table 3.3 the formal best fit solutions for Models 1 and 2 are given.

The behaviour of Models 1 and 2 (the first assuming a specta of type O9 V for the companion, while the second considers a spectral type of O9 III) is distinctly different. Let us consider them in turn.

Model 1. At small WR temperatures, the best fit is achieved by the combination of a partial geometric eclipse and wind absorption of the non-eclipsed parts of the O-star disk. The reason for this is that wind-only absorption (at smaller inclination) would lead to an eclipse wider than observed. A partial geometric eclipse allows one to decrease the wind absorption and to fit both the observed eclipse depth and width. As the WR temperature (and hence its intrinsic flux) increases, the flux ratio O/WR decreases and one needs a larger geometric eclipse (hence a higher inclination). As the non-eclipsed part of the O star disk becomes smaller, one needs to increase the wind absorption to achieve a good fit. At $T_{\rm WR}$ of about 60 000 K, the reflection effect (irradiation of the WR emission by the O star) becomes important (see Fig.3.8). It creates excess emission on both sides of the geometric eclipse so further increase in wind absorption is needed in order to reduce it to the observed level. Finally, the orbital inclination reaches the partial eclipse limit (the whole O star disk is eclipsed and touches the circumference of the WR disk at the moment of conjunction, see Fig.3.10). At this inclination, the eclipse depth is defined by the flux ratio only. Wind absorption only affects the eclipse width (see Fig.3.8, left panel). With a further increase of the WR temperature, the reflected emission continues to increase, thus the wind optical depth also increases to reduce it.

Let us now consider the behavior of the flux ratio $F_{\rm O}/F_{\rm WR}$ in the left panel of Fig.3.7. At a given orbital phase, the O star flux is the sum of its intrinsic flux (defined by the star's temperature) and the flux caused by reflection of the WR emission off the O star surface. The WR star flux is the intrinsic flux (defined by the WR temperature) processed (absorbed) by the WR's own wind [3]. The flux ratio shown in Fig.3.7 is computed at the orbital phase 0.25 where the reflection effect is negligible. Thus, the O-star flux is constant and the plotted flux ratio depends only on the WR temperature and wind optical depth. The WR intrinsic flux increases with temperature. At the same time, the wind optical depth increases to fit the observed eclipse. The resulting emerging WR flux increases but not as fast as if there were no wind absorption. The flux ratio $F_{\rm O}/F_{\rm WR}$ decreases correspondingly. When the orbital inclination reaches the maximum value allowed by partial geometric eclipse, the flux ratio stops decreasing as the increase of the intrinsic WR flux is fully compensated by the increase of the wind optical depth.

Model 2. At small WR temperatures the behavior of this model is qualitatively similar to Model 1. As in the latter, the best fit is achieved when the model eclipse is a combination of wind absorption and a geometric eclipse. The inclination angle is smaller as the O-star radius

---

[3] The A13 code accounts for mutual irradiation. As the WR star in WR22 is much brighter than the O star, the effect of the O star emission reflected off the WR star is negligible.

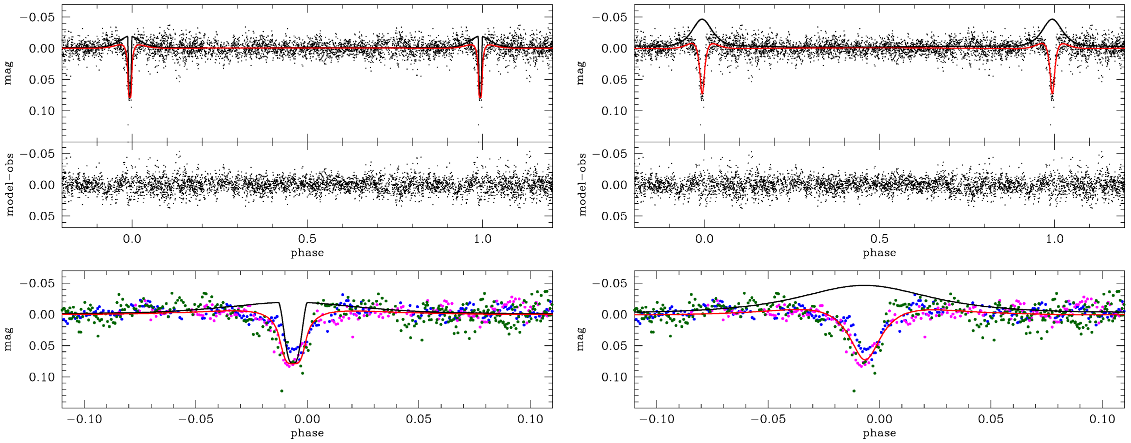

Figure 3.8. Best-fit light-curves corresponding to the respective χ^2 minima from the previous figure. Left : Model 1. Right : Model 2. The red solid line is the best fit Roche+Wind light-curve. The black solid line shows the Roche model component only, i.e. not including the wind absorption of the O-star flux. The colors of the observed data points in the lower panel correspond to those in the L96 best fit plot.

is about 1.7 times larger than in Model 1. With increasing WR temperature, the inclination angle also slightly increases. However, after the WR temperature reaches about 50 000 K, the orbital inclination begins to decrease again (see Fig.3.7, right panel). The reason is that the reflection effect becomes important. Due to a larger O star radius in Model 2, the reflection effect is more pronounced than in Model 1 (Fig.3.8). The only way to reduce the excess emission is to increase the wind absorption. However, this also increases the model eclipse depth. To prevent this, the minimization routine must decrease the inclination. Another factor which prevents the increase of the inclination is the large O-star flux and hence the flux ratio in Model 2. The O-star flux is roughly proportional to $R_{\rm O}^2$, thus at a comparable wind optical depth, the flux ratio in Model 2 is about 2.8 times larger than that in Model 1. The increase of the inclination combined with the increase of wind absorption would render the model eclipse too deep.

Since the excess emission due to the reflection effect in Model 2 is larger than in Model 1, the wind absorption at high WR temperatures is larger and increases faster than that in Model 1 (see the τ_0 plots in Fig.3.7). Thus, unlike Model 1, wind absorption increases more rapidly than the intrinsic WR flux. This results in a decrease of the emerging WR flux and an increase of $F_{\rm O}/F_{\rm WR}$ at high WR temperatures.

In Fig.3.10 the sky plane view of best fit Models 1 and 2 is shown at orbital phases immediately before, at the moment, and after the upper conjunction.

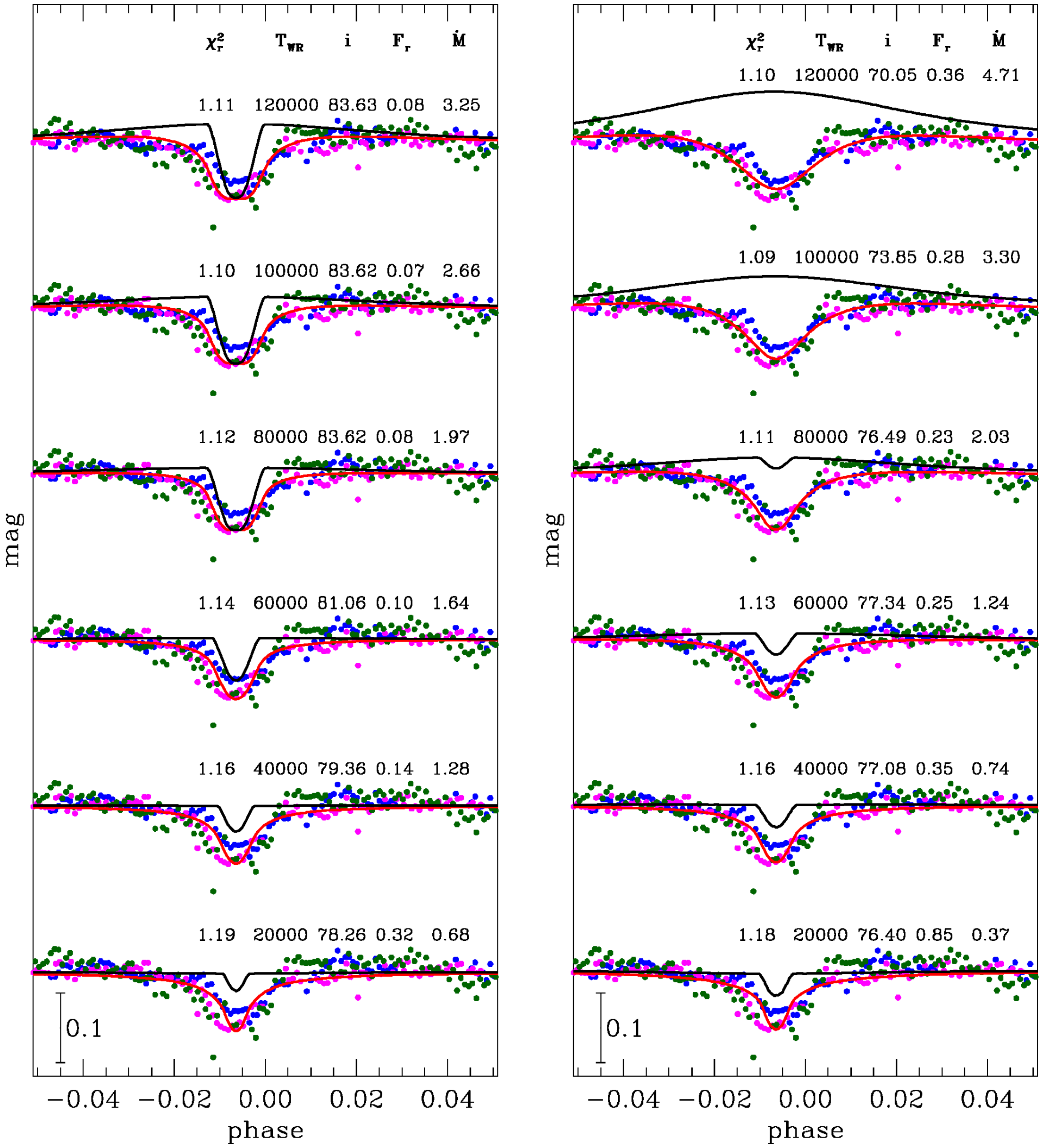

Figure 3.9. Characteristic best fit light-curves for Model 1 (left) and 2 (right). The observed light-curve is shown by colored dots (the color legend as above). The model light-curves are shown by solid red lines. The black lines show the Roche component of light-curves, i.e. not including wind absorption of the O star. The values of reduced χ^2, T_{WR}, inclination, flux ratio, and $\dot{M}$ (in units $10^{-5}\,\mathrm{M}_{o}dot\,\mathrm{yr}^{-1}$) are shown at each individual light-curve.

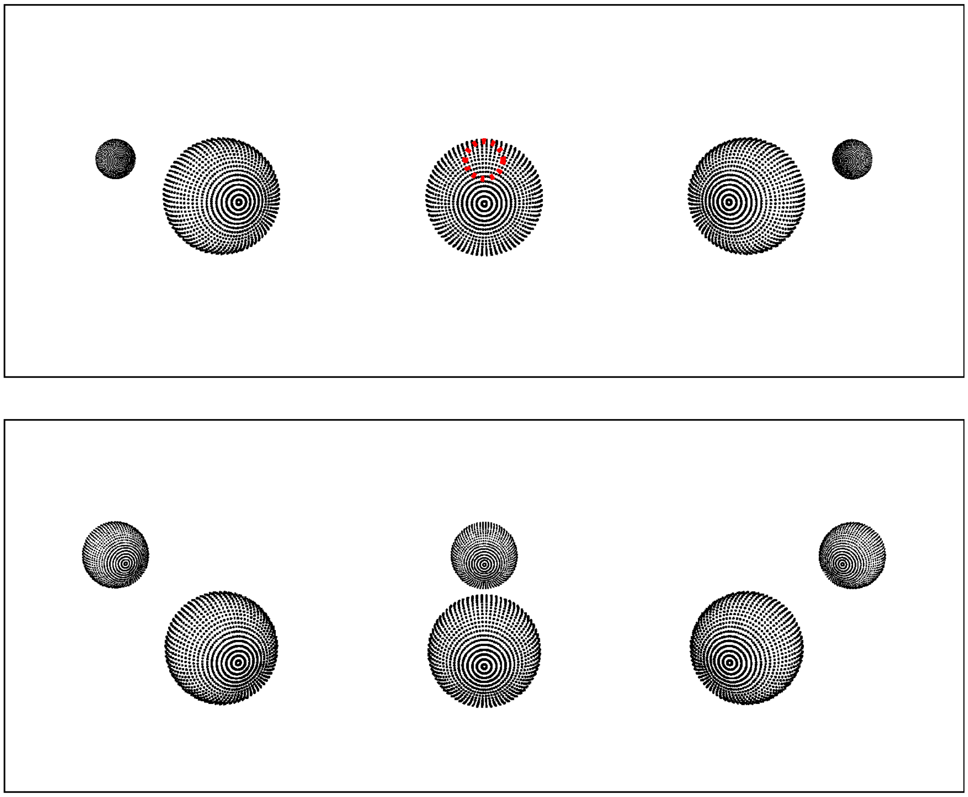

Figure 3.10. Sky plane view of the system in best fit Models 1 (top) and 2 (bottom) at orbital phases before, at the moment, and after conjunction.The phase difference with the conjunction moment is ±0.01.

4. Discussion

Are both models acceptable ? Statistically, the answer is yes. On the other hand, the solution obtained with the Lamontagne et al. (1996) atmospheric-eclipse model yields an inclination equal to the critical value such that the projection of the O-star point source on the plane of the sky just touches the WR disk at conjunction. With such a solution it is clear that the assumption of the point-source O star does not hold and that a more complex model is required to determine whether the eclipse is partially atmospheric or totally photospheric.

Recall that the WR temperature is just the flux scaling parameter and cannot be directly compared e.g. to the WR22 temperature of Hamann et al. (2019). However, the flux ratio is physically sound. In Model 1, the flux ratio is 0.074. Recall that this ratio is computed at the orbital phase 0.25. At the moment of conjunction it may be larger due to the reflection effect. In our best fit Model 2 the flux ratio is 0.28.

Rauw et al. (1996) obtained the values $\sim 0.08 - 0.2$ from different spectral lines. Schweickhardt et al. (1999) estimated the flux ratio as being ~ 0.08 by assuming that the eclipse is total. These estimates seem to give preference to our Model 1. However, both authors state that the O-star lines were only marginally detected and the errors of measured equivalent widths/line intensities are very large.

We conclude that our analysis with the A13 model has shown that it is impossible to give a unique value of the orbital inclination and WR mass-loss rate based solely on the photometric observations. Additional information is required, most importantly the O/WR flux ratio. Note however, that even if a reliable flux ratio is obtained from high precision spectroscopy, this will not necessarily lead to firm constraints on the inclination and the mass-loss rate. The reason is that, as demonstrated by our Model 2 (Fig.3.7), the same value of the flux ratio can be obtained in two very different cases : (i) a cool WR star and a small wind optical depth and (ii) a hot WR star and a large wind optical depth. Thus, to get a reasonable result, it is highly desirable to refine the luminosity class of the O9 components by using high precision spectroscopic data. Once the spectroscopic information about the flux ratio and luminosity class is available, the proper inclination angle and mass-loss rate can be obtained from Fig.3.7.

In the A13 Models 1 and 2 we have used a single fixed WR radius and two fixed values of the radius for the O star. Evidently, the actual stellar radius may be different. How strongly the change in radius will affect the results ? We already showed that increasing the O-star radius by a factor of ~ 1.7 has significantly changed the results. Such a large change is possible because the luminosity class of the O star is unknown. There are no reasons to assume that the WR radius may be changed by the same degree. As we discussed in the previous section, the rough estimate of its uncertainty is $\sim 26\%$. We re-ran fitting in both Models 1 and 2 (at a single selected WR temperature) with the WR radius increased and decreased by this amount. The results were not very different from the ones presented above. The inclination angle changed by a few tens of degree and the mass-loss rate changed accordingly. As for the other possible combinations of WR and O radii, recall that a binary light-curve possess information about relative values (ratios) of temperatures and radii. Our Models 1 and 2 correspond to two values of $R_{\mathrm{WR}}/R_{\mathrm{O}}$. If other radii are suggested, one could roughly estimate the expected results by interpolating ours between the Models 1 and 2, to the desired radius ratio.

5. Conclusions

Thanks to the ability of the BRITE satellites to lock onto a field for up to six months, we were able to obtain a light-curve for WR22 that reveals three complete single eclipses. A value for the mass-loss rate of $\dot{M}_{\mathrm{WR}} = (2.16 \pm 0.14) \times 10^{-5}\mathrm{M}_{\odot}$ /year was obtained using the simple L96 atmospheric eclipse model, which is normal for a WN7 star and an angle of inclination $i = 80.56°$. However this model aims at caracterizing atmospheric eclipses while at a large visual distance between their disks and as such considers the O star as a point-source, which is not a reasonable assumption in this case. The A13 model has shown that it is impossible to give a unique value of the orbital inclination and WR mass-loss rate based solely on the photometric observations and that prior knowledge of the O/WR flux ratio is necessary, as the resulting fit values for $\dot{M}_{\star}$ and i are highly dependent on it. Using these results, we conclude that the eclipse certainly is not fully atmospheric. Better constraints on the flux ratio of the components is however required to affirm the partially atmospheric or totally photospheric nature of this eclipse.

Acknowledgements

NSL & AFJM are grateful to NSERC (Canada) for financial aid.

References

E. A. Antokhina. Synthesis of Theoretical Lightcurves of Close Binary Systems. *Soviet Astronomy*, 32 :608, Dec 1988.

E. A. Antokhina. Synthesis of theoretical radial velocity curves and light curves for close binary systems with eccentric orbits. *Astronomy Reports*, 40(4) :483–493, Jul 1996.

E. A. Antokhina, I. I. Antokhin, and A. M. Cherepashchuk. Modelling light curves of binary systems : accounting for extended winds. *Astronomical and Astrophysical Transactions*, 28(1) :3–8, May 2013.

Eleonora A. Antokhina, Anthony F. J. Moffat, Igor I. Antokhin, Jean-François Bertrand, and Robert Lamontagne. Light Curve Solution of HD 93205 (O3 V+O8 V) Containing the Earliest Known Star in a Well-studied Binary. *Astrophysical Journal*, 529(1) :463–476, Jan 2000. doi : 10.1086/308228.

L. A. Balona, J. Egan, and F. Marang. Intensive photometry of southern Wolf-Rayet stars. *Monthly Notices of the RAS*, 240 :103–115, September 1989. doi : 10.1093/mnras/240.1.103.

E. Gosset, M. Remy, J. Manfroid, J. M. Vreux, L. A. Balona, C. Sterken, and G. A. P. Franco. WR 22 is an Eclipsing Binary Star. *Information Bulletin on Variable Stars*, 3571 :1, March 1991.

W. R. Hamann, G. Gräfener, A. Liermann, R. Hainich, A. A. C. Sander, T. Shenar, V. Ramachand ran, H. Todt, and L. M. Oskinova. The Galactic WN stars revisited. Impact of Gaia distances on fundamental stellar parameters. *Astronomy and Astrophysics*, 625 :A57, May 2019. doi : 10.1051/0004-6361/201834850.

Robert Lamontagne, Anthony F. J. Moffat, Laurent Drissen, Carmelle Robert, and Jaymie M. Matthews. Photometric Determination of Orbital Inclinations and Mass Loss Rates for Wolf-Rayet Stars in WR+O Binaries. *Astronomical Journal*, 112 :2227, November 1996. doi : 10.1086/118175.

Sebastien Lepine and Anthony F. J. Moffat. Is Clumping Universal in Hot Star Winds ? NOAO Proposal, August 1999.

Sébastien Lépine and Anthony F. J. Moffat. Direct Spectroscopic Observations of Clumping in O-Star Winds. *Astronomical Journal*, 136(2) :548–553, August 2008. doi : 10.1088/0004-6256/136/2/548.

F. Martins, D. Schaerer, and D. J. Hillier. A new calibration of stellar parameters of Galactic O stars. *Astronomy and Astrophysics*, 436(3) :1049–1065, June 2005. doi : 10.1051/0004-6361:20042386.

H. Pablo, G. N. Whittaker, A. Popowicz, S. M. Mochnacki, R. Kuschnig, C. C. Grant, A. F. J. Moffat, S. M. Rucinski, J. M. Matthews, A. Schwarzenberg-Czerny, G. Handler, W. W. Weiss, D. Baade, G. A. Wade, E. Zocłońska, T. Ramiaramanantsoa, M. Unterberger, K. Zwintz, A. Pigulski, J. Rowe, O. Koudelka, P. Orleański, A. Pamyatnykh, C. Neiner, R. Wawrzaszek, G. Marciniszyn, P. Romano, G. Woźniak, T. Zawistowski, and R. E. Zee. The BRITE Constellation Nanosatellite Mission : Testing, Commissioning, and Operations. *Publications of the ASP*, 128(970) :125001, December 2016. doi : 10.1088/1538-3873/128/970/125001.

A. Pigulski, H. Cugier, A. Popowicz, R. Kuschnig, A. F. J. Moffat, S. M. Rucinski, A. Schwarzenberg-Czerny, W. W. Weiss, G. Handler, G. A. Wade, O. Koudelka, J. M. Matthews, St. Mochnacki, P. Orleański, H. Pablo, T. Ramiaramanantsoa, G. Whittaker, E. Zocłońska, and K. Zwintz. Massive pulsating stars observed by BRITE-Constellation. I. The triple system β Centauri (Agena). *Astronomy and Astrophysics*, 588 :A55, April 2016. doi : 10.1051/0004-6361/201527872.

A. Popowicz, A. Pigulski, K. Bernacki, R. Kuschnig, H. Pablo, T. Ramiaramanantsoa, E. Zocłońska, D. Baade, G. Handler, A. F. J. Moffat, G. A. Wade, C. Neiner, S. M. Rucinski, W. W. Weiss, O. Koudelka, P. Orleański, A. Schwarzenberg-Czerny, and K. Zwintz. BRITE Constellation : data processing and photometry. *Astronomy and Astrophysics*, 605 :A26, September 2017. doi : 10.1051/0004-6361/201730806.

Adam Popowicz. *Image processing in the BRITE nano-satellite mission*, volume 9904 of *Society of Photo-Optical Instrumentation Engineers (SPIE) Conference Series*, page 99041R. 2016. doi : 10.1117/12.2229141.

Tahina Ramiaramanantsoa, Richard Ignace, Anthony F. J. Moffat, Nicole St-Louis, Evgenya L. Shkolnik, Adam Popowicz, Rainer Kuschnig, Andrzej Pigulski, Gregg A. Wade, Gerald Handler, Herbert Pablo, and Konstanze Zwintz. The chaotic wind of WR 40 as probed by BRITE. *Monthly Notices of the RAS*, 490(4) :5921–5930, December 2019. doi : 10.1093/mnras/stz2895.

G. Rauw, J. M. Vreux, E. Gosset, D. Hutsemekers, P. Magain, and K. Rochowicz. WR22 : the most massive Wolf-Rayet star ever weighed. *Astronomy and Astrophysics*, 306 :771, February 1996.

J. Schweickhardt, W. Schmutz, O. Stahl, Th. Szeifert, and B. Wolf. Revised mass determination of the super massive Wolf-Rayet star WR 22. *Astronomy and Astrophysics*, 347 : 127–136, July 1999.

Tilo Strutz. *Data Fitting and Uncertainty (2nd edition)*. 01 2016. ISBN 978-3-658-11455-8.

W. van Hamme. New Limb-Darkening Coefficients for Modeling Binary Star Light Curves. *Astronomical Journal*, 106 :2096, November 1993. doi : 10.1086/116788.

H. von Zeipel. Radiative equilibrium of a double-star system with nearly spherical components. *Monthly Notices of the RAS*, 84 :702, June 1924. doi : 10.1093/mnras/84.9.702.

W. W. Weiss, S. M. Rucinski, A. F. J. Moffat, A. Schwarzenberg-Czerny, O. F. Koudelka, C. C. Grant, R. E. Zee, R. Kuschnig, St. Mochnacki, J. M. Matthews, P. Orleanski, A. Pamyatnykh, A. Pigulski, J. Alves, M. Guedel, G. Handler, G. A. Wade, and K. Zwintz.

BRITE-Constellation : Nanosatellites for Precision Photometry of Bright Stars. *Publications of the ASP*, 126(940) :573, June 2014. doi : 10.1086/677236.

R. E. Wilson. Eccentric orbit generalization and simultaneous solution of binary star light and velocity curves. *Astrophysical Journal*, 234 :1054–1066, Dec 1979. doi : 10.1086/157588.

Robert E. Wilson and Edward J. Devinney. Realization of Accurate Close-Binary Light Curves : Application to MR Cygni. *Astrophysical Journal*, 166 :605, Jun 1971. doi : 10.1086/150986.

Troisième article.

A study of the stochastic photometric variability in the winds of Galactic Wolf-Rayet stars

par

Guillaume Lenoir-Craig[1], N. St-Louis[1], A.F.J. Moffat[1] et H. Pablo[2]

([1]) Dépt. de physique, Univ. de Montréal, C.P. 6128, Succ. C-V, Montréal, QC, H3C 3J7, Canada, and Centre de Recherche en Astrophysique du Québec

([2]) American Association of Variable Star Observers, 49 Bay State Road, Cambridge, MA 02138, USA

Cet article a été soumis dans Monthly Notices of the Royal Astronomical Society.

Contributions de Guillaume Lenoir-Craig à l'article

Mes contributions à cet articles sont les suivantes : dé-corrélation des données BRITE et TESS utilisées, caractérisation des spectres d'amplitude à l'aide du modèle de bruit semi-Lorentzien, recherche de corrélations entre les résultats des fits et plusieurs paramètres stellaires, comparaison de la variabiltié observée et celle produite par un modèle de clumps diffusant du flux stellaire, rédaction de la grande majorité du texte de l'article, création de toutes les figures et tableaux et formatage du texte aux standard LateX. Nicole St-Louis a grandement contribué en tant que rédactrice secondaire de l'article et Anthony Moffat a aussi apporté une grande contribution à la réalisation de cet article par de nombreuses discussions pertinentes.

RÉSUMÉ. Tout comme pour leurs progénitrices O sur la séquence principale, les observations photométriques des étoiles Wolf-Rayet y révèlent la présence généralisée de variabilité stochastique à court-terme. Afin d'explorer comment cette variabilité est reliée à diverses caractéristiques stellaires, nous avons étudié la variabilité stochastique observée dans la photométrie d'un ensemble de 55 étoiles Wolf-Rayet (WR) en utilisant 70 courbes de lumières collectées par les satellites BRITE-Constellation, TESS et MOST. Une fois les signaux associés à des variations périodiques individuelles retirées par une procédure de pré-blanchiment des données des étoiles dans lesquelles ils sont connus, nous avons calculés la Transformée de Fourier Distrète (DFT) de nos courbes de lumières et observé qu'elles sont caractérisées par une forêt de pics dans l'intervalle $0.1-0.5$ jours^{-1}, parfois suivis par une baisse en amplitude aux fréquences plus courtes. Nous avons modélisé la variabilité aléatoire résiduelle dans les périodogrammes avec une fonction semi-Lorentzienne représentant une combinaison de signaux dits de bruit rouge et blanc. Nous avons cherché des corrélations entre les paramètres fittés et plusieurs caractéristiques des étoiles et vents observés et trouvé une forte corrélation entre l'amplitude de variabilité et la température stellaire, les étoiles plus chaudes étant nettement moins variables. Nous avons aussi trouvé une corrélation entre le paramètre de raideur de l'augmentation de la variabilité aux hautes fréquences et la luminosité bolométrique. Nous discutons de plusieurs processus physiques pouvant conduire à la variabilité stochastique observée et à la corrélation observée entre l'amplitude et la température stellaire.

Mots clés : étoiles : Wolf-Rayet ; techniques : photométrie

Abstract. Like their main-sequence O-star progenitors, Wolf-Rayet stars ubiquitously exhibit short-term stochastic variability in their photometric observations. In order to explore how this variability is related to various stellar caracteristics, we studied the stochastic photometric variability of a sample of 55 Galactic Wolf-Rayet (WR) stars using 70 light-curves obtained by the BRITE-Constellation, TESS and MOST satellites. After an initial pre-whitening procedure to remove the signals associated with previously known individual periods for stars in which they were known to exist, we calculated the Discrete Fourier Transform of all our light-curves and found that they were characterized by a forest of peaks showing an increase in power starting around $0.1-0.5$ d^{-1} sometimes followed by a decrease at lower frequencies. We fitted the remaining random variability in the periodograms with a semi-Lorentzian function representing a combination of white and red noise signals. We searched for correlations of the fitted parameters with various stellar and wind characteristics and found a strong correlation between the amplitude of variability and the stellar temperature, hotter stars being found to be less variable. We also found a correlation between the steepness parameter and the Bolometric luminosity. We discuss various physical processes that can lead to the observed stochastic variability and the correlation we find between its amplitude and the stellar temperature.

Keywords: stars : Wolf-Rayet ; techniques : photometric

1. Introduction

Massive stars are known to show photometric and spectroscopic variability, from either intrinsic (e.g. pulsational or rotational modulation) or extrinsic (e.g. binary) sources. In the last few decades, with the increasing availability of space-borne observing capabilities and the development of asteroseismology, a growing number of investigations on their internal and external (i.e. wind) structures were conducted and much has been learned.

Hot, massive stars have strong radiatively driven winds. Their driving is by the transfer of the momentum of photons to the wind through the absorption or scattering by multiple spectral lines (Lucy and Solomon, 1970). Because of the dependence of the driving on the velocity gradient, this is a highly unstable mechanism as has been suggested by Lucy and White (1980) and shown by Owocki et al. (1988). This process, referred to as the line de-shadowing instability (LDI), leads to the formation of density inhomogeneities and perturbations in the wind velocity structure and as a consequence, the winds of massive, hot stars are highly clumped. More recent 2D numerical simulations of typical O-type winds by Sundqvist and Owocki (2013) and Sundqvist et al. (2018) have shown that complex density and velocity structures naturally form very close to the base of stellar outflows as a consequence of the LDI and that these are embedded in much larger low-density regions. Their results for rotating stars show that the same small-scale clumps form but that they are now embedded in larger columns of ascending matter extending down to the base of the wind. Those column actually are corotating interaction regions (CIRs), suggesting that rotating LDI models could lead to the combination of small- and large-scale structures that could explain both the observed stochastic and quasi-periodic spectroscopic variability in the optical lines (e.g. HeII) and the observed discrete absorption components (DACs) in the UV P Cygni absorption components.

The presence in the winds of these density and velocity inhomogeneities is most likely the source of much of the observed stochastic variability in photometry, polarimetry and spectroscopy. For example, Ramiaramanantsoa et al. (2019) have shown that it is possible to reproduce the observed characteristics of the non-periodic BRITE-Constellation optical light-curve of the WN8 star WR40 by including in the wind a distribution of clumps (either a power-law or all equal sizes) that Thomson-scatter the continuum light from the optical photosphere.

This clumpy nature of hot, massive-star winds could also be linked to processes occurring at the stellar photosphere. Some ten years ago, Cantiello et al. (2009) showed that massive stars should develop a sub-surface iron convection zone (FeCZ) generated by an iron-peak opacity bump that drives both pressure and gravity modes. These can produce density and velocity field perturbations that could subsequently be amplified by the LDI in the wind. These stars are also thought to harbour an ensemble of internal gravity modes (IGMs) formed at the interface between the convective core and the radiative envelope (eg. Bowman et al., 2020, 2019; Rogers et al., 2013; Edelmann et al., 2019; Horst et al., 2020), which then travel through the star's interior to its surface. This produces a large tangential velocity field that can explain the ubiquitous macroturbulence spectral broadening observed in the absorption-line profiles of main sequence massive stars (Aerts and Rogers, 2015) and can also serve as a seed for instabilities in the wind.

The study of classical (i.e. He-burning) Wolf-Rayet (WR) stars, the evolutionary descendants of main-sequence (MS) O stars (note that some WR stars, the WNh stars, represent the extension of the H-burning MS to higher masses), presents additional challenges compared to their main-sequence counterparts due to their very dense and optically thick stellar winds. The opaque winds of both cWR and WNh stars prevent the direct observation of the hydrostatic surface of these stars, complicating any attempt to carry out asteroseismology of these objects and to look for correlations between processes occurring in the wind and at the hidden surface. Although WR stars (including both cWR and WNh) show many instances of stochastic variability in photometry (eg. Lamontagne and Moffat, 1987), polarimetry (eg. Robert et al., 1989) and spectroscopy (eg. Lepine and Moffat, 1999), no link between these variations and the presence of a FeCZ or IGWs has been clearly demonstrated.

In this paper, we present an investigation aiming at first characterizing the non-periodic photometric variability observed in the winds of these stars and at finding observable links between WR wind variations and potential causes of this variability. To this end, we used 70 independent photometric datasets collected for 55 different Galactic WR stars by the best means possible, i.e. from space-based photometry with the TESS (Transiting Exoplanet Survey Satellite), BRITE (BRIght Target Explorer) and MOST (Microvariability and Oscillations of STars) satellites. Section 2 describes the observations we used in this study and Section 3 presents the first quantitative characterization of the non-periodic photometric variability observed in Wolf-Rayet stars. We discuss our results in Section 4 and present our conclusions in Section 5.

2. Observations

2.1. BRITE Photometry

BRITE-Constellation (Weiss et al., 2014; Pablo et al., 2016) consists of five nanosatellites, each housing a 35-mm KAI-11002M CCD photometer fed by a 30-mm diameter f/2.3 telescope through either a blue (390 − 460 nm) or a red (545 − 695 nm) filter. They are named BRITE-Austria (BAb), Uni-BRITE (UBr), BRITE-Heweliusz (BHr), BRITE-Lem (BLb) and BRITE-Toronto (BTr), the last letter of the abbreviations denoting the filter ("b" for blue and "r" for red). All the satellites were launched into low-Earth orbits with orbital

Tableau 4.1. BRITE photometric datasets of WR stars used in this study.

Star (year of observation)	Spectral Type	Observing Interval (days)	Satellite(s)
WR6 (2015)	WN4-s	56	BTr
WR11 (2014, 2015, 2016, 2017, 2018)	WC8+O7.5III-V	71, 70, 10, 70, 154	BTr, BAb, UBr, BLb
WR22 (2017, 2018)	WN7h+O9III-V	153, 150	BHz, BTr
WR24 (2016, 2017, 2018)	WN6ha	163, 153, 62	BTr, BHz, BTr
WR40 (2016)	WN8h	130	BHr

periods ∼100 minutes. With a $\sim 24^\circ \times 20^\circ$ effective field of view, each component of BRITE-Constellation performs the simultaneous monitoring of 15 to 30 stars brighter than $V \sim 6$. A given field is observed typically over a ∼ 6-month time period. As much as possible, at least two satellites equipped with different filters are set to monitor the field to ensure dual-band observations.

After an initial treatment with the BRITE reduction pipeline, the data are further inspected by the quality-control team to ensure the removal of charge transfer inefficiencies and hot pixels (Pablo et al., 2016). Then, the data are made available in the BRITE archive. However, at this stage, the photometry could still be correlated with many satellite parameters, which are quantified by a variable in the data file depending on the data release version. The BRITE datasets used in this analysis are all from the fifth data release (DR5), and the intrinsic parameters against which the data can be de-correlated are presented in Table A.1 of Pablo et al. (2016). The de-correlation procedure we applied to our observations is the same as that presented in Appendix A of Pigulski et al. (2016).

Fourteen observing runs including WR stars in the targeted fields have been performed between 2014 and 2019 by BRITE-Constellation. In Table 4.1 we list the star's name and the year it was observed, its spectral type, the satellite used and the time interval over which it was observed. Unfortunately, due to progressive radiation damage of the CCD of the BTr satellite, the data quality of the WR22 (HD92740) observations in 2019 is too poor to yield useful photometric data after reduction. Also, the variability observed in 2016 in the triple system WR48 (Theta Muscae) is caused mainly by the late-O supergiant (Lenoir-Craig et al. in prep) and is thus not included in our sample, leaving us with twelve usable datasets. An example of a BRITE light-curve is shown in Figure 4.1, where we show mean fluxes per orbit measurements for the WN6ha star WR24 as a function of the Heliocentric Julian Date. The mean flux value has been subtracted from all datapoints.

The main advantage of the BRITE photometry is the duration of the observations of each field, which ranges from 56 to 163 days for the data used in the present study. This allows for a much more accurate probing of the variability in the low-frequency range.

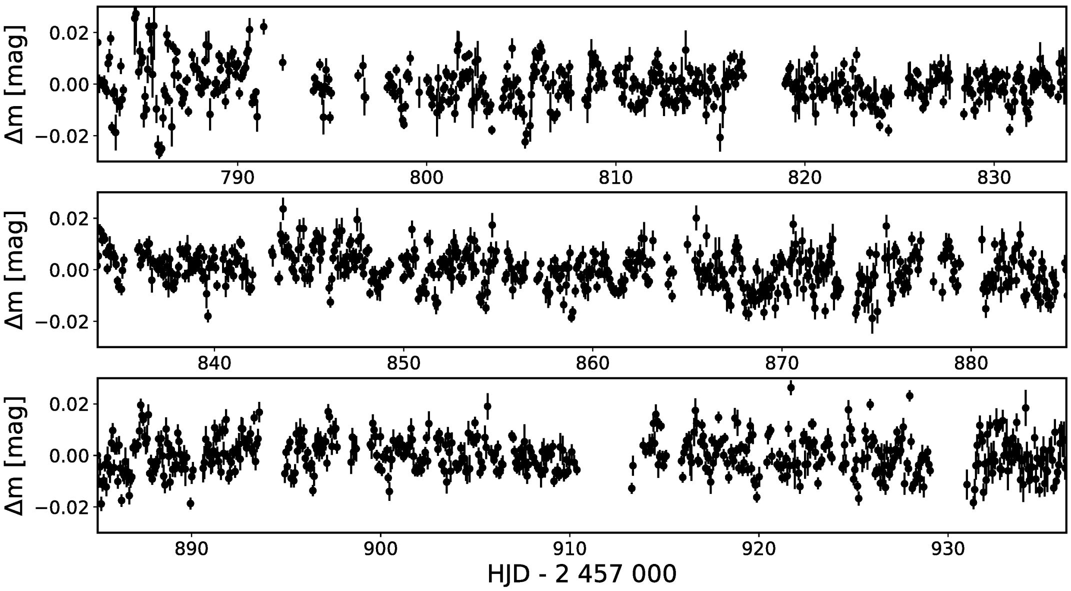

Figure 4.1. Brite orbital-mean magnitudes of WR24 as a function of the Heliocentric Julian Date, after subtraction of the mean, showing the stochastic photometric variability of this star.

2.2. TESS Photometry

The TESS satellite has a 90° x 24° field of view with its four main cameras and performs observations of stars brighter than V $\sim$ 12 in the 600 − 1000 nm range. Its average observing interval on a specific field is 27 days and it uses either a 2 or 30 minutes cadence. Its acurate photometry makes this satellite ideal for observing short-term variability in the winds of WR stars in the [0.03, 350] d^{-1} domain. TESS data are publicly available on the Mikulski Archive for Space Telescopes (MAST) and can be accessed through various means. We used the Lightkurve package for Python (Lightkurve Collaboration et al., 2018) to obtain Target Pixel Files (TPFs) for 51 stars, most of them with one standard 27-day observing interval and some with two or three consecutive intervals. The details of the retrieved TESS datasets are presented in Table 4.2, where we list the star's name, its spectral type, the time interval over which it was observed and the cadence used.

Aperture photometry with a custom aperture size was performed on each individual dataset, with the MAST online tool providing confirmation of the location of each star in the downloaded field. A Principal Component Analysis (PCA) was then performed to remove instrumental noise and systematics from each and every data set, following Lightkurve's Regression Corrector method. An example of the resulting photometry (with the average value

Tableau 4.2. TESS photometric datasets of WR stars used in this study.

WR	Spectral Type	Observing Interval (days)	Cadence (minutes)
3	WN3ha	27.8	2
4	WC5	27.8	30
5	WC6	27.8	30
6	WN4b	55.6	2
8	WN7o/CE	27.6	30
9	WC4+O7	55.6	30
10	WN5h	55.6	30
11	WC8+O7.5III-V	83.4	2
12	WN8h	55.6	30
13	WC6	55.6	30
14	WC7	55.6	30
15	WC6	55.6	30
17	WC5	55.6	30
22	WN7h+O9III-V	27.8	2
23	WC6	27.8	30
24	WN6ha-w(WNL)	27.8	2
25	WN6h-w+O(WNL)	27.8	30
27	WC6	27.8	30
33	WC5	27.8	30
38	WC4	55.6	30
40	WN8h	27.8	2
45	WC6	55.6	30
52	WC4	27.8	30
53	WC8d	27.8	30
56	WC7	27.8	30
57	WC8	55.6	30
59	WC9d	27.8	30
60	WC8	27.8	30
64	WC7	55.6	30
65	WC9d	27.8	2
68	WC7	27.8	2
69	WC9d	27.8	30
71	WN6-w	27.8	30
79a	WN9ha	27.8	2
79b	WN9ha	55.6	2
80	WC9d	27.8	30
81	WC9	27.8	30
90	WC7	27.8	30
92	WC9	27.8	30
103	WC9d	27.8	30
132	WC6	27.8	30
135	WC8	55.6	30
139	WN5+O6II-V	55.6	2
142	WO2	55.6	30
144	WC4	55.6	30
148	WN7ha+O5V	55.6	30
150	WC5	27.8	30
153	WN6o+O6I	27.8	2
154	WC6	55.6	30
155	WN6o+O9II-Ib	27.8	2

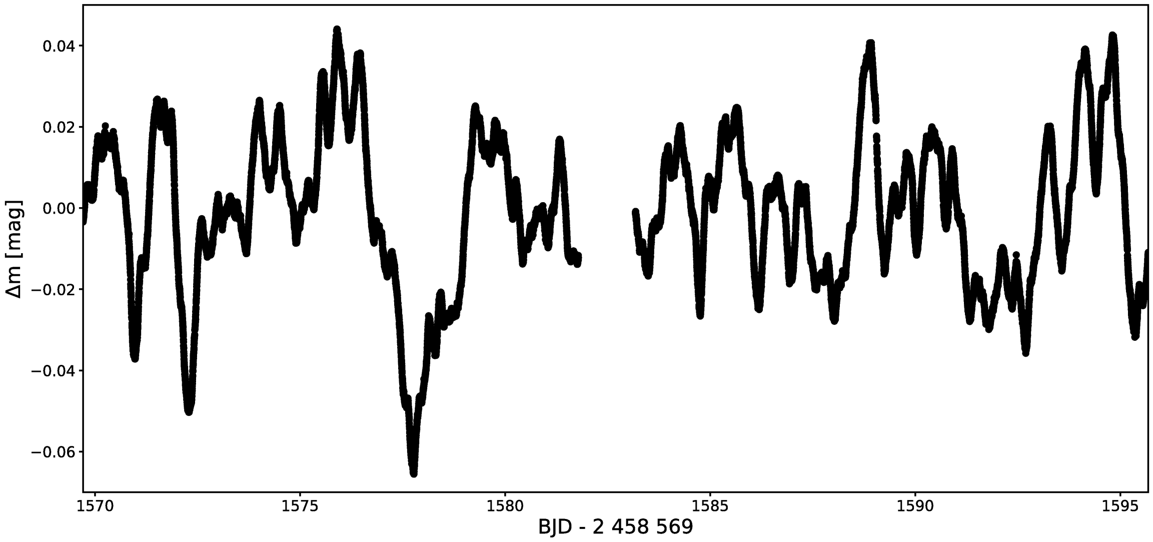

Figure 4.2. TESS light-curve of WR40 after subtration of the mean magnitude.

subtracted) is shown as a function of the Barycentric Julian Date (BJD) in Figure 4.2, where we present the TESS light-curve of the WN8h star WR40.

2.3. MOST Photometry

The MOST satellite (Walker, Matthews et al. 2003 ; Matthews et al. 2004) housed a 15-cm optical telescope feeding a CCD photometer through a single custom broadband (400 – 700 nm) filter. It followed a polar Sun-synchronous orbit at 820 km altitude, enabling it to monitor stars in its equatorial Continuous Viewing Zone for up to 8 weeks without interruption.

Our sample includes 6 WR stars (WR71, 92, 112, 115, 119, 120 and 121) observed with MOST. However, only the data for WR92, 115 and 120 had parameters related to the satellite's onboard instruments available in their data files. The others had already been treated by previous users. Again, the decorrelation procedure from Pigulski et al. (2016) was performed for the three stars with available satellite parameters. The data for the three other stars were used as is. As an example, we present the MOST light-curve of the WC9d star WR121 in Figure 4.3

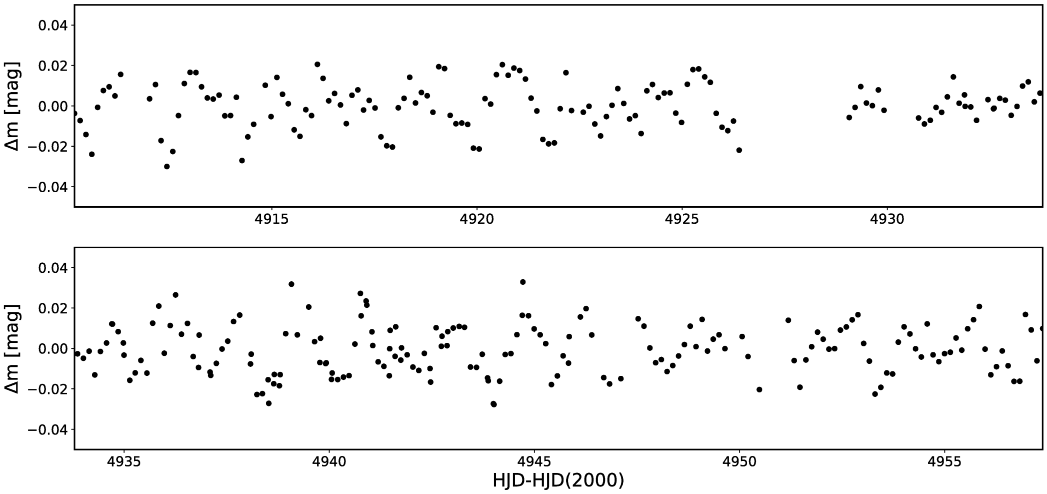

Figure 4.3. MOST light-curve of WR121.

3. Data Analysis

3.1. Frequency Analysis

All the light-curves analysed in this work can be found in Annex A. In order to characterize them, We first carried out period searches to identify the dominant frequencies present in the photometry of each star using the discrete Fourier transform (DFT) method implemented in the PERIOD04 software (Lenz and Breger, 2005) to obtain periodograms for each dataset of all stars in our sample. These are presented in Annex B.

As we are interested in the stochastic variability of these WR stars, we must first remove any known periodicities from our observations before carrying out our analysis. The BRITE sample contains two stars with known periodic signals which are expected to exhibit distinct individual peaks in their periodograms. First, WR6 presents variations in photometry, polarimetry and spectroscopy with a period of 3.76 d that can be explained by the presence of Corotating Interaction Regions in its wind (eg. Morel et al., 1997), although Schmutz and Koenigsberger (2019) for example prefer a somewhat complicated binary scenario. Second, WR22 is an eclipsing binary with a period of 80.336 days (e.g. Schweickhardt et al., 1999). An iterative pre-whitening procedure was conducted for WR6 by first carrying-out a time-dependant frequency (TF) analysis (also known as Gabor transform) to localise the time intervals over which the various harmonics of the signals are present, and then removing those signals by subtracting a sinusoidal function with the harmonic's frequency, amplitude and phase. For WR22, an eclipse model was used to fit the eclipse signal and remove it

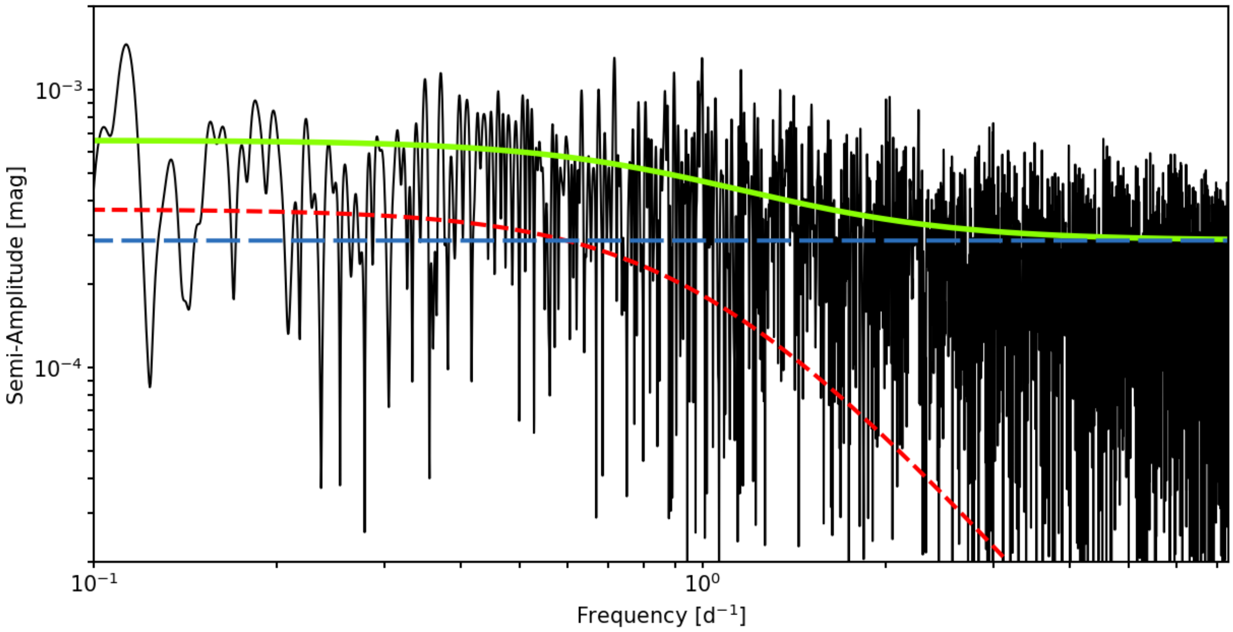

Figure 4.4. Amplitude spectrum of WR24 as observed by BHr in 2017 (black solid line). The solid green line corresponds to the fit of the semi-lorentzian distribution and the red and white noise components are respectively shown as red- and blue-dashed lines.

following the methodology presented in Antokhin (2011). The analysis of these periodic variations will be presented elsewhere (Lenoir-Craig et al. in prep for WR22 and St-Louis et al. in prep for WR6). In the TESS sample, seven stars are also known to show periodic signals that could be detected within TESS's ∼27-day exposures : WR6, 9, 12, 139, 148, 153 and 155. The periodic signals and their harmonics were removed using the same methodology as for the BRITE data. No such periodic signals are known for the stars of the MOST sample.

A thorough analysis of all the WR periodograms in our sample revealed no single outstanding peak other than the ones corresponding to the periods already known. Instead, their periodograms all show a forest of a large number of peaks with an increasing amplitude towards low frequencies, starting from ~ 0.5 d^{-1} down to ~ 0.1 d^{-1}, followed by a decrease in amplitude below 0.1 d^{-1}, similarly to what had been observed by Ramiaramanantsoa et al. (2019) for the WN8 star WR40. An example of an amplitude spectrum we obtained for the WN6 star WR24 is shown in Figure 4.4. All other fitted periodograms are presented in Annex B.

3.2. Fit of the Stochastic Variability

In order to characterize the stochastic, low-frequency variability for our sample of WR stars, we fitted a combination of white and red noises to our whole amplitude spectra as described, for example, in Bowman et al. (2019) by applying a Markov chain Monte Carlo algorithm using the Python code Emcee (Foreman-Mackey et al., 2013) to fit the amplitude spectrum of each light-curve with a semi-lorentzian distribution :

$$\alpha(\nu) = \frac{\alpha_0}{1 + (\dfrac{\nu}{\nu_{char}})^{\gamma}} + C_W \tag{3.1}$$

where α_0 corresponds to the amplitude at a frequency of zero of the frequency-dependent component, ν_{char} is the characteristic frequency of the stochastic variability present in the light-curve, which is the inverse of the characteristic timescale following $\nu_{char} = (2\pi\tau)^{-1}$ and γ is the logarithmic amplitude gradient. The first term on the right of this equation corresponds to the frequency-dependent red noise term, and C_W is the frequency-independent white noise term. It is important to note that both white and red "noises" actually are genuine intrinsic signals from the star, and not noise in the traditional sense. We then tested the goodness of the fit against a white-noise-only model using the Akaike Information Criterion (AIC) based on the chi-square test. In all cases, we found the red noise component to be significant. An example of such a fit to a periodogram is shown in Figure 4.4 for WR24 superposed on the observations plotted in black. The red and white noise components are plotted as red and blue dashed curves respectively while the resulting fit is shown as a solid green curve.

Our first goal is to compare the various fitted curves since the data we are using in this study have been acquired by telescopes observing in neighboring and/or overlapping wavelength ranges, we assume that the wavelength dependence of the observed red noise will not have a significant impacts on the fitted parameters α_0, ν_{char} and γ for data from different satellites. Also, the observational length sets the lowest significant frequency in the amplitude spectra, which for data covering multiple weeks will always be below the red noise frequency range of [0.1, 0.5]d^{-1}, so this will not affect the fits either. On the other hand, the white noise component is known to be dependent on the satellite cadence of observations and on the photometric accuracy (Bowman et al. 2020). Since the TESS data have a higher accuracy than BRITE or MOST observations that share a much more similar photometric accuracy, we cannot directly compared the fitted curves. We also separate the TESS curves with different cadences since this greatly affects the level of the white noise.

In order to quantify the influence of the cadence on the white noise levels, we used the 2-minutes cadence TESS light-curve of the WN6ha star WR24 and made several duplicates, each time halving the cadence by binning together points in multiples of 2. Our sampled cadences are 2, 4, 8, 16, 32, 64, 128 and 256-minutes. Those data sets were then analyzed following the same procedure as with our sample stars. We show the values of the corresponding white noise C_w against the sampled cadences in Figure 4.5. The first datapoint starting from the left on the x-axis corresponds to the 256-mins cadence which causes the

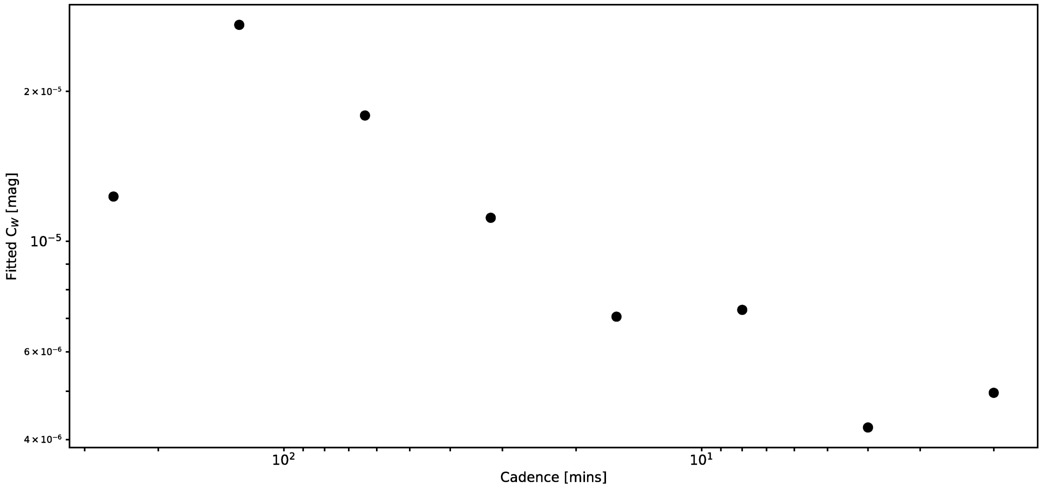

Figure 4.5. Fitted white noise levels plotted against their corresponding cadence, for the TESS light-curve of WR24.

Nyquist frequency to be located in the red-noise range of the amplitude spectra, rendering the fitting of a white-noise component irrelevant as the amplitude spectra is completely frequency-dependant. As can be seen, the white noise level in the periodogram is expected to decrease with increasing cadence almost by an order of magnitude which warrants the separation of the TESS fits for data obtained with the two different cadences.

All amplitude spectra of our available light-curves were fitted with the above equation 3.1 and a superposition of all these resulting fits is presented in Figure 4.6. In this figure, the curves for the various stars are colour-coded with the bolometric luminosity of the star taken from Sander et al. (2019) for WC stars and from Hamann et al. (2019) for WN stars. As can be seen, no clear correlation with this quantity is found, contrary to the results of Bowman et al. (2020) for main-sequence stars of O and B type who found higher luminosity stars to be characterized by larger values of α_0.

We then looked for correlations of the variables describing the red noise component of the photometric changes observed in our stars with various stellar and wind parameters. In Figure 4.7, we plot the logarithms values of α_0, ν_{char} and γ as a function of the logarithms of the wind terminal velocity and mass-loss rate in the first two columns and on the stellar temperature, a absolute magnitude in the v band, stellar radius and Bolometric luminosity in the last four columns. The wind and stellar parameters we taken from Hamann et al. (2019) for WN stars and Sander et al. (2019) for WC stars. For stars for which no values were available, we used the average value for stars of the same spectral type. Red symbols are for MOST data, black for BRITE and blue for TESS observations. Inverted triangles are

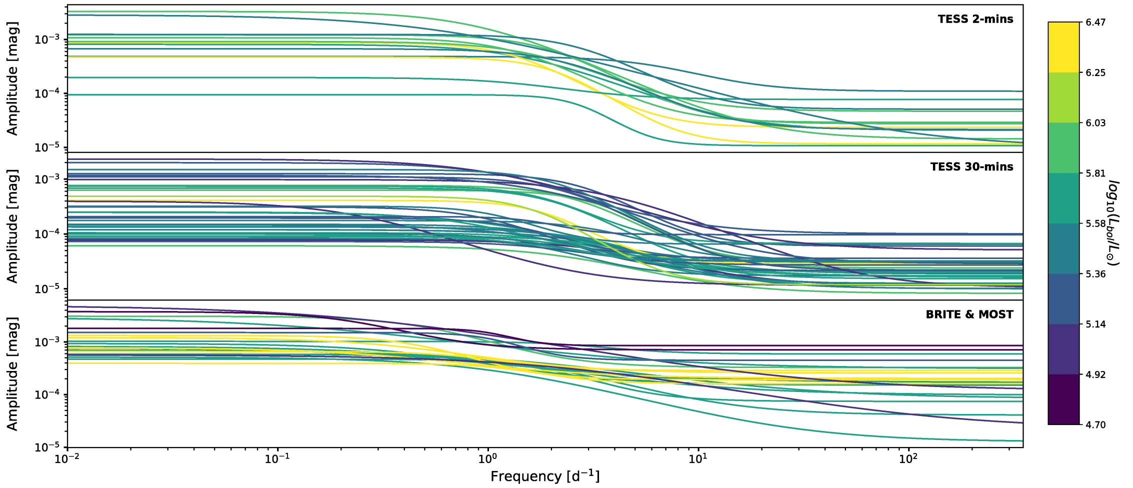

Figure 4.6. Superimposed fits of the semi-lorentzian profiles of the WR stars in our sample characterizing the morphology of low-frequency variability, color-coded by bolometric luminosity and separated by satellite cadence and data accuracy.

for WC stars and filled circles are for WN stars. We fitted a straight line to all these datasets and overploted the result as a dashed black line. The value of the slope and its corresponding error is given in the top right corner of each panel. If more than one dataset existed for a given star, we linked the fitted values of the red-noise component with a horizontal line to show the extent of the values we obtain for the various observations.

The only two plots showing the most significant slopes within the errors are $\log \alpha_0$ versus $\log v_\infty$ and $\log \alpha_0$ versus $\log T_*$, suggesting that stars with faster or hotter winds generally present smaller-amplitude variability. Note that these two parameters are known to be correlated ; stars with hotter winds tend to be hotter although this has not been formally quantified (eg. Hamann et al., 2019). We present a zoomed in version of the plot of $\log \alpha_0$ versus $\log T_*$ in Figure 4.8 where we have also colour-coded the symbols with the Bolometric luminosity. The absence of a correlation with this parameter is clear. The only two other significant correlations are between the γ parameter and the absolute v-band magnitude and Bolometric luminosity, indicating that brighter or more luminous stars have a steeper red noise component.

3.3. Wavelet Analysis

In order to obtain a different perspective on the timescales of the variability present in our photometric observations, we carried out wavelet analyses on all our datasets for the stars in our sample. An example, is shown in Figure 4.9 for WR24. The top panel shows a reconstruction of the TESS light-curve of this star using 60-min bins and the bottom

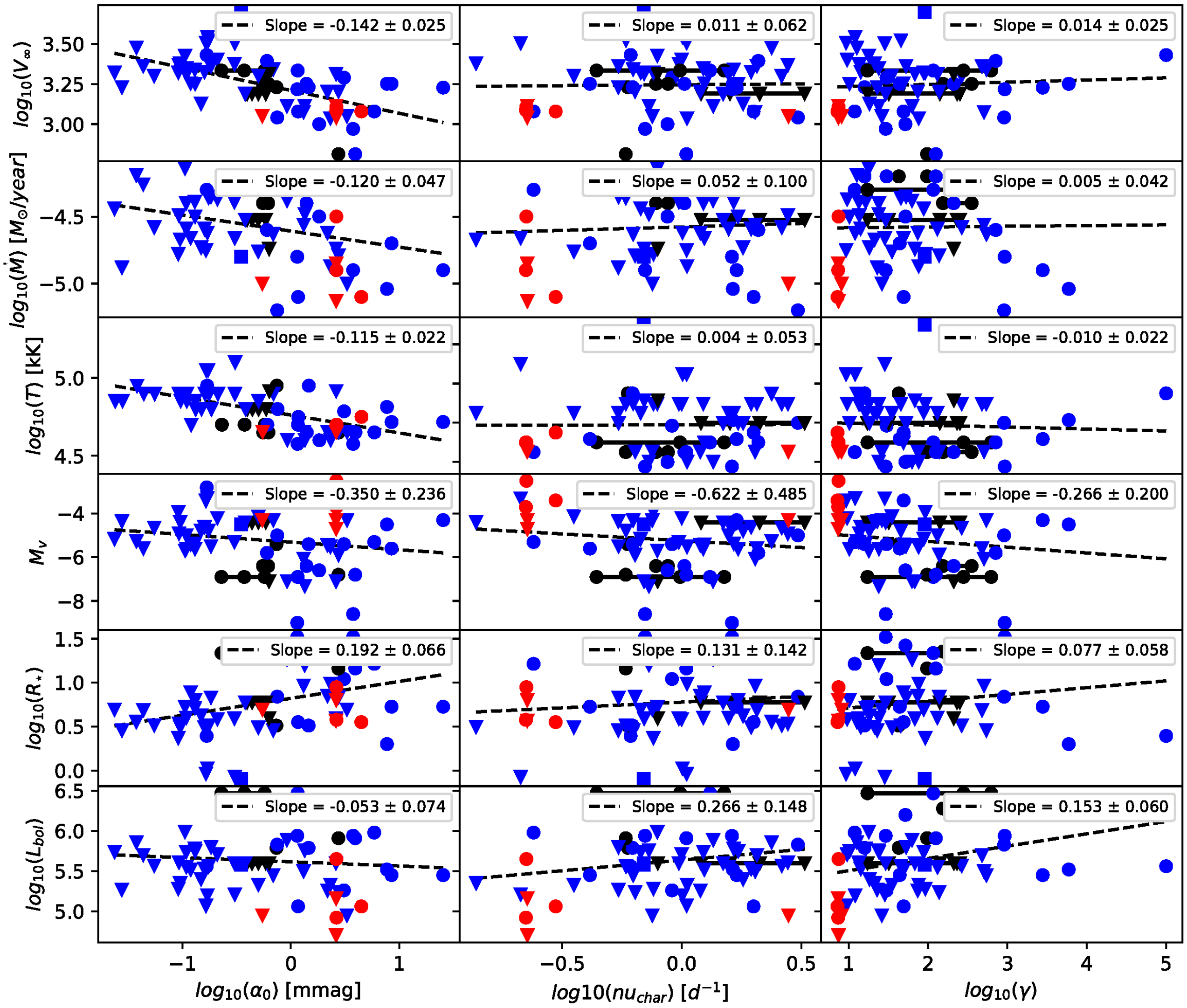

Figure 4.7. Fitted parameters of the red noise component, α_0, ν_{char} and γ as a function of various wind and stellar parameters. Blue points are for TESS data, black for BRITE and red for MOST. Inverted triangles are for WC stars and filled circles are for WN stars. The slope of the fitted straight lines together with its error is given in the top-right corner of each panel.

panel shows the wavelet power-spectrum of this dataset. We find that the most powerful signals have periods in the 1−5 day range. This is not in disagreement with the results of our periodogram analysis presented in the previous section in which we find average

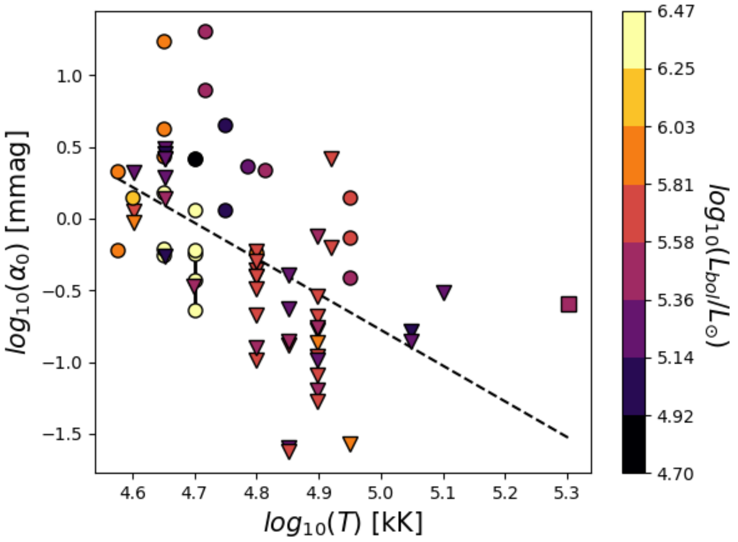

Figure 4.8. Zoom of the anti correlation between the level of variability characterized by the α_0 parameter with the stellar temperature. The points are colour-coded with the bolometric luminosity.

characteristic frequencies, ν_{char} for the red noise component of the variability of all our light-curves of 1.3 d^{-1}, with a standard deviation of ± 1.1 d^{-1} (see middle panels of Figure 4.7). All wavelet analysis plots can be found in Annex C.

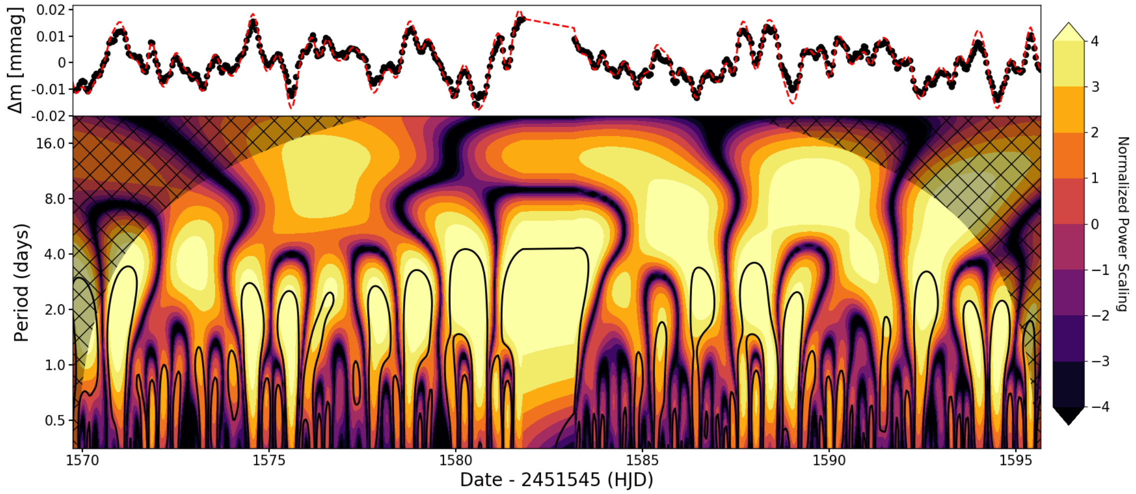

Figure 4.9. Top : two-minute sampled TESS light-curve of WR24 binned to have one data-point per hour. The red dashed line is the result of the Inverse Wavelet Transform of the wavelet analysis performed using the Mexican-hat mother function on the signal. Bottom : The power-spectrum of the wavelet analysis. The hashed region corresponds to the cone of influence (COI) of the period of the wavelets. The large, relatively uniform feature observed around t = 1582 d corresponds to the lack of data as seen in the light-curve. The contour lines enclose regions with greater than 95% confidence for a red-noise process, with a lag-1 auto-correlation coefficient between successive data points of 0.72.

4. Discussion

In view of the correlation we have found between the typical amplitude of variability characterized by the α_0 parameter and either the stellar temperature or wind terminal velocity, we discuss in this section the various physical processes that could lead to stochastic variability in WR winds. Note that a similar correlation has been found for the spectroscopic variability of WR stars by Chené et al. (2020, submitted). As the continnum is thought to be formed somewhere in the dense wind for WR stars, this result is perhaps not surprising.

4.1. Line De-Shadowing Instability

As the LDI is intrinsic to the driving of hot-star winds, could this process alone explain the observed photometric variability we found in WR stars ?

Sundqvist et al. (2018) have shown that for a wind with a velocity structure described by a beta velocity law, the LDI produces clump sizes of the order of the Sobolev length, $l_{Sob} = v_{th}/(dv/dr) \propto v_{th}/(v_\infty/R_*) \propto R_*\sqrt{T}/v_\infty$. Since the thermal speed is expected to be about 1% of the terminal speed, this process is expected to lead only to very small clumps.

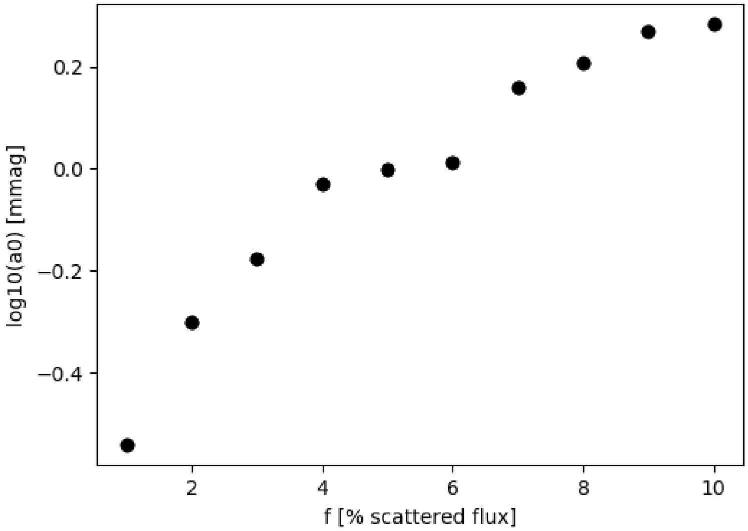

Figure 4.10. Amplitude of variability α_0 versus the percentage f of scattered starlight for the biggest simulated clump.

It is far from clear if such small structures can lead to the level of photometric variability observed in WR winds.

On the other hand, if WR winds are self similar, a more appropriate parameter to consider would then be l_{Sob}/R_*, which is proportional to the square root of the temperature divided by the terminal velocity. As faster winds are known to be hotter, it is possible, if the correlation between v_∞ and T_* is steeper than the square root, that the Sobolev length inversely correlates with the temperature, i.e. hotter winds have smaller Sobolev length and therefore potentially smaller wind structures. This in turn can lead to a smaller level of variability as larger clumps are expected to scatter more flux.

In order to check that increasing clump size directly leads to increased variability, we used the same simple clumping model as presented in Ramiaramanantsoa et al. (2019) who where able to produce similar light-curves to the one observed with BRITE-Constellation for the WN8h star WR40 by populating its wind with a distribution of clumps and calculating the resulting continuum-light that is Thomson-scattered off these clumps as they travel through the wind. The f parameter in the model sets the percentage of incoming stellar flux that is Thomson-scattered by the biggest clump. Smaller clumps scatter less flux, following a negative-index power law of their size with exponent $-2/3$. Using increasing values of f to simulate the increasing clump size, multiple synthetic light-curves were produced and their amplitude spectra were extracted. Following the same recipe as with our sample stars, our artificial light-curves were then fitted with the semi-lorentzian distribution previously shown. Figure 4.10 shows the fitted amplitude of variability plotted against the various f values used.

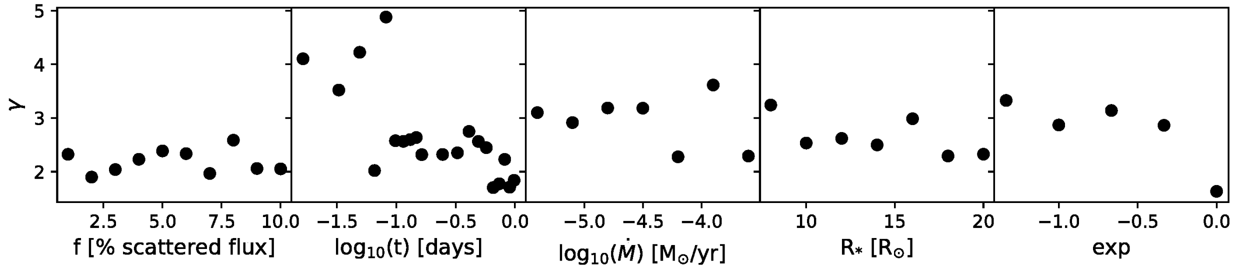

Figure 4.11. steepness of the periodogram γ as a function of various model parameters of the scattering of stellar light on clumps in the wind and versus the mass-loss rate and stellar radius.

As expected, a clear positive trend appears, showing that stars with bigger clumps in their winds are expected to show an increased amplitude of variability in their periodogram similarly to the observed trend.

In Figure 4.11 we present the values found in our simulations for the steepness parameter of the red component of the stochastic variability, γ, as a function of various model parameters (f, the lifetime of clumps, t, and the exponent of the size distribution, *exp*) and stellar and wind parameters ($\dot{M}$, M and R_*). Although no correlation is found, note that all the light-curves produced by the model have an associated γ value in the range $1.5 < \gamma < 3.0$, with the exception of simulations with a clump lifetime parameter t below 2 hours for which the range becomes $3.5 < \gamma < 5.0$.

Krtička and Feldmeier (2018) have recently put forward that variable wind blanketing that results in extra heating of the stellar photosphere can explain the stochastic varibility in optically thin winds of O stars. Indeed, a variable mass-loss rate caused by the LDI can in turn produce detectable light variability at the photosphere of the order of tens of millimagnitudes. Although this effect is unlikely to contribute directly to the photometric Variability since the photosphere is hidden by the opaque stellar outflow, it might propagate in the wind and contribute somehow to the wind variability in the observable parts of the wind.

Therefore, it is not impossible that the LDI can play an important role in generating the observed stochastic photometric variability and even lead to an anti-correlation between the level of the photometric and spectroscopic stochastic variability, as observed in the winds of WR stars, with the stellar temperature with hotter winds having smaller clumps, leading to a lower level of variability. However, this does not exclude that an additional process occurring at the stellar surface could seed the instabilities and affect the clump characteristics in the winds. In the next two sections, we discuss two such possible processes.

4.2. Sub-Surface Convection Zones

Following the original work of Cantiello et al. (2009) on the existence of sub-surface convection zones in massive stars caused by an iron-peak opacity bump (FeCZ) and its effect on the optically thin winds of OB stars, Grassitelli et al. (2016) studied the effects of this convective zone on the radiative envelope of WR stars in the 2-17 $M_\odot$ mass range. Although only small-amplitude ($\sim$ 1 km/s) velocity perturbations were found for lower-mass stars, they found that for masses larger than $\sim$10 $M_\odot$ surface convective velocities of the order of 10 km/s where expected. More precisely, they predicted a linear increase in convective velocities with stellar mass from 2 to 26 km s^{-1}, approaching the local sound speed for the higher masses. Although these turbulent surface velocity fields are predicted to be somewhat attenuated in the radiative zones above the FeCZ, the predicted surface velocities, v_{surf} are of the same order of magnitude as the convective velocities and are predicted to follow the same increase with mass. These predictions are supported by observations of stochastic spectroscopic variations of WN stars that are found to show an increase in amplitude with increasing mass (see their Figure 10).

The range of dominant frequencies of the variability (ν_{char}) can help shed more light on the physical mechanism behind the observed variability. FeCZ are expected to have a typical turnover frequency of 6-60 μHz (0.5-5 d^{-1}) (Cantiello et al., 2009; Cantiello and Braithwaite, 2011, 2019), which can be transmitted to the above radiative layer since it is below the Brunt-Väisälä frequency of 0.1 - 1 mHz (Cantiello et al., 2009). As shown in Figure 4.7, almost all the stars in our sample have a characteristic frequency in this expected range. This supports the suggestion that convective waves reaching the surface of WR stars could possibly propagate into the wind while retaining their original frequency.

The temperature of the outer hydrostatic layers of WR stars is expected to be an important parameter in the surface variability produced by the FeCZ (Cantiello et al., 2009; Grassitelli et al., 2015) because it has a direct influence on the location of FeCZ caused by the partial ionization of Fe-peak elements at $log(T/K) \approx 5.3$. For higher temperatures, the FeCZ will be located closer to the surface and therefore the observed photometric variability will be reduced because the convective mass flux perturbing the base of the wind will be smaller. This effect could be an important factor in the anti-correlation we find in our sample between the amplitude of photometric variability and the stellar temperature T_{eff}. (see Figure 4.8). This supports the idea that a subsurface convection zone can directly influence the formation of clumps in the winds of Wolf-Rayet stars, particularly for star above a mass of $\sim$10 $M_\odot$.

4.3. Core-Generated Gravity Waves

Another possible source of variability in hot massive stars that have been put forward in recent literature are a large number of internal gravity waves (IGWs), excited by turbulent convection at the interface of the convective core and the radiative zone lying above it (Aerts and Rogers, 2015; Bowman et al., 2019, 2020). These IGWs have been used to explain the ubiquitous macroturbulence broadening observed in the absorption lines of main-sequence O and B supergiants (Aerts and Rogers, 2015; Simón-Díaz et al., 2017) as they have been shown to produce the required tangential velocity field. Furthermore, a strong correlation is found between the surface macroturbulent speed and the amplitude of stochastic variability in OB stars (Bowman et al., 2020) who also showed that IGWs become increasingly important in stars with larger spectroscopic masses and luminosities. As Wolf-Rayet stars are among the most luminous stars, IGWs could play a role in their internal structure as well. However, Contrary to massive main sequence stars, we do not see the surface of these stars directly and therefore we can only see these perturbations if they propagate in the wind. For the optically thin wind of the O9.5 supergiant star HD188209, Simón-Díaz et al. (2017) have shown that this is indeed the case. It remains to be shown what happens in the optically thick winds of WR stars.

The steepness of the amplitude spectrum of the stochastic photometric variability (characterized by the γ exponent) can also help shed some light on the cause of the stochastic variability. Recent 3D simulations by Edelmann et al. (2019) predict that IGWs are compatible with a steepness of amplitude exponent $0.8 < \gamma < 3.0$. As shown in Figure 4.12, which is a zoom of the correlation shown in Figure 4.7, we find that the vast majority of WR stars in our sample have a γ exponent in that range. Here the correlation seems to indicate that brighter stars have a tendency of showing steeper power spectra. No such correlation was found for blue supergiants by Bowman et al. (2019). It remains to be explained what is generating this correlation for these optically thin winds.

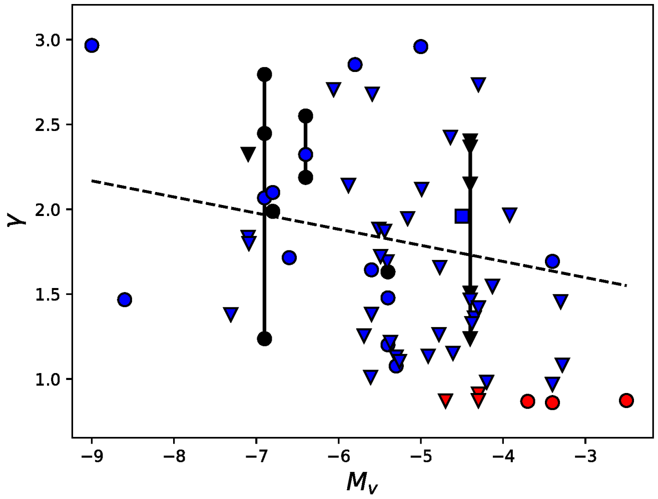

Figure 4.12. Steepness of amplitude spectrum γ as a function of absolute magnitude

5. Conclusions

In this paper we presented an analysis of the stochastic photometric variability of 55 Galactic WR stars using 70 light-curved obtained with the BRITE-Constellation, TESS and MOST satellites. We calculated the Discrete Fourier Transform off all the light-curves and fitted the power spectrum with a semi-Lorentzian profile representing a combination of white and red noises. We searched for correlations of the fitted parameters with wind and stellar parameters in an attempt to shed new light on the physical processes responsible for the stochastic variability.

We find a correlation between the level of photometric variability and the stellar temperature. This is reminiscent of the correlation between the level of spectroscopic variability and temperature found by previous authors.

We discuss various physical processes that can be responsible for the stochastic photometric variability. The line de-shadowing instability is found to be a plausible process but we do not exclude that either a sub-surface convection zone or internal gravity waves can contribute to an increase the level of variability.

We conclude that these three physical processes can contribute to the generation of a clumpy wind, which can then lead to the observed variability when continuum light is scattered off clumps of various sizes into our line-of-sight as they travel within the stellar wind. Models for the generation of clumps by the LDI process in the optically thick winds of WR stars are required to determine what their characteristics would be. It would be useful to explore what the influence of either a FeCZ or IGM would be on the formation of these clumps and how they affect the wind structure of these stars.

Acknowledgements

NSL & AFJM are grateful to NSERC (Canada) for financial aid.

Bibliographie

C. Aerts and T. M. Rogers. Observational Signatures of Convectively Driven Waves in Massive Stars. *Astrophysical Journall*, 806(2) :L33, June 2015. doi : 10.1088/2041-8205/806/2/L33.

Igor I. Antokhin. Solving light curves of WR+O binaries : the regularization approach. *Bulletin de la Societe Royale des Sciences de Liege*, 80 :549–554, January 2011.

D. M. Bowman, S. Burssens, S. Simón-Díaz, P. V. F. Edelmann, T. M. Rogers, L. Horst, F. K. Röpke, and C. Aerts. Photometric detection of internal gravity waves in upper main-sequence stars. II. Combined TESS photometry and high-resolution spectroscopy. *Astronomy and Astrophysics*, 640 :A36, August 2020. doi : 10.1051/0004-6361/202038224.

Dominic M. Bowman, Siemen Burssens, May G. Pedersen, Cole Johnston, Conny Aerts, Bram Buysschaert, Mathias Michielsen, Andrew Tkachenko, Tamara M. Rogers, Philipp V. F. Edelmann, Rathish P. Ratnasingam, Sergio Simón-Díaz, Norberto Castro, Ehsan Moravveji, Benjamin J. S. Pope, Timothy R. White, and Peter De Cat. Low-frequency gravity waves in blue supergiants revealed by high-precision space photometry. *Nature Astronomy*, 3 :760–765, May 2019. doi : 10.1038/s41550-019-0768-1.

M. Cantiello and J. Braithwaite. Magnetic spots on hot massive stars. *Astronomy and Astrophysics*, 534 :A140, October 2011. doi : 10.1051/0004-6361/201117512.

M. Cantiello, N. Langer, I. Brott, A. de Koter, S. N. Shore, J. S. Vink, A. Voegler, D. J. Lennon, and S. C. Yoon. Sub-surface convection zones in hot massive stars and their observable consequences. *Astronomy and Astrophysics*, 499(1) :279–290, May 2009. doi : 10.1051/0004-6361/200911643.

Matteo Cantiello and Jonathan Braithwaite. Envelope Convection, Surface Magnetism, and Spots in A and Late B-type Stars. *Astrophysical Journal*, 883(1) :106, September 2019. doi : 10.3847/1538-4357/ab3924.

P. V. F. Edelmann, R. P. Ratnasingam, M. G. Pedersen, D. M. Bowman, V. Prat, and T. M. Rogers. Three-dimensional Simulations of Massive Stars. I. Wave Generation and Propagation. *Astrophysical Journal*, 876(1) :4, May 2019. doi : 10.3847/1538-4357/ab12df.

Daniel Foreman-Mackey, David W. Hogg, Dustin Lang, and Jonathan Goodman. emcee : The MCMC Hammer. *Publications of the ASP*, 125(925) :306, March 2013. doi : 10.1086/670067.

L. Grassitelli, A. N. Chené, D. Sanyal, N. Langer, N. St-Louis, J. M. Bestenlehner, and L. Fossati. Diagnostics of the unstable envelopes of Wolf-Rayet stars. *Astronomy and Astrophysics*, 590 :A12, May 2016. doi : 10.1051/0004-6361/201527873.

Luca Grassitelli, N. Langer, D. Sanyal, Luca Fossati, and J. Bestenlehner. Instabilities in the envelope of wolf-rayet stars. 01 2015.

W. R. Hamann, G. Gräfener, A. Liermann, R. Hainich, A. A. C. Sander, T. Shenar, V. Ramachand ran, H. Todt, and L. M. Oskinova. The Galactic WN stars revisited. Impact of Gaia distances on fundamental stellar parameters. *Astronomy and Astrophysics*, 625 :A57, May 2019. doi : 10.1051/0004-6361/201834850.

L. Horst, P. V. F. Edelmann, R. Andrassy, F. K. Roepke, D. M. Bowman, C. Aerts, and R. P. Ratnasingam. Fully compressible simulations of waves and core convection in main-sequence stars. *arXiv e-prints*, art. arXiv :2006.03011, June 2020.

J. Krtička and A. Feldmeier. Light variations due to the line-driven wind instability and wind blanketing in O stars. *Astronomy and Astrophysics*, 617 :A121, September 2018. doi : 10.1051/0004-6361/201731614.

Robert Lamontagne and Anthony F. J. Moffat. Precision Photometric Monitoring of Southern Variable Wolf-Rayet Stars with a Comment on the Overall Continuum Variability of WR Stars. *Astronomical Journal*, 94 :1008, October 1987. doi : 10.1086/114535.

P. Lenz and M. Breger. Period04 User Guide. *Communications in Asteroseismology*, 146 : 53–136, June 2005. doi : 10.1553/cia146s53.

Sebastien Lepine and Anthony F. J. Moffat. Is Clumping Universal in Hot Star Winds ? NOAO Proposal, August 1999.

Lightkurve Collaboration, J. V. d. M. Cardoso, C. Hedges, M. Gully-Santiago, N. Saunders, A. M. Cody, T. Barclay, O. Hall, S. Sagear, E. Turtelboom, J. Zhang, A. Tzanidakis, K. Mighell, J. Coughlin, K. Bell, Z. Berta-Thompson, P. Williams, J. Dotson, and G. Barentsen. Lightkurve : Kepler and TESS time series analysis in Python. Astrophysics Source Code Library, December 2018.

L. B. Lucy and P. M. Solomon. Mass Loss by Hot Stars. *Astrophysical Journal*, 159 :879, March 1970. doi : 10.1086/150365.

L. B. Lucy and R. L. White. X-ray emission from the winds of hot stars. *Astrophysical Journal*, 241 :300–305, October 1980. doi : 10.1086/158342.

Thierry Morel, Nicole St-Louis, and Sergey V. Marchenko. Optical Spectroscopy of EZ Canis Majoris : Indication for Large-Scale Structures in a Wolf-Rayet Wind. *Astrophysical Journal*, 482(1) :470–489, June 1997. doi : 10.1086/304122.

Stanley P. Owocki, John I. Castor, and George B. Rybicki. Time-dependent Models of Radiatively Driven Stellar Winds. I. Nonlinear Evolution of Instabilities for a Pure Absorption Model. *Astrophysical Journal*, 335 :914, December 1988. doi : 10.1086/166977.

H. Pablo, G. N. Whittaker, A. Popowicz, S. M. Mochnacki, R. Kuschnig, C. C. Grant, A. F. J. Moffat, S. M. Rucinski, J. M. Matthews, A. Schwarzenberg-Czerny, G. Handler, W. W. Weiss, D. Baade, G. A. Wade, E. Zocłońska, T. Ramiaramanantsoa, M. Unterberger, K. Zwintz, A. Pigulski, J. Rowe, O. Koudelka, P. Orleański, A. Pamyatnykh, C. Neiner, R. Wawrzaszek, G. Marciniszyn, P. Romano, G. Woźniak, T. Zawistowski, and R. E. Zee. The BRITE Constellation Nanosatellite Mission : Testing, Commissioning, and Operations. *Publications of the ASP*, 128(970) :125001, December 2016. doi : 10.1088/1538-3873/128/970/125001.

A. Pigulski, H. Cugier, A. Popowicz, R. Kuschnig, A. F. J. Moffat, S. M. Rucinski, A. Schwarzenberg-Czerny, W. W. Weiss, G. Handler, G. A. Wade, O. Koudelka, J. M. Matthews, St. Mochnacki, P. Orleański, H. Pablo, T. Ramiaramanantsoa, G. Whittaker, E. Zocłońska, and K. Zwintz. Massive pulsating stars observed by BRITE-Constellation. I. The triple system β Centauri (Agena). *Astronomy and Astrophysics*, 588 :A55, April 2016. doi : 10.1051/0004-6361/201527872.

Tahina Ramiaramanantsoa, Richard Ignace, Anthony F. J. Moffat, Nicole St-Louis, Evgenya L. Shkolnik, Adam Popowicz, Rainer Kuschnig, Andrzej Pigulski, Gregg A. Wade, Gerald Handler, Herbert Pablo, and Konstanze Zwintz. The chaotic wind of WR 40 as probed by BRITE. *Monthly Notices of the RAS*, 490(4) :5921–5930, December 2019. doi : 10.1093/mnras/stz2895.

Carmelle Robert, Anthony F. J. Moffat, Pierre Bastien, Laurent Drissen, and Nicole St. -Louis. Polarization Variability among Wolf-Rayet Stars. V. Linear Polarization of the Bright Cygnus Stars and an Anticorrelation of Variability with Wind Speed. *Astrophysical Journal*, 347 :1034, December 1989. doi : 10.1086/168194.

T. M. Rogers, D. N. C. Lin, J. N. McElwaine, and H. H. B. Lau. Internal Gravity Waves in Massive Stars : Angular Momentum Transport. *Astrophysical Journal*, 772(1) :21, July 2013. doi : 10.1088/0004-637X/772/1/21.

W. Schmutz and G. Koenigsberger. Long uninterrupted photometric observations of the Wolf-Rayet star EZ CMa by the Toronto BRITE satellite reveal a very fast apsidal motion. *Astronomy and Astrophysics*, 624 :L3, April 2019. doi : 10.1051/0004-6361/201935094.

J. Schweickhardt, W. Schmutz, O. Stahl, Th. Szeifert, and B. Wolf. Revised mass determination of the super massive Wolf-Rayet star WR 22. *Astronomy and Astrophysics*, 347 : 127–136, July 1999.

S. Simón-Díaz, M. Godart, N. Castro, A. Herrero, C. Aerts, J. Puls, J. Telting, and L. Grassitelli. The IACOB project . III. New observational clues to understand macroturbulent broadening in massive O- and B-type stars. *Astronomy and Astrophysics*, 597 :A22, January 2017. doi : 10.1051/0004-6361/201628541.

J. O. Sundqvist, S. P. Owocki, and J. Puls. 2D wind clumping in hot, massive stars from hydrodynamical line-driven instability simulations using a pseudo-planar approach. *Astronomy and Astrophysics*, 611 :A17, March 2018. doi : 10.1051/0004-6361/201731718.

Jon O. Sundqvist and Stanley P. Owocki. Clumping in the inner winds of hot, massive stars from hydrodynamical line-driven instability simulations. *Monthly Notices of the RAS*, 428 (2) :1837–1844, January 2013. doi : 10.1093/mnras/sts165.

W. W. Weiss, S. M. Rucinski, A. F. J. Moffat, A. Schwarzenberg-Czerny, O. F. Koudelka, C. C. Grant, R. E. Zee, R. Kuschnig, St. Mochnacki, J. M. Matthews, P. Orleanski, A. Pamyatnykh, A. Pigulski, J. Alves, M. Guedel, G. Handler, G. A. Wade, and K. Zwintz. BRITE-Constellation : Nanosatellites for Precision Photometry of Bright Stars. *Publications of the ASP*, 126(940) :573, June 2014. doi : 10.1086/677236.

Conclusion

Grâce aux missions spatiales BRITE-Constellation, TESS et MOST, nous avons pu présenter dans ce mémoire trois articles traitant de la variabilité photométrique des étoiles Wolf-Rayet.

Nous avons tout d'abord étudié la lumière provenant du système multiple Θ Muscae, pour tenter d'y observer une éclipse atmosphérique du sous-système binaire WR48(WC5/6+O). L'observation continue du système pendant plus de 150 jours par le satellite BRITE-Toronto ne nous a pas permis de détecter de façon significative une variation lumineuse périodique suivant la période orbitale du sous-système. Nous avons toutefois pu déterminer que le taux de perte de masse de la composante WR est au plus de $4.7 \times 10^{-5} M_{\odot}/an$. Aussi, en supposant que le $\dot{M}$ de la WR correspond à la moyenne pour les étoiles WC5/6 ($4.7 \times 10^{-5} M_{\odot}/an$), nous avons pu calculer le nombre de cycles orbitaux de WR48 minimalement requis pour observer l'éclipse de ce système à l'aide d'un satellite de la BRITE-Constellation, soit 12±2 cycles pour atteindre une confiance en la détection de 99% et 20±3 cycles pour 99.9%.

Nous avons ensuite étudié les 3 courbes de lumières du système binaire WR22 collectées par BRITE-Constellation en 2016, 2017 et 2018, afin premièrement de tenter de déterminer si l'éclipse apparaissant dans ces dernières est purement atmosphérique ou bien si une composante de coeur est présente, et ensuite d'en extraire des paramètres physiques pertinents. Malgré une modélisation visuellement satisfaisante, les résultats du modèle L96 ont dû être écartés, puisque ce dernier a été conçu pour modéliser des éclipses strictement atmosphériques dans des systèmes binaires où les disques stellaires restent éloignés. Un second modèle d'éclipse (numérique), incluant l'éclipse du compagnon de type O par le vent de la WR ainsi que l'éclipse des coeurs et donc n'ayant pas les limitations du premier, a ensuite été utilisé afin d'explorer l'espace de paramètres des solutions. Cependant, en l'absence de valeurs précises pour les rayons des étoiles et pour le ratio des flux lumineux des composantes, aucun estimé précis de l'inclinaison orbitale ou du taux de perte de masse de la composante WR n'a pu être déterminé.

Dans le troisième et dernier article, nous avons étudié la variabilité stochastique observée dans 70 séries de données issues de 55 étoiles WR galactiques. Nous avons tout d'abord caractérisé les spectres d'amplitude des courbes de lumières à l'aide d'un modèle semi-Lorentzien ayant des composantes de bruits rouge et blanc. Notez que ces derniers ne sont pas du bruit instrumental ou d'observation comme on l'entend généralement mais bien des variantions intrinsèques stochastiques prenant naissance dans le vent des étoiles. Nous avons par la suite cherché des corrélations entre les paramètres ajustés de ces signaux et des paramètres des vents stellaires et des étoiles elles-mêmes, dans le but de mettre en lumière des phénomènes physiques potentiellement responsables de la variabilité observée.

Une première corrélation a été observée entre l'amplitude de variabilité photométrique de la composante de bruit rouge et la température de l'étoile. L'instabilité de désombrage de raie est aussi démontrée comme étant un phénomène plausible pouvant contribuer à la variabilité, tout comme la présence d'une zone de convection subsurface et d'ondes gravitationnelles internes. Ces trois phénomènes peuvent ainsi contribuer à la formation d'un vent stellaire contenant des inhomogénéités en densité de tailles variées, qui diffusent la lumière du continuum dans notre ligne de visée pendant leurs déplacements dans le vent stellaire, générant ainsi la variabilité photométrique stochastique observée.

L'analyse de données photométriques d'étoiles WR permet ainsi d'obtenir beaucoup d'informations sur la variabilité de ces étoiles, qu'elle soit due à la binarité, à des phénomènes prenant naissance dans l'intérieur stellaire ou à des événements se produisant dans les vents stellaires. Cependant, la photométrie seule ne suffit pas pour brosser un portrait complet des méchanismes à la base de cette variabilité et devra, dans les années à venir, être complémentée par des observations spectrométriques et polarimétriques, ainsi que par des modélisations hydrodynamiques de vents stellaires optiquement épais.

Annexe A : Courbes de lumières

TESS

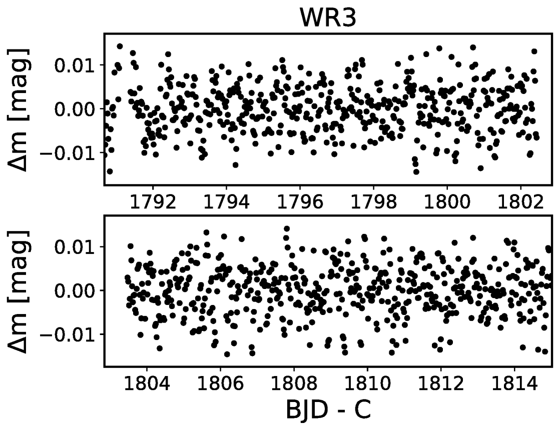

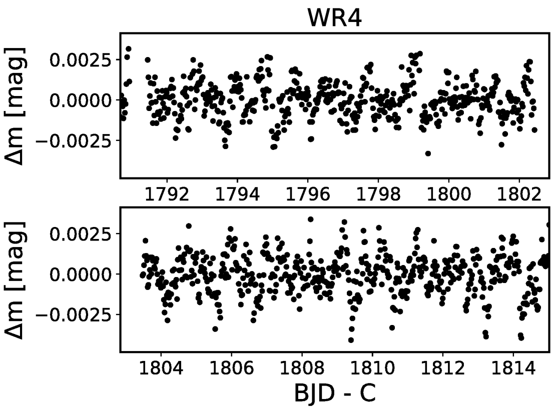

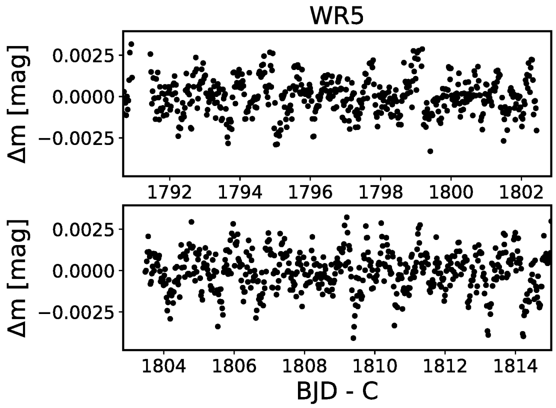

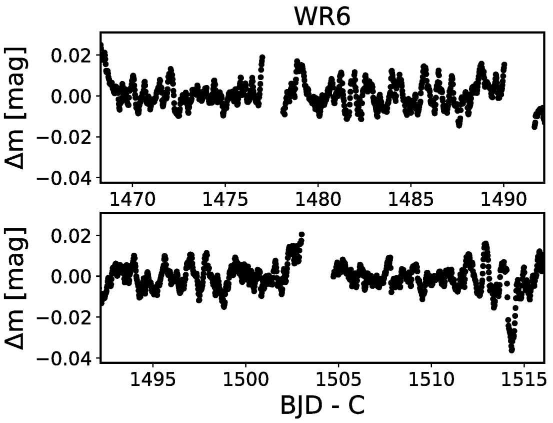

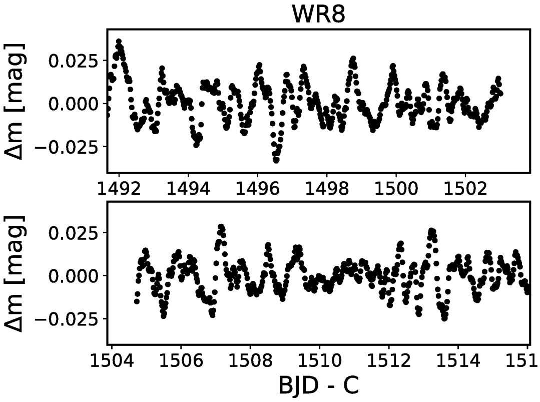
WR8
Δm [mag]
0.025
0.000
−0.025
1492
1494
1496
1498
1500
1502
1504
1506
1508
1510
1512
1514
1516
BJD - C

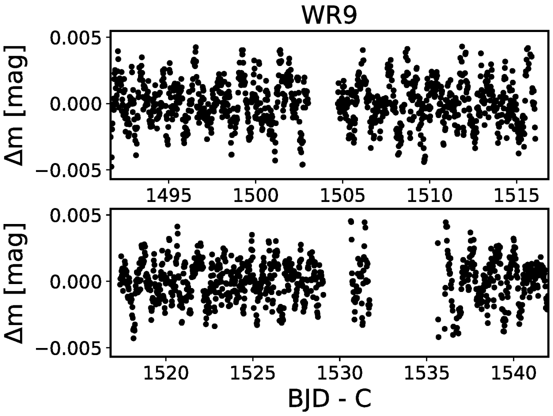
WR9
Δm [mag]
0.005
0.000
−0.005
1495
1500
1505
1510
1515
1520
1525
1530
1535
1540
BJD - C

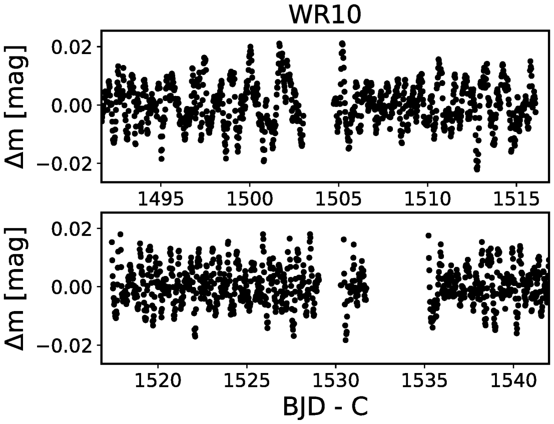
WR10
Δm [mag]
0.02
0.00
−0.02
1495
1500
1505
1510
1515
1520
1525
1530
1535
1540
BJD - C

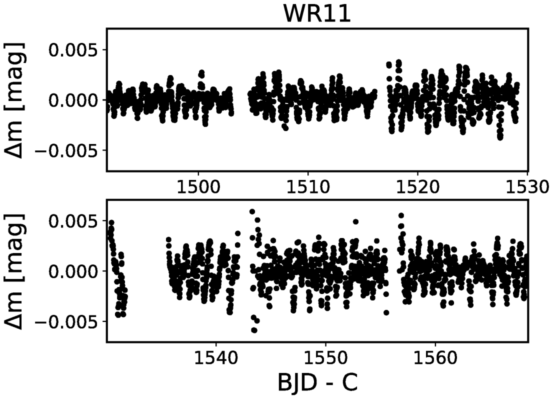
WR11
Δm [mag]
0.005
0.000
−0.005
1500
1510
1520
1530
1540
1550
1560
BJD - C

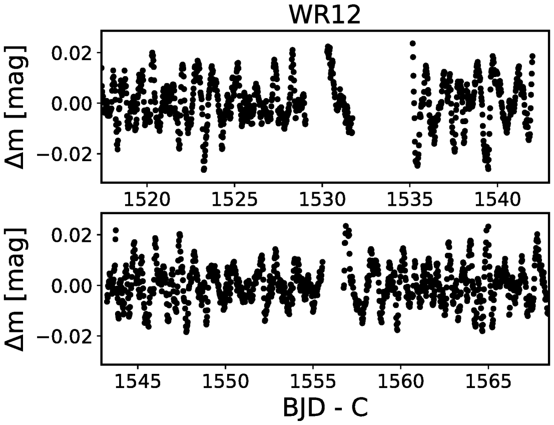
WR12
Δm [mag]
0.02
0.00
−0.02
1520
1525
1530
1535
1540
1545
1550
1555
1560
1565
BJD - C

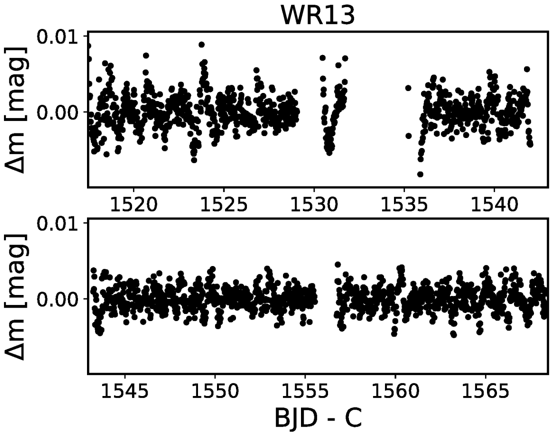
WR13
Δm [mag]
0.01
0.00
1520
1525
1530
1535
1540
1545
1550
1555
1560
1565
BJD - C

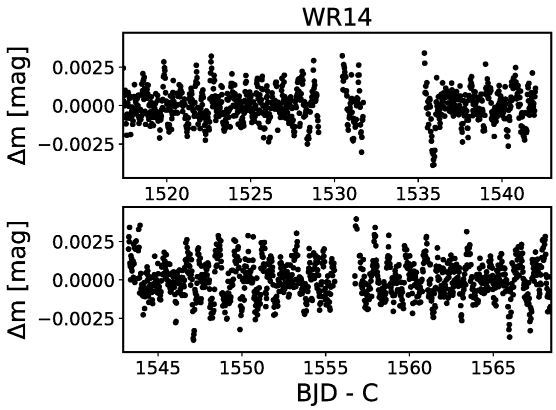
WR14
Δm [mag]
0.0025
0.0000
−0.0025
1520
1525
1530
1535
1540
Δm [mag]
0.0025
0.0000
−0.0025
1545
1550
1555
1560
1565
BJD - C

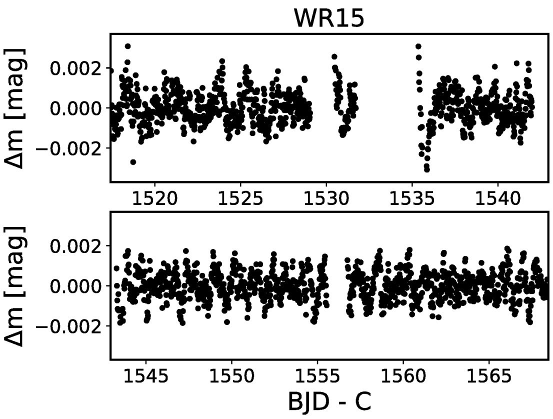
WR15
Δm [mag]
0.002
0.000
−0.002
1520
1525
1530
1535
1540
Δm [mag]
0.002
0.000
−0.002
1545
1550
1555
1560
1565
BJD - C

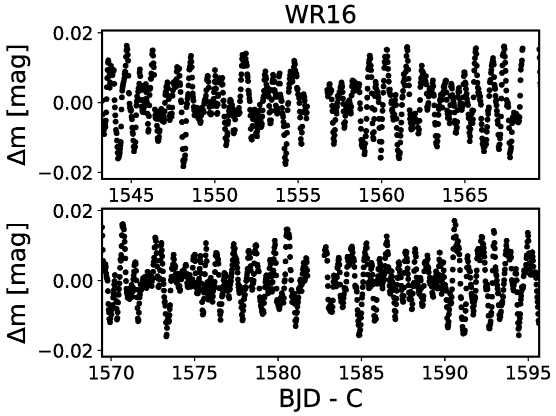
WR16
Δm [mag]
0.02
0.00
−0.02
1545
1550
1555
1560
1565
Δm [mag]
0.02
0.00
−0.02
1570
1575
1580
1585
1590
1595
BJD - C

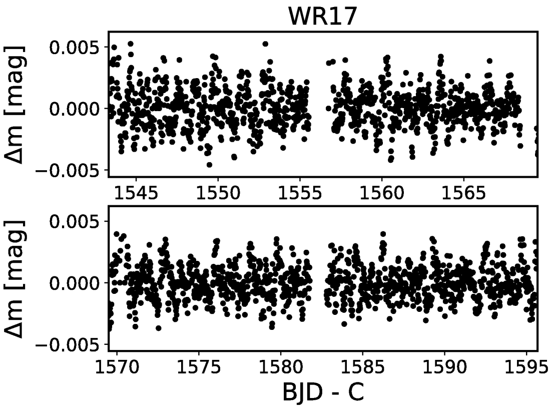
WR17
Δm [mag]
0.005
0.000
−0.005
1545
1550
1555
1560
1565
Δm [mag]
0.005
0.000
−0.005
1570
1575
1580
1585
1590
1595
BJD - C

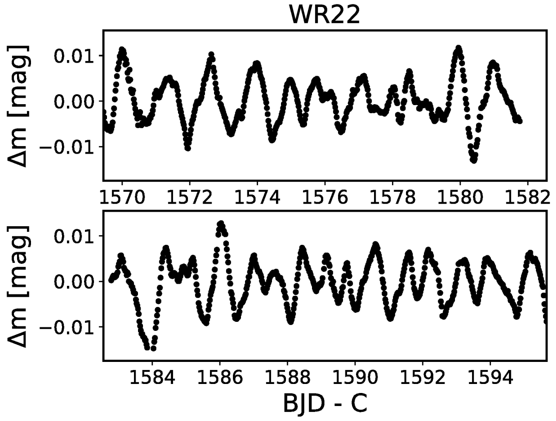
WR22
Δm [mag]
0.01
0.00
−0.01
1570
1572
1574
1576
1578
1580
1582
Δm [mag]
0.01
0.00
−0.01
1584
1586
1588
1590
1592
1594
BJD - C

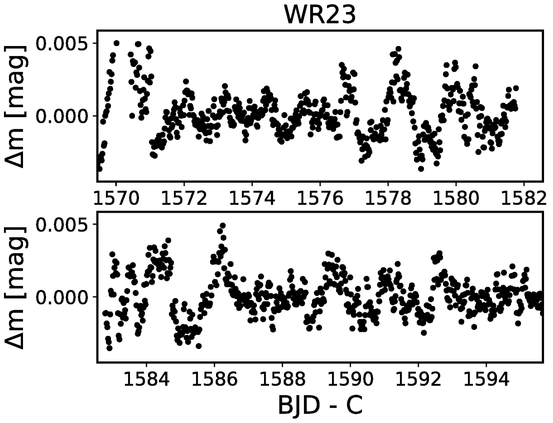
WR23
Δm [mag]
0.005
0.000
1570
1572
1574
1576
1578
1580
1582
Δm [mag]
0.005
0.000
1584
1586
1588
1590
1592
1594
BJD - C

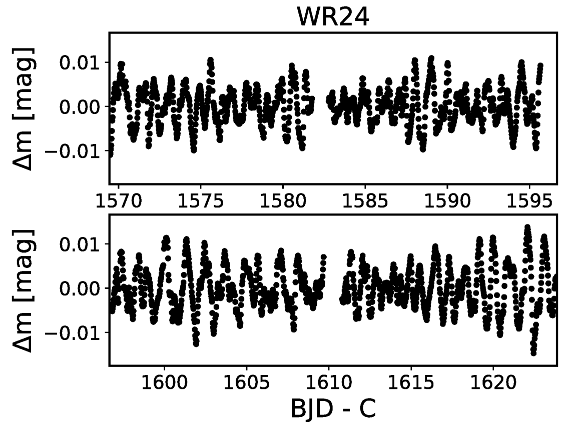
WR24
Δm [mag]
0.01
0.00
−0.01
1570
1575
1580
1585
1590
1595
Δm [mag]
0.01
0.00
−0.01
1600
1605
1610
1615
1620
BJD - C

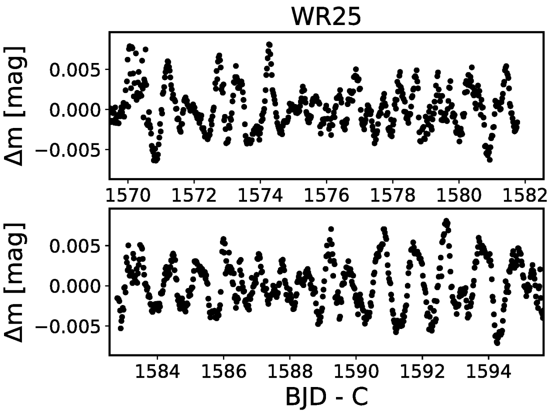
WR25
Δm [mag]
0.005
0.000
−0.005
1570
1572
1574
1576
1578
1580
1582
Δm [mag]
0.005
0.000
−0.005
1584
1586
1588
1590
1592
1594
BJD - C

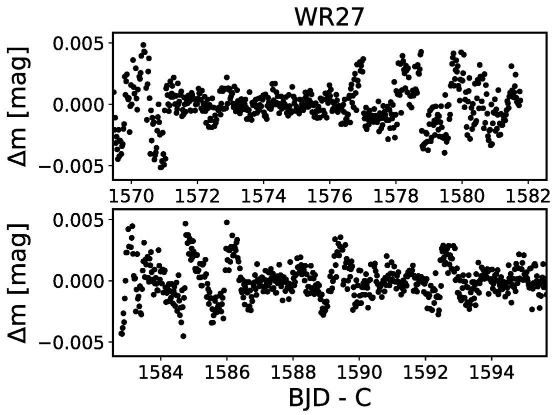
WR27
Δm [mag]
0.005
0.000
−0.005
1570
1572
1574
1576
1578
1580
1582
Δm [mag]
0.005
0.000
−0.005
1584
1586
1588
1590
1592
1594
BJD - C

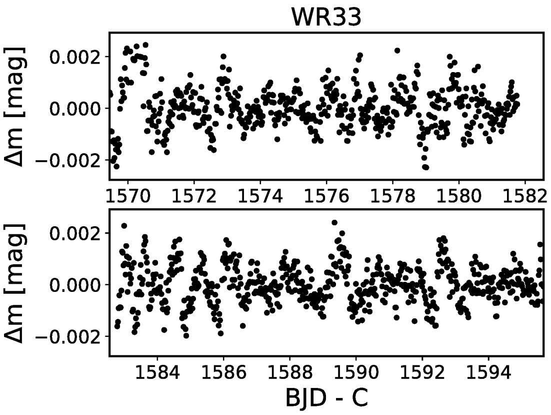
WR33
Δm [mag]
0.002
0.000
−0.002
1570
1572
1574
1576
1578
1580
1582
Δm [mag]
0.002
0.000
−0.002
1584
1586
1588
1590
1592
1594
BJD - C

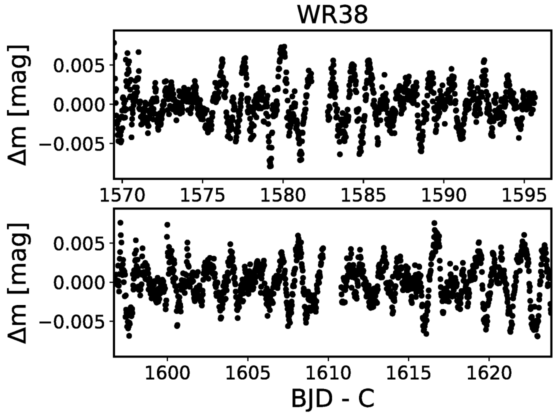
WR38
Δm [mag]
0.005
0.000
−0.005
1570
1575
1580
1585
1590
1595
Δm [mag]
0.005
0.000
−0.005
1600
1605
1610
1615
1620
BJD - C

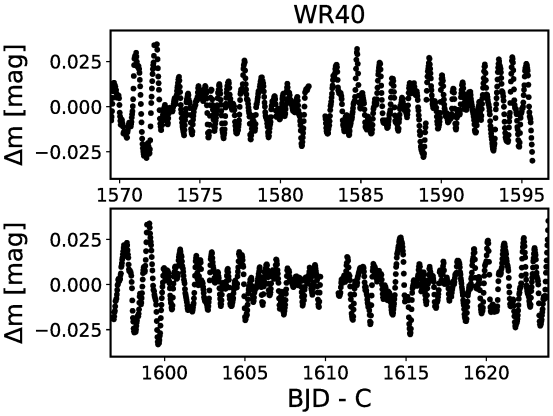
WR40
Δm [mag]
0.025
0.000
−0.025
1570
1575
1580
1585
1590
1595
Δm [mag]
0.025
0.000
−0.025
1600
1605
1610
1615
1620
BJD - C

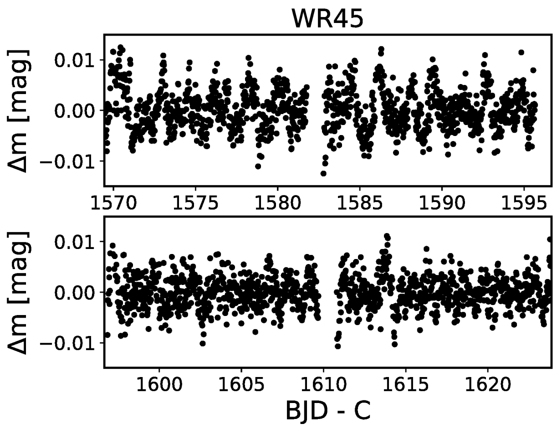
WR45
Δm [mag]
0.01
0.00
−0.01
1570
1575
1580
1585
1590
1595
Δm [mag]
0.01
0.00
−0.01
1600
1605
1610
1615
1620
BJD - C

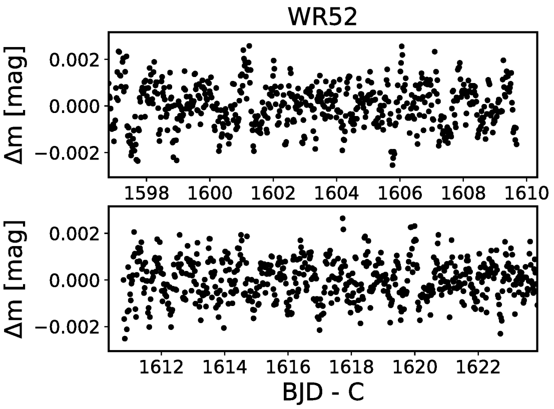
WR52
Δm [mag]
0.002
0.000
−0.002
1598
1600
1602
1604
1606
1608
1610
Δm [mag]
0.002
0.000
−0.002
1612
1614
1616
1618
1620
1622
BJD - C

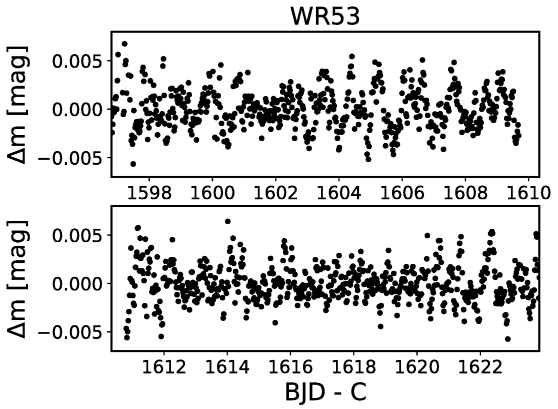
WR53
Δm [mag]
0.005
0.000
−0.005
1598
1600
1602
1604
1606
1608
1610
Δm [mag]
0.005
0.000
−0.005
1612
1614
1616
1618
1620
1622
BJD - C

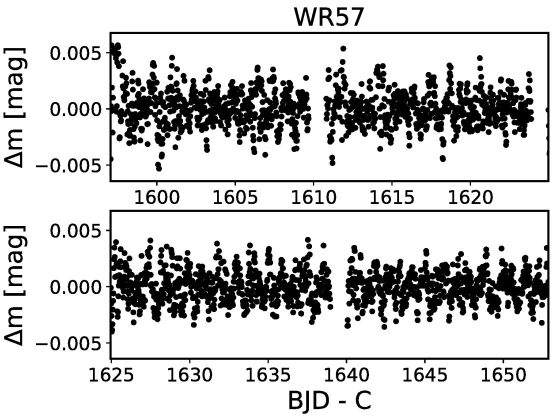
WR57
Δm [mag]
0.005
0.000
−0.005
1600
1605
1610
1615
1620
Δm [mag]
0.005
0.000
−0.005
1625
1630
1635
1640
1645
1650
BJD - C

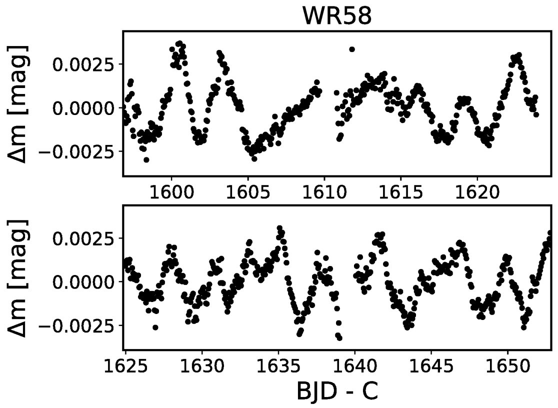
WR58
Δm [mag]
0.0025
0.0000
−0.0025
1600
1605
1610
1615
1620
Δm [mag]
0.0025
0.0000
−0.0025
1625
1630
1635
1640
1645
1650
BJD - C

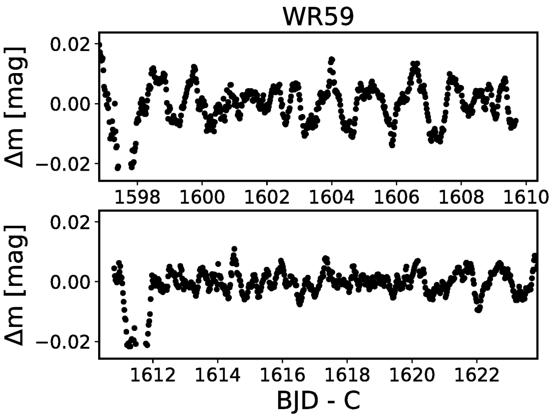
WR59
Δm [mag]
0.02
0.00
−0.02
1598
1600
1602
1604
1606
1608
1610
Δm [mag]
0.02
0.00
−0.02
1612
1614
1616
1618
1620
1622
BJD - C

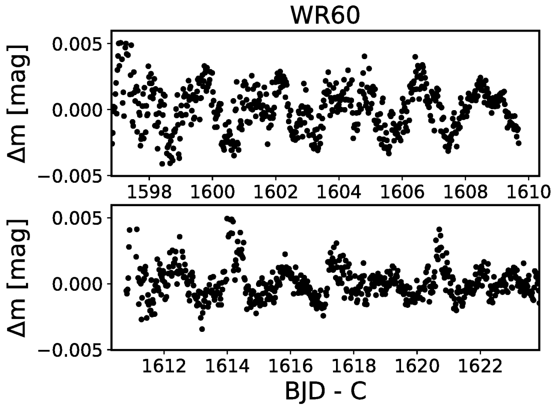
WR60
Δm [mag]
0.005
0.000
−0.005
1598
1600
1602
1604
1606
1608
1610
Δm [mag]
0.005
0.000
−0.005
1612
1614
1616
1618
1620
1622
BJD - C

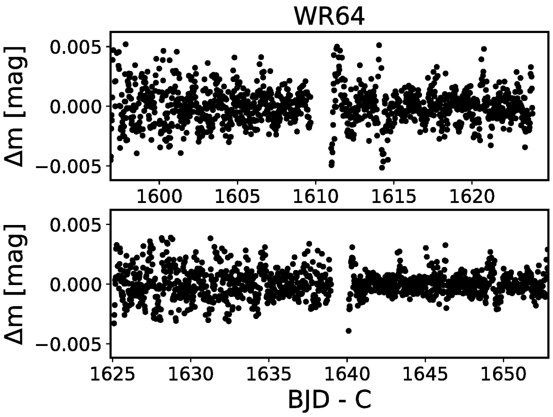
WR64
Δm [mag]
0.005
0.000
−0.005
1600
1605
1610
1615
1620
Δm [mag]
0.005
0.000
−0.005
1625
1630
1635
1640
1645
1650
BJD - C

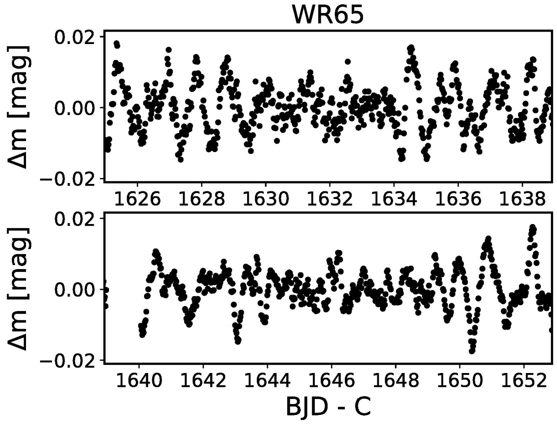
WR65
Δm [mag]
0.02
0.00
−0.02
1626
1628
1630
1632
1634
1636
1638
Δm [mag]
0.02
0.00
−0.02
1640
1642
1644
1646
1648
1650
1652
BJD - C

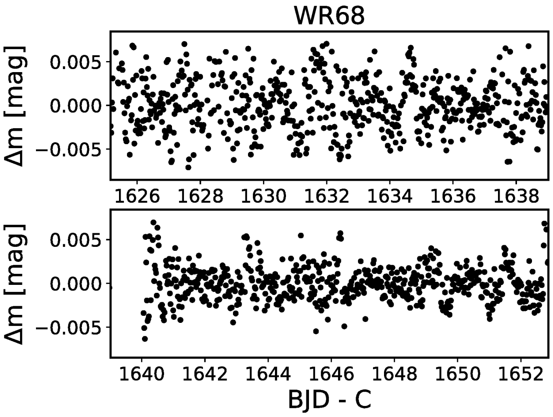
WR68
Δm [mag]
0.005
0.000
−0.005
1626
1628
1630
1632
1634
1636
1638
Δm [mag]
0.005
0.000
−0.005
1640
1642
1644
1646
1648
1650
1652
BJD - C

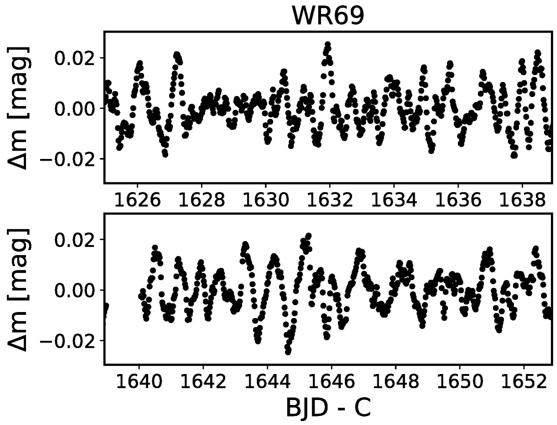
WR69
Δm [mag]
0.02
0.00
−0.02
1626
1628
1630
1632
1634
1636
1638
Δm [mag]
0.02
0.00
−0.02
1640
1642
1644
1646
1648
1650
1652
BJD - C

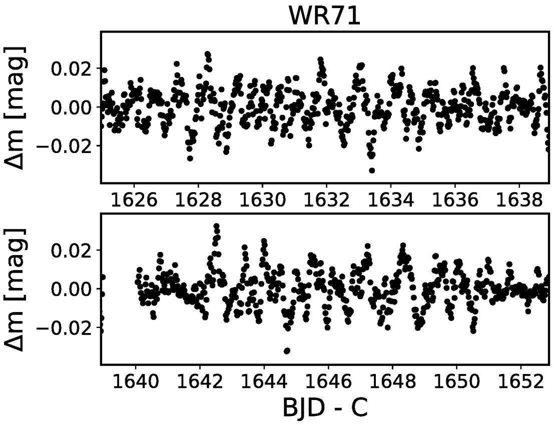
WR71
Δm [mag]
0.02
0.00
−0.02
1626
1628
1630
1632
1634
1636
1638
Δm [mag]
0.02
0.00
−0.02
1640
1642
1644
1646
1648
1650
1652
BJD - C

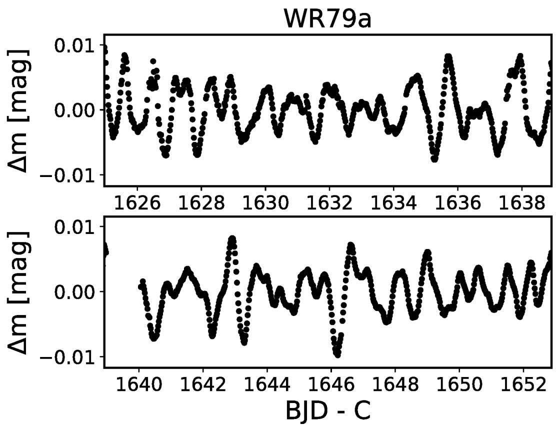
WR79a
Δm [mag]
0.01
0.00
−0.01
1626 1628 1630 1632 1634 1636 1638
1640 1642 1644 1646 1648 1650 1652
BJD - C

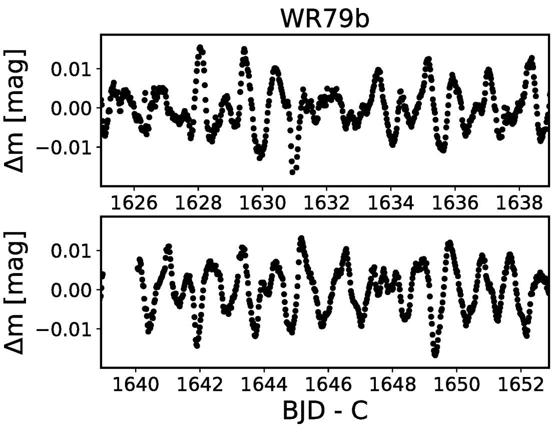
WR79b
Δm [mag]
0.01
0.00
−0.01
1626 1628 1630 1632 1634 1636 1638
1640 1642 1644 1646 1648 1650 1652
BJD - C

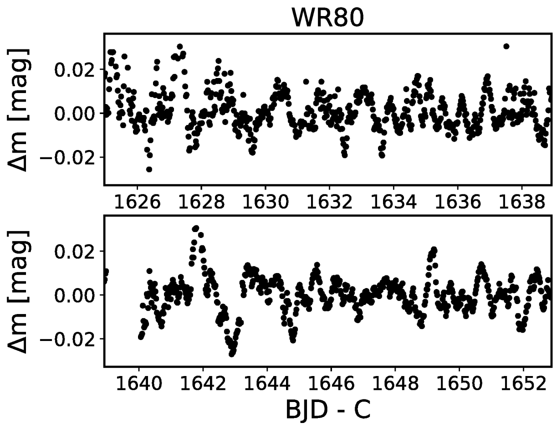
WR80
Δm [mag]
0.02
0.00
−0.02
1626 1628 1630 1632 1634 1636 1638
1640 1642 1644 1646 1648 1650 1652
BJD - C

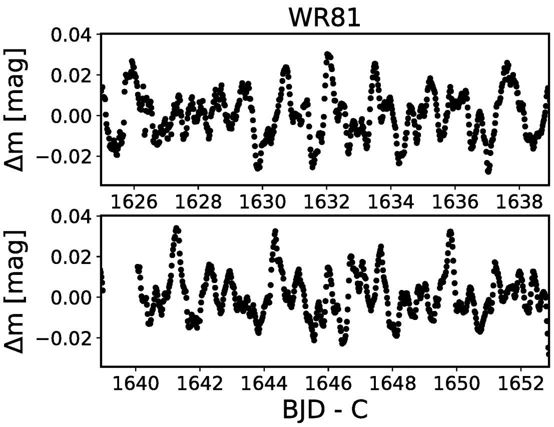
WR81
Δm [mag]
0.04
0.02
0.00
−0.02
1626 1628 1630 1632 1634 1636 1638
1640 1642 1644 1646 1648 1650 1652
BJD - C

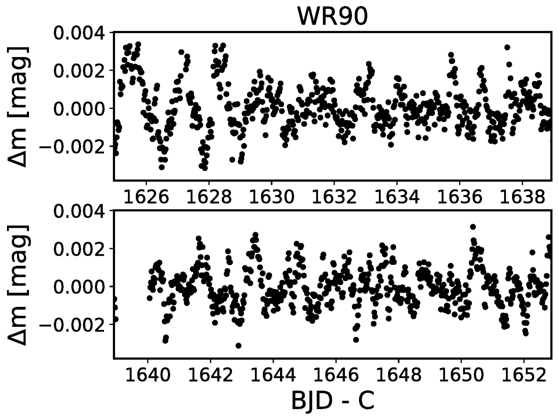
WR90
Δm [mag]
0.004
0.002
0.000
−0.002
1626 1628 1630 1632 1634 1636 1638
1640 1642 1644 1646 1648 1650 1652
BJD - C

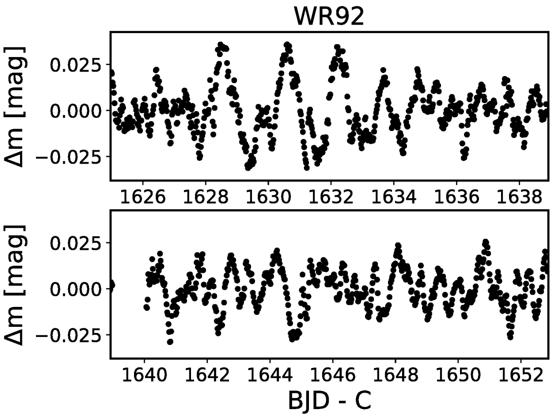
WR92
Δm [mag]
0.025
0.000
−0.025
1626 1628 1630 1632 1634 1636 1638
1640 1642 1644 1646 1648 1650 1652
BJD - C

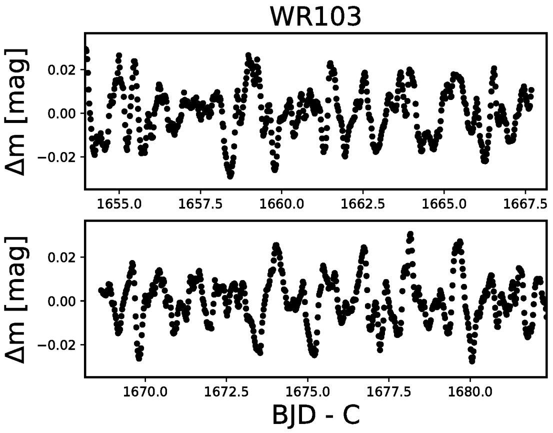
WR103
Δm [mag]
0.02
0.00
−0.02
1655.0
1657.5
1660.0
1662.5
1665.0
1667.5
1670.0
1672.5
1675.0
1677.5
1680.0
BJD - C

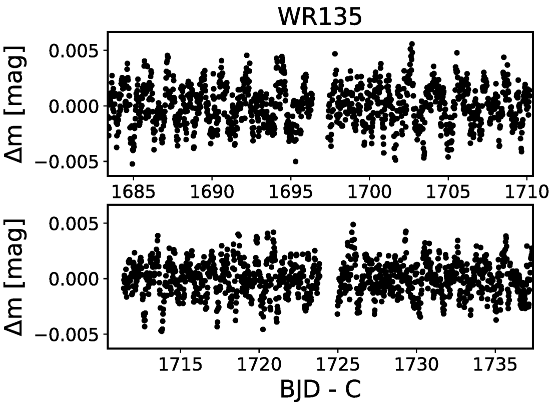
WR135
Δm [mag]
0.005
0.000
−0.005
1685
1690
1695
1700
1705
1710
1715
1720
1725
1730
1735
BJD - C

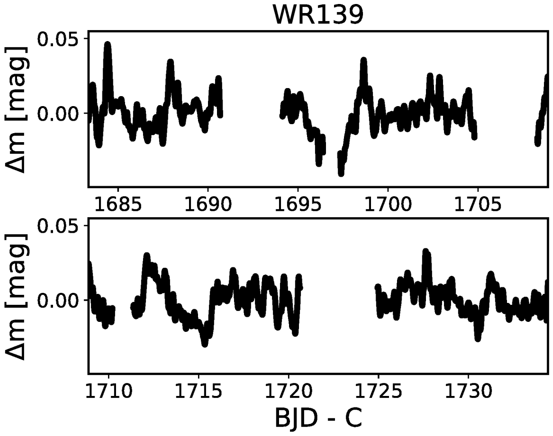
WR139
Δm [mag]
0.05
0.00
1685
1690
1695
1700
1705
1710
1715
1720
1725
1730
BJD - C

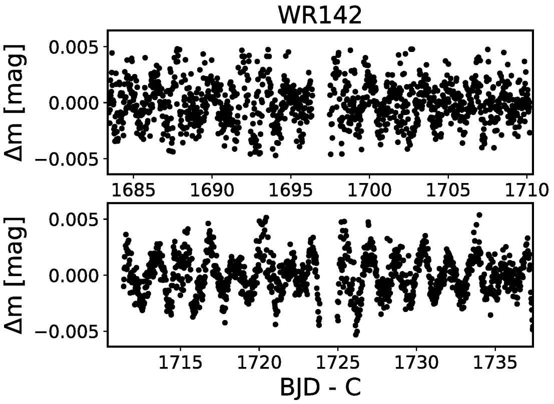
WR142
Δm [mag]
0.005
0.000
−0.005
1685
1690
1695
1700
1705
1710
1715
1720
1725
1730
1735
BJD - C

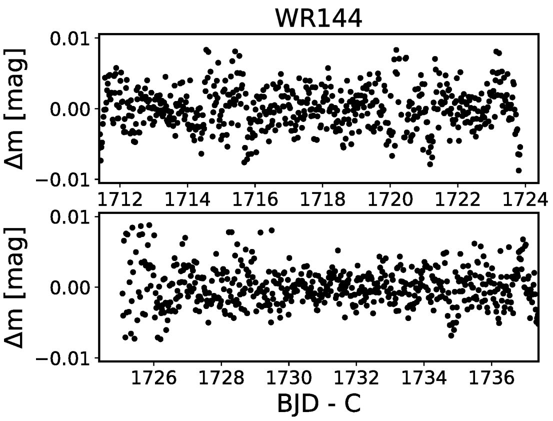
WR144
Δm [mag]
0.01
0.00
−0.01
1712
1714
1716
1718
1720
1722
1724
1726
1728
1730
1732
1734
1736
BJD - C

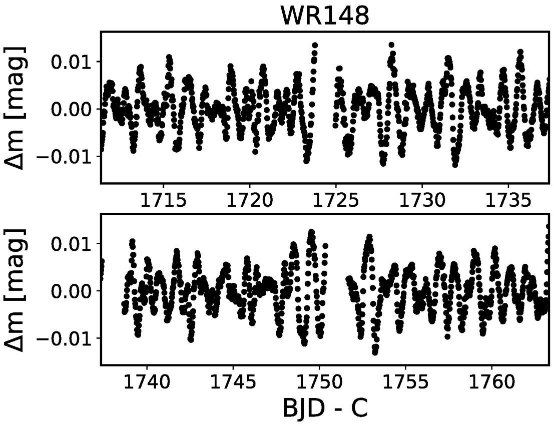
WR148
Δm [mag]
0.01
0.00
−0.01
1715
1720
1725
1730
1735
1740
1745
1750
1755
1760
BJD - C

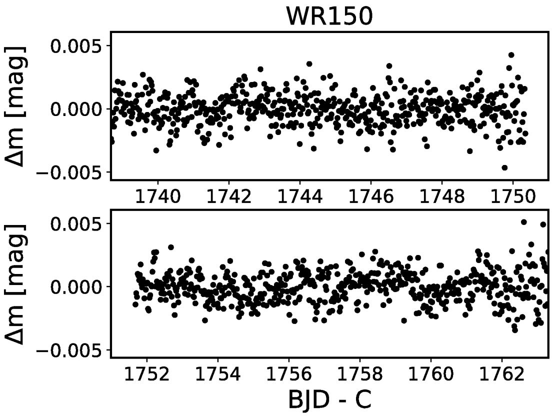
WR150
Δm [mag]
0.005
0.000
−0.005
1740
1742
1744
1746
1748
1750
Δm [mag]
0.005
0.000
−0.005
1752
1754
1756
1758
1760
1762
BJD - C

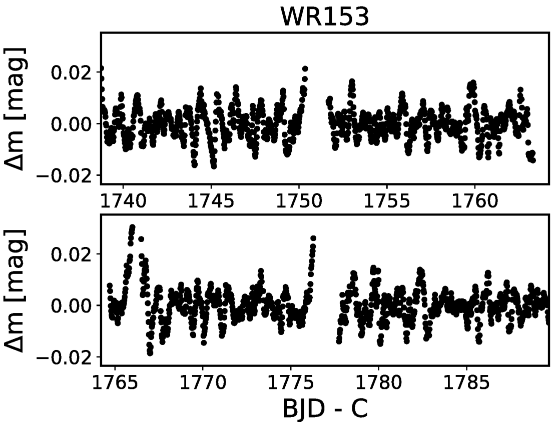
WR153
Δm [mag]
0.02
0.00
−0.02
1740
1745
1750
1755
1760
Δm [mag]
0.02
0.00
−0.02
1765
1770
1775
1780
1785
BJD - C

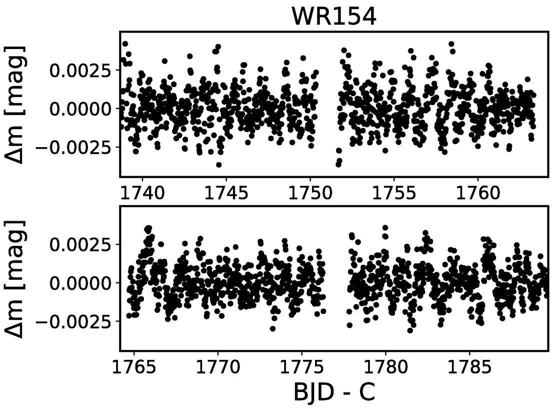
WR154
Δm [mag]
0.0025
0.0000
−0.0025
1740
1745
1750
1755
1760
Δm [mag]
0.0025
0.0000
−0.0025
1765
1770
1775
1780
1785
BJD - C

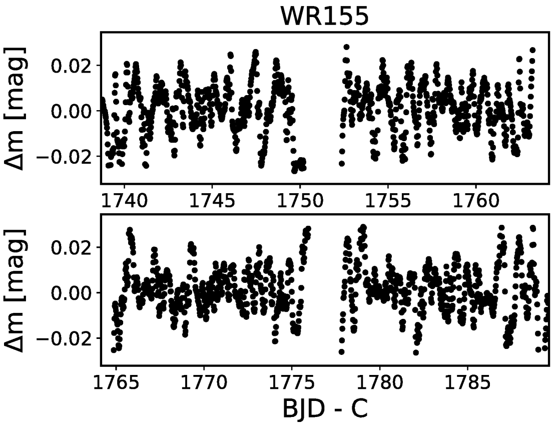
WR155
Δm [mag]
0.02
0.00
−0.02
1740
1745
1750
1755
1760
Δm [mag]
0.02
0.00
−0.02
1765
1770
1775
1780
1785
BJD - C

BRITE

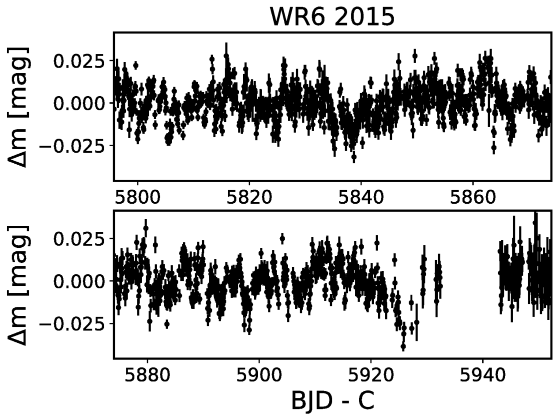
WR6 2015
Δm [mag]
0.025
0.000
−0.025
5800
5820
5840
5860
Δm [mag]
0.025
0.000
−0.025
5880
5900
5920
5940
BJD - C

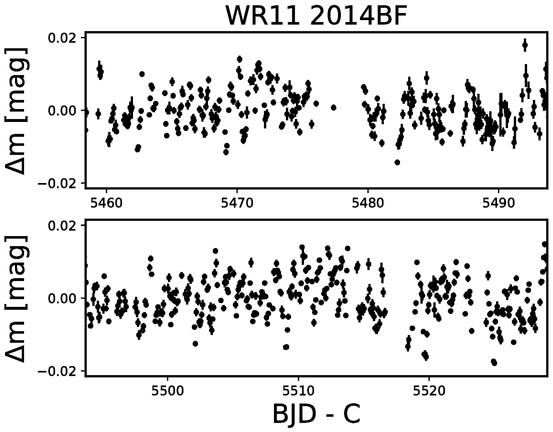
WR11 2014BF
Δm [mag]
0.02
0.00
−0.02
5460
5470
5480
5490
Δm [mag]
0.02
0.00
−0.02
5500
5510
5520
BJD - C

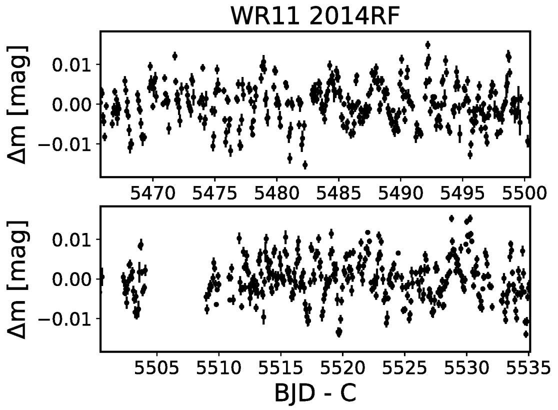
WR11 2014RF
Δm [mag]
0.01
0.00
−0.01
5470
5475
5480
5485
5490
5495
5500
Δm [mag]
0.01
0.00
−0.01
5505
5510
5515
5520
5525
5530
5535
BJD - C

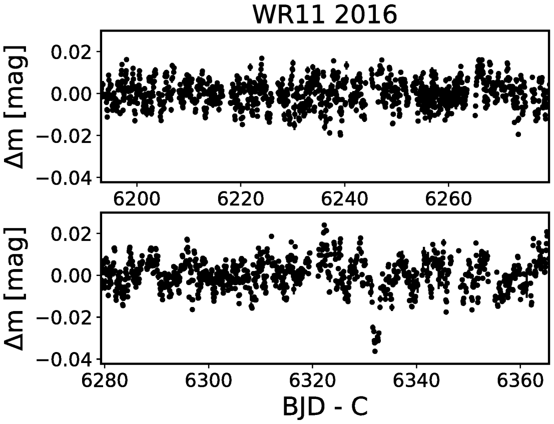
WR11 2016
Δm [mag]
0.02
0.00
−0.02
−0.04
6200
6220
6240
6260
Δm [mag]
0.02
0.00
−0.02
−0.04
6280
6300
6320
6340
6360
BJD - C

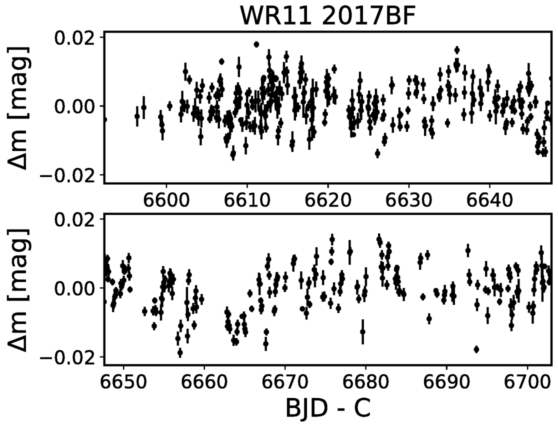
WR11 2017BF
Δm [mag]
0.02
0.00
−0.02
6600
6610
6620
6630
6640
Δm [mag]
0.02
0.00
−0.02
6650
6660
6670
6680
6690
6700
BJD - C

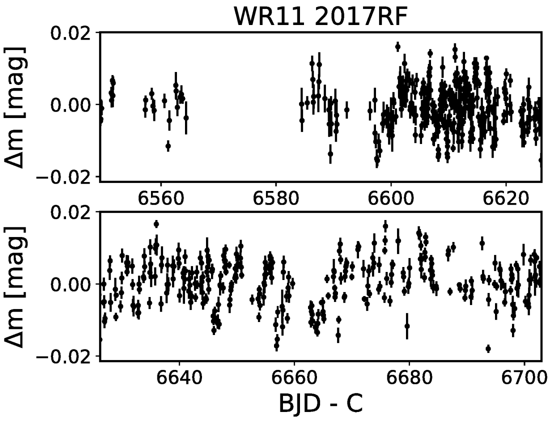
WR11 2017RF
Δm [mag]
0.02
0.00
−0.02
6560
6580
6600
6620
Δm [mag]
0.02
0.00
−0.02
6640
6660
6680
6700
BJD - C

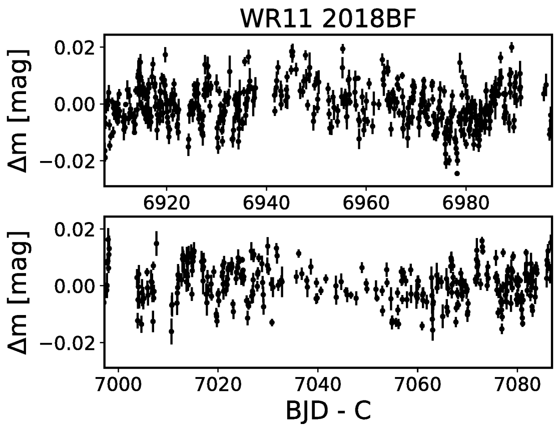
WR11 2018BF

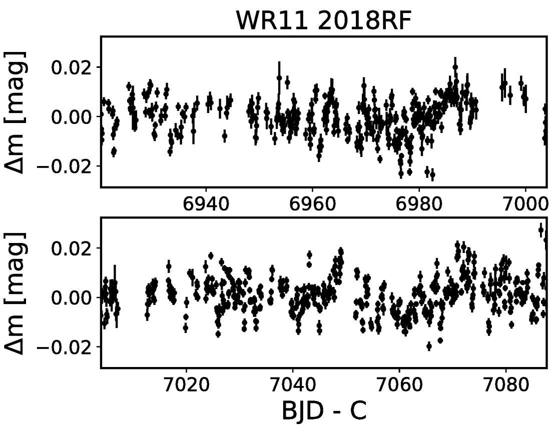
WR11 2018RF

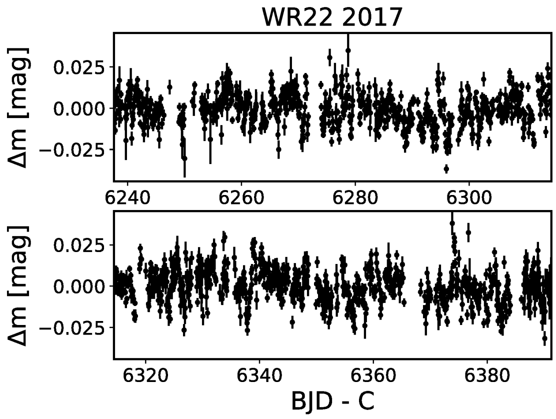
WR22 2017

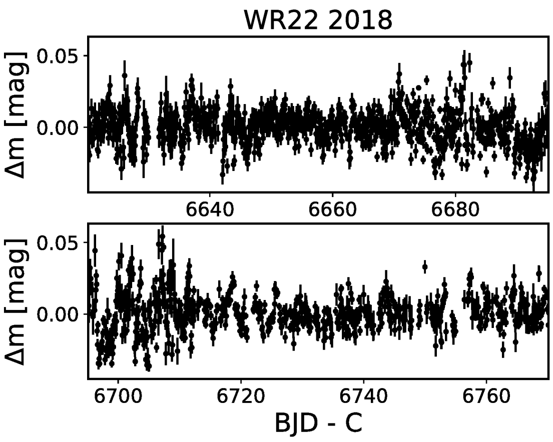
WR22 2018

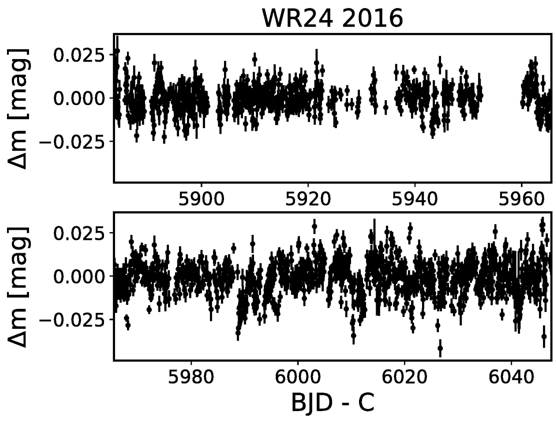
WR24 2016

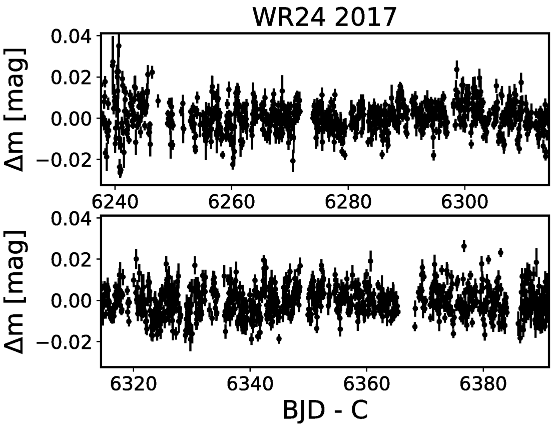
WR24 2017

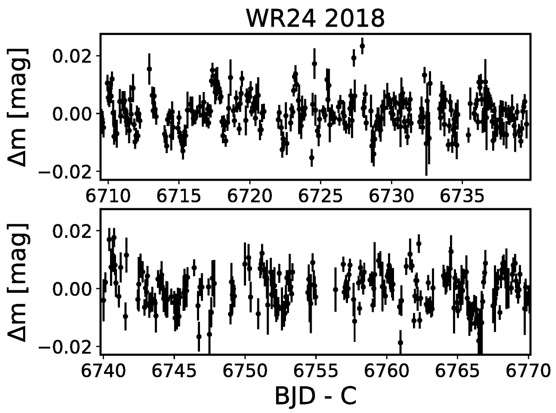
WR24 2018
Δm [mag]
0.02
0.00
−0.02
6710
6715
6720
6725
6730
6735
Δm [mag]
0.02
0.00
−0.02
6740
6745
6750
6755
6760
6765
6770
BJD - C

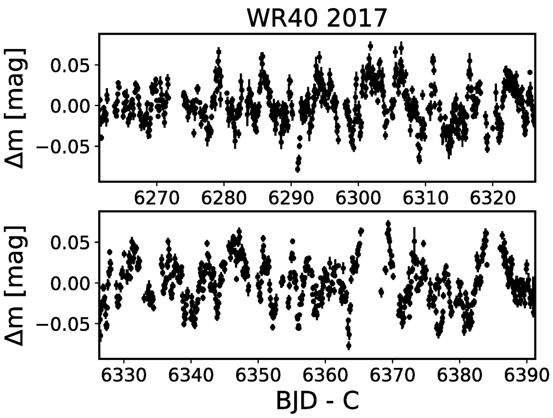
WR40 2017
Δm [mag]
0.05
0.00
−0.05
6270
6280
6290
6300
6310
6320
Δm [mag]
0.05
0.00
−0.05
6330
6340
6350
6360
6370
6380
6390
BJD - C

MOST

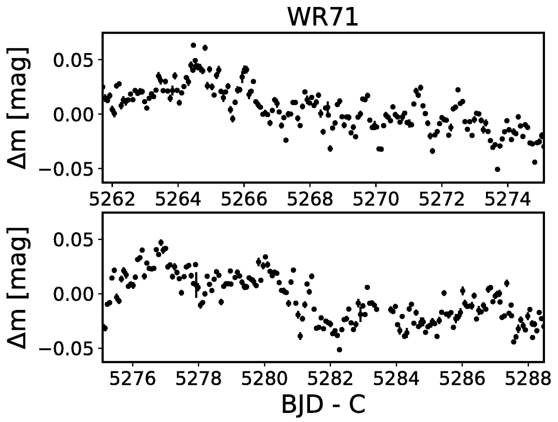
WR71
Δm [mag]
0.05
0.00
−0.05
5262
5264
5266
5268
5270
5272
5274
Δm [mag]
0.05
0.00
−0.05
5276
5278
5280
5282
5284
5286
5288
BJD - C

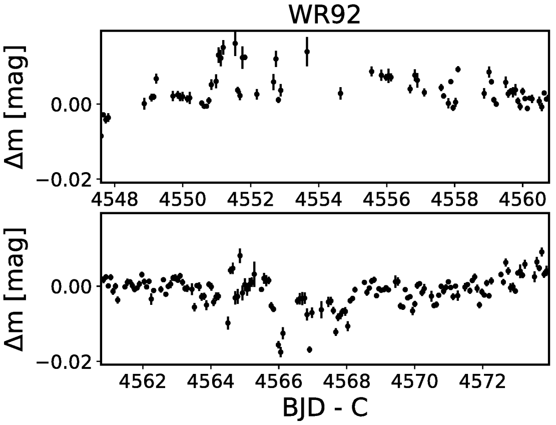
WR92
Δm [mag]
0.00
−0.02
4548
4550
4552
4554
4556
4558
4560
Δm [mag]
0.00
−0.02
4562
4564
4566
4568
4570
4572
BJD - C

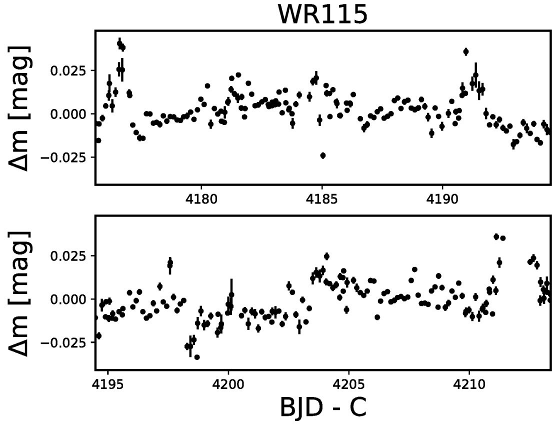
WR115
Δm [mag]
0.025
0.000
−0.025
4180
4185
4190
Δm [mag]
0.025
0.000
−0.025
4195
4200
4205
4210
BJD - C

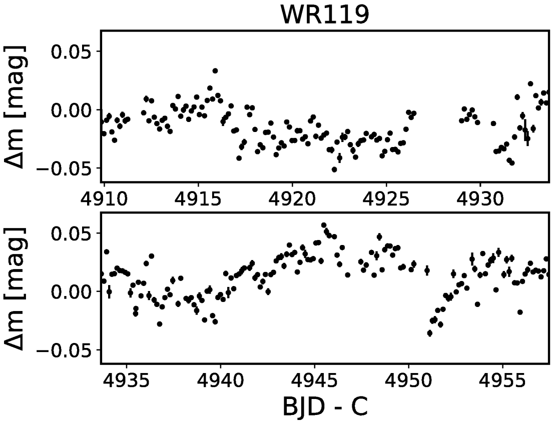
WR119
Δm [mag]
0.05
0.00
−0.05
4910
4915
4920
4925
4930
Δm [mag]
0.05
0.00
−0.05
4935
4940
4945
4950
4955
BJD - C

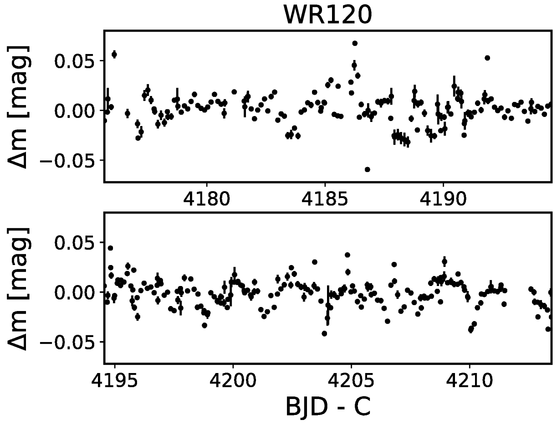
WR120
Δm [mag]
0.05
0.00
−0.05
4180
4185
4190
Δm [mag]
0.05
0.00
−0.05
4195
4200
4205
4210
BJD - C

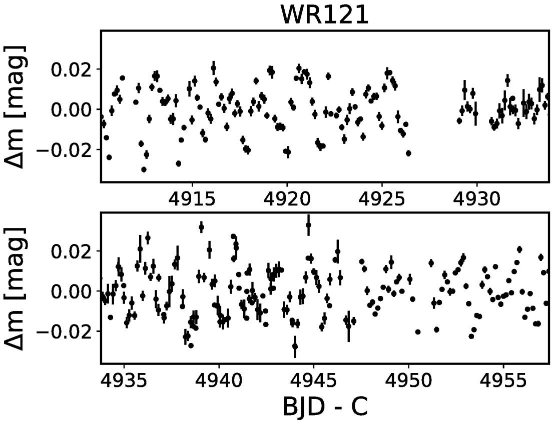
WR121
Δm [mag]
0.02
0.00
−0.02
4915
4920
4925
4930
Δm [mag]
0.02
0.00
−0.02
4935
4940
4945
4950
4955
BJD - C

Annexe B : Périodogrammes avec modèle de bruit ajusté

TESS

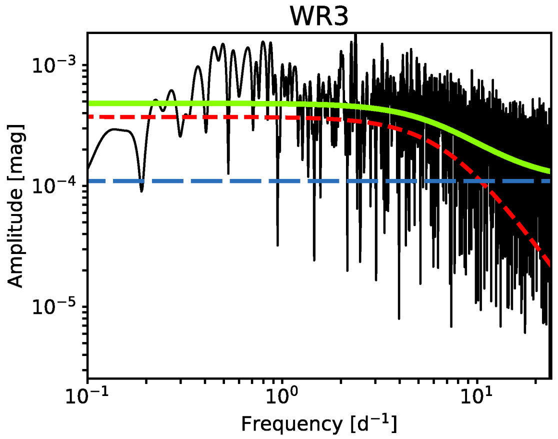
WR3

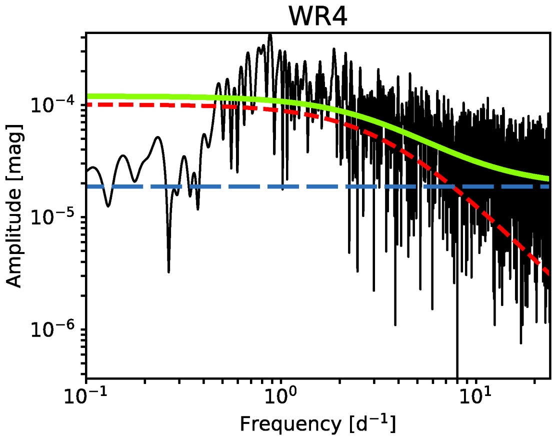
WR4

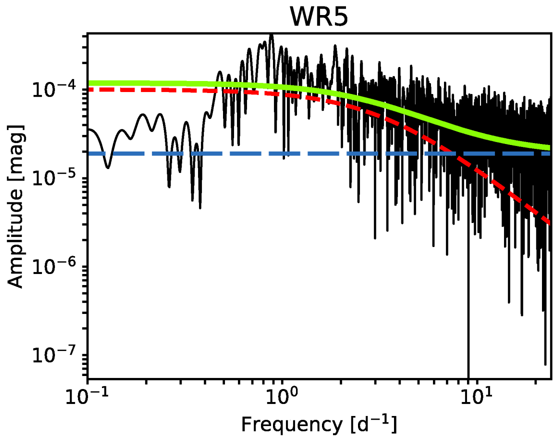
WR5

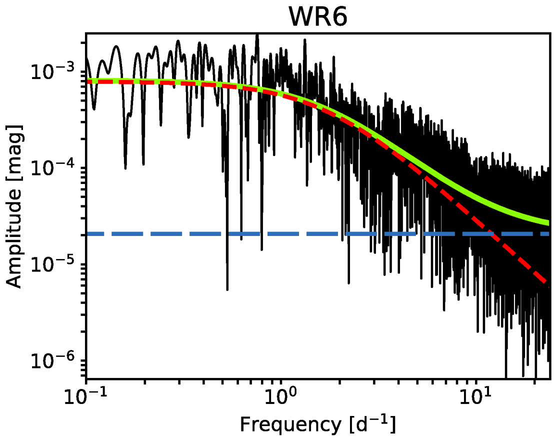
WR6

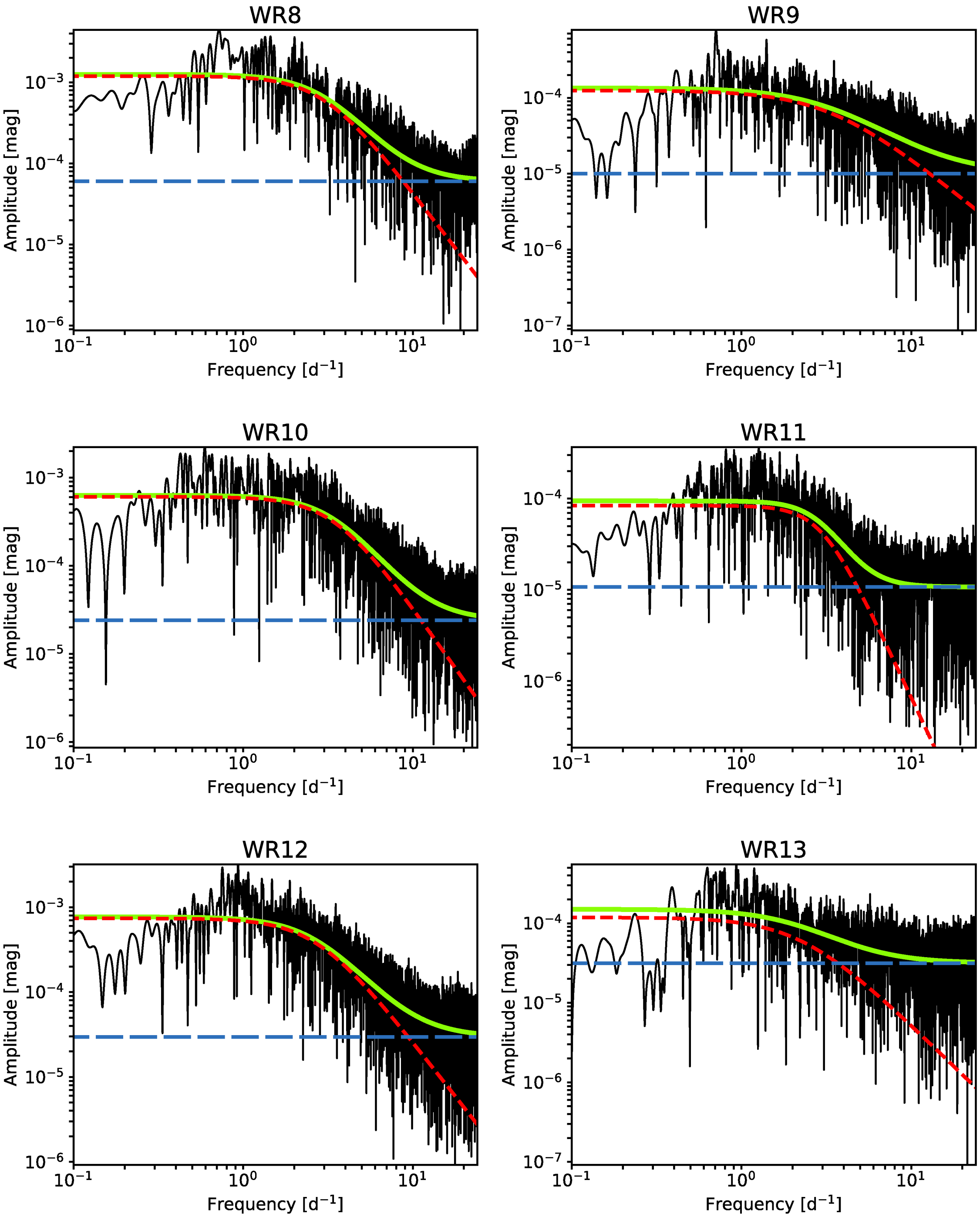
WR8
WR9
WR10
WR11
WR12
WR13
Amplitude [mag]
Frequency [d^{-1}]
10^{-1}
10^{0}
10^{1}
10^{-3}
10^{-4}
10^{-5}
10^{-6}
10^{-7}

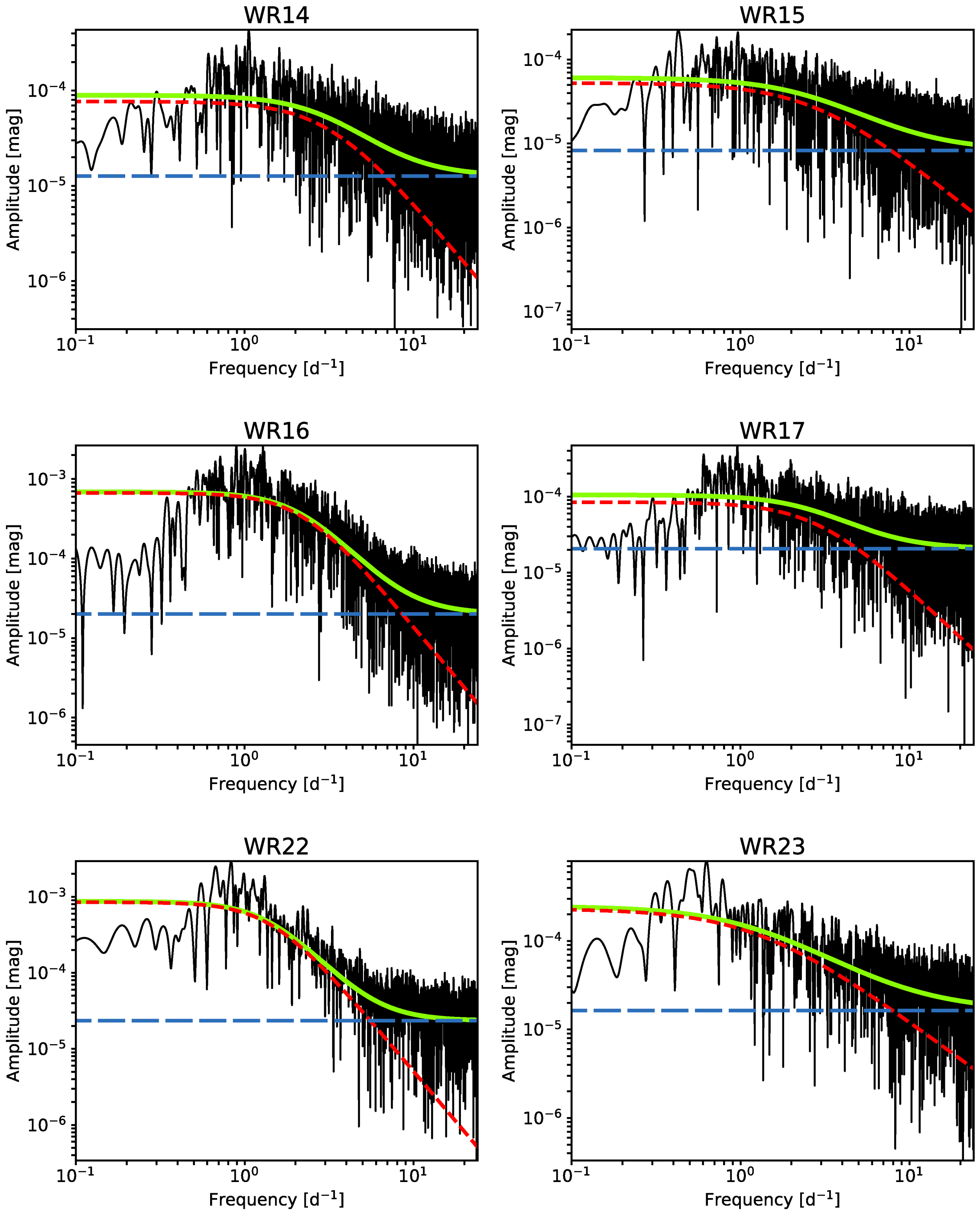
WR14
WR15
WR16
WR17
WR22
WR23
Amplitude [mag]
Frequency [d^{-1}]
10^{-7}
10^{-6}
10^{-5}
10^{-4}
10^{-3}
10^{-1}
10^{0}
10^{1}

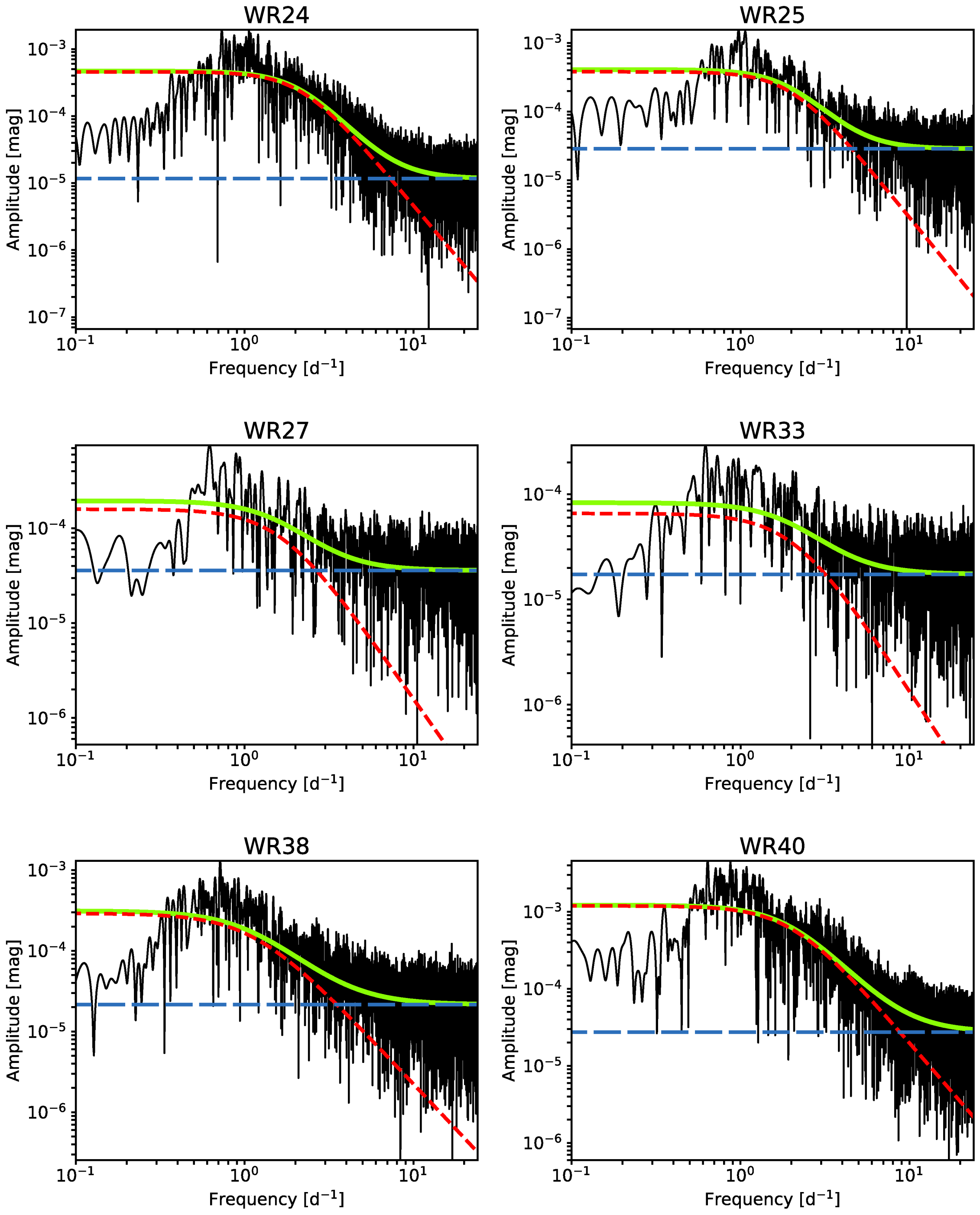
WR24
WR25
WR27
WR33
WR38
WR40
Amplitude [mag]
Frequency [d^{-1}]
10^{-1}
10^{0}
10^{1}
10^{-3}
10^{-4}
10^{-5}
10^{-6}
10^{-7}

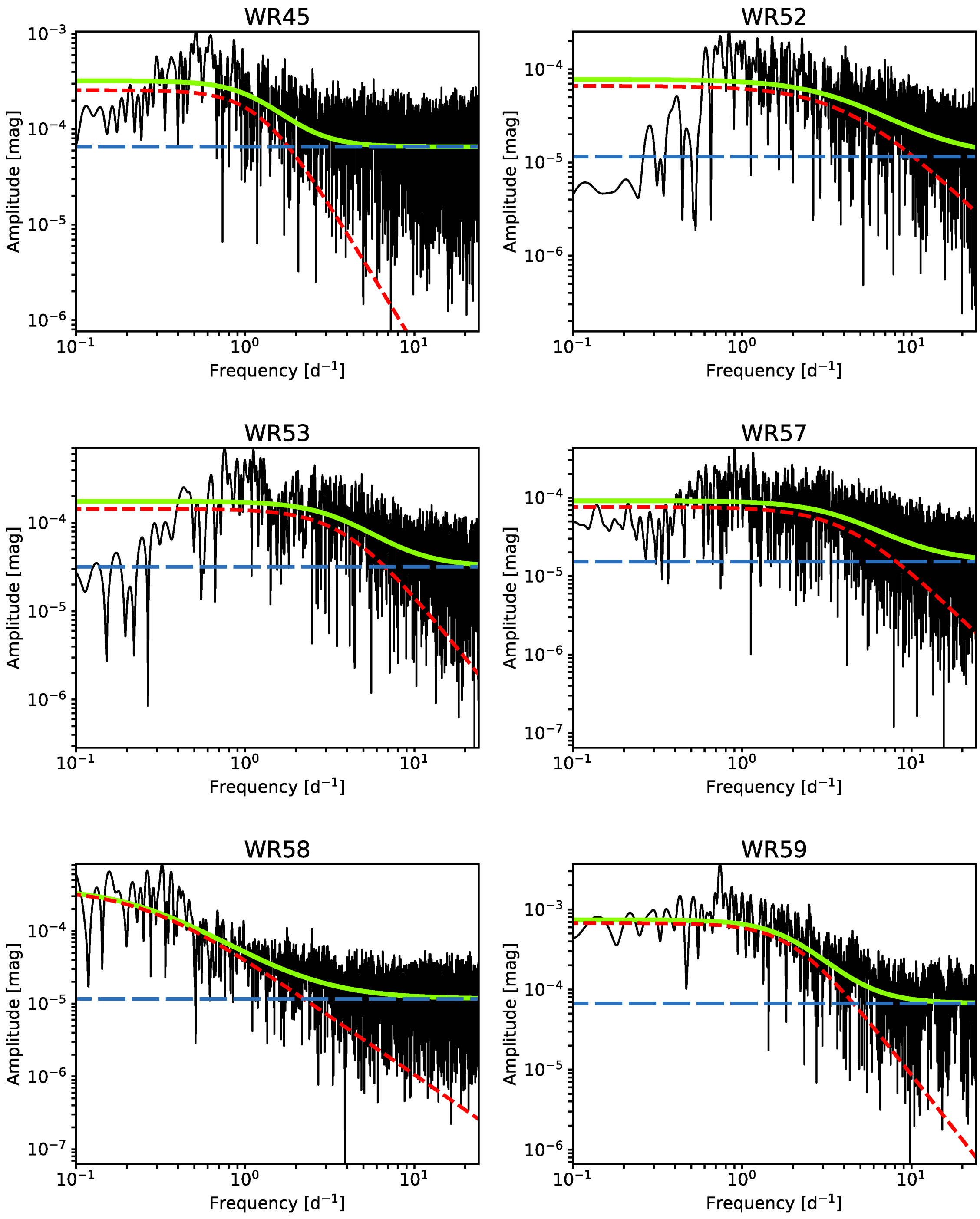
WR45
WR52
WR53
WR57
WR58
WR59
Amplitude [mag]
Frequency [d^{-1}]
10^{-1}
10^{0}
10^{1}
10^{-3}
10^{-4}
10^{-5}
10^{-6}
10^{-7}

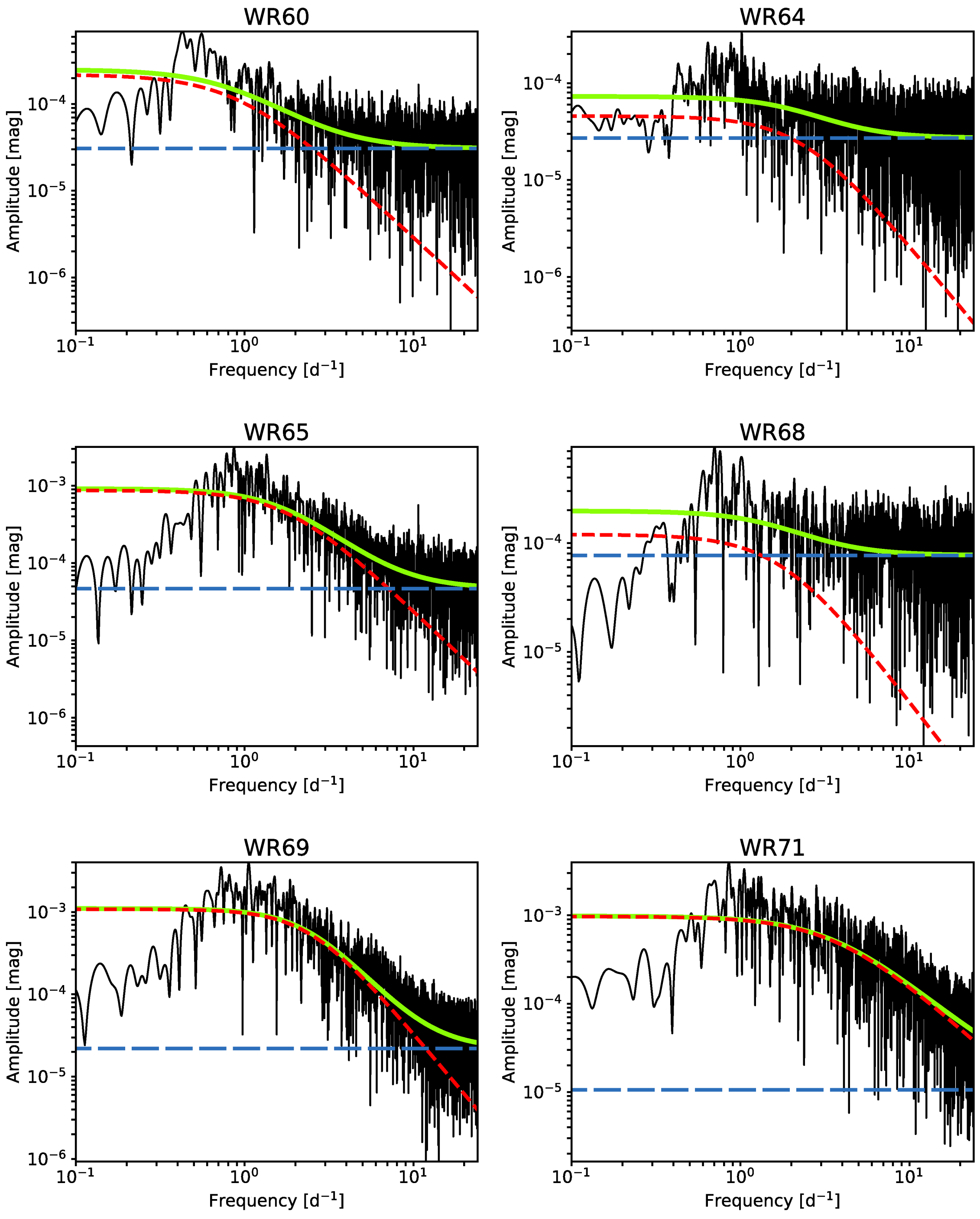
WR60
WR64
WR65
WR68
WR69
WR71
Amplitude [mag]
Frequency [d^{-1}]
10^{-1}
10^{0}
10^{1}
10^{-3}
10^{-4}
10^{-5}
10^{-6}

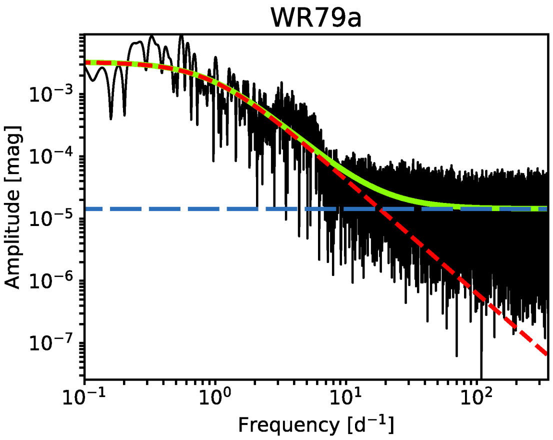
WR79a
Amplitude [mag]
10^-3
10^-4
10^-5
10^-6
10^-7
10^-1
10^0
10^1
10^2
Frequency [d^-1]

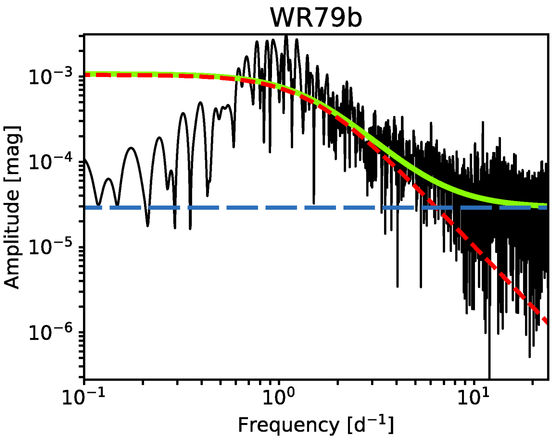
WR79b
Amplitude [mag]
10^-3
10^-4
10^-5
10^-6
10^-1
10^0
10^1
Frequency [d^-1]

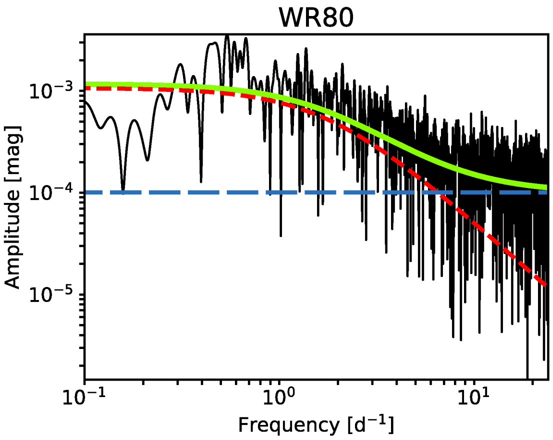
WR80
Amplitude [mag]
10^-3
10^-4
10^-5
10^-1
10^0
10^1
Frequency [d^-1]

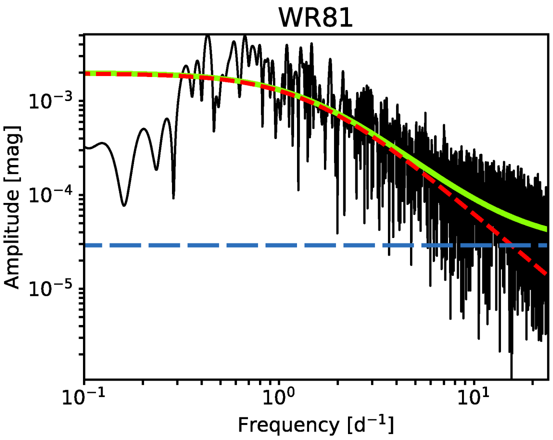
WR81
Amplitude [mag]
10^-3
10^-4
10^-5
10^-1
10^0
10^1
Frequency [d^-1]

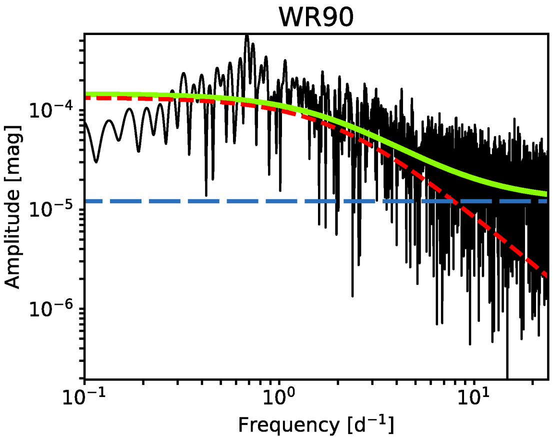
WR90
Amplitude [mag]
10^-4
10^-5
10^-6
10^-1
10^0
10^1
Frequency [d^-1]

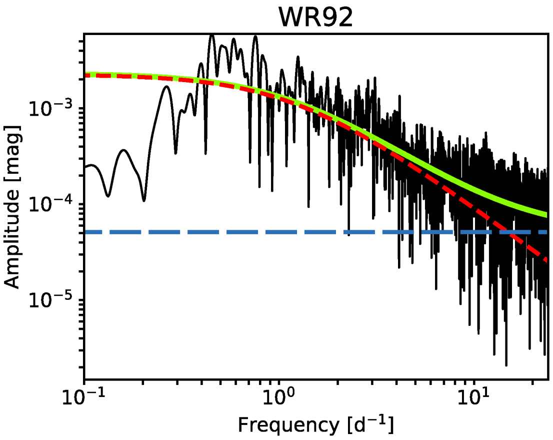
WR92
Amplitude [mag]
10^-3
10^-4
10^-5
10^-1
10^0
10^1
Frequency [d^-1]

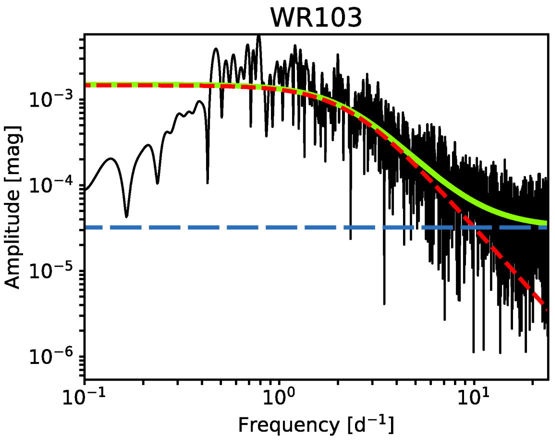
WR103
Amplitude [mag]
Frequency [d^{-1}]
10^{-3}
10^{-4}
10^{-5}
10^{-6}
10^{-1}
10^{0}
10^{1}

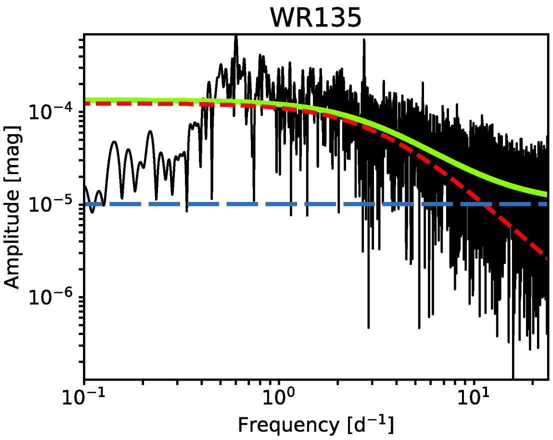
WR135
Amplitude [mag]
Frequency [d^{-1}]
10^{-4}
10^{-5}
10^{-6}
10^{-1}
10^{0}
10^{1}

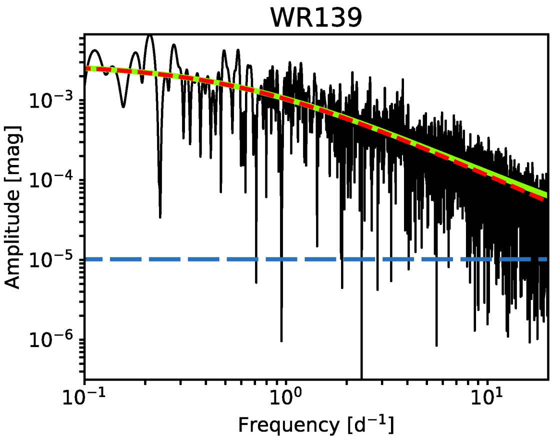
WR139
Amplitude [mag]
Frequency [d^{-1}]
10^{-3}
10^{-4}
10^{-5}
10^{-6}
10^{-1}
10^{0}
10^{1}

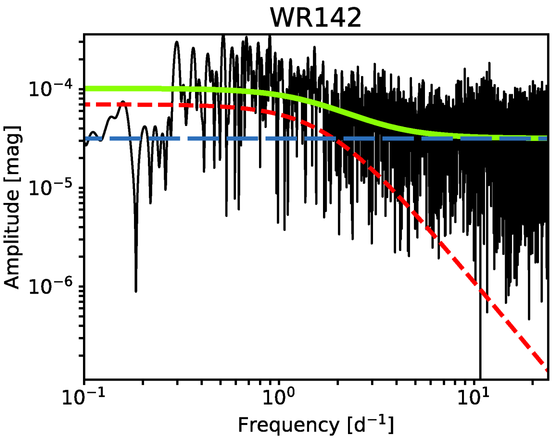
WR142
Amplitude [mag]
Frequency [d^{-1}]
10^{-4}
10^{-5}
10^{-6}
10^{-1}
10^{0}
10^{1}

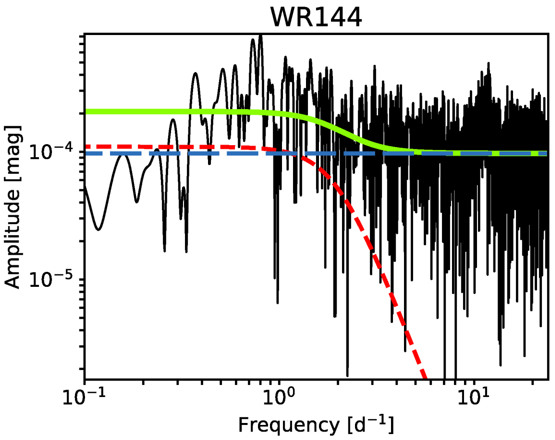
WR144
Amplitude [mag]
Frequency [d^{-1}]
10^{-4}
10^{-5}
10^{-1}
10^{0}
10^{1}

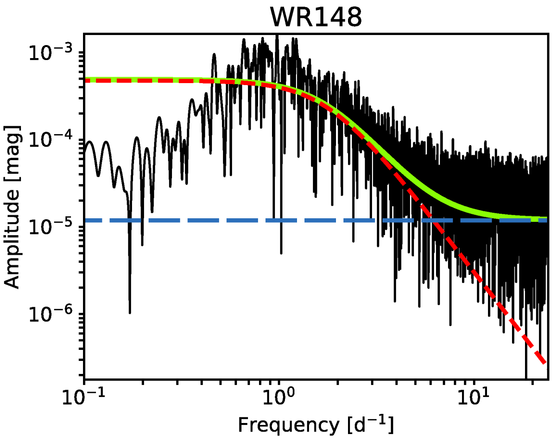
WR148
Amplitude [mag]
Frequency [d^{-1}]
10^{-3}
10^{-4}
10^{-5}
10^{-6}
10^{-1}
10^{0}
10^{1}

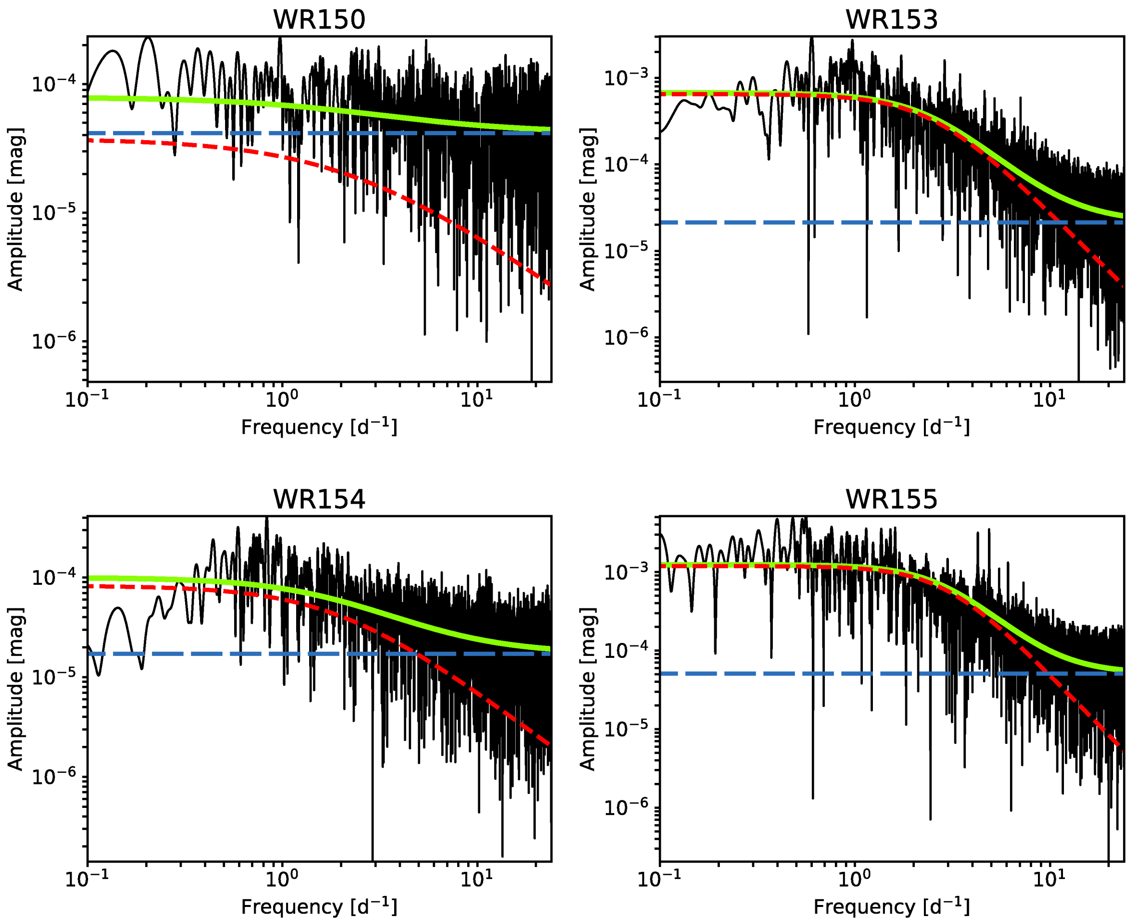
WR150
WR153
WR154
WR155
Amplitude [mag]
Frequency [d^{-1}]
10^{-1}
10^{0}
10^{1}
10^{-3}
10^{-4}
10^{-5}
10^{-6}

BRITE

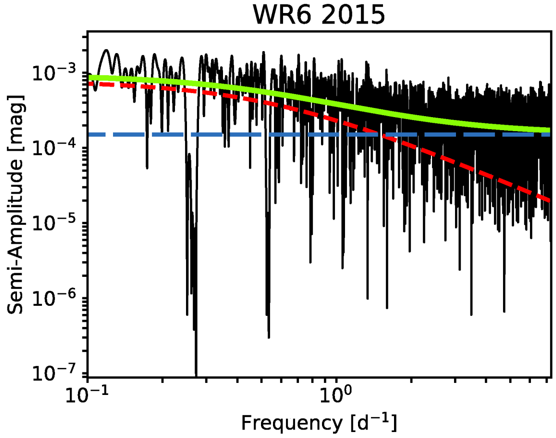
WR6 2015
Semi-Amplitude [mag]
10^{-3}
10^{-4}
10^{-5}
10^{-6}
10^{-7}
10^{-1}
10^{0}
Frequency [d^{-1}]

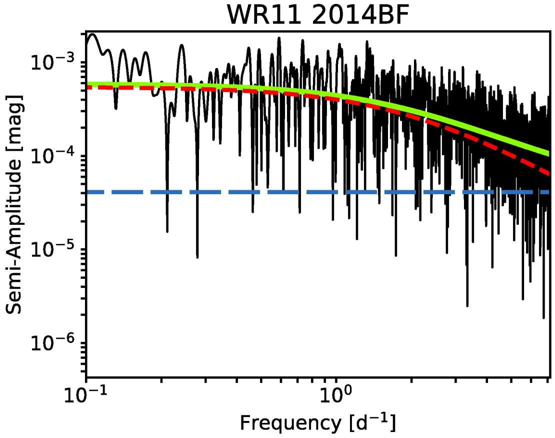
WR11 2014BF
Semi-Amplitude [mag]
10^{-3}
10^{-4}
10^{-5}
10^{-6}
10^{-1}
10^{0}
Frequency [d^{-1}]

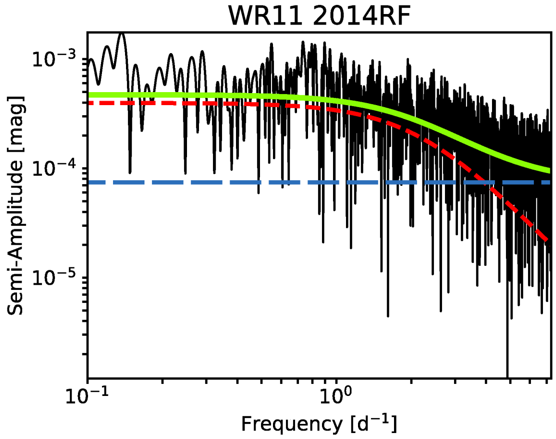
WR11 2014RF
Semi-Amplitude [mag]
10^{-3}
10^{-4}
10^{-5}
10^{-1}
10^{0}
Frequency [d^{-1}]

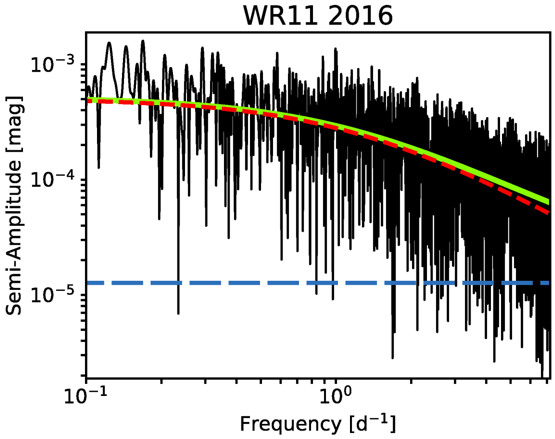
WR11 2016
Semi-Amplitude [mag]
10^{-3}
10^{-4}
10^{-5}
10^{-1}
10^{0}
Frequency [d^{-1}]

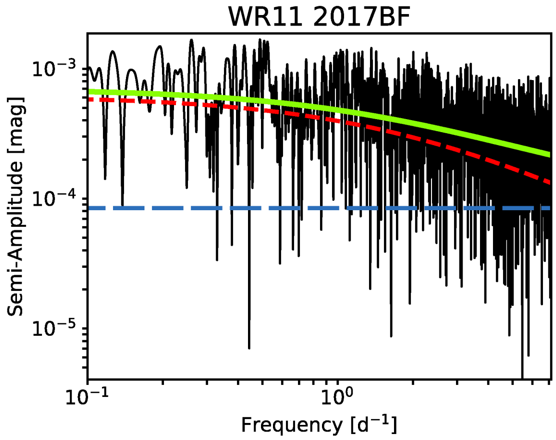
WR11 2017BF
Semi-Amplitude [mag]
10^{-3}
10^{-4}
10^{-5}
10^{-1}
10^{0}
Frequency [d^{-1}]

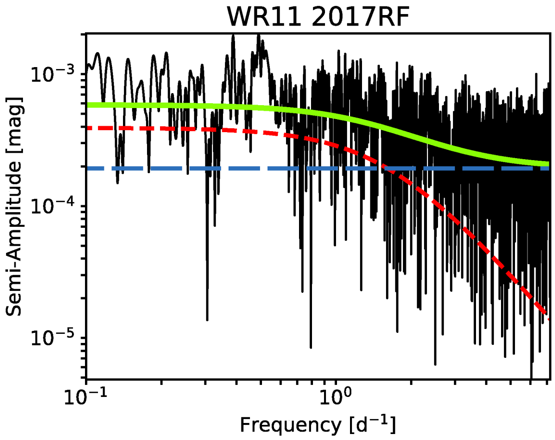
WR11 2017RF
Semi-Amplitude [mag]
10^{-3}
10^{-4}
10^{-5}
10^{-1}
10^{0}
Frequency [d^{-1}]

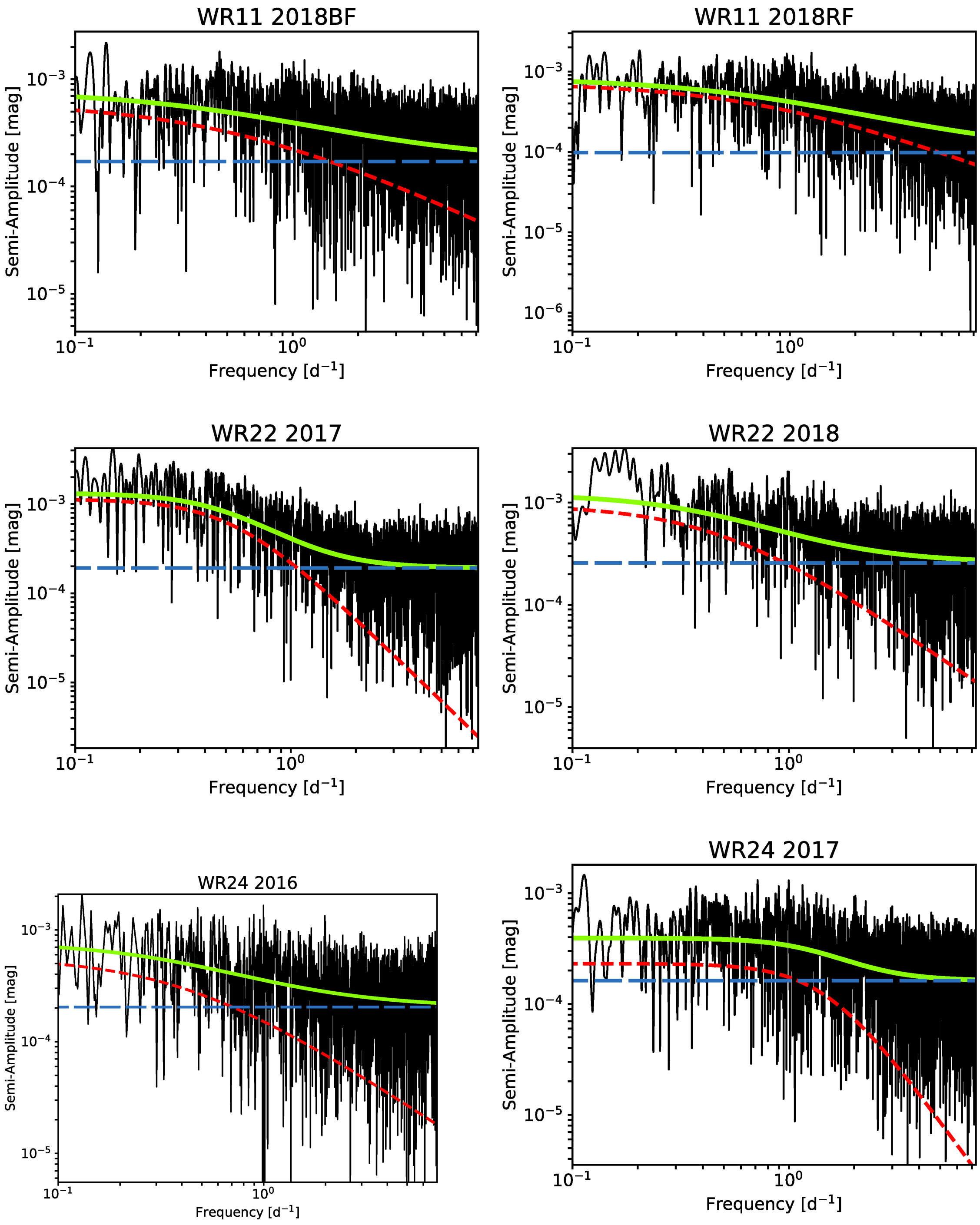
WR11 2018BF
WR11 2018RF
WR22 2017
WR22 2018
WR24 2016
WR24 2017
Semi-Amplitude [mag]
Frequency [d^{-1}]
10^{-6}
10^{-5}
10^{-4}
10^{-3}
10^{-1}
10^{0}

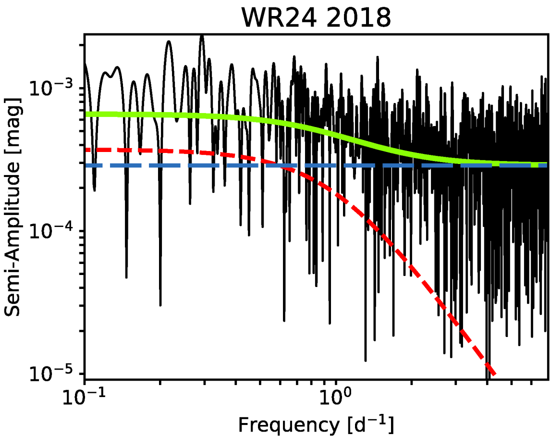
WR24 2018
Semi-Amplitude [mag]
10^{-3}
10^{-4}
10^{-5}
10^{-1}
10^{0}
Frequency [d^{-1}]

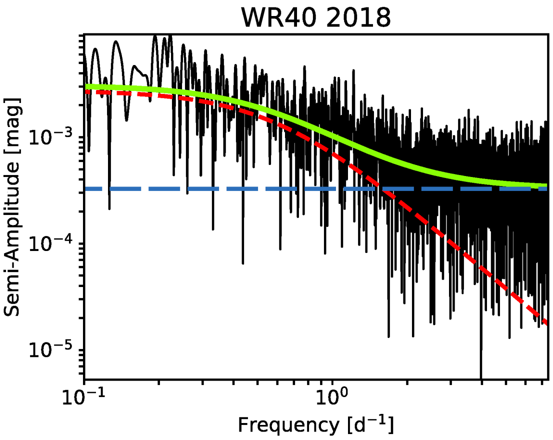
WR40 2018
Semi-Amplitude [mag]
10^{-3}
10^{-4}
10^{-5}
10^{-1}
10^{0}
Frequency [d^{-1}]

MOST

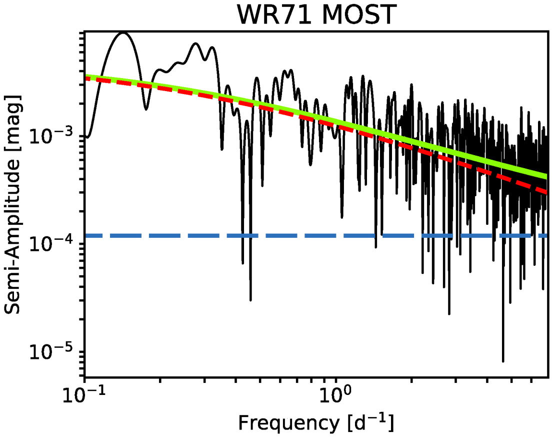
WR71 MOST
Semi-Amplitude [mag]
10^-3
10^-4
10^-5
10^-1
10^0
Frequency [d^-1]

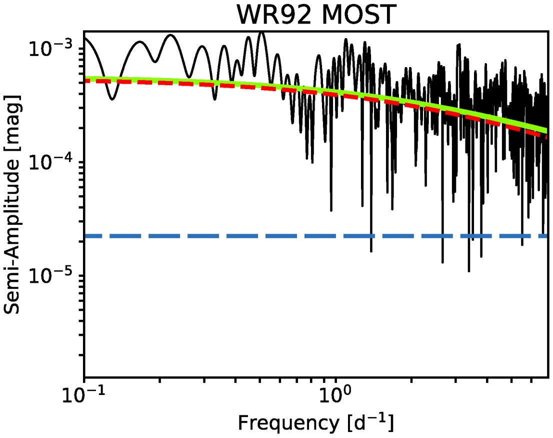
WR92 MOST
Semi-Amplitude [mag]
10^-3
10^-4
10^-5
10^-1
10^0
Frequency [d^-1]

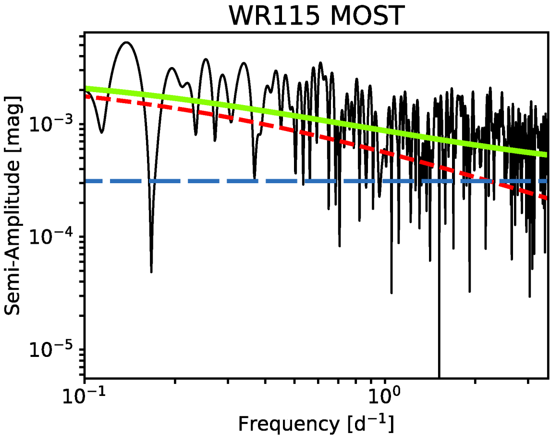
WR115 MOST
Semi-Amplitude [mag]
10^-3
10^-4
10^-5
10^-1
10^0
Frequency [d^-1]

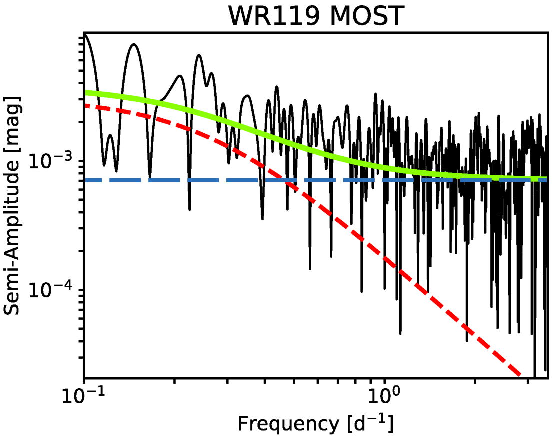
WR119 MOST
Semi-Amplitude [mag]
10^-3
10^-4
10^-1
10^0
Frequency [d^-1]

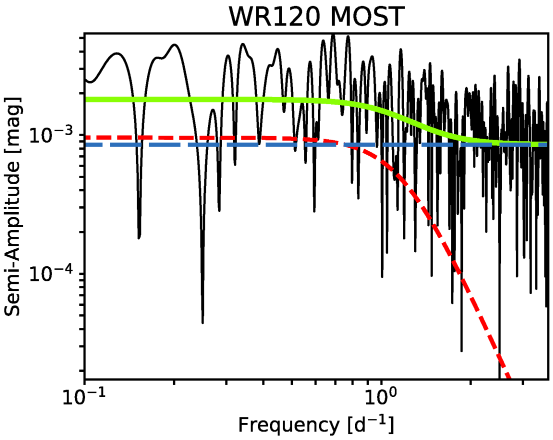
WR120 MOST
Semi-Amplitude [mag]
10^-3
10^-4
10^-1
10^0
Frequency [d^-1]

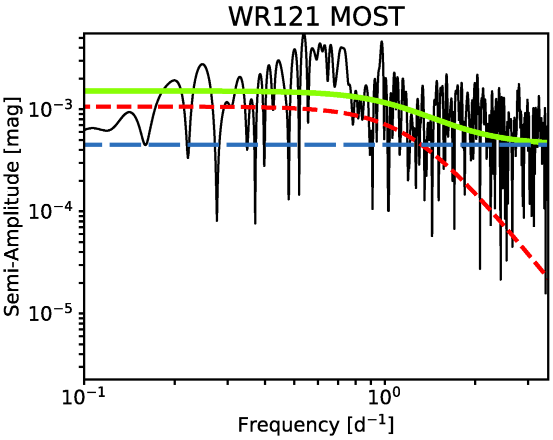
WR121 MOST
Semi-Amplitude [mag]
10^-3
10^-4
10^-5
10^-1
10^0
Frequency [d^-1]

Annexe C : Analyses en ondelettes

Le cône d'influence (COI) des ondelettes apparaît en noir dans la section qui suit. Toutes ces analyses ont été produites en utilisant une fonction mère dérivée de gaussienne, aussi appelée « chapeau mexicain ».

TESS

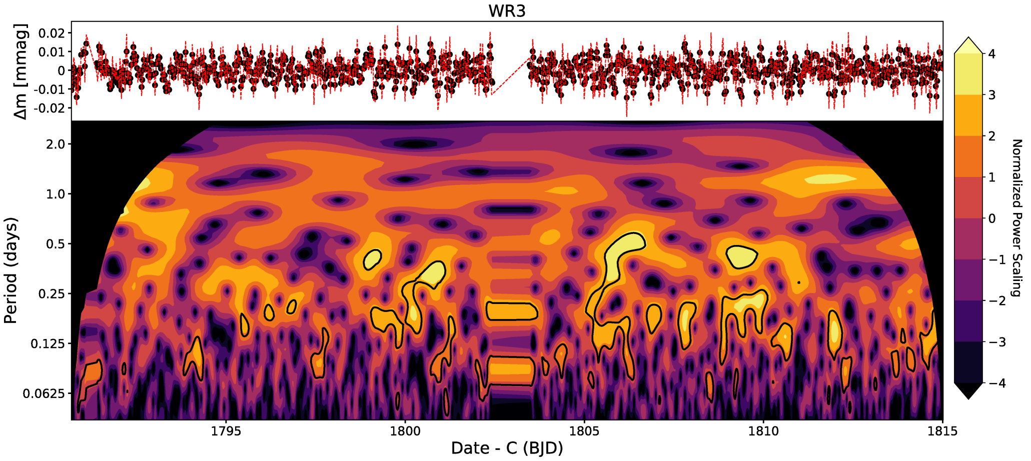

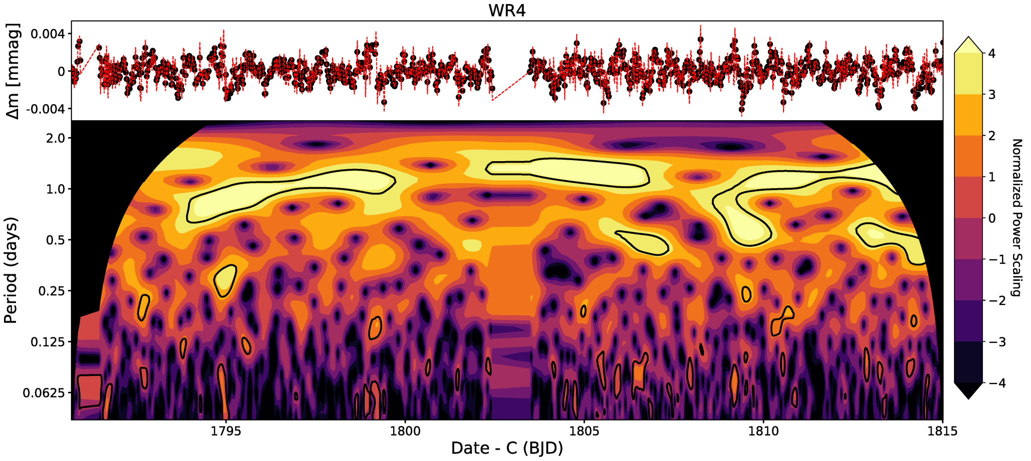

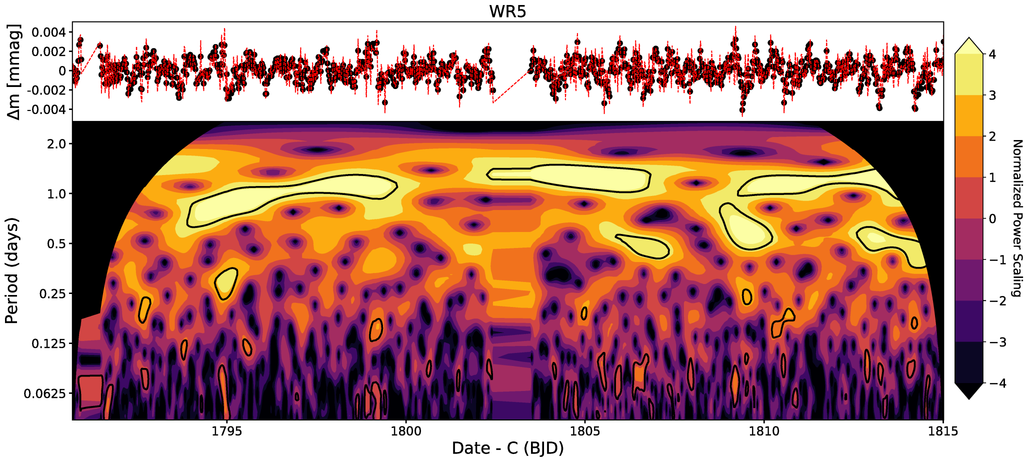
WR5
Δm [mmag]
0.004
0.002
0
-0.002
-0.004
Period (days)
2.0
1.0
0.5
0.25
0.125
0.0625
1795
1800
1805
1810
1815
Date - C (BJD)
Normalized Power Scaling
4
3
2
1
0
−1
−2
−3
−4

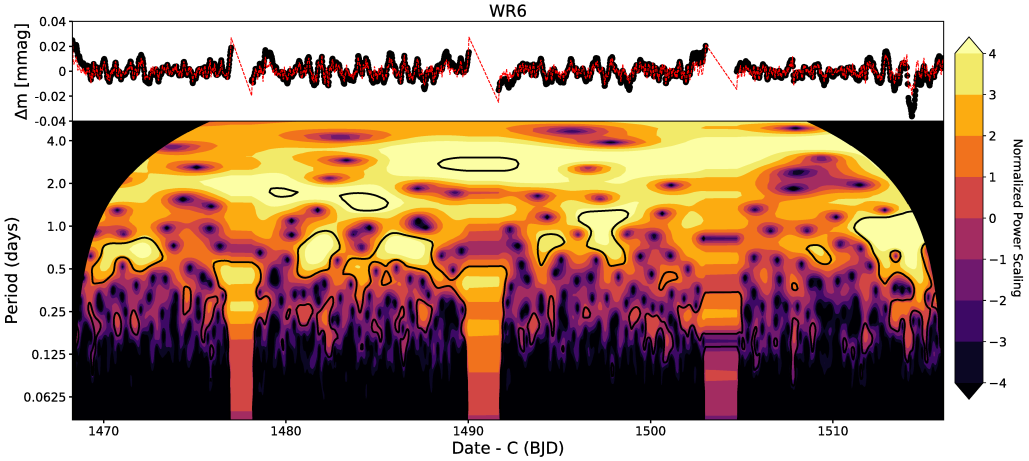
WR6
Δm [mmag]
0.04
0.02
0
-0.02
-0.04
Period (days)
4.0
2.0
1.0
0.5
0.25
0.125
0.0625
1470
1480
1490
1500
1510
Date - C (BJD)
Normalized Power Scaling
4
3
2
1
0
−1
−2
−3
−4

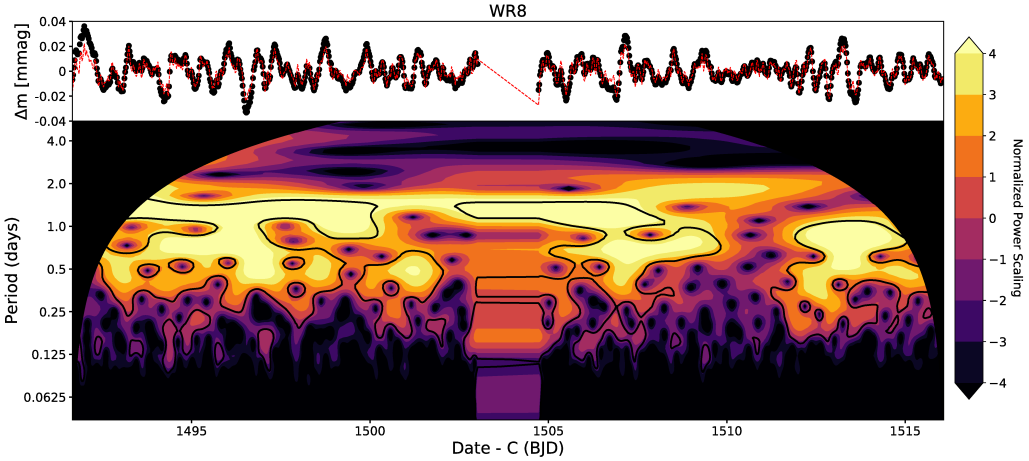
WR8
Δm [mmag]
0.04
0.02
0
-0.02
-0.04
Period (days)
4.0
2.0
1.0
0.5
0.25
0.125
0.0625
1495
1500
1505
1510
1515
Date - C (BJD)
Normalized Power Scaling
4
3
2
1
0
−1
−2
−3
−4

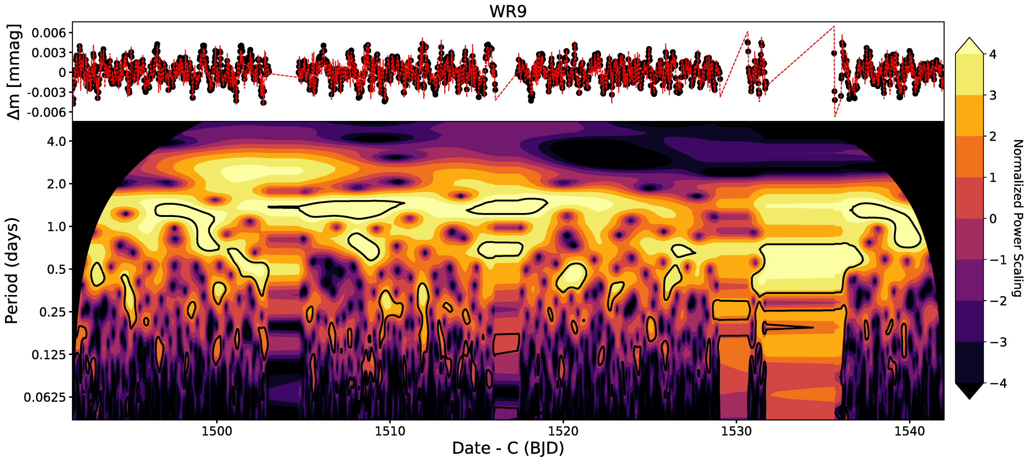
WR9
Δm [mmag]
0.006
0.003
0
-0.003
-0.006
Period (days)
4.0
2.0
1.0
0.5
0.25
0.125
0.0625
1500
1510
1520
1530
1540
Date - C (BJD)
Normalized Power Scaling
4
3
2
1
0
−1
−2
−3
−4

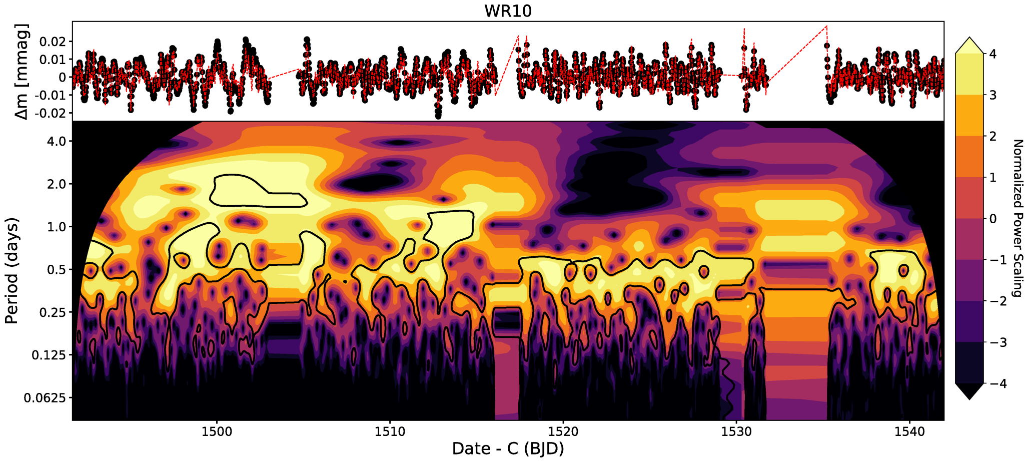
WR10
Δm [mmag]
0.02
0.01
0
-0.01
-0.02
Period (days)
4.0
2.0
1.0
0.5
0.25
0.125
0.0625
1500
1510
1520
1530
1540
Date - C (BJD)
Normalized Power Scaling
4
3
2
1
0
−1
−2
−3
−4

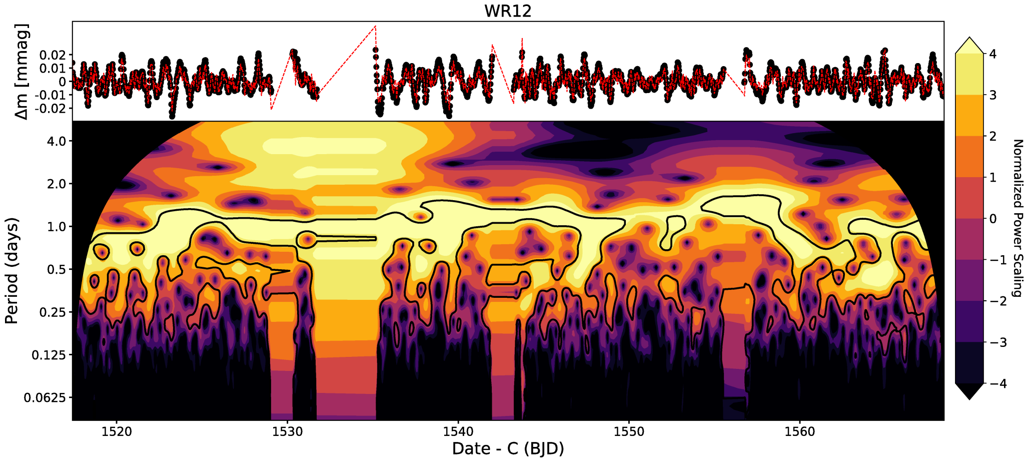
WR12
Δm [mmag]
0.02
0.01
0
-0.01
-0.02
Period (days)
4.0
2.0
1.0
0.5
0.25
0.125
0.0625
1520
1530
1540
1550
1560
Date - C (BJD)
Normalized Power Scaling
4
3
2
1
0
−1
−2
−3
−4

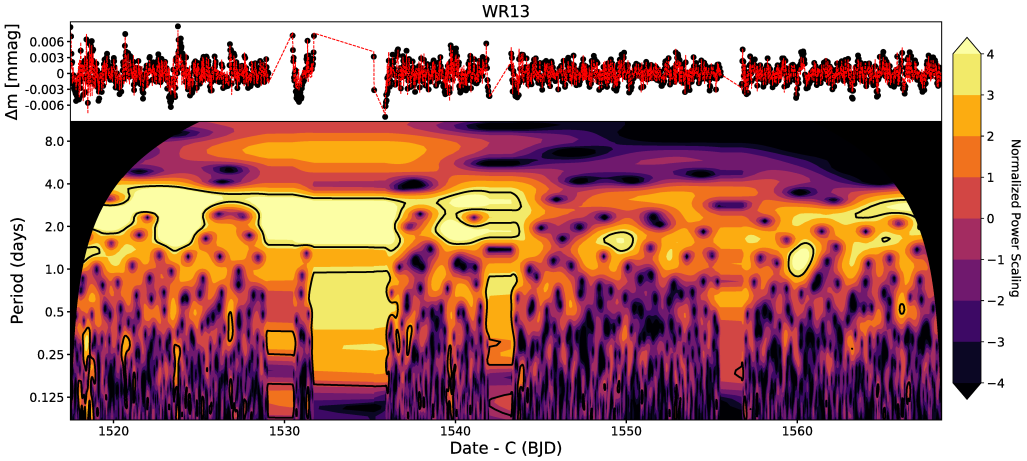
WR13
Δm [mmag]
0.006
0.003
0
-0.003
-0.006
Period (days)
8.0
4.0
2.0
1.0
0.5
0.25
0.125
1520
1530
1540
1550
1560
Date - C (BJD)
Normalized Power Scaling
4
3
2
1
0
−1
−2
−3
−4

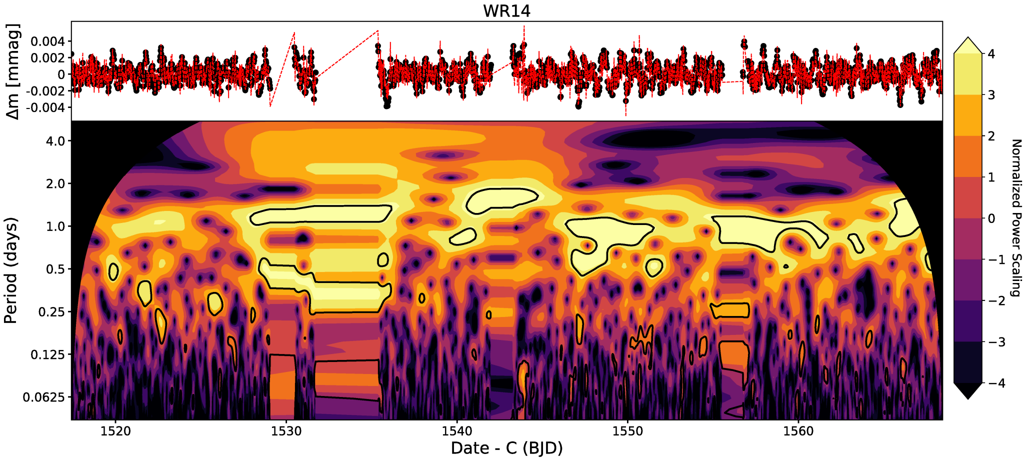
WR14
Δm [mmag]
0.004
0.002
0
-0.002
-0.004
Period (days)
4.0
2.0
1.0
0.5
0.25
0.125
0.0625
1520
1530
1540
1550
1560
Date - C (BJD)
Normalized Power Scaling
4
3
2
1
0
−1
−2
−3
−4

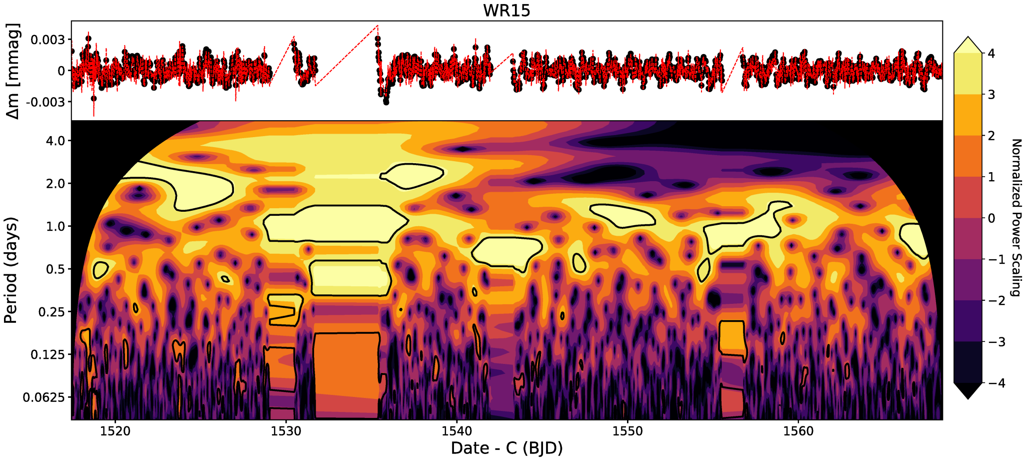
WR15
Δm [mmag]
0.003
0
-0.003
Period (days)
4.0
2.0
1.0
0.5
0.25
0.125
0.0625
1520
1530
1540
1550
1560
Date - C (BJD)
Normalized Power Scaling
4
3
2
1
0
−1
−2
−3
−4

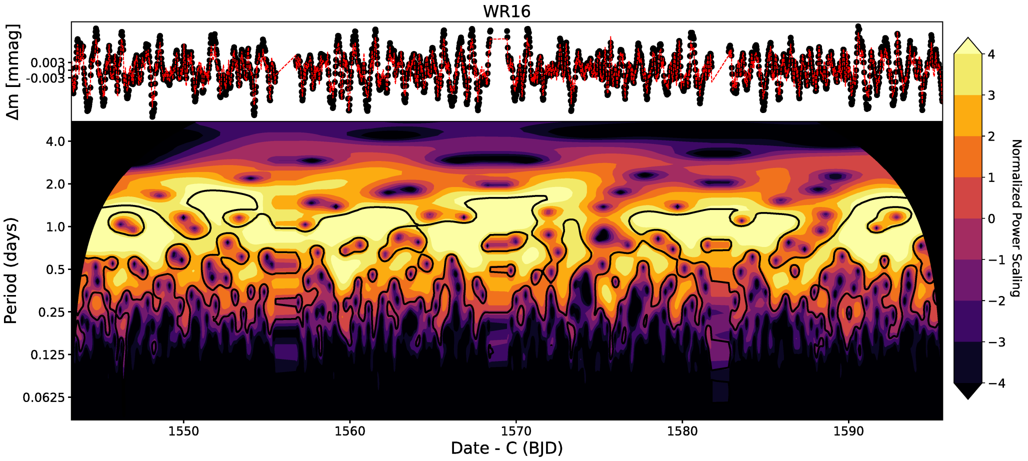
WR16
Δm [mmag]
0.003
-0.003
Period (days)
4.0
2.0
1.0
0.5
0.25
0.125
0.0625
1550
1560
1570
1580
1590
Date - C (BJD)
Normalized Power Scaling
4
3
2
1
0
−1
−2
−3
−4

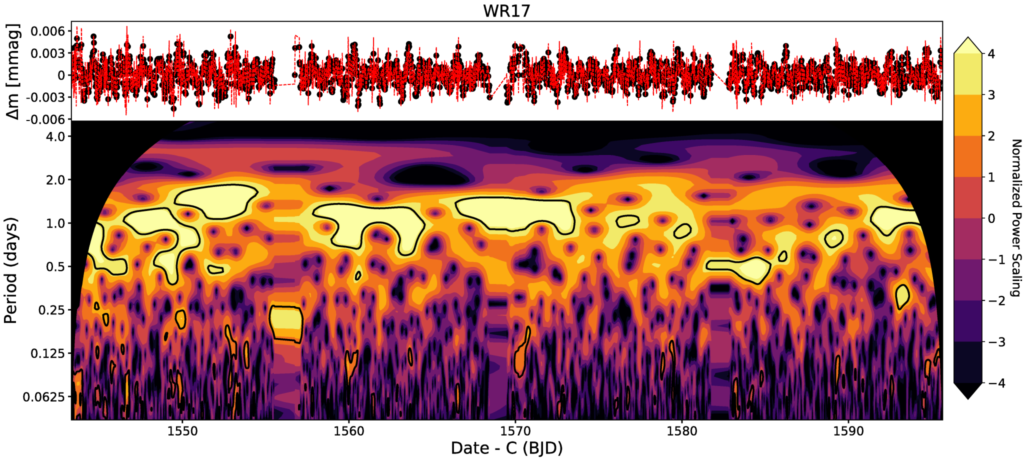
WR17
Δm [mmag]
0.006
0.003
0
-0.003
-0.006
Period (days)
4.0
2.0
1.0
0.5
0.25
0.125
0.0625
1550
1560
1570
1580
1590
Date - C (BJD)
Normalized Power Scaling
4
3
2
1
0
−1
−2
−3
−4

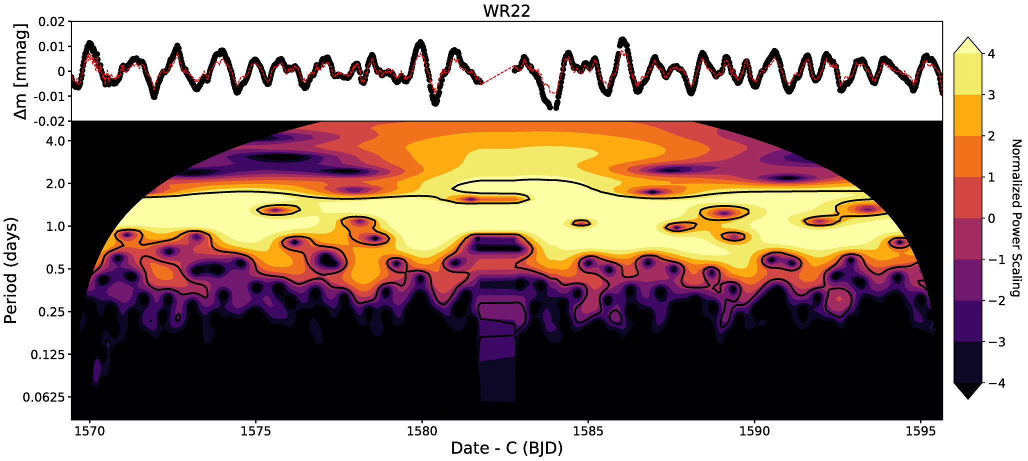
WR22
Δm [mmag]
0.02
0.01
0
-0.01
-0.02
Period (days)
4.0
2.0
1.0
0.5
0.25
0.125
0.0625
1570
1575
1580
1585
1590
1595
Date - C (BJD)
Normalized Power Scaling
4
3
2
1
0
−1
−2
−3
−4

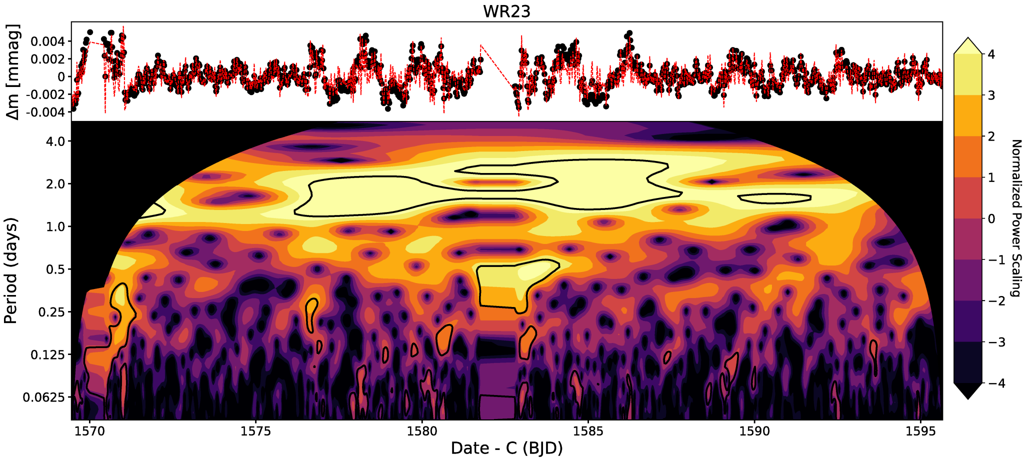
WR23

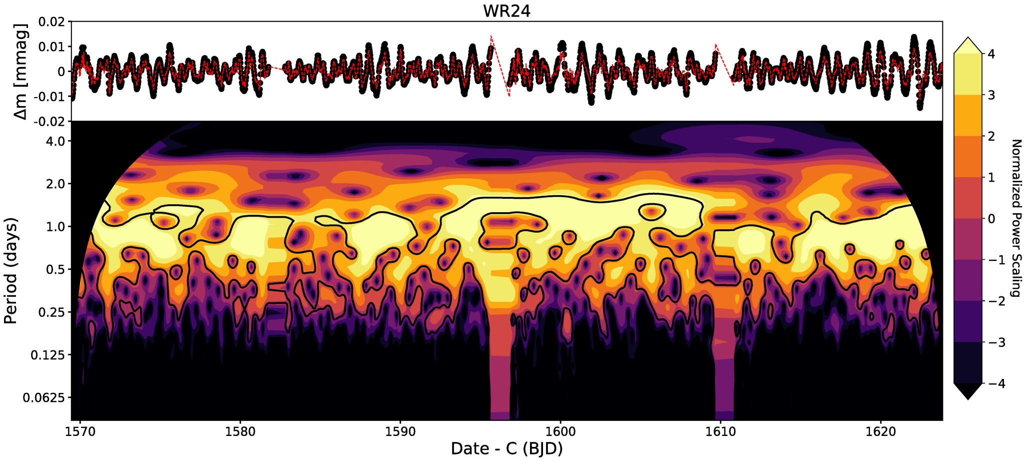
WR24

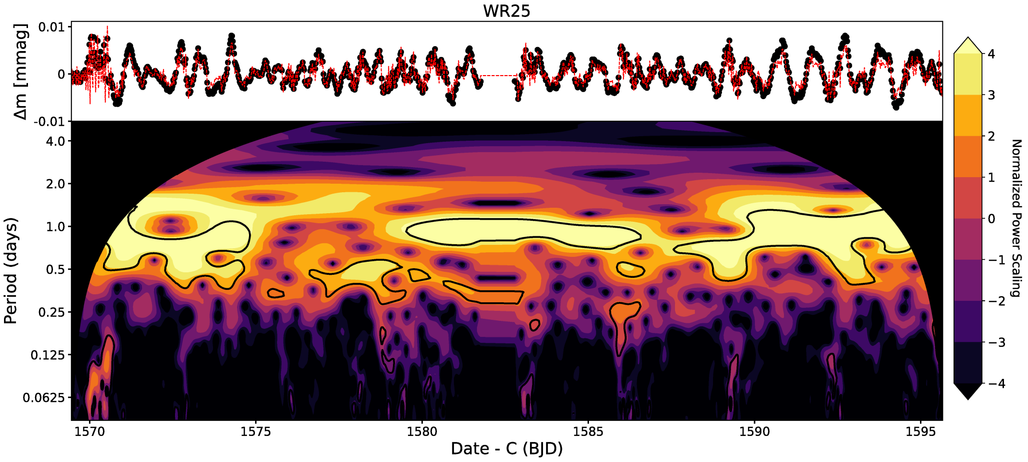
WR25

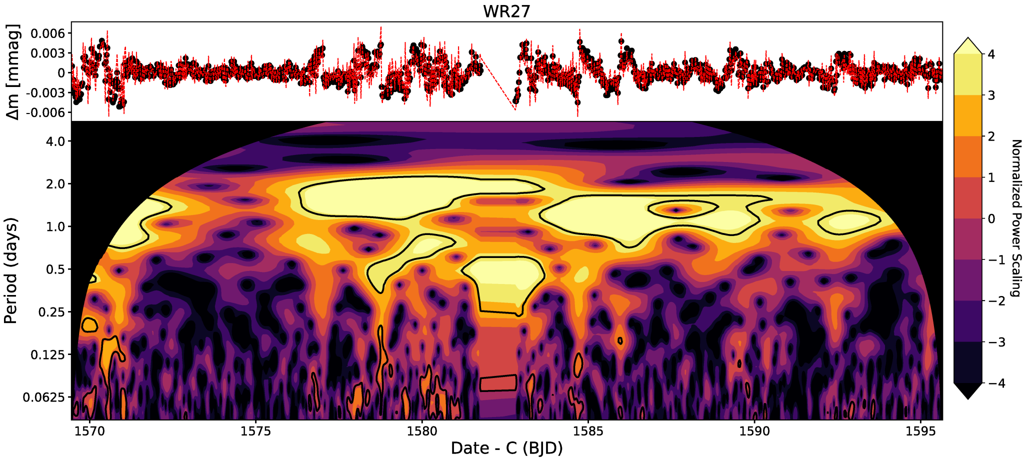
WR27

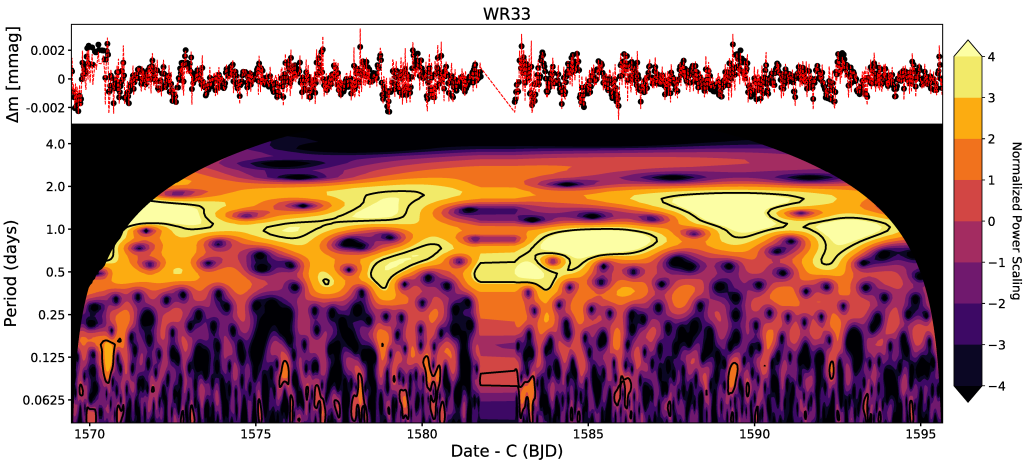
WR33

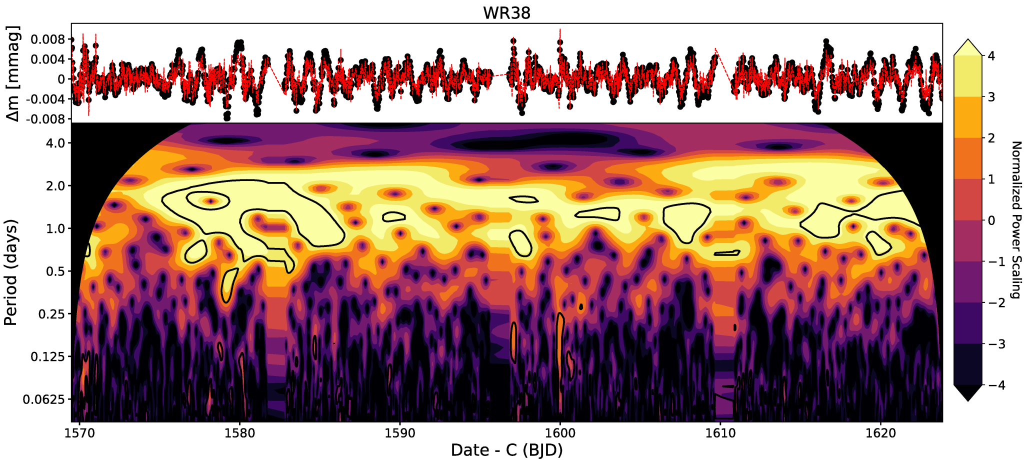
WR38

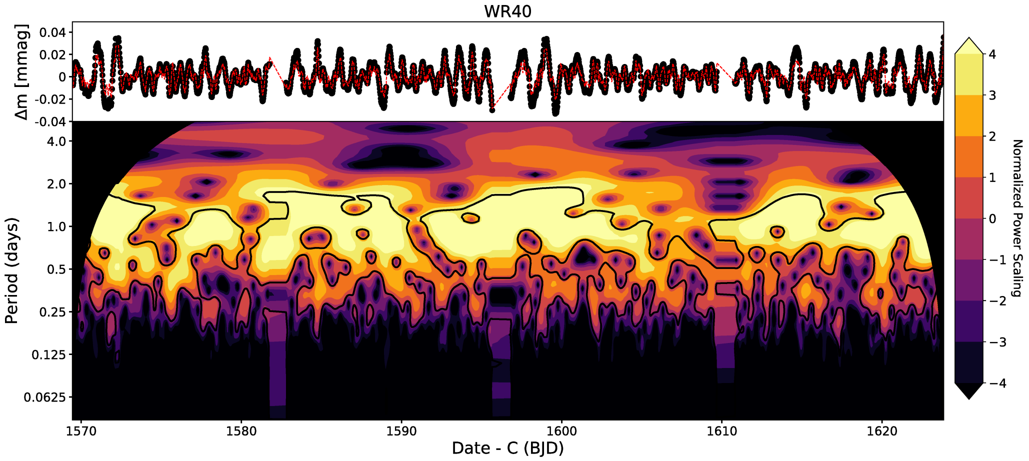
WR40

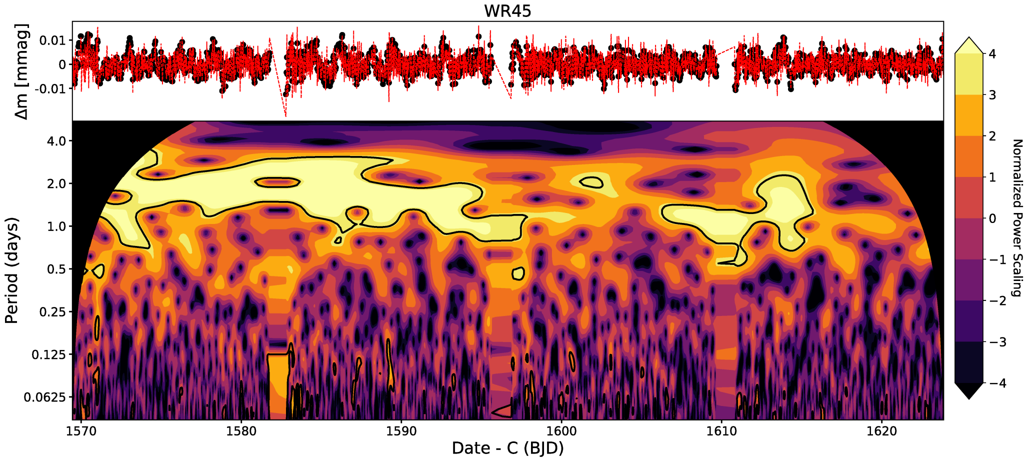
WR45

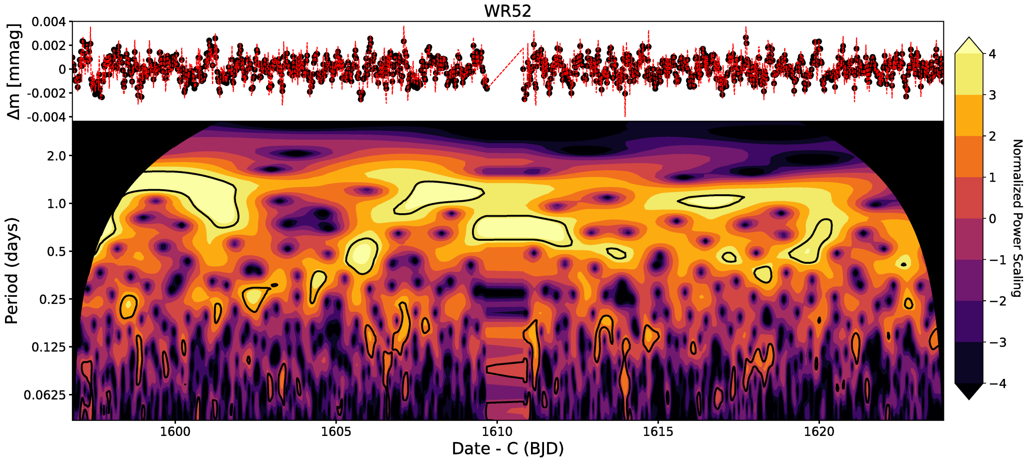
WR52

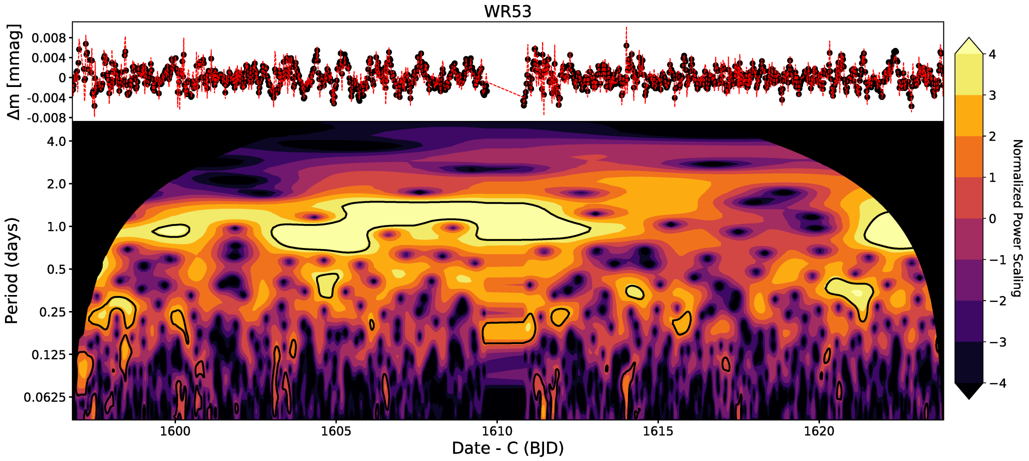
WR53

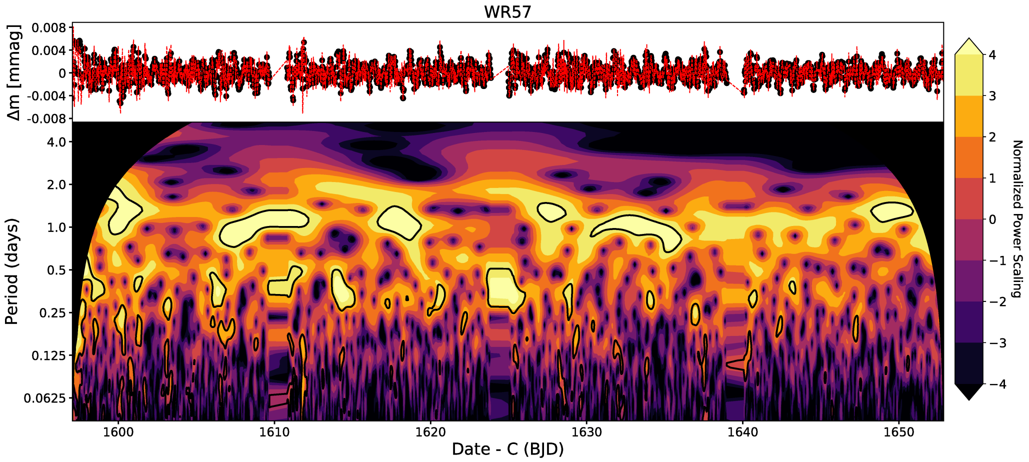
WR57

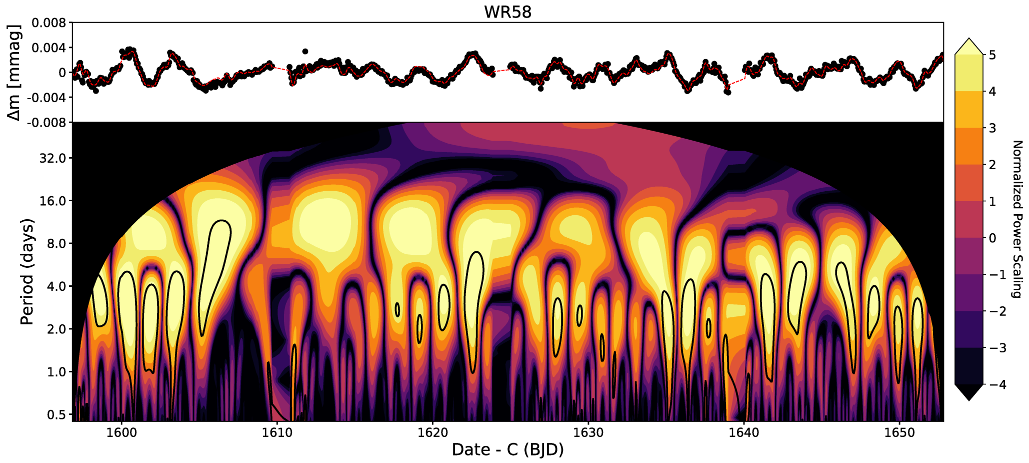
WR58

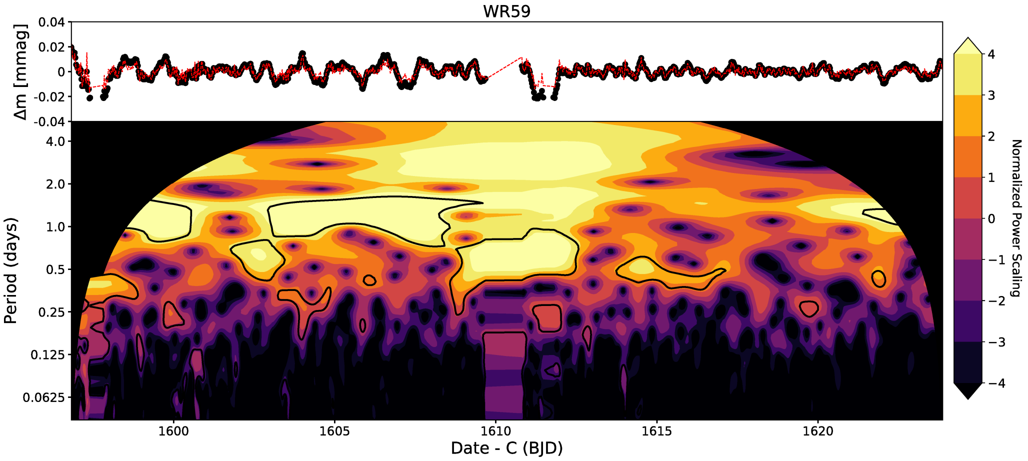
WR59
Δm [mmag]
0.04
0.02
0
-0.02
-0.04
Period (days)
4.0
2.0
1.0
0.5
0.25
0.125
0.0625
1600
1605
1610
1615
1620
Date - C (BJD)
Normalized Power Scaling
4
3
2
1
0
−1
−2
−3
−4

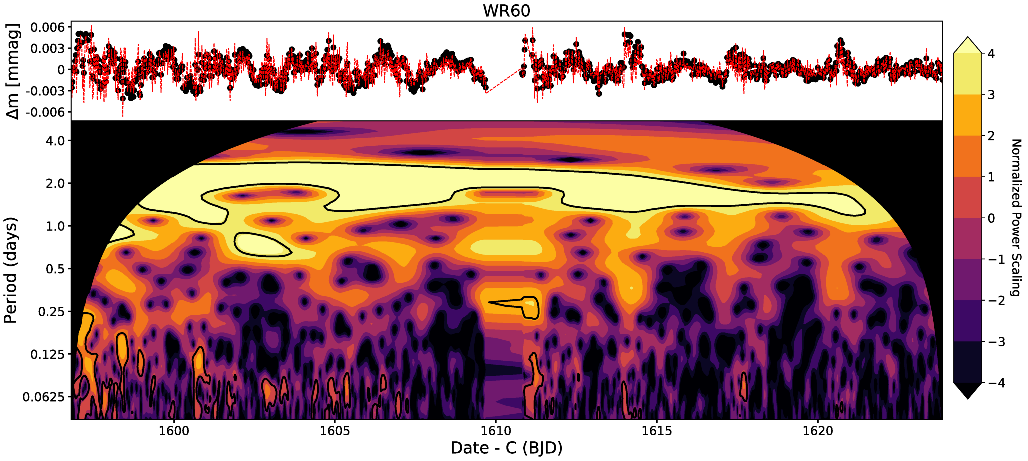
WR60
Δm [mmag]
0.006
0.003
0
-0.003
-0.006
Period (days)
4.0
2.0
1.0
0.5
0.25
0.125
0.0625
1600
1605
1610
1615
1620
Date - C (BJD)
Normalized Power Scaling
4
3
2
1
0
−1
−2
−3
−4

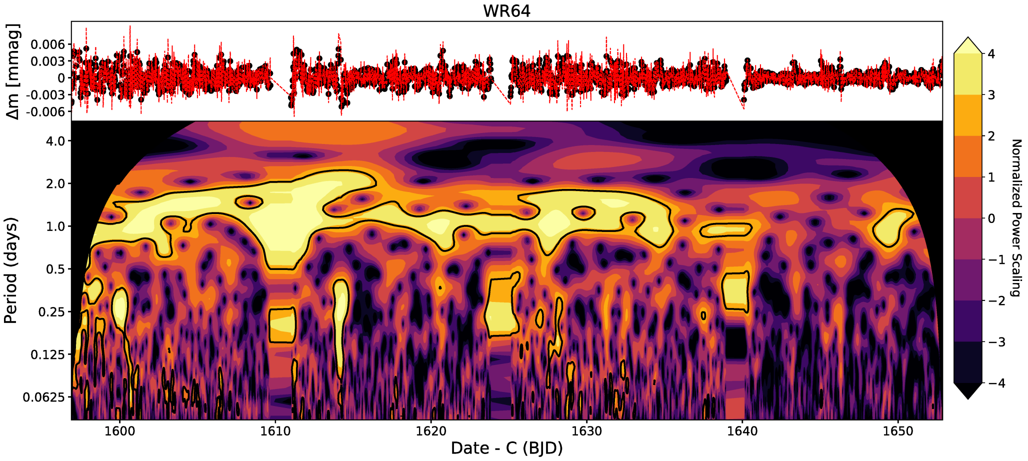
WR64
Δm [mmag]
0.006
0.003
0
-0.003
-0.006
Period (days)
4.0
2.0
1.0
0.5
0.25
0.125
0.0625
1600
1610
1620
1630
1640
1650
Date - C (BJD)
Normalized Power Scaling
4
3
2
1
0
−1
−2
−3
−4

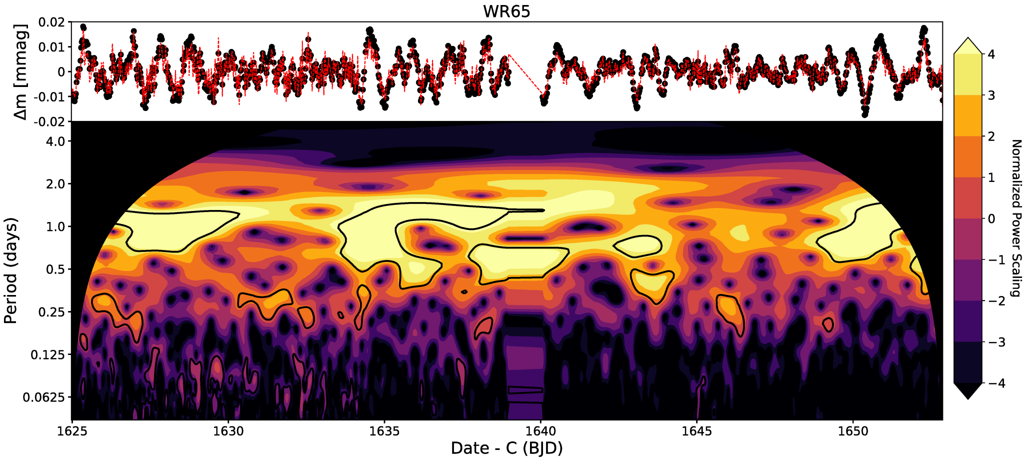
WR65
Δm [mmag]
0.02
0.01
0
-0.01
-0.02
Period (days)
4.0
2.0
1.0
0.5
0.25
0.125
0.0625
1625
1630
1635
1640
1645
1650
Date - C (BJD)
Normalized Power Scaling
4
3
2
1
0
−1
−2
−3
−4

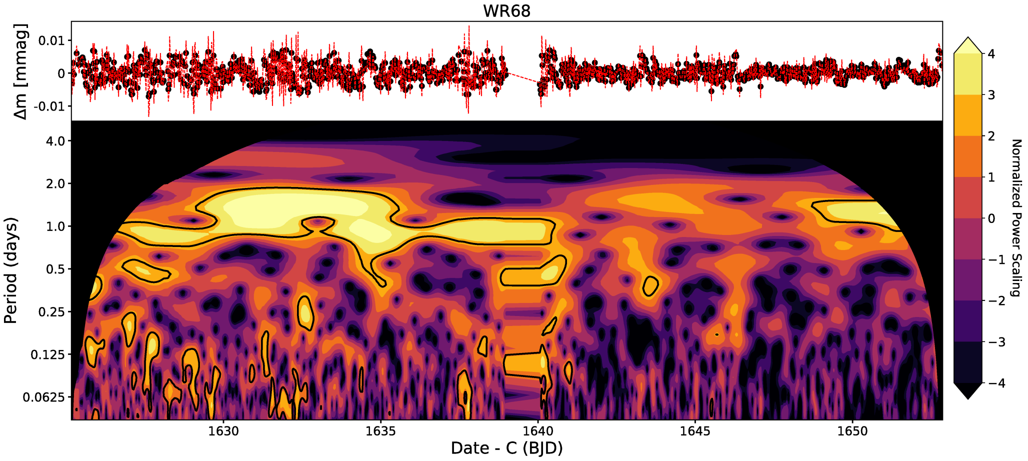
WR68
Δm [mmag]
0.01
0
-0.01
Period (days)
4.0
2.0
1.0
0.5
0.25
0.125
0.0625
1630
1635
1640
1645
1650
Date - C (BJD)
Normalized Power Scaling
4
3
2
1
0
−1
−2
−3
−4

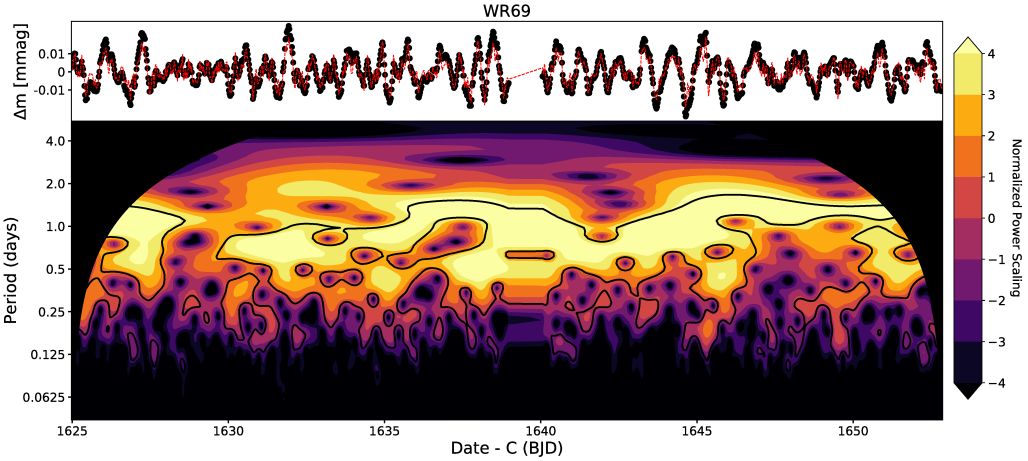
WR69
Δm [mmag]
0.01
0
-0.01
Period (days)
4.0
2.0
1.0
0.5
0.25
0.125
0.0625
1625
1630
1635
1640
1645
1650
Date - C (BJD)
Normalized Power Scaling
4
3
2
1
0
−1
−2
−3
−4

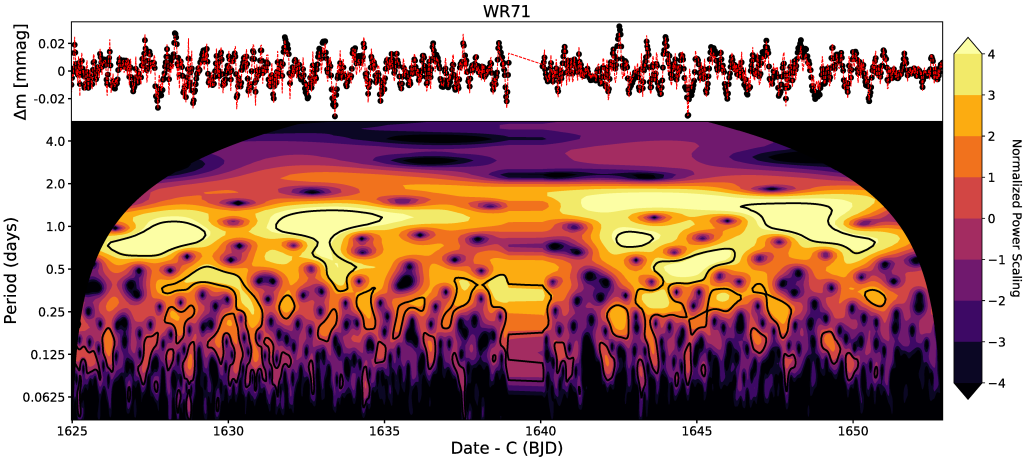
WR71
Δm [mmag]
0.02
0
-0.02
Period (days)
4.0
2.0
1.0
0.5
0.25
0.125
0.0625
1625
1630
1635
1640
1645
1650
Date - C (BJD)
Normalized Power Scaling
4
3
2
1
0
−1
−2
−3
−4

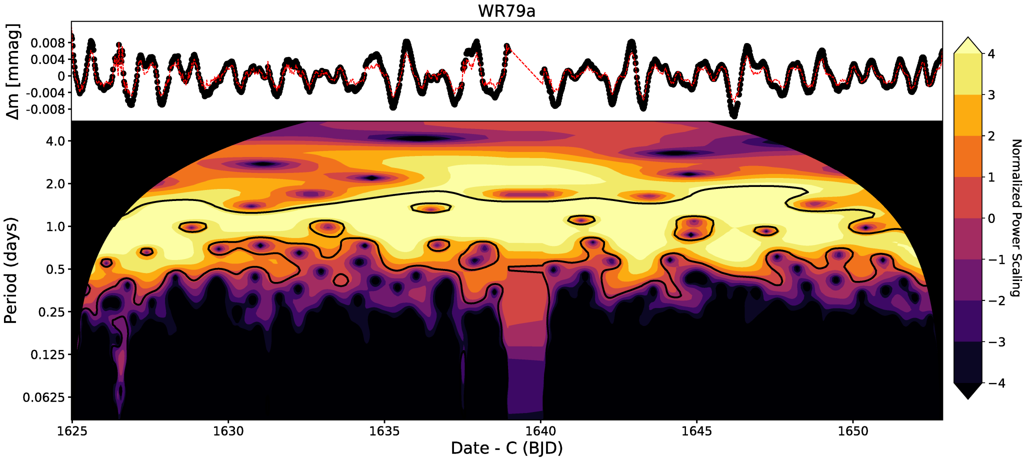
WR79a
Δm [mmag]
0.008
0.004
0
-0.004
-0.008
Period (days)
4.0
2.0
1.0
0.5
0.25
0.125
0.0625
1625
1630
1635
1640
1645
1650
Date - C (BJD)
Normalized Power Scaling
4
3
2
1
0
−1
−2
−3
−4

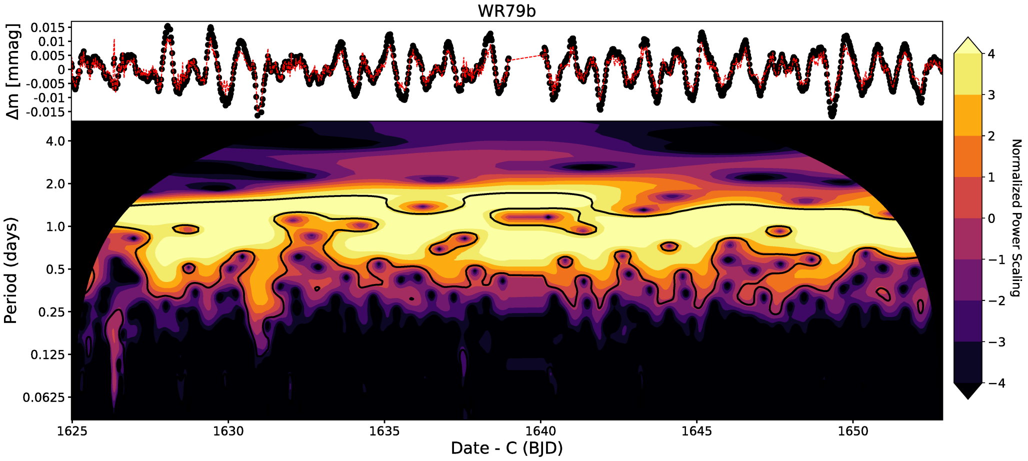
WR79b
Δm [mmag]
0.015
0.01
0.005
0
-0.005
-0.01
-0.015
Period (days)
4.0
2.0
1.0
0.5
0.25
0.125
0.0625
1625
1630
1635
1640
1645
1650
Date - C (BJD)
Normalized Power Scaling
4
3
2
1
0
−1
−2
−3
−4

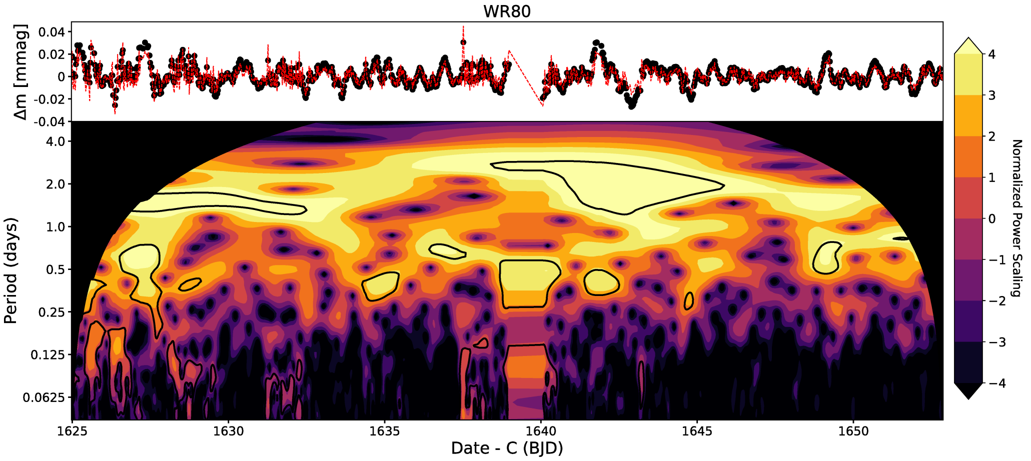

WR80

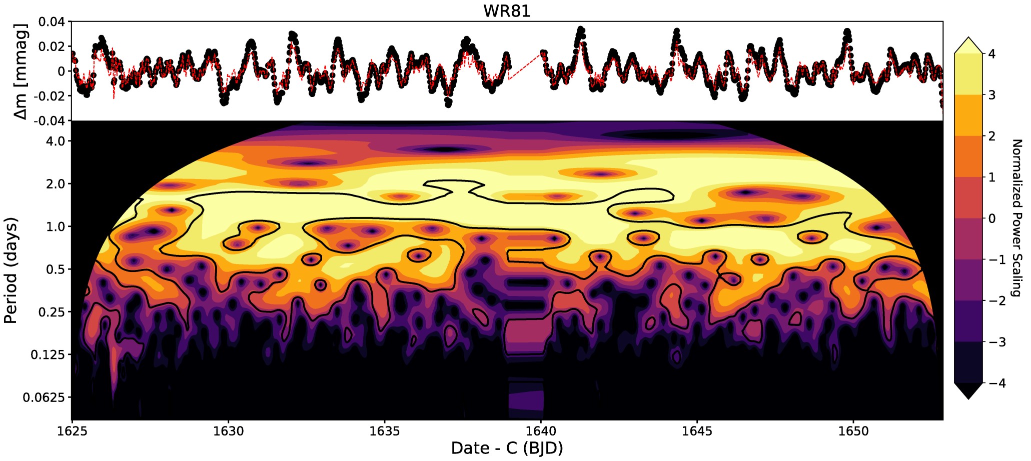

WR81

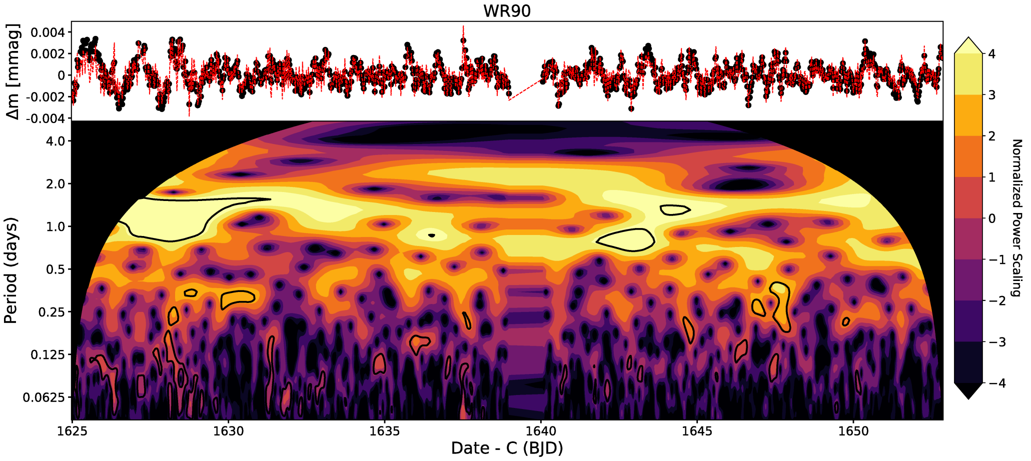

WR90

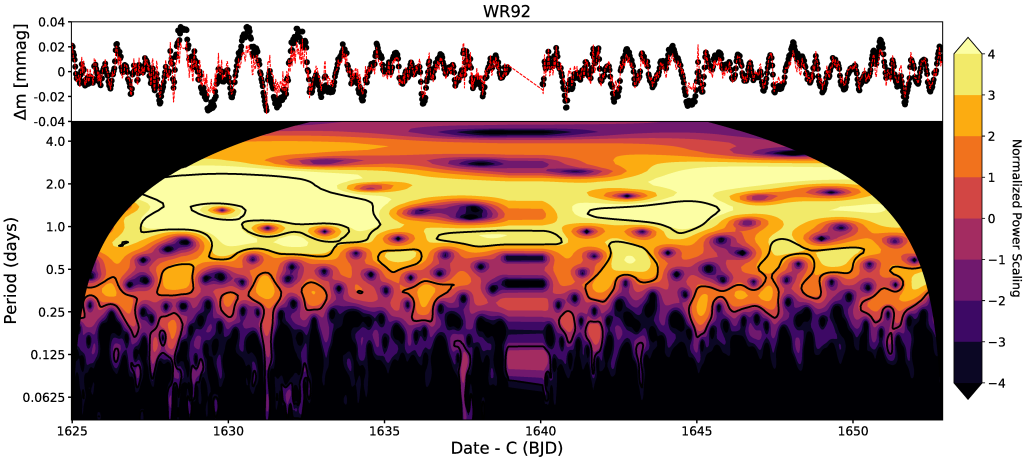
WR92
Δm [mmag]
0.04
0.02
0
-0.02
-0.04
Period (days)
4.0
2.0
1.0
0.5
0.25
0.125
0.0625
1625
1630
1635
1640
1645
1650
Date - C (BJD)
Normalized Power Scaling
4
3
2
1
0
−1
−2
−3
−4

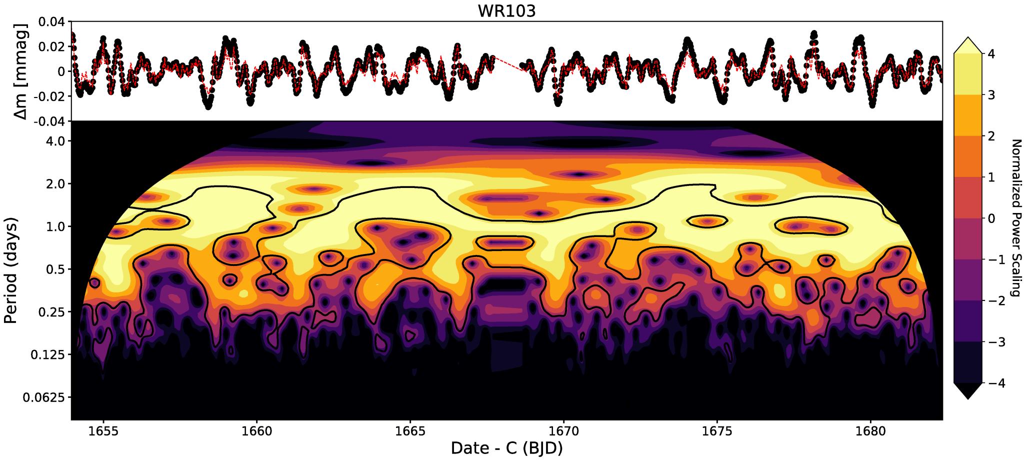
WR103
Δm [mmag]
0.04
0.02
0
-0.02
-0.04
Period (days)
4.0
2.0
1.0
0.5
0.25
0.125
0.0625
1655
1660
1665
1670
1675
1680
Date - C (BJD)
Normalized Power Scaling
4
3
2
1
0
−1
−2
−3
−4

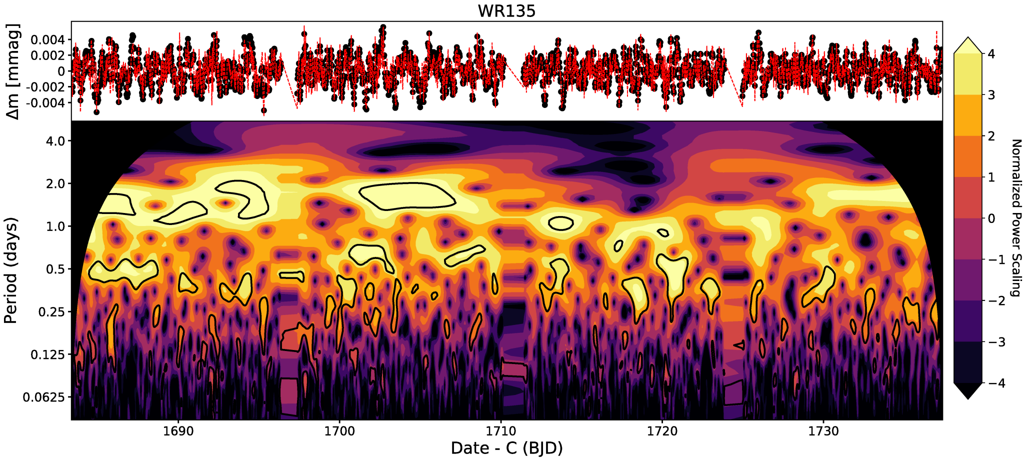
WR135
Δm [mmag]
0.004
0.002
0
-0.002
-0.004
Period (days)
4.0
2.0
1.0
0.5
0.25
0.125
0.0625
1690
1700
1710
1720
1730
Date - C (BJD)
Normalized Power Scaling
4
3
2
1
0
−1
−2
−3
−4

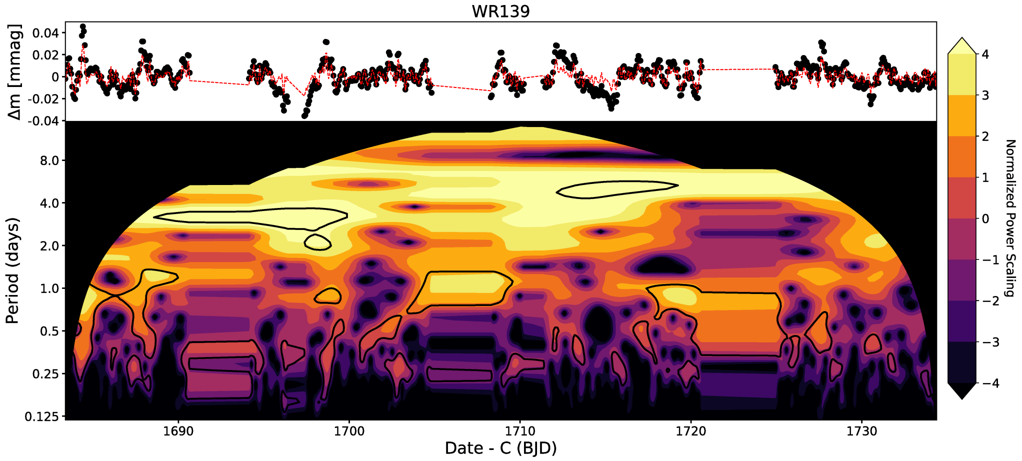
WR139
Δm [mmag]
0.04
0.02
0
-0.02
-0.04
Period (days)
8.0
4.0
2.0
1.0
0.5
0.25
0.125
1690
1700
1710
1720
1730
Date - C (BJD)
4
3
2
1
0
−1
−2
−3
−4
Normalized Power Scaling

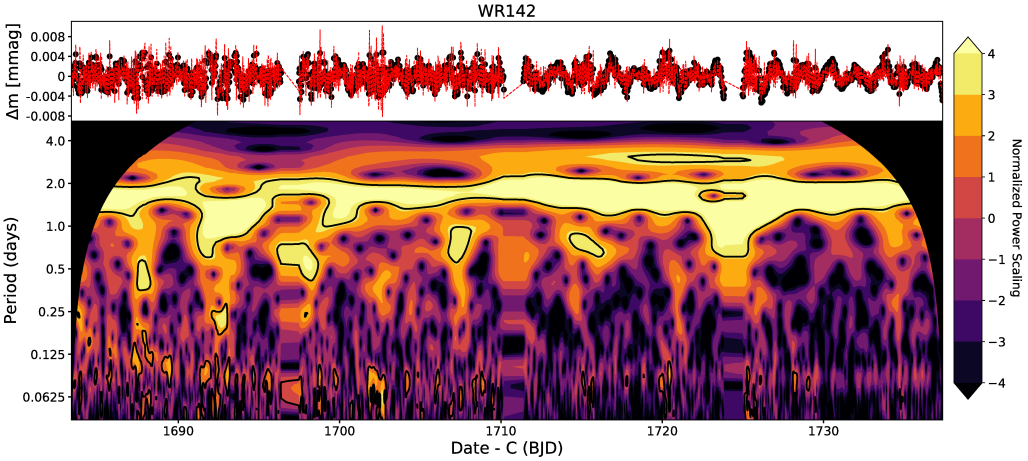
WR142
Δm [mmag]
0.008
0.004
0
-0.004
-0.008
Period (days)
4.0
2.0
1.0
0.5
0.25
0.125
0.0625
1690
1700
1710
1720
1730
Date - C (BJD)
4
3
2
1
0
−1
−2
−3
−4
Normalized Power Scaling

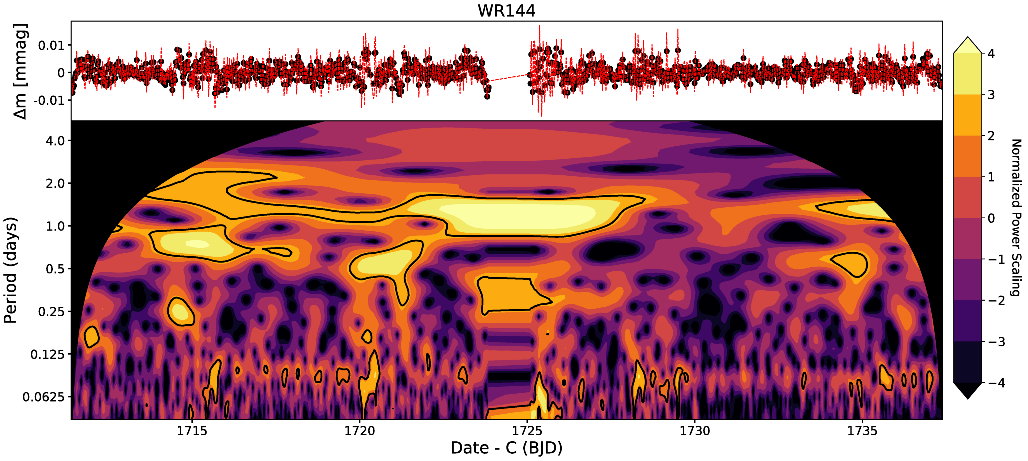
WR144
Δm [mmag]
0.01
0
-0.01
Period (days)
4.0
2.0
1.0
0.5
0.25
0.125
0.0625
1715
1720
1725
1730
1735
Date - C (BJD)
4
3
2
1
0
−1
−2
−3
−4
Normalized Power Scaling

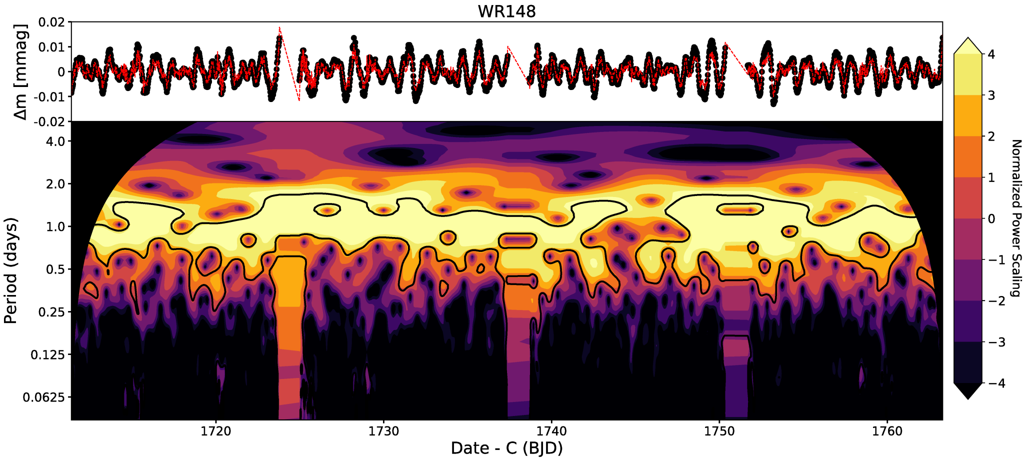
WR148
Δm [mmag]
0.02
0.01
0
-0.01
-0.02
Period (days)
4.0
2.0
1.0
0.5
0.25
0.125
0.0625
1720
1730
1740
1750
1760
Date - C (BJD)
Normalized Power Scaling
4
3
2
1
0
−1
−2
−3
−4

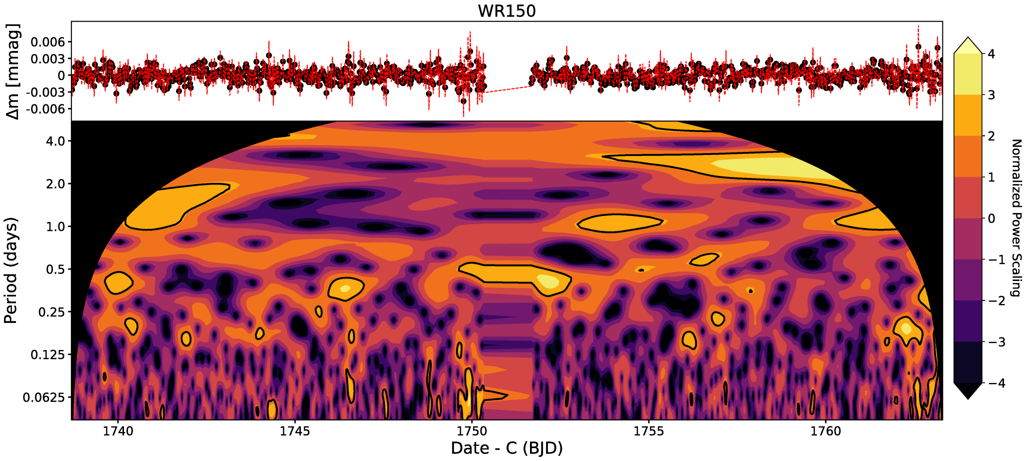
WR150
Δm [mmag]
0.006
0.003
0
-0.003
-0.006
Period (days)
4.0
2.0
1.0
0.5
0.25
0.125
0.0625
1740
1745
1750
1755
1760
Date - C (BJD)
Normalized Power Scaling
4
3
2
1
0
−1
−2
−3
−4

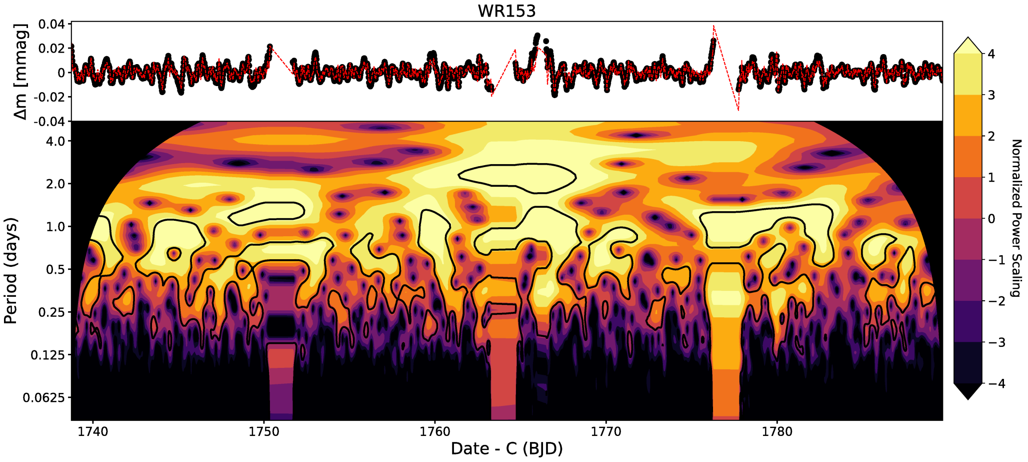
WR153
Δm [mmag]
0.04
0.02
0
-0.02
-0.04
Period (days)
4.0
2.0
1.0
0.5
0.25
0.125
0.0625
1740
1750
1760
1770
1780
Date - C (BJD)
Normalized Power Scaling
4
3
2
1
0
−1
−2
−3
−4

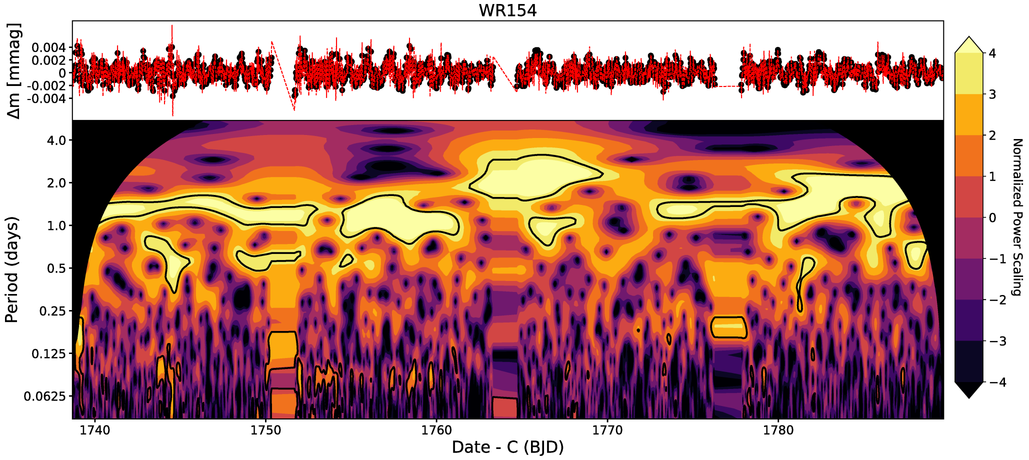
WR154
Δm [mmag]
0.004
0.002
0
-0.002
-0.004
Period (days)
4.0
2.0
1.0
0.5
0.25
0.125
0.0625
1740
1750
1760
1770
1780
Date - C (BJD)
Normalized Power Scaling
4
3
2
1
0
−1
−2
−3
−4

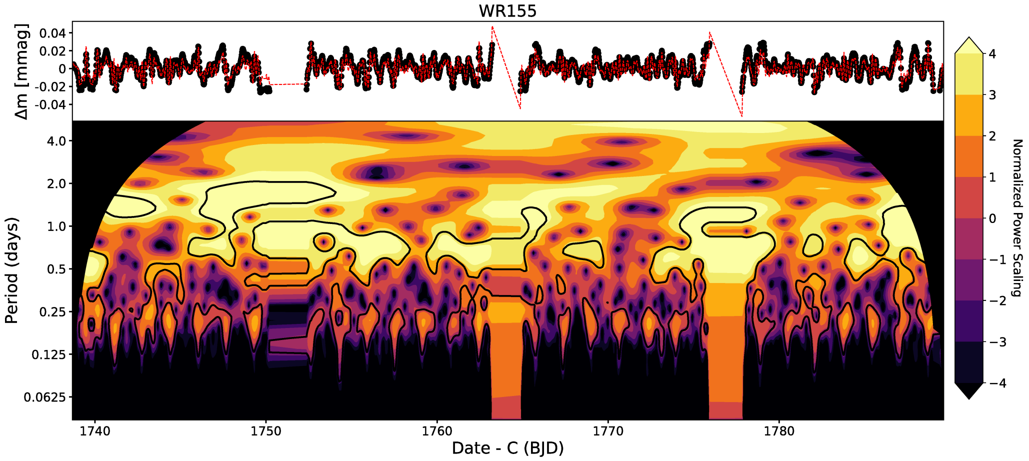
WR155
Δm [mmag]
0.04
0.02
0
-0.02
-0.04
Period (days)
4.0
2.0
1.0
0.5
0.25
0.125
0.0625
1740
1750
1760
1770
1780
Date - C (BJD)
Normalized Power Scaling
4
3
2
1
0
−1
−2
−3
−4

BRITE

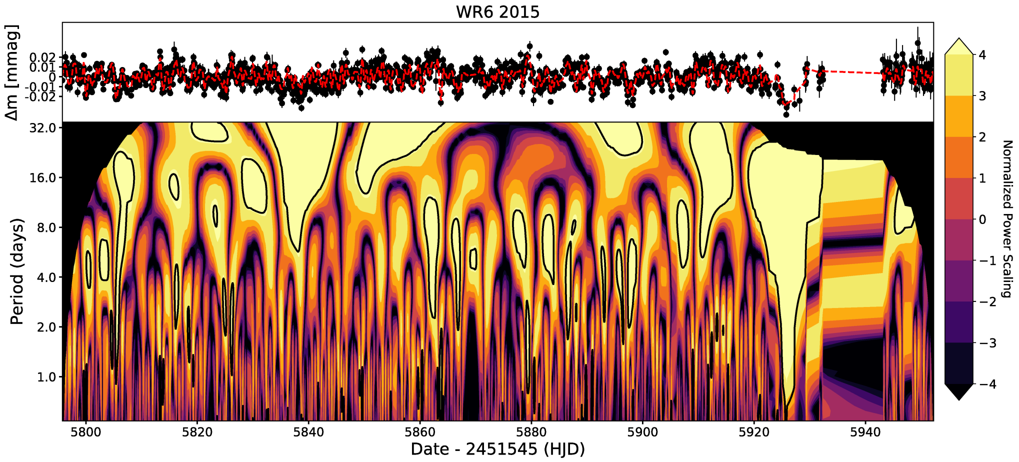
WR6 2015
Δm [mmag]
0.02
0.01
0
-0.01
-0.02
Period (days)
32.0
16.0
8.0
4.0
2.0
1.0
5800
5820
5840
5860
5880
5900
5920
5940
Date - 2451545 (HJD)
Normalized Power Scaling
4
3
2
1
0
−1
−2
−3
−4

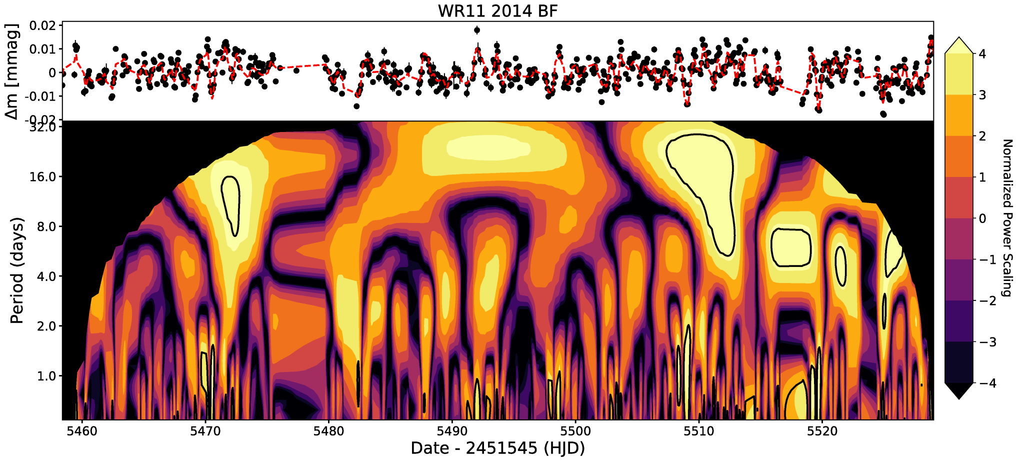
WR11 2014 BF
Δm [mmag]
0.02
0.01
0
-0.01
-0.02
Period (days)
32.0
16.0
8.0
4.0
2.0
1.0
5460
5470
5480
5490
5500
5510
5520
Date - 2451545 (HJD)
Normalized Power Scaling
4
3
2
1
0
−1
−2
−3
−4

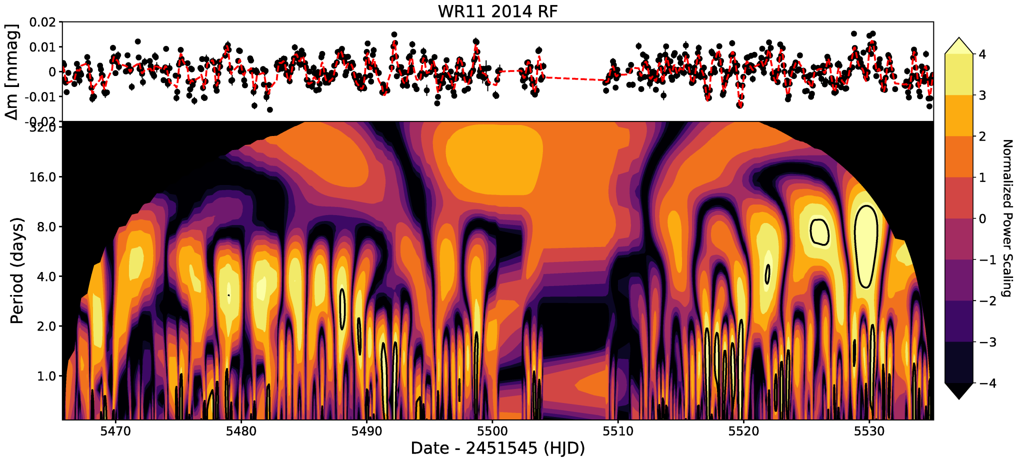
WR11 2014 RF

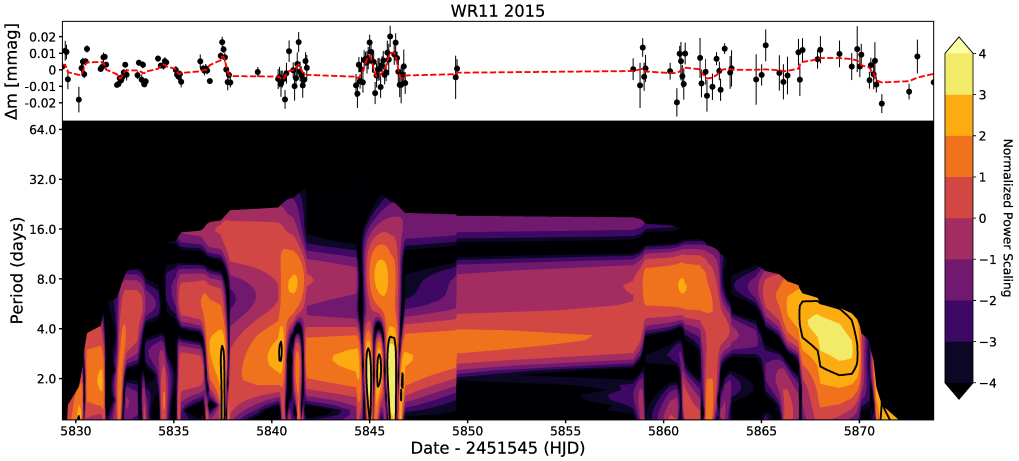
WR11 2015

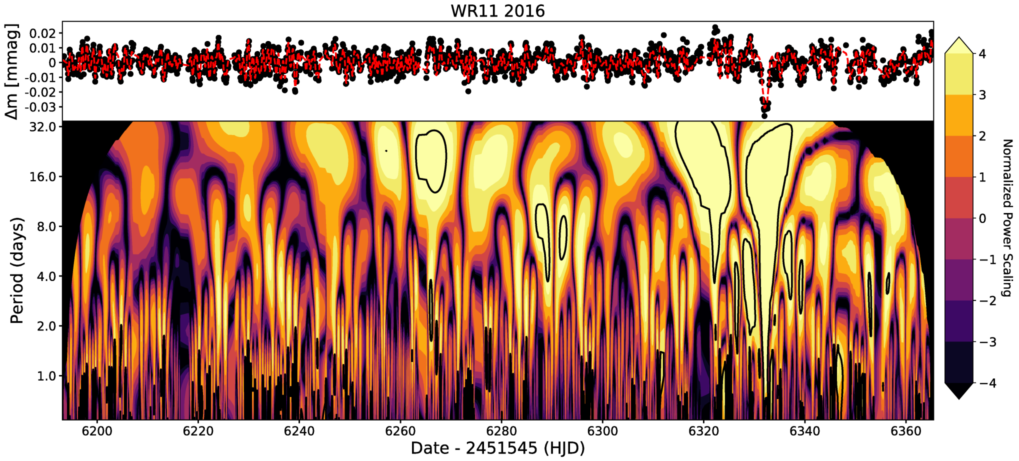
WR11 2016

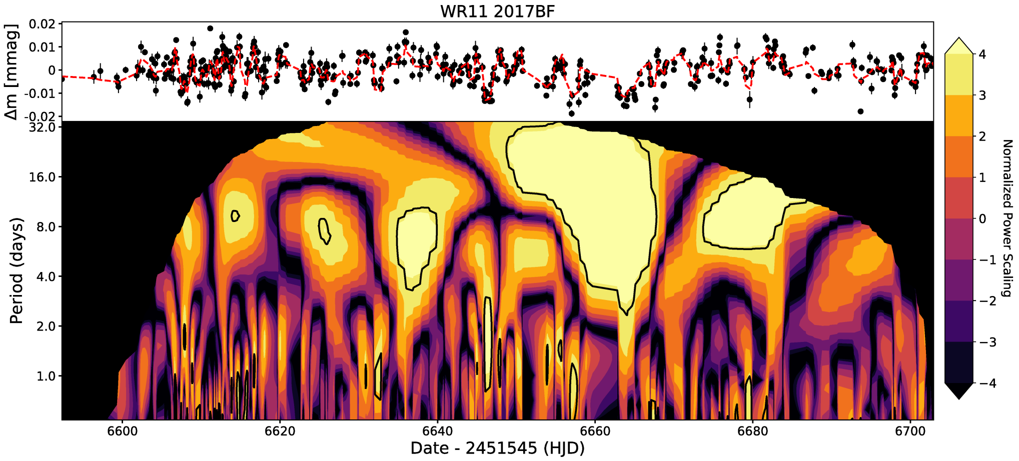
WR11 2017BF

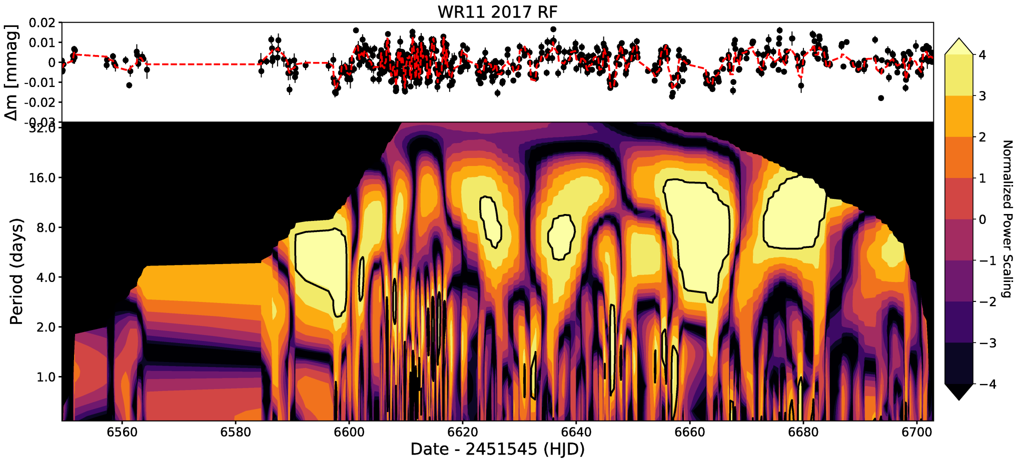
WR11 2017 RF

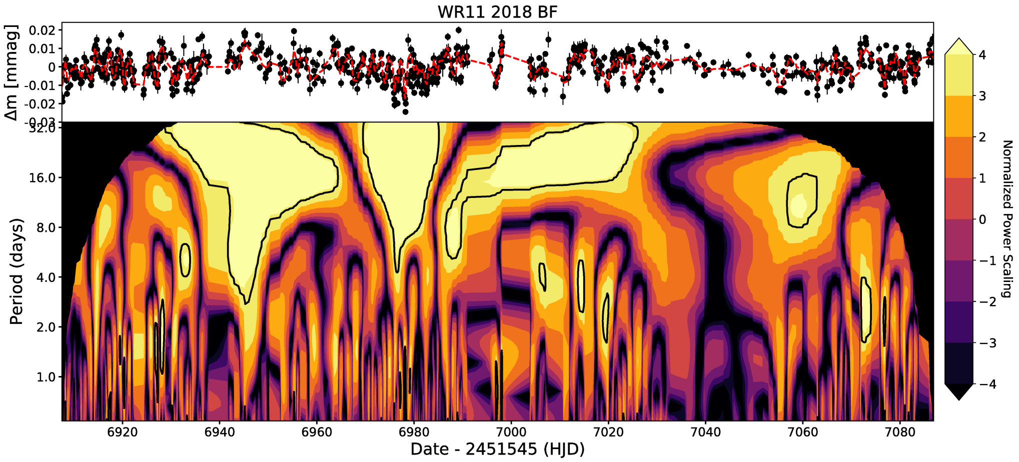
WR11 2018 BF

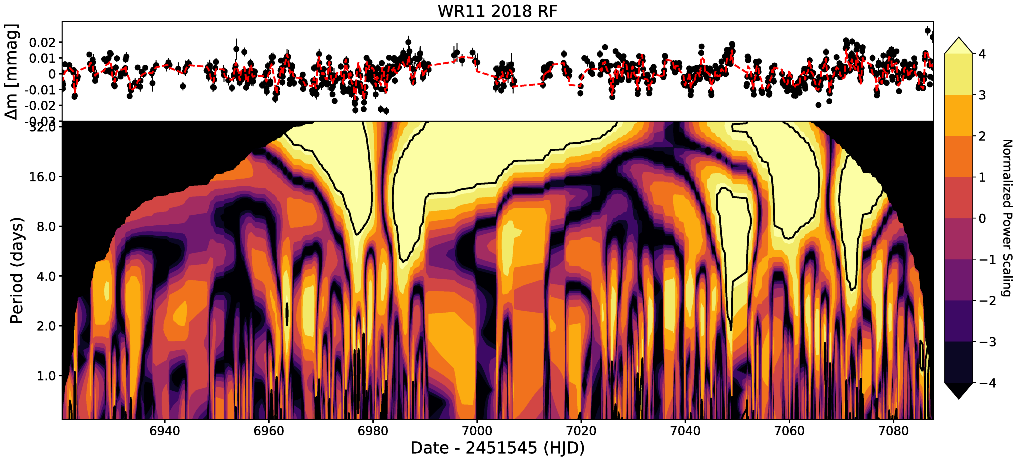
WR11 2018 RF
Δm [mmag]
0.02
0.01
0
-0.01
-0.02
-0.03
32.0
16.0
8.0
4.0
2.0
1.0
Period (days)
6940
6960
6980
7000
7020
7040
7060
7080
Date - 2451545 (HJD)
4
3
2
1
0
−1
−2
−3
−4
Normalized Power Scaling

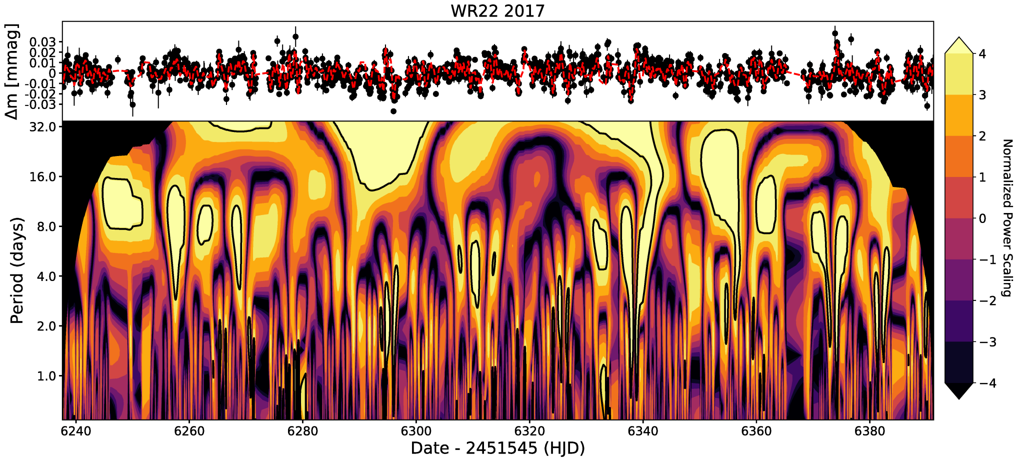
WR22 2017
Δm [mmag]
0.03
0.02
0.01
0
-0.01
-0.02
-0.03
32.0
16.0
8.0
4.0
2.0
1.0
Period (days)
6240
6260
6280
6300
6320
6340
6360
6380
Date - 2451545 (HJD)
4
3
2
1
0
−1
−2
−3
−4
Normalized Power Scaling

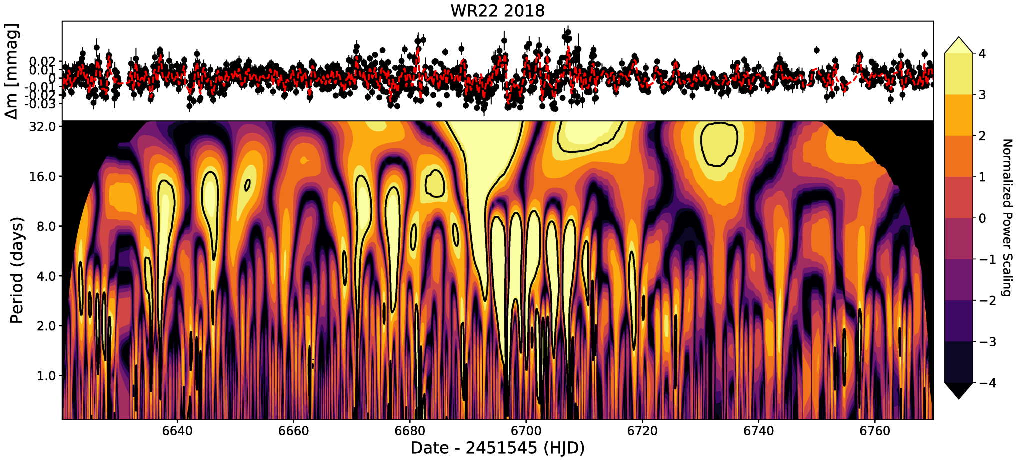
WR22 2018
Δm [mmag]
0.02
0.01
0
-0.01
-0.02
-0.03
32.0
16.0
8.0
4.0
2.0
1.0
Period (days)
6640
6660
6680
6700
6720
6740
6760
Date - 2451545 (HJD)
4
3
2
1
0
−1
−2
−3
−4
Normalized Power Scaling

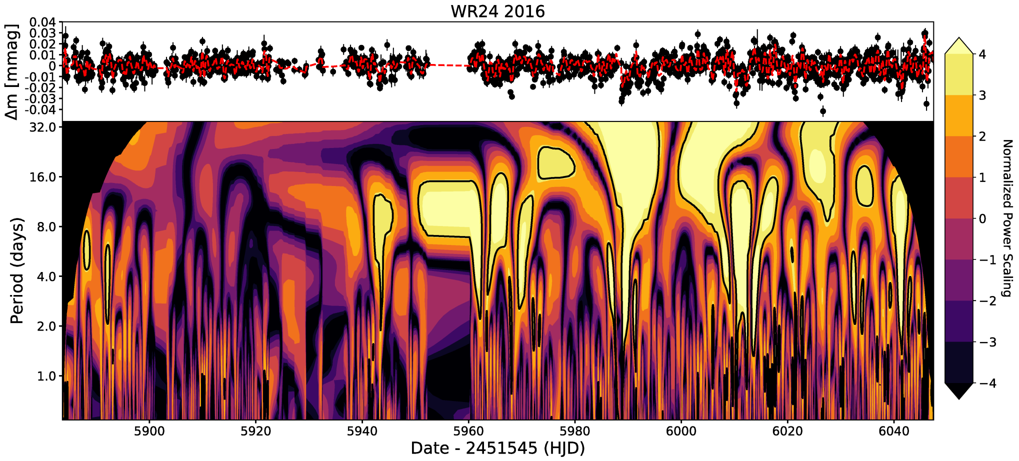
WR24 2016

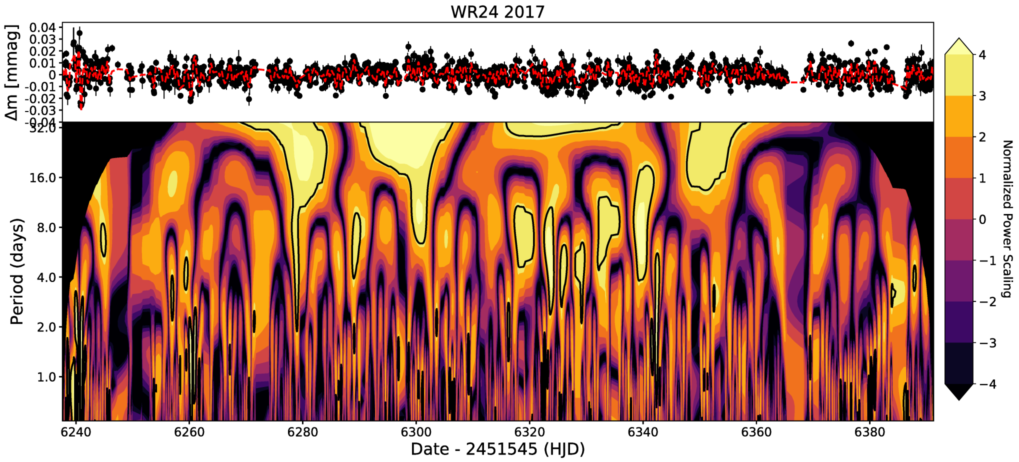
WR24 2017

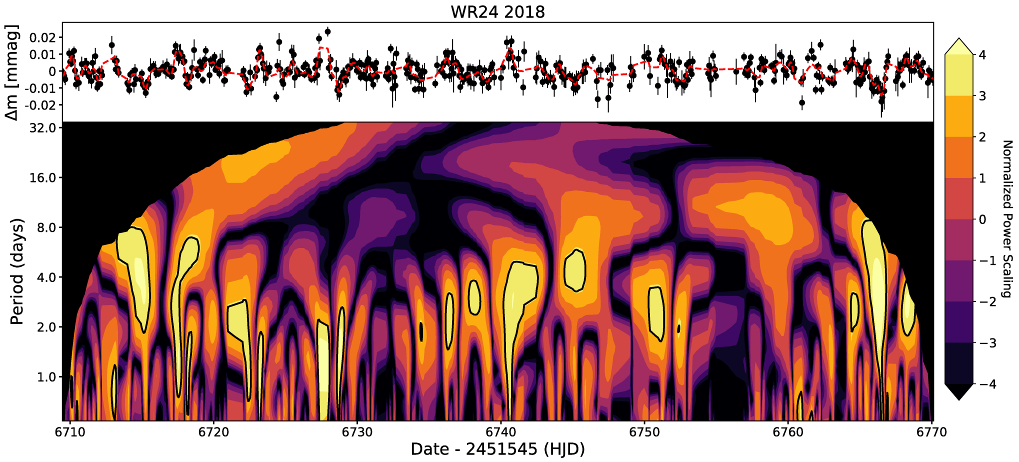
WR24 2018

MOST

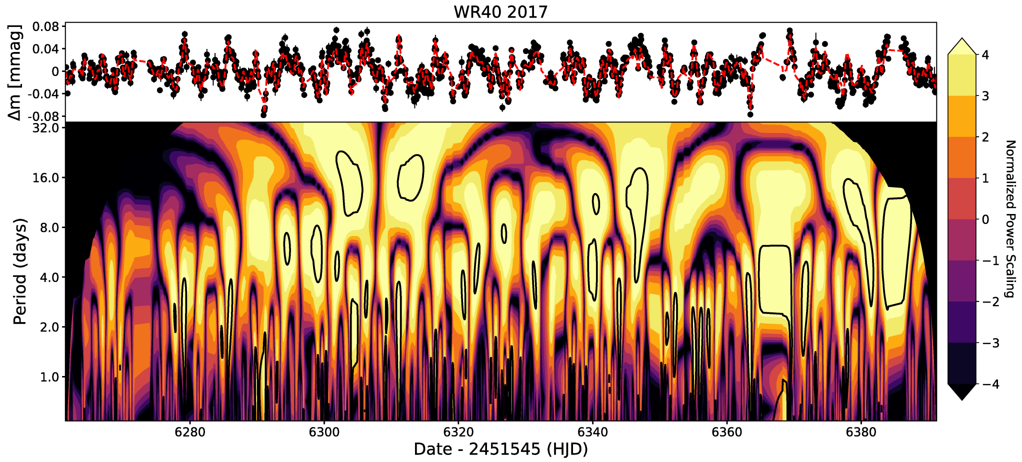

WR40 2017
Δm [mmag]
0.08
0.04
0
-0.04
-0.08
Period (days)
32.0
16.0
8.0
4.0
2.0
1.0
6280
6300
6320
6340
6360
6380
Date - 2451545 (HJD)
Normalized Power Scaling
4
3
2
1
0
-1
-2
-3
-4

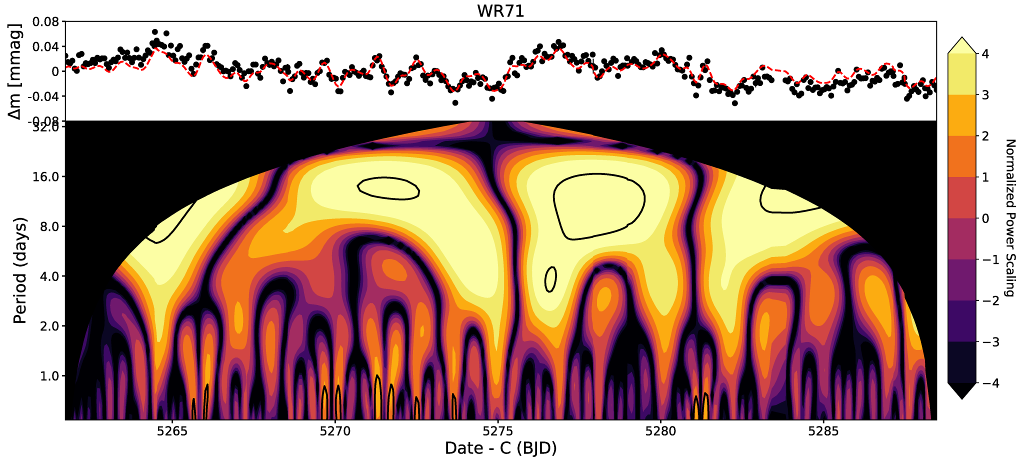

WR71
Δm [mmag]
0.08
0.04
0
-0.04
-0.08
Period (days)
32.0
16.0
8.0
4.0
2.0
1.0
5265
5270
5275
5280
5285
Date - C (BJD)
Normalized Power Scaling
4
3
2
1
0
-1
-2
-3
-4

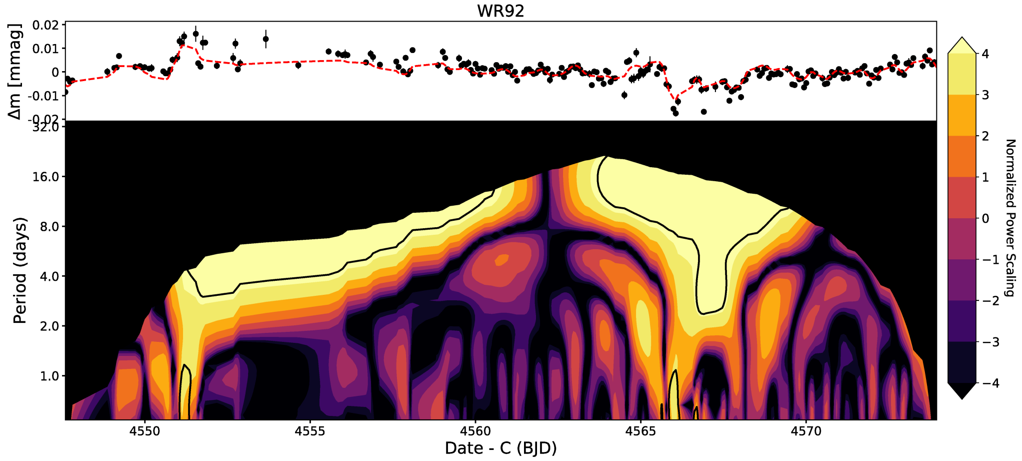

WR92
Δm [mmag]
0.02
0.01
0
-0.01
-0.02
Period (days)
32.0
16.0
8.0
4.0
2.0
1.0
4550
4555
4560
4565
4570
Date - C (BJD)
Normalized Power Scaling
4
3
2
1
0
-1
-2
-3
-4

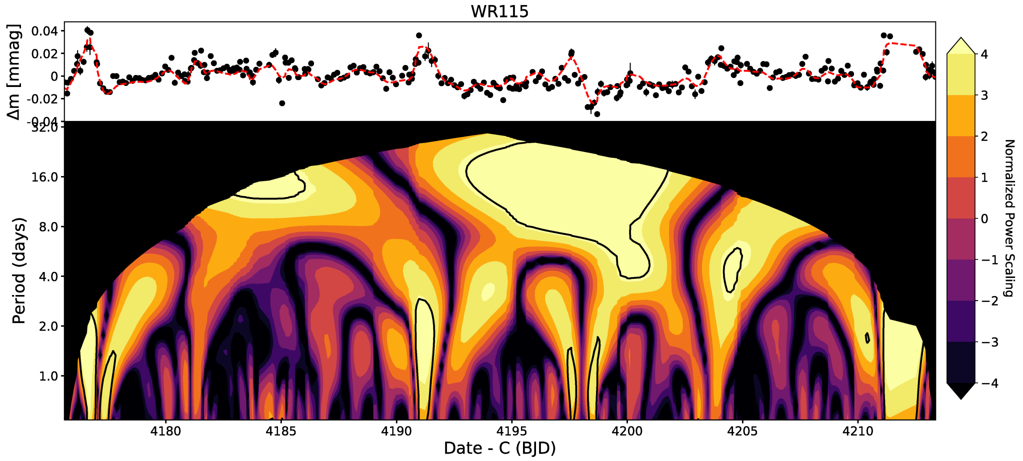
WR115
Δm [mmag]
0.04
0.02
0
-0.02
-0.04
32.0
16.0
8.0
4.0
2.0
1.0
Period (days)
4180
4185
4190
4195
4200
4205
4210
Date - C (BJD)
4
3
2
1
0
−1
−2
−3
−4
Normalized Power Scaling

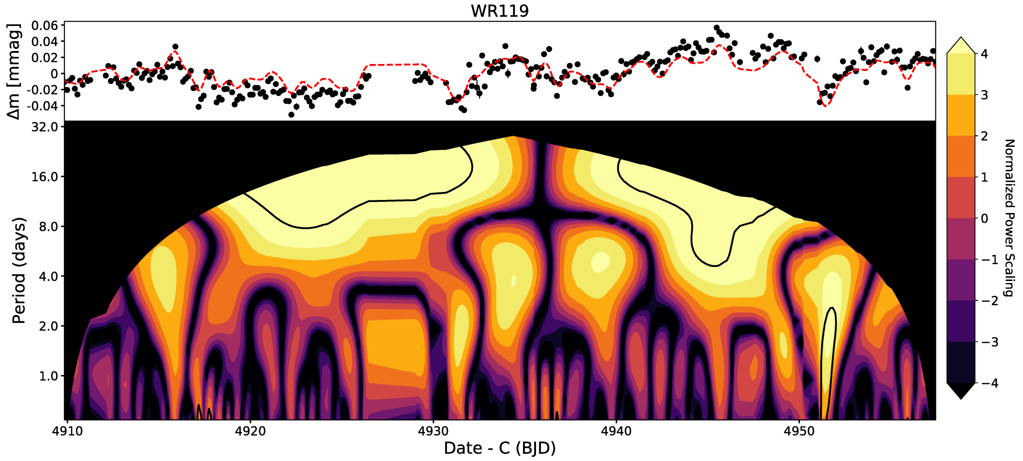
WR119
Δm [mmag]
0.06
0.04
0.02
0
-0.02
-0.04
32.0
16.0
8.0
4.0
2.0
1.0
Period (days)
4910
4920
4930
4940
4950
Date - C (BJD)
4
3
2
1
0
−1
−2
−3
−4
Normalized Power Scaling

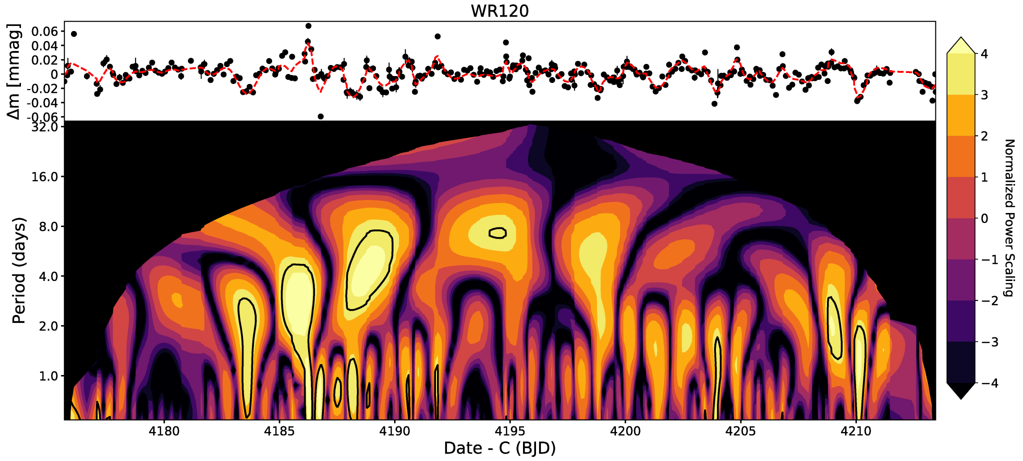
WR120
Δm [mmag]
0.06
0.04
0.02
0
-0.02
-0.04
-0.06
32.0
16.0
8.0
4.0
2.0
1.0
Period (days)
4180
4185
4190
4195
4200
4205
4210
Date - C (BJD)
4
3
2
1
0
−1
−2
−3
−4
Normalized Power Scaling

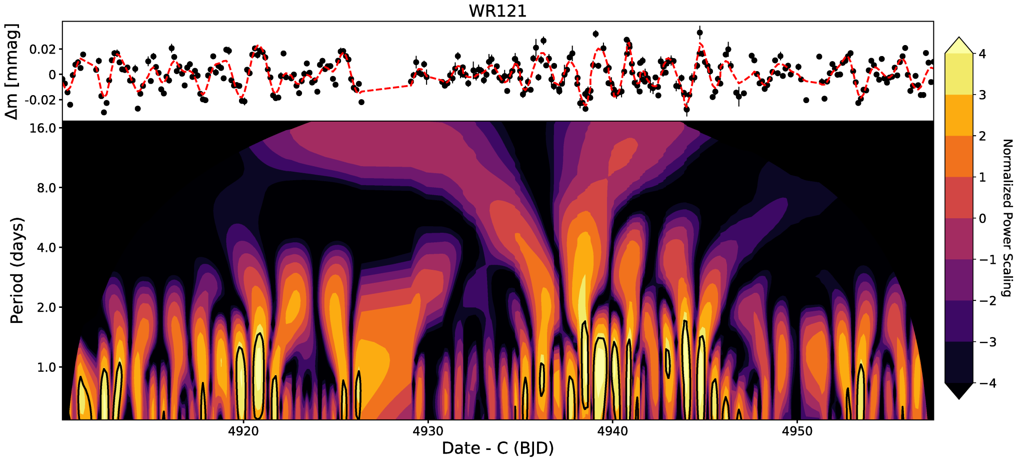
WR121
Δm [mmag]
0.02
0
-0.02
16.0
8.0
4.0
2.0
1.0
Period (days)
4920
4930
4940
4950
Date - C (BJD)
4
3
2
1
0
−1
−2
−3
−4
Normalized Power Scaling